NOTTINGHAM TRENT UNIVERSITY

Non-Equilibrium Polymeric Complex Fluids

by

David Willmer

A thesis submitted in partial fulfillment for the
degree of Doctor of Philosophy

in the
Department of Mathematics and Physics
School of Science and Technology

January 2011

"Physics isn't a religion. If it were, we'd have a much easier time raising money."

Nobel Laureate Professor Leon Lederman

"There is no democracy in physics. We can't say that some second-rate guy has as much right to opinion as Fermi."

Nobel Laureate Luis Walter Alvarez, 1911-1988

"Reports that say that something hasn't happened are always interesting to me, because as we know, there are known knowns; there are things we know we know. We also know there are known unknowns; that is to say we know there are some things we do not know. But there are also unknown unknowns - the ones we don't know we don't know."

Donald Rumsfeld

Abstract

Complex fluids are commercially- and industrially-important materials which exhibit ordering on scales much larger than atomic. Their usage is typically in non-equilibrium conditions, however traditional methods for measuring rheology are not appropriate for measuring samples with gradients present, such as temperature and concentration. In this work a safe and easy to use optical tweezer (OT) apparatus has been developed in order to facilitate the investigation of various systems during dilution or drying. In contrast to other OT setups, this equipment is safe to use without laser goggles or interlocked rooms, yet still allows full access to the microscope. Proof-of-concept experiments are performed on aqueous poly (ethylene oxide) (PEO) solutions to demonstrate the changes in viscosity and concentration over time, and the OT is then used in a rheological investigation into a commercially-relevant wormlike micelle (WLM) system, in conjunction with Diffusing Wave Spectroscopy (DWS) and traditional bulk rheology.

It is shown for the first time that equimolar (eM) SDS:CAPB WLM samples can be considered 'model' systems, and form close approximations of Maxwellian systems on the addition of extra salt or surfactant above 0.1eM. The effect of an uncharged polymer (PEO 4M MW) on this WLM network structure was subsequently investigated; its effects are consistent with current theories of polymer-surfactant interactions. The effect of a conditioning polyelectrolyte on the network structure was also studied; its effect was highly dependent on surfactant and electrolyte concentration, but hinted at the previously unreported behaviour of a polyelectrolyte initiating micellar branching.

A precursor investigation into evaporation of sessile droplets of aqueous PEO solutions is presented last, reporting a previously unseen droplet evaporation regime in which the solid deposits grow to nearly twice their starting height. This research concludes that the growth phenomena is due to the unusual solvation mechanism of PEO, and a predictive theory is presented in support of this.

Acknowledgements

It was Tim Minchin who penned the phrase "*that feeling we all get sometimes, where we're the smallest doll in a Babushka doll*"; I had always assumed that by adhering to the 'rites of passage' of an undergraduate degree and a Ph.D., that my Babushka status would increase. I was completely wrong - the more I have learnt and strived to learn, the more my utter ignorance has become apparent. I believe that this conversion of *unknown unknowns* into *known unknowns* does not come about by a single 'Eureka' moment, but through a long, painful, tiring and frustrating journey involving many hours poring over books in the library and searching for errors in source code which appear to be related to the lunar cycle. The rest of the world call this journey a Ph.D, but I feel the Swahili word for 'journey' gives a much better indication of the excitement and danger encountered - the word is 'safari'. As we all know, even the longest safari starts with a single step, but not many are supported by so many people along the way - people whose only payment is a wholly inadequate mention on a slightly philosophical acknowledgements page. The fact that this thesis exists is therefore testament to the patience and perseverance of the following people:

From NTU; Mike Newton, Glen McHale, Robin Turner, Martin Bencsik, Siddharth Patwardhan, Dave Belton, Rob Morris, Olivier Deschaume, Kyle Brown, Charles Kwartnik, Hans Adriaensen, Sam Lawman and all the guys who played 5-a-side football.

From Unilever; Samiul Amin, Andrea Ferrante and Smita Puntambekar.

From the rest of the world; Tom Bull and Prof. John McBride from Taicaan, Andy Ward from CLF at RAL, Bettina Wolf from Nottingham University and Mike Evans from Leeds University.

I'd like to give special thanks to my supervisor Dr. David Fairhurst for his expert guidance and infectious enthusiasm for all things soft matter, not to mention the tri-country pub crawls.

I thank my sister Karen for constantly calling me up from exotic and far away places, unwittingly putting everything in perspective!

My parents deserve more credit than I can give for putting me through, and putting up with me through, my education - cheers Mum and Dad!

And last but not least, my lovely Laura for looking after me all these years with hugs, kisses and spaghetti bolognaise.

Contents

List of Tables

List of Figures

Abbreviations

AOD	Acousto-Optical Deflector
AT	Acoustic Tweezers
BD	Base Diameter
BFPI	Back-Focal-Plane Interferometry
CAPB	Cocamidopropyl Betaine
CD	Charge Density
CMC	Critical Micelle Concentration
CPBr	Cetyl Pyridinium Bromide
CTAB	Cetyl Trimethylammonium Bromide
DAQ	Data Acquisition
DFT	Density Functional Theory
DH	Droplet Height
DLS	Dynamic Light Scattering
DSA	Drop Shape Analysis
DWS	Diffusive Wave Spectroscopy
eM	equi-Molar
EM	Electromagnetic
ETAW	Evans-Tassieri-Auhl-Waigh
FDT	Fluctuation-Dissipation Theorem
FT	Fourier Transform
FWHM	Full-Width Half-Maximum
GLE	Generalised Langevin Equation
GMM	Generalised Maxwell Model
IACF	Intensity Autocorrelation Function
IR	Infra-red
J	Evaporative flux
LASER	Light Amplification by Stimulated Emission of Radiation
LCD	Liquid Crystal Display
LT	Laplace Transform
MD	Molecular Dynamics
MRI	Magnetic Resonance Imaging
MSD	Mean Squared Displacement
MT	Magnetic Tweezers

MW	Molecular Weight
NA	Numerical Aperture
Nd:YAG	Neodymium-doped Yttrium Aluminium Garnet
NMR	Nuclear Magnetic Resonance
OCT	Optical Coherence Tomography
OT	Optical Tweezer
OTI	Optical Trapping Interferometry
PEG	poly(ethylene glycol)
PEO	poly(ethylene oxide)
pN	picoNewtons
PSD	Power Spectral Displacement
QPD	Quadrant Photodiode
RAL	Rutherford Appleton Laboratory
RPM	Revolutions Per Minute
SAW	Surface Acoustic Wave
SDS	Sodium Dodecyl Sulphate
SEM	Scanning Electron Microscopy
TEM	Transmission Electron Microscopy
TEM_{00}	Transverse Electromagnetic
THF	Tetrahydrofuran
UCST	Upper Critical Solubility Temperature
V	Volume
WD	Working distance
WL	White Light
WLM	Wormlike micelle

Physical Constants

Å	Ångstrom	1×10^{-10}	m
c	Speed of light in a vacuum	$2.997\ 924\ 58 \times 10^{8}$	ms^{-2}
e	Base of the natural logarithm	2.718 281 828 459...	DIMENSIONLESS
i	Square root of -1	$\sqrt{-1}$	DIMENSIONLESS
k_{B}	Boltzmann's constant	$1.380\ 650\ 3 \times 10^{-23}$	$\mathrm{m}^2\ \mathrm{kg}\ \mathrm{s}^{-2}\ \mathrm{K}^{-1}$
N_{A}	Avogadro's number	$6.022\ 141\ 793 \times 10^{23}$	mol^{-1}
π	Ratio of a circle's circumference to its diameter	3.141 592 653 589...	DIMENSIONLESS

1 Introduction

"παντα ρει και ουδεν μενει" (Everything flows, nothing stands still)

Heraclitus, 535-475 B.C.

1.1 Introduction

Fluids are ubiquitous in our daily lives, from the water we drink for hydration to the liquid fuels which ignite in rocket engines. Accurate control and understanding of fluids is therefore of upmost importance to many commercial and industrial processes, as well as being of academic interest. Whilst liquids such as water are relatively well understood[1], there exists a class of substances called 'complex fluids' - where the components exhibit a degree of ordering on scales much larger than atomic - which have revolutionised the world we live in. Plastics, rubber, detergents, liquid crystal displays (LCDs), shampoo, food technology [5, 6] and inkjet printing [7, 8] are all examples of products or techniques which have been made possible or improved by research into complex fluids.

[1] In terms of its long-time behaviour in equilibrium conditions at room temperature, water is relatively well understood. There is much research interest in water as it has been shown, for example, to be viscoelastic at picosecond time scales [4].

One example of a complex fluid is formed when surfactant[2] molecules self-assemble into structures called 'wormlike micelles' (discussed in detail in §2.3.2), which are pumped underground by energy companies in order to extract more hydrocarbons using less energy [9]. The same micellar network structures are used in shampoos and conditioners in order to deposit active material such as silicone on hair [10, 11, 12], and a different variety of micelles are under investigation as a method for enhancing drug delivery by the pharmaceutical industry [13, 14].

Whilst the static properties of these fluids are relatively well understood, their industrial value depends on their dynamic, or non-equilibrium properties, for which as yet there is no comprehensive theory [15, 16, 17, 18]. One example of this is with the molecule poly(ethylene oxide) (PEO) (discussed in detail in §2.4); this molecule is used as a viscosifier in many food [19] and personal care products [20], yet is also used to reduce turbulence in fire hoses [21], two effects which may appear to be contradictory, but are the result of a change in the Reynold's number.

The research presented here looks at the non-equilibrium properties of various commercially-relevant complex fluids.

1.1.1 Thesis Layout and Motivation

This research was partially funded by Unilever PLC who are interested in understanding the non-equilibrium properties of their products such as shampoo, detergent, deodorant and food. In order to create a solid basis for further research, we started with a one-component polymeric system and investigated the effects of concentration gradients. A concentration gradient can be introduced in one of two ways; either an overall increase

[2] *Surfactant* is a portmanteau of *surface active agent*, referring to molecules which decrease surface tension, typically due to opposite ends having hydrophobic and hydrophilic properties.

in concentration is created through evaporation, or a decrease through dilution. Evaporation was investigated first as it is easier to perform, and this was then extended to dilution later, as this is more relevant to Unilever's products. A brief description of the various chapters is included below.

Chapter 2 - On the Physics and Rheology of Polymers in Solution

All the work presented in this thesis concerns either 'standard' polymers or 'living' polymers, so this chapter presents an overview of polymer physics, with special attention paid to poly(ethylene oxide) which is used throughout. Many measurements shown in this work are rheological studies of polymers, therefore an introduction to the field of rheology is also included.

Chapter 3 - Optical Tweezers and their use with Complex Fluids

A type of laser trap called an 'optical tweezer' (OT) has been employed to study complex fluids during dilution, of which multiple geometries were designed and built in order to find the most effective solution. This chapter comprises an in depth study into the physics, engineering and operation of these OTs, with some proof-of-concept experiments performed for later work.

Chapter 4 - Wormlike Micelle Rheology and Microrheology

A common component of Unilever's products is the aforementioned wormlike micelle (WLM) network structure. This chapter reports an investigation undertaken into the behaviour in equilibrium and non-equilibrium conditions of a 'model' WLM system, whilst the system complexity was gradually increased towards a commercially-viable system.

Chapter 5 - Bootstrap droplets

The investigation into evaporating sessile droplets is presented with experimental data from aqueous PEO samples in the context of current evaporation theories, and ends with a proposed theory attempting to explain the behaviour shown.

2

On the Physics and Rheology of Polymers in Solution

"I have stretched ropes from steeple to steeple; garlands from window to window; golden chains from star to star, and I dance."

Arthur Rimbaud, 1854-1891

2.1 Introduction to Polymeric Complex Fluids

Complex fluids are liquid states of matter in which small scale ordering at the atomic or molecular level induces macroscopic behaviour that is not seen in so-called 'simple' fluids. Examples of such ordering include micelles, spherical vesicles, hexagonal packing and lamellar phases; the richness of behaviour in complex fluids comes directly from this ordering. Typically the rearrangement dynamics that occur when a stress is applied are frequency dependent, and the bulk system may display fluid- or solid-like properties depending on the nature of the perturbation.

All fluids have a characteristic property called viscosity η, a measure of the resistance to the rate of deformation, defined as a coefficient relating the shear stress σ to the shear rate $\dot{\gamma}$ where $\sigma = \eta\dot{\gamma}$. Whilst complex fluids also have a viscous property, the entanglements

between network structures can store energy when compressed; the attempt to minimise the energy stored in entanglements produces a bulk elastic response. As a result these fluids are termed *viscoelastic*, and whether the fluid stores (elastic regime) or dissipates energy (viscous regime) depends on the timescale of the applied force. This elastic response can also be considered a coefficient, giving $\sigma = E\gamma$, where E is Young's modulus of the sample[1].

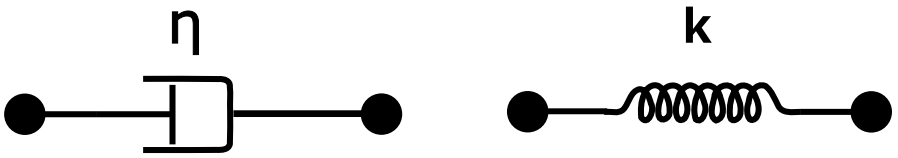

FIGURE 2.1: Schematic diagram showing a dashpot and a spring, representative of the viscous and elastic moduli, respectively. The elastic component from the spring is usually referred to as E or G in polymer systems, however in this analogy it is shown as the spring constant k.

In macroscopic physical terms the elastic and viscous responses are analogous to springs and dashpots[2] respectively, as shown in Figure 2.1. In series, these two components create a mechanical representation of the Maxwell model of viscoelasticity, and in parallel they form the Kelvin-Voigt model [22, 23]. A consequence of this behaviour is that the boundary between solid and liquid becomes harder to define, with many materials showing properties consistent with both liquids and solids, depending on how the measurement is performed.

[1] E and G are the elastic modulus and shear modulus, respectively, however they are proportional for incompressible elastic materials.

[2] A dashpot is a piston filled with viscous material.

2.2 Theoretical and Experimental Rheology

For experimental measurement of samples with frequency-dependent behaviour, an oscillation can be applied with varying periodicity to extract rheological parameters[3]. Traditionally this has been performed using a cone and plate rheometer as shown in Figure 2.2.

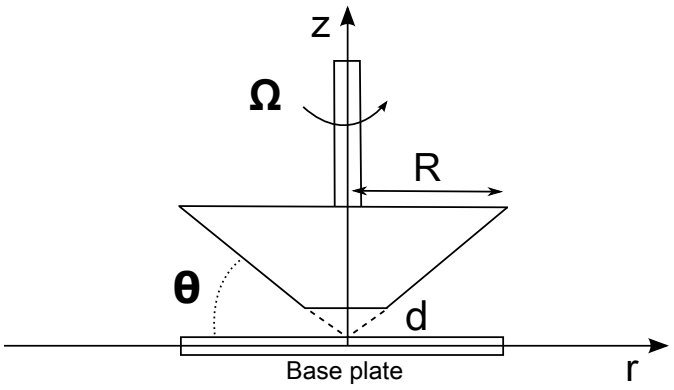

FIGURE 2.2: Schematic of cone and plate geometry for bulk rheology, where θ is the cone angle, Ω is the rotation speed of the cone, R is the cone radius and d is the distance between the tip of the cone and the base plate.

A truncated cone with a very shallow cone angle is placed at a precise distance d away from a flat plate; d is the distance from the plate the tip of the cone would be if the untruncated cone were placed with the tip just touching the base plate. There is usually a torque sensor on the shaft of the cone, and either the cone or the plate can be used to drive the sample. There are two main methods for measuring rheological parameters using a mechanical rheometer; strain-controlled or stress-controlled. In a strain-controlled rheometer a motor is used to drive the cone shaft at a given speed, and the torque spring attached to the base plate measures the torque required to keep the plate static. In a stress-controlled rheometer the drive shaft is given a constant torque, and the rotation of the cone is measured using an optical encoder [24, 25, 26]. Due to the differences in force application a strain-controlled rheometer performs experiments that are suited to

[3]Frequency-dependent behaviour can also be extracted using non-oscillatory methods, such as creep experiments.

stress relaxation experiments, and a stress-controlled rheometer performs experiments in a method similar to a shear creep test. Further to this, during shear an elastic sample will exert a small but measurable force on both the cone and plate from which the first normal stress difference can be calculated.

Rheological experiments require the measurement of η; to achieve this with a cone and plate geometry one requires σ and $\dot{\gamma}$. The shear stress σ in the sample can be found by considering the torque $\mathbb{T}$ on the cone [25, 27], which for Newtonian fluids is given by;

$$\mathbb{T} = \frac{2\pi R^3 \ \sigma \ \cos^2\theta}{3} \tag{2.1}$$

where R is the radius of the cone, θ is the cone angle and σ is the stress at the cone. Where θ is small, $\cos\theta \approx 1$, $\therefore$

$$\sigma = \frac{3\mathbb{T}}{2\pi R^3} \tag{2.2}$$

which is independent of r, θ and ϕ, and therefore σ is constant across the sample. For non-Newtonian fluids, the equivalent calculation yields

$$\mathbb{T} = \frac{2R^3\dot{\gamma}\eta(\dot{\gamma})}{3} \tag{2.3}$$

where the shear rate $\dot{\gamma} = \frac{\Omega}{\theta}$, where Ω is the rotation speed of the cone [28]. $\dot{\gamma}$ is also constant throughout the sample due to the small angle approximation mentioned previously, therefore measuring the torque $\mathbb{T}$ as a function of the rotation speed Ω yields rheological data directly.

If a sinusoidal stress is applied to a viscoelastic sample, the strain response contains both an in phase (elastic) and an out of phase (viscous) sinusoidal component, where the phase angle between the stress and the strain is δ. Thus the forced oscillation can be defined as

$$\gamma(t) = \gamma_0 e^{iwt} \tag{2.4}$$

where γ_0 represents the strain amplitude [29]. The shear stress can therefore be expressed as

$$\sigma(t) = \sigma_0 e^{i[\omega t+\delta]}. \tag{2.5}$$

Given these two definitions a complex shear modulus G^* can be defined as

$$G^* = \frac{\sigma(t)}{\gamma(t)} = \frac{\sigma_0}{\gamma_0}(\cos\delta + i\sin\delta) = \mathrm{G}' + \mathrm{iG}'', \tag{2.6}$$

where G' and G'' are the storage and loss moduli, respectively. The storage modulus (G') represents the elastic energy stored by the system (the spring component), and the loss modulus (G'') represents the energy dissipated due to viscous forces (the dashpot component).

In order to fully explain the rheological parameters introduced in the remainder of this chapter, I will now show some example data from a bulk rheology experiment.

Figure 2.3 shows representative rheology data from an oscillation experiment performed on an ARES LS1 rheometer. The storage and loss moduli (G' and G'', respectively) are

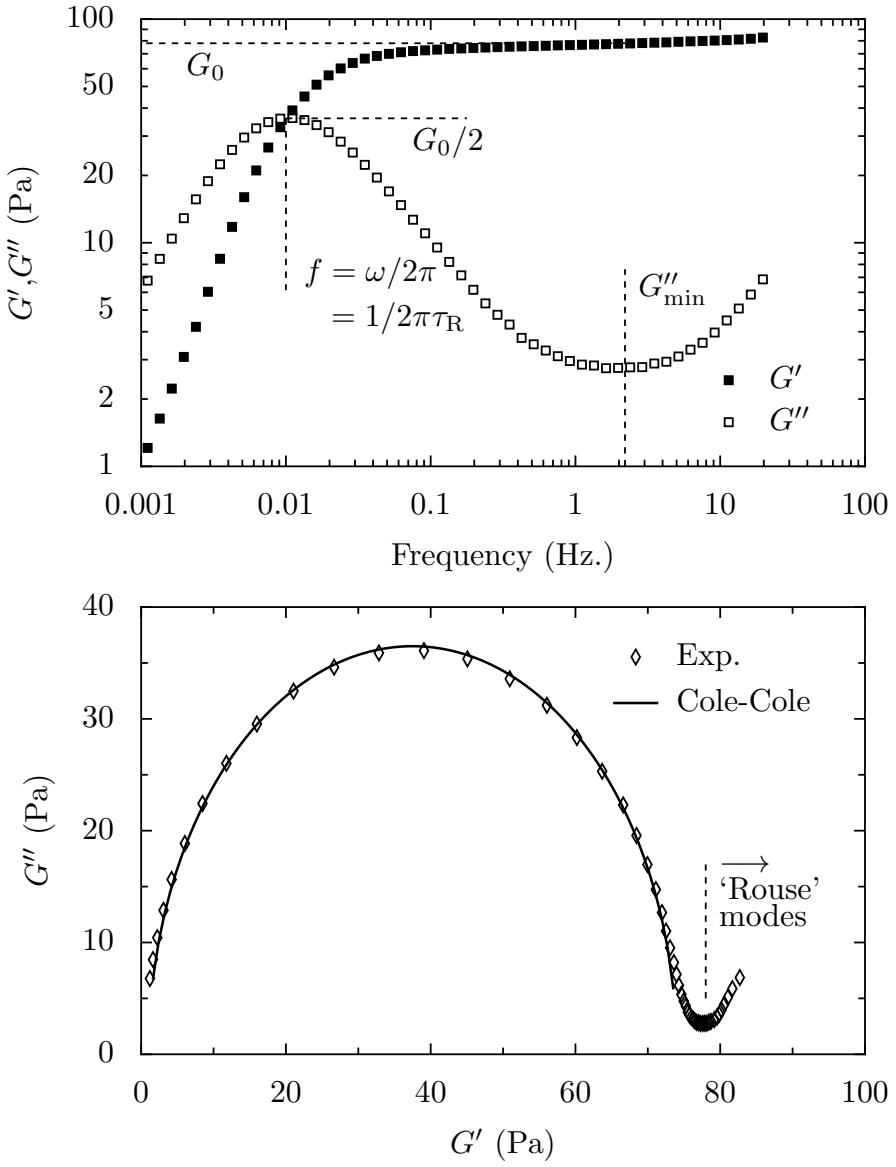

FIGURE 2.3: Representative rheology data for a Maxwellian fluid; experimental data is from the bulk rheology of 0.1 equi-Molar SDS:CAPB wormlike micelle (WLM) system performed on an ARES LS1 rheometer (explained in detail in §4). **Upper:** G',G'' vs ω, where G_0 is the plateau (elastic) modulus at $f = G''_{\text{min}}$, **Lower:** $G''(G')$, known as a 'Cole-Cole' plot for the same data (discussed in §2.2.1).

shown on the upper graph, and the parameters used in the rheological data throughout this work are labelled with dashed lines. G_0 is the plateau modulus, which indicates a highly elastic system when the plateau is well-defined. The minima in G'' (labelled G''_{min}) indicates the frequency at which we take $G' = G_0$. The frequency f at which G' and G''

cross is equal to $\frac{1}{2\pi\tau_R}$ where τ_R is the relaxation time of the system[4]. This relaxation time τ_R indicates the conversion from viscous- to elastic-dominated behaviour; the larger G' values for $f > \frac{1}{2\pi\tau_R}$ show that elasticity dominates, and conversely the larger G'' values for $f < \frac{1}{2\pi\tau_R}$ show that viscous effects dominate. At these low frequencies in the viscous region, $G' \to \omega^2$ and $G'' \to \omega$ for this sample. This is referred to as the *terminal region*, and is important in later calculations. The lower graph shows $G''(G')$, the importance of which is described in §2.2.1 and §2.2.2.

If a shear is applied to a material and σ is linearly proportional to $\dot{\gamma}$, the deformation is said to be in the *linear viscoelastic regime*,

$$\sigma(t) = \int_{-\infty}^{t} G(t-t')\dot{\gamma}(t')dt', \tag{2.7}$$

where $G(t)$ is the relaxation modulus. For polymeric complex fluids this usually occurs when the applied force is small. For a Newtonian fluid, the relaxation modulus $G(t) = \eta\delta(t)$ (where $\delta(t)$ is the phase angle, not the Dirac delta function), and substituting into Equation 2.7 gives

$$\sigma(t) = \int_{-\infty}^{t} \eta\delta(t-t')\dot{\gamma}(t')dt' = \eta\dot{\gamma}(t). \tag{2.8}$$

Rheological measurements in the non-linear viscoelastic regime are possible, but are more complex and harder to interpret; in this work all experiments were performed in the linear viscoelastic regime.

[4]In this work all rheological data is presented in Hertz, where traditionally it may have been given in radians/sec. This work compares microrheological data (optical tweezers and Diffusing Wave Spectroscopy, both introduced later) with bulk rheology experiments; since no oscillatory stress is being applied in the passive microrheological work, I think it inappropriate to deal with radians. However, where quantitative τ_R values are given, they are calculated as $\frac{1}{\omega_{G'=G''}}$ where angular frequency ω is in radians/sec ($\omega = 2\pi f$).

The complex viscosity η^* is the complex shear modulus divided by the angular frequency,

$$\eta^* = \frac{G^*(\omega)}{i\omega}, \tag{2.9}$$

the magnitude of which can be calculated by $\frac{|G^*(\omega)|}{\omega}$ [29].

The zero-shear viscosity η_0 is the viscosity a sample has when unperturbed, i.e. in the low-shear limit. η_0 is related to the plateau modulus multiplied by the characteristic relaxation time [29],

$$\eta_0 \approx G_0 \tau_R, \tag{2.10}$$

and can be approximated by extrapolating η^* to the low-frequency limit, however the measurement of η_0 is only valid when the Cox-Merz rule applies [30].

2.2.1 Maxwellian Fluids

A perfect Maxwellian fluid is one which can be described by a single relaxation time, where the mechanical representation is an ideal spring and dashpot in series as mentioned in §2.1. In a viscoelastic Maxwell fluid, the storage and loss moduli are given by

$$G' = G_0 \frac{(\omega\tau_{\mathrm{R}})^2}{1 + (\omega\tau_{\mathrm{R}})^2} \tag{2.11}$$

$$G'' = G_0 \frac{\omega\tau_{\mathrm{R}}}{1 + (\omega\tau_{\mathrm{R}})^2} \tag{2.12}$$

where τ_{R} is the characteristic relaxation time of the system. Using these definitions one can show that the intersection of G' and G'' (shown in Figure 2.3) is given by

$$\begin{aligned} G' &= G'' \\ G_0 \frac{(\omega\tau_{\mathrm{R}})^2}{1+(\omega\tau_{\mathrm{R}})^2} &= G_0 \frac{\omega\tau_{\mathrm{R}}}{1+(\omega\tau_{\mathrm{R}})^2} \\ \omega\tau_{\mathrm{R}} &= 1 \end{aligned} \tag{2.13}$$

which gives the characteristic relaxation time as

$$\tau_R = \omega^{-1}_{G'=G''}. \tag{2.14}$$

This allows us to quantify the relaxation processes in a system from the rheological data. Maxwellian fluids can be easily determined using the following criteria [11], as shown on Figure 2.3;

- G' intersects with G'' at G''_{max}
- $G''_{max} \approx \frac{G_0}{2}$
- $\frac{\eta_0}{G_0} \approx \frac{1}{\omega_{G'=G''}}$

where η_0 is the zero shear viscosity and G_0 is the plateau modulus, or elastic modulus, which is a measure of the elasticity of the system. This last definition shows the two methods of calculating τ_{R}; the closer these two quantities are, the narrower the spectrum of relaxation times.

The quintessential observation which denotes a Maxwellian fluid is a semi-circular Cole-Cole plot (see §2.2.2), where a semi-circle represents a singular relaxation time, as one would expect from a spring and dashpot in series. A consequence of these definitions is that where a Cole-Cole plot cannot be fit with a semi-circle, one must assume the existence of additional relaxation times, equivalent to extra springs and dashpots in parallel with each other as shown in Figure 2.4.

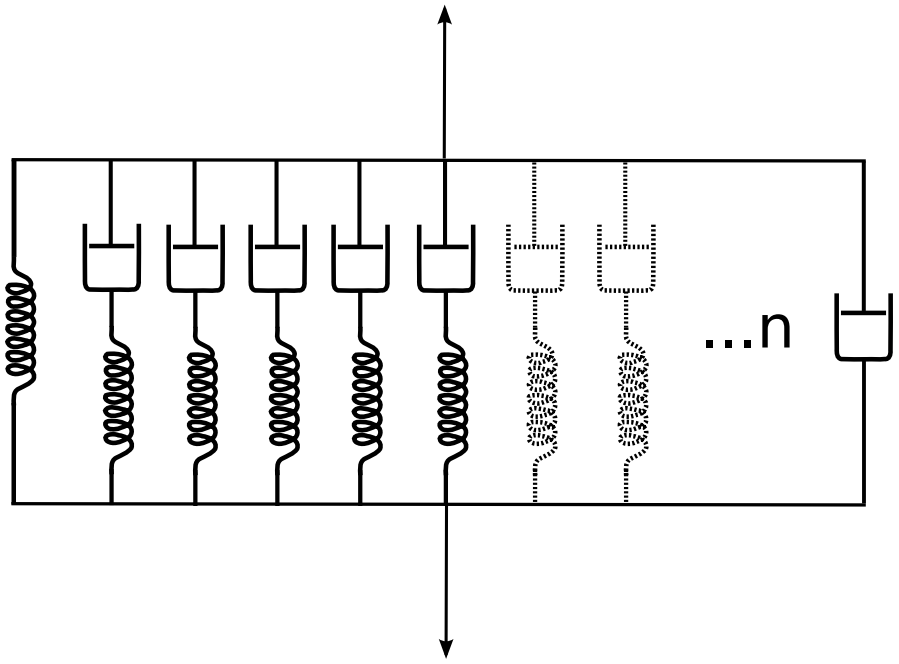

FIGURE 2.4: Generalised Maxwell Model (GMM) shown as a mechanical representation of springs and dashpots.

Figure 2.4 shows the Generalised Maxwell Model (GMM) for viscoelasticity in a mechanical representation of springs and dashpots in parallel. Each spring and dashpot set represents a relaxation time of the system, for as many τ_R values as are necessary to fully describe the behaviour. The GMM model gives limited insight into rheological behaviour as the relaxation times are still described by discrete spring-dashpot pair parameters rather than a continuous spectrum.

2.2.2 Cole-Cole Plots

Cole and Cole [31] were working on dielectric relaxation, and subsequently modified the Debye equation to account for discrepancies between theoretical and experimental values. They proposed that the distribution of relaxation times in a dielectric system could be described by

$$\epsilon^*(i\omega) - \epsilon_\infty = \frac{(\epsilon_s - \epsilon_\infty)}{1 + (i\omega\lambda)^{(1-\alpha)}} \tag{2.15}$$

where λ is the dielectric relaxation time, α is the dispersion parameter, and which reduces to the Debye equation when $\alpha = 0$ [32]. It was subsequently shown by Havriliak and Negami [33] that the molecular mechanisms underlying dielectric relaxation and mechanical relaxation are identical (above the glass transition temperature T_g [34]); as a result the Cole-Cole plot has become widely used when quantifying polymeric systems [35, 36, 37].

2.2.3 Protocol for bulk rheology experiments

In order to ensure that these rheological studies were accurate and repeatable, the following protocol was used in all mechanical rheology experiments;

1. The sample was placed carefully on the rheometer base plate.

2. The cone was lowered slowly, in stages, with the excess sample cleaned at each stage (care was taken with the removal of excess so as not to fracture the sample/-meniscus).

3. A solvent trap was placed over the cone and plate geometry to inhibit evaporation from the sample (this allowed experiments up to ∼4 hours before the sample had to be re-loaded).

4. The sample was left to equilibrate for a minimum of 5 minutes.

5. A strain sweep test was performed from low to high strain in order to find the linear response region (ie. the maximum strain value for which the sample can still be considered to be in the linear viscoelastic regime); this step is clarified below.

6. The sample was left to equilibrate for a minimum of 5 minutes.

7. A frequency sweep test was performed from high to low frequency, with a fixed strain set around the middle of the linear region found previously (in all experiments the strain was between 7-10%).

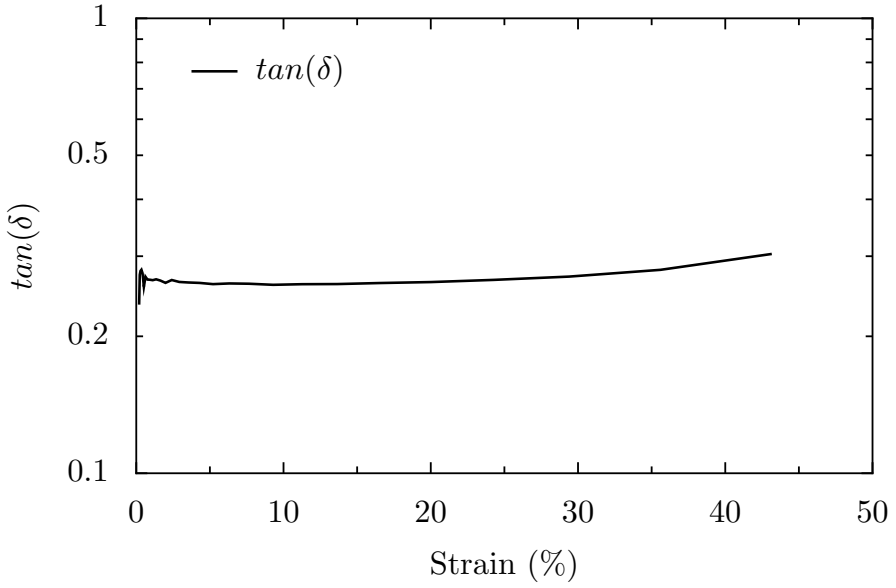

FIGURE 2.5: $tan(\delta)$ against strain for a strain sweep performed as part of the bulk rheology experimental protocol for a WLM sample.

Figure 2.5 shows the data from a strain sweep performed as described in the experimental protocol above. The strain is initially at a low value ($< 1\%$), and is gradually increased until the $tan(\delta)$ value starts to rise. At this point, $\approx$ 30-40% in Figure 2.5, the

strain is sufficiently high that the sample can be considered to be entering the non-linear viscoelastic region. The linear region is signified by the large plateau between $\sim$ 5-30% strain. A value within the linear region was then set for the constant strain value during the frequency sweep, which was usually around 10% for the samples in this work.

To confirm that this protocol does not damage the sample, a highly entangled multi-component system was chosen for a study in which 5 experiments were performed;

1. The experiment was performed as described above.
2. The experiment was performed with an additional pre-shear of 1/s for 120 s. immediately before the frequency sweep.
3. The same sample as for the pre-shear test above was left for 20 minutes (it was not re-loaded), and a frequency sweep was performed.
4. The same sample as for the previous 2 experiments was left for a further 20 minutes (40 minutes in total, sample not re-loaded), and a frequency test was performed.
5. The sample was re-loaded and the original protocol described was performed again (ie. the same as experiment 1 in this study).

Figure 2.6 shows the change in behaviour between the original and re-loaded samples with identical experimental protocols (Experiments 1 and 5 above). The plateau modulus shows no discernible change, and there are only minor variations in G'', which can be considered within experimental error. We can therefore be confident that the experimental protocol produces consistent behaviour.

Figure 2.7 shows the rheological changes in the system when a pre-shear is applied to the sample (Experiments 1,2 and 3 above). The pre-shear was at a constant rate of 1/s

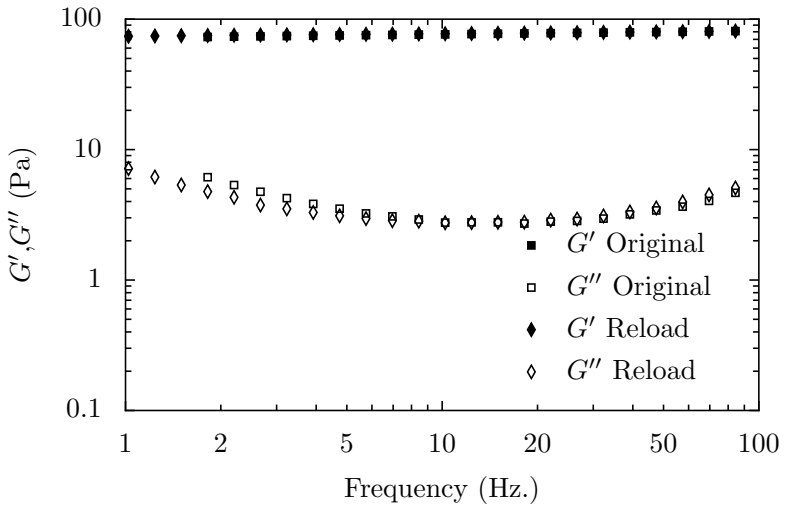

FIGURE 2.6: Viscoelastic moduli for an entangled, multi-component system. This shows the difference in results when the sample is reloaded, with identical experimental protocols. For clarity the data has been truncated between 1-100Hz.

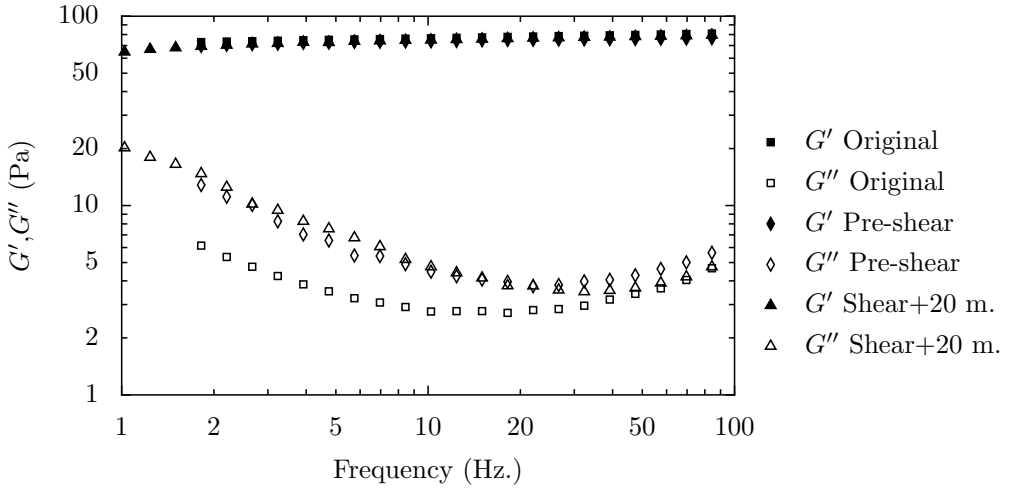

FIGURE 2.7: Viscoelastic moduli for an entangled, multi-component system. The original data is the same as that shown in Figure 2.6, the Pre-shear shows the sample which was pre-sheared at 1/s for 120s, and the 'Shear+20m.' data is the same sample after a 20 minute delay, as described above.

for 120 s., and was immediately followed by the frequency sweep. The data labelled 'Original' is the same as that in Figure 2.6. The pre-shear changed the system rheology significantly, seen in the large deviations in G'', however the plateau modulus remained constant throughout. This shows that the elasticity of the system was not affected by the pre-shear, but the viscous component was affected. The triangles show the same frequency sweep performed after a 20 minute delay, and show that at short times (f >50

Hz.) the G'' behaviour has returned to its original state, but at long times the shear-effect remains. We can therefore conclude that the sample is sensitive to its shear history, but the original measurements were of the sample in its equilibrium state, to which the sample gradually returns over time. In conjunction with the data from Experiments 1 and 5 above, this shows that the loading protocol does not induce sufficient shear to affect the sample rheology. We can also see that as the sample equilibrates to its original state, the high frequency behaviour is the quickest to change. The data from Experiment 4 (40 minute delay) showed no obvious change from Experiment 3 (20 minute delay), and therefore for clarity was removed from Figure 2.7.

2.3 Polymers

The label 'polymer' refers to any long-chain molecule consisting of identical linked sub-units, or 'monomers', repeated many times. As these long chains entangle and interact, they give rise to behaviour unseen in so-called 'simple' materials.

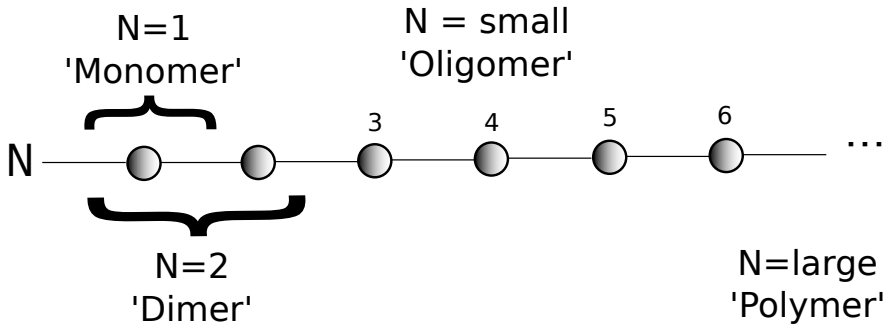

FIGURE 2.8: Diagram showing the names attributed to various degrees of polymerisation. The shaded dots on the line represent individual units (monomers) being repeated; this could be an atom or molecule, for example each dot could represent -C-C-O- in a poly(ethylene oxide) chain, or -C- in a surfactant tail.

Figure 2.8 shows the usual names given to chains with varying degrees of polymerisation, N. These names come from the Greek words *mono* (one), *dio* (two), *oligos* (few) and *poly* (many). Polymer chains very rarely, if ever, form a linear chain as shown in Figure

2.8; the brownian motion of each individual atom bonded along the chain implies that when considered macroscopically, the chain appears as a random coil [38]. However at short lengths individual sections of a polymeric molecule can be considered to be rigid rods. We can therefore define a length above which a polymer chain is flexible, this is the *persistence length* l_p and can be described thermodynamically by $l_p = l_0 \exp\left(\frac{\Delta\epsilon}{k_B T}\right)$ where l_0 is a length of a few Angströms (Å), T is the temperature and $\Delta\epsilon$ is the energy difference between minima in the atomic bonds [38, 39]. The persistence length is also half of the Kuhn length b, defined as the minimum length so that a section of chain of length b can be considered freely jointed to the next.

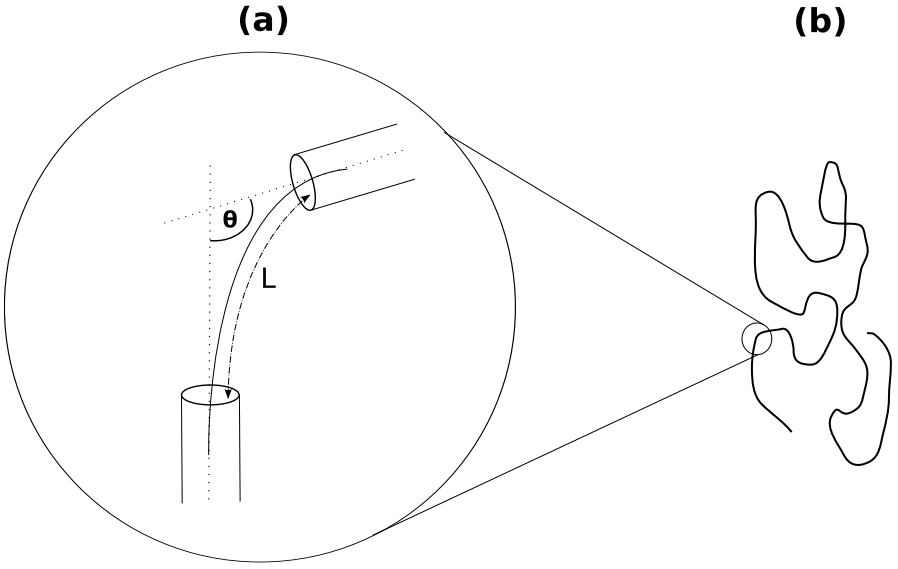

FIGURE 2.9: Schematic showing **(a)** the persistence length for a flexible polymer in relation to **(b)** the macroscopic polymer chain. θ represents the angle between tangents after a given length L, shown in Equation 2.16.

Figure 2.9**(a)** shows a representative section of a polymer 'random' coil to clarify the persistence length. θ is the angle between tangents to the polymer direction from the initial and final positions after a length L, which gives the definition of persistence length l_p as:

$$\langle cos(\theta) \rangle = e^{-\frac{L}{l_p}} \tag{2.16}$$

where $\langle cos(\theta) \rangle$ is the expected value of the angle. This is more useful as a definition of the persistence length as it shows l_p to be the length over which θ correlations fade to 0. We can therefore define the flexibility of a chain by considering the ratio of the persistence length to the total length L, where $\frac{l_p}{L} \ll 1$ yields a flexible molecule at large scales, and conversely $\frac{l_p}{L} \gg 1$ yields a rigid rod (at intermediate values the molecule can be considered semi-flexible).

For a flexible polymer in a good solvent, the random coil can be treated theoretically as a fractal object; the characteristic size of each fractal r_g is termed the *radius of gyration*. For $N \to \infty$ this is given by

$$r_g = \kappa a N^{\nu} \tag{2.17}$$

where κ is a constant, a is the distance between consecutive bonds, N is the degree of polymerisation and the exponent ν depends on whether the polymer is being treated as self-avoiding [38, 40]. Equation 2.17 introduces a quintessential aspect of polymer physics - scaling laws; this example shows how r_g scales with N for a homologous series in which ν, a and κ will be constant, and many other aspects of polymer behaviour are governed by power laws [38, 41, 42]. To show the importance of these power laws, and to further clarify r_g, the exponent ν will now be defined mathematically for a self-avoiding and non self-avoiding polymer.

If the polymer is not being treated as self-avoiding, it can be considered to be a freely jointed chain undergoing a random walk. In a random walk an object takes a series of $\mathbb{N}$ steps[5], where each step is towards a nearest-neighbour site and each site has an equal

[5]Here the steps in a random walk are labelled $\mathbb{N}$ so as to avoid confusion with the level of polymerisation N.

statistical probability of being 'chosen', irrespective of direction. For an ideal chain in thermodynamic equilibrium, where no interactions exist between monomer units, the step length is equal to the Kuhn length b and the end to end distance vector $\vec{r}$ is given by

$$\vec{r} = \mathbf{a}_1 + \mathbf{a}_2 + ... + \mathbf{a}_\mathrm{N} = \sum_{n=1}^{N} \mathbf{a}_n \tag{2.18}$$

and therefore the mean end-to-end distance is

$$\langle \vec{r} \cdot \vec{r} \rangle = \left\langle \left(\sum_{i=1}^{N} \mathbf{a}_i \right) \cdot \left(\sum_{j=1}^{N} \mathbf{a}_j \right) \right\rangle = \left\langle \sum_i \sum_j \mathbf{a}_i \cdot \mathbf{a}_j \right\rangle . \tag{2.19}$$

Separating out the $i = j$ cases gives $\langle \vec{r}^2 \rangle = Na^2 + \left\langle \sum_{i \neq j} \mathbf{a}_i \cdot \mathbf{a}_j \right\rangle$ and the $i \neq j$ terms disappear when the mean is taken, yielding

$$\langle \vec{r}^2 \rangle = Na^2, \tag{2.20}$$

showing that the average end-to-end distance is proportional to $\sqrt{N}$ [38, 43, 44]. Thus for an ideal chain, the exponent $\nu = \frac{1}{2}$ (from Equation 2.17).

When chain-chain interactions are accounted for, therefore changing the model to a self-avoiding random walk, the exponent ν can be calculated with the introduction of excluded volume effects, first demonstrated by Flory [40, 44]. Excluded volume effects arise from the fact that solid objects cannot overlap, and therefore experience an effective repulsion. If these objects are spheres of volume v, modelled as a gas of N objects[6] in a volume V,

[6]Here the N objects in a gas are the monomers in a polymer chain, therefore the symbol N is the same as the degree of polymerisation.

the entropy for each object is reduced by $k_{\mathrm{B}} v \frac{N}{V}$ [44]. Applying this to a polymer which occupies a volume r^3, and therefore has a segment concentration $c_{\mathrm{seg}} \sim \frac{N}{r^3}$,we find the free energy from the excluded volume F_{exc}:

$$F_{\mathrm{exc}} = k_{\mathrm{B}} T v \frac{N^2}{2r^3}, \tag{2.21}$$

to which we can add an elastic term from the configurational entropy F_{conf} [44], giving the total free energy as

$$\begin{aligned} F_{\mathrm{total}} &= F_{\mathrm{exc}} + F_{\mathrm{conf}} && (2.22)\\ F_{\mathrm{total}} &= k_{\mathrm{B}} T v \frac{N^2}{2r^3} + k_{\mathrm{B}} T \frac{r^2}{Na^2} && (2.23)\\ \therefore r &\sim a N^{3/5} && (2.24) \end{aligned}$$

showing that for a self-avoiding polymer, the exponent $\nu = \frac{3}{5}$ (in a good solvent) [38, 40, 44]. This is a mean-field result as there are no fluctuations present; the addition of a renormalisation group is necessary in order to account for these effects.

In summary, for an ideal chain $r_{\mathrm{g}} \propto N^{1/2}$ and for a self-avoiding chain $r_{\mathrm{g}} \propto N^{3/5}$. Therefore in taking into account the chain-chain interactions at all distances we find the polymer coil swollen relative to an ideal random walk[7].

The Rouse Model is a variation of the random walk, where the polymer is approximated by a series of beads connected by Hookean springs, with the beads undergoing Brownian

[7]The actual value of ν for self-avoiding chains has been calculated to be 0.588, therefore the Flory model is a very close approximation to a real polymer.

motion (see §3.1.2), therefore the step length can change [38, 45, 46, 47]. This theory was then extended by Zimm in order to account for hydrodynamic interactions [48].

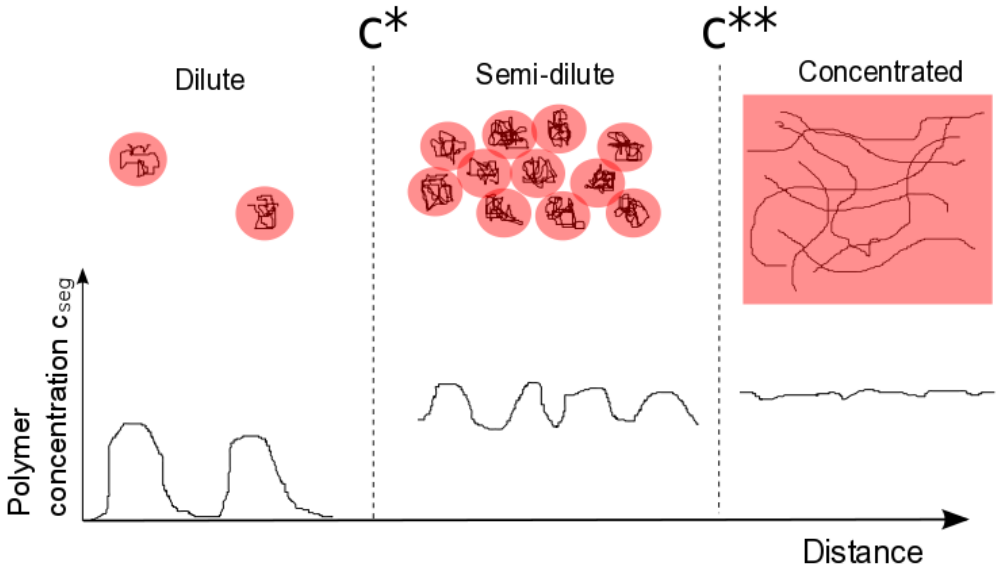

FIGURE 2.10: Schematic diagram showing the definitions of polymer concentration regimes.

r_g is not just a mathematical entity, it is an important quantity when discussing the rheological behaviour of polymeric solutions. These solutions are usually described as being in one of three regimes; dilute, semi-dilute or concentrated. Although the boundaries of these regimes are sometimes vague, in this work I will use the following definitions as shown in Figure 2.10:

- SINGLE-STAR BOUNDARY: c^* is the polymer concentration at which the random coils begin to touch/overlap, and is known as the *overlap concentration*. ϕ^* is the corresponding volume fraction. This is the boundary between the dilute and semi-dilute regimes.

- DOUBLE-STAR BOUNDARY: c^{**} is the polymer concentration at which elasticity first arises (ie. there is a crossing-point in the viscoelastic moduli). ϕ^{**} is the

corresponding volume fraction. This is the boundary between the semi-dilute and concentrated regimes.

From Figure 2.10 we see that for the dilute and semi-dilute regimes the polymer segment concentration c_{seg} plotted against position shows noticeable peaks and troughs, whereas for the concentrated regime there is no discernible difference between polymers. We can also differentiate between dilute and semi-dilute, as c_{seg} will drop to zero in the dilute regime .

2.3.1 The Reptation Model

Long polymeric chains in a free solution ($c \ll c^*$) diffuse via this random walk process discussed above. In an entangled system, where $c > c^*$, there are many obstacles in their path (ie. other polymers), and the reptation model defines a curvilinear diffusion occurring between these obstacles in a conceptually similar way to a snake's movement. This argument was put forth by de Gennes who described the method of reptation as "similar to unravelling a knot", whereby one section creates some slack and the molecule progresses through diffusion of this stored length [38, 49]. Edwards expanded on this by forming the idea of a tube inside of which the molecule can move freely, and the process of reptation acts to remove a section from one end of the tube and add it to the other end [43, 50]. Within the reptation model we can define a terminal, or reptation time τ_{rep}, the time taken for a tube to be completely renewed. It can also be shown that the diffusion co-efficient of the tube D_{tube} is given by

$$D_{\text{tube}} = \mu_{\text{tube}} T = \frac{D_1}{N}, \tag{2.25}$$

where μ_{tube} is the tube mobility, T is the temperature and D_1 is a diffusion constant independent of N. In order to occupy a tube which is not in contact with the original tube, the molecule must diffuse via reptation over a distance on the order of its own length L, thus

$$\tau_{\text{rep}} \cong \frac{L^2}{D_{\text{tube}}} \cong \frac{NL^2}{D_1}, \tag{2.26}$$

however L obviously scales linearly with N, therefore

$$\tau_{\text{rep}} \propto N^3. \tag{2.27}$$

Reptation is just one of a multitude of relaxation processes present in high concentration polymeric systems; the Rouse model described above can be considered a continuous relaxation function, for example [51, 52]. Where deviations from the Maxwell model are present in high-frequency data, this is often attributed to Rouse *modes* arising, an example of which can be seen in Figure 2.3 on p.10.

2.3.2 'Living' Polymers

Micelles are self-assembled aggregates of surfactant molecules which exhibit macroscopic and nanoscopic phase changes as their concentration is varied.

Figure 2.11 shows a representative visualisation of micelle phases; this is a simplified system where various liquid-crystalline phases have been ignored, and these only apply to single-tailed surfactants. At very dilute concentrations **(a)**, the surfactant molecules are distinct and separate; at a pre-defined concentration labelled the *critical aggregation*

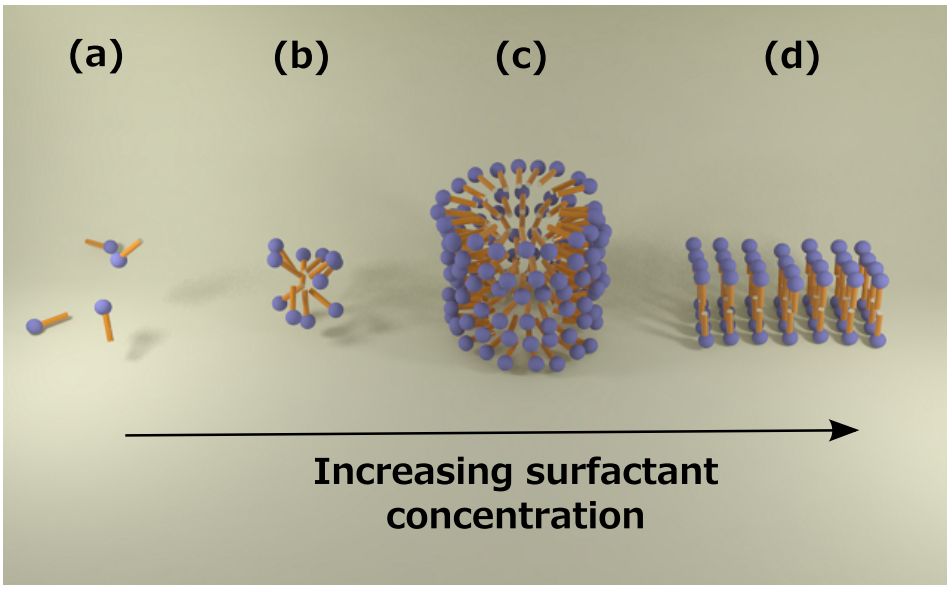

FIGURE 2.11: Visualisation of micellar phases with increasing surfactant concentration. **(a)** At concentrations below the critical micelle concentration (CMC) the surfactants have no structure, **(b)** at higher concentrations the hydrophobic tails are shielded from the water by hydrophilic heads creating spherical micelles, **(c)** as the concentration is increased further the spherical micelles condense into wormlike (cylindrical) micelles, and **(d)** at very high concentrations the surfactant molecules form a dense lamellar phase (image created using Ruby and V-Ray).

concentration or *critical micelle concentration* (CMC), the hydrophobic tails will attempt to minimise the surface area in contact with water by condensing together with the head groups directed radially outwards **(b)**. As the concentration is increased, the spheres elongate, gradually forming cylindrical rods with spherical ends. Further increases in the concentration lead to **(c)** the formation of 'wormlike' micelles (WLMs), which can be millimetres long, yet only nanometres in diameter [11, 12]. At high concentrations, surfactants will form lamellar bilayers **(d)**, however in this work we only concern ourselves with wormlike micelles and concentrations below this (Figure 2.11 **(a-c)**). These micellar phases are also dependent on the surfactant geometry; this work deals with single-tailed surfactants, where the effective volume can be considered to be a cone, therefore facilitating the creation of spheres/cylinders. Dual-tailed surfactants have an effective volume that is closer to a cube, and therefore have a very different phase diagram.

As WLMs elongate they also become entangled, as per normal polymers, however in

contrast to traditional polymeric molecules the length of a WLM is constantly changing through reversible scission and recombination processes with other micelles, even when the bulk system is at rest [53, 54]. It is this variation in length which denotes the phrase 'living' polymers. Applying the mean-field theory to WLM network structures yields an exponential[8] length distribution of the micelles [55, 56]. This mean length, or average contour length, $\bar{L}$ varies with surfactant volume fraction ϕ as

$$\bar{L} \sim \phi^{1/2} e^{E_c/k_B T} \tag{2.28}$$

where E_c is the end-cap energy; the energy required to form a curved surface at the end of each micelle [57].

The dynamics of a living polymer system are highly dependent on two quantities; τ_{rep} introduced in Equation 2.26, and the average time before a scission, or breaking, event τ_{break}. If $\tau_{break} \gg \tau_{rep}$, then reptation is faster and dominates; the micelles behave like unbreakable chains, albeit with exponential polydispersity, and a stress relaxation function given by

$$\sigma(t) \sim \exp\left[-\left(\frac{t}{\tau}\right)^{1/4}\right] \tag{2.29}$$

which would be transformed into a standard exponential decay if the system was monodisperse [57]. Conversely there is the case where scission dominates over reptation ($\tau_{break} \ll \tau_{rep}$); this is Maxwellian behaviour in which the stress relaxation is given by a single exponential decay,

[8] The distribution can be considered peaked in certain cases, such as systems containing actin filaments.

$$\tau_{\mathrm{R}} = \sqrt{\tau_{\mathrm{break}}\tau_{\mathrm{rep}}} \tag{2.30}$$

where τ_{R} represents the characteristic relaxation time of the bulk system, discussed in §2.2.1. Another important quantity in micellar systems is the entanglement length l_{e}, which is the average distance between entanglements measured along the contour, and for flexible micelles is given by

$$G_0 = \frac{k_{\mathrm{B}}T}{\xi^3} = \frac{k_{\mathrm{B}}T}{l_{\mathrm{e}}^{9/5} l_{\mathrm{p}}^{6/5}}, \tag{2.31}$$

where ξ is the correlation length which gives the average mesh size of the network structure [11, 57]. In certain situations [57] the entanglement length can also be calculated using

$$\frac{G''_{\mathrm{min}}}{G_0} = \frac{l_{\mathrm{e}}}{\bar{L}}, \tag{2.32}$$

or alternatively if l_{e} is known, Equation 2.32 can be used to estimate the value of $\bar{L}$ [12, 58].

In charged systems such as SDS [59], CTAB-CPBr [60], CTAT-SDBS [61] and SDS-CAPB [62], the addition of an electrolyte can screen the charges along the micelle causing $\bar{L}$ to increase. This can be conceptualised in terms of the head-group interactions; if the electrolyte screens the charges between head groups, then surfactant heads can fit closer together without feeling a repulsion. As a result of this tighter packing at the end-caps, it takes a larger free-energy difference to create the required radius of curvature. The micelles will therefore favour fewer end-caps for a given concentration, creating

longer micelles. Another consequence of additional electrolyte is that the micelles become more flexible (l_p decreases), due to the charge screening. On the addition of sufficient electrolyte or extra surfactants into a micellar network, $\bar{L}$ may increase to a point at which the micelles begin to branch; this branching has been verified experimentally using cryo-TEM [63], and leads to various rheological changes in the bulk system. The branching can also be explained by considering the free energy; a branch has the opposite curvature to an end-cap, therefore given sufficient length and flexibility, the micelle may favour branching to reduce the free energy difference from the end-caps.

2.4 The structure and properties of poly(ethylene oxide) (PEO)

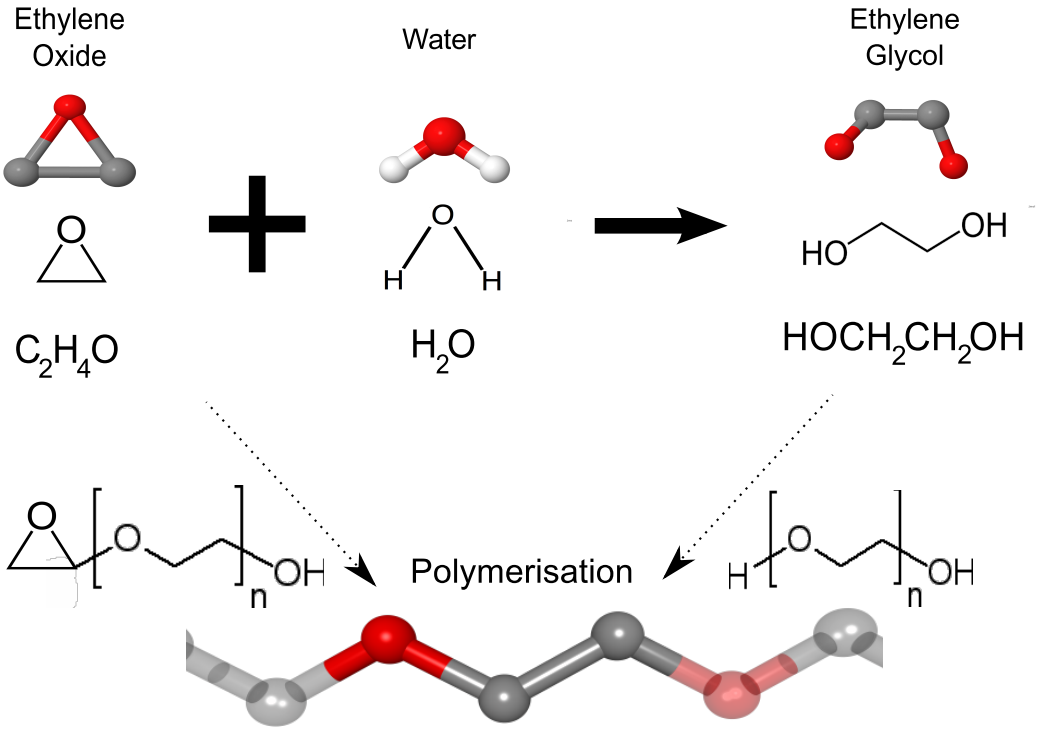

FIGURE 2.12: A PEO monomer (opaque) shown in a chain (transparent), without Hydrogen atoms for clarity; the grey and red balls represent carbon and oxygen atoms, respectively (created using Python, BallVIEW and POV-Ray).

Poly(ethylene oxide) (PEO) refers to polymeric molecules consisting of repeated C-C-O sub-units (carbon-carbon-oxygen), where the carbon atoms are each bonded to 2 hydrogen atoms, although in visualisations the hydrogens are usually implicit as shown in Figure 2.12. The acronym PEO is sometimes used interchangeably with that of poly(ethylene glycol) (PEG), with PEO and PEG both referring to C-C-O-backbone polymers.

Historically the acronym PEG has been used to refer to short-chain molecules ($\lesssim 20k$ MW) and PEO has been used for chains $\gtrsim 20k$ MW. This situation arose from the various techniques used for polymerisation, where polymerisation of ethylene glycol ($C_2H_6O_2$) could originally only yield low MW product; as the techniques were refined the range of MWs accessible from each technique increased and today the two terms are usually used synonymously [64]. Figure 2.12 shows how PEG/PEO can be polymerised from the respective monomers; ethylene glycol can be formed by reacting ethylene oxide with water, and a C-C-O-backbone polymer can be created from either monomer. The products differ by the end-groups created; ethylene glycol will be hydroxyl-terminated (OH), and ethylene oxide will be CH_2CHO-terminated. As a result, shorter polymers may display different behaviour as the end-groups are significant, however for most polymers the difference is negligible and both PEO and PEG can be considered identical. In this work where a molecule is referred to as PEO or PEG, the last letter refers to the method of polymerisation (and therefore implicitly the type of end-group), rather than an implication as to the length of the molecule.

In the last 80 years, PEO/PEG have been synthesized from ethylene oxide/glycol monomers using a variety of chemicals including succinic acid [65], stannic chloride [66], boron triflouride [67] and tetrahydrofuran (THF) [68], to name just a few. PEG/PEO has many wide and varied uses including soft drinks, drag reduction in fire hoses [21], repairing

damaged axons [69, 70], preserving waterlogged wood such as shipwrecks [71], and as a viscosifier in personal care products [11, 12, 72].

Molecular weight-independent properties

Table 2.1 shows the basic attributes of PEO/PEG molecules which are irrespective of molecular weight.

Table 2.1: Molecular weight-independent properties of PEO/PEG.

Property	**Value**
Formula	$C_{2n}H_{4n+2}O_{n+2}$
Molar Mass	44n+18
Density	1.13g cm^{-3}
Scaling exponent ν^{LS}	0.583 ± 0.031
Scaling exponent ν^{CHARMM}	0.515 ± 0.023
Persistence length $l_{\mathrm{p}}^{\mathrm{AFM}}$	3.8 ± 0.02Å
Persistence length $l_{\mathrm{p}}^{\mathrm{CHARMM}}$	3.75 ± 0.05 Å
Mean Carbon-Carbon bond length $l_{\mathrm{C-C}}$	1.53 Å
Mean Carbon-Oxygen bond length $l_{\mathrm{C-O}}$	1.43 Å

The scaling exponent ν shows how r_{g} scales with N (from Equation 2.17); ν_{LS} is from static and dynamic light scattering experiments for 86,000 < MW < 1,000,000 performed by Devanand and Selser [73]. The persistence length $l_{\mathrm{p}}^{\mathrm{AFM}}$ is from Kienberger *et al* who performed an extended worm-like chain (eWLC) fit to force-extension profiles from an Atomic Force Microscope (AFM) [74], $l_{\mathrm{p}}^{\mathrm{CHARMM}}$ and ν^{CHARMM} are from Lee *et al* who ran molecular dynamics (MD) simulations using CHARMM for low MW PEG/PEO chains (N = 9, 18, 27 and 36) [75]. It is interesting to note that Lee *et al* differentiate between PEO and PEG in their MD simulations, giving l_{p} = 3.7Å and 3.8Å for PEO and PEG, respectively. The mean bond lengths are from Bowen and Sutton [76] who calculated the interatomic distances for a wide range of chemical bonds using experimental structural data; their results have subsequently been verified specifically for PEO using X-ray crystallography [77].

The scaling exponent values tell us about the behaviour of PEO/PEG at various length scales; as mentioned above ν^{LS} is the experimental value for 86k-1M MW, which is comparable to the exponent in the Flory model for a self-avoiding chain. Conversely ν^{CHARMM} is the simulation value for short chain PEO/PEG, which is comparable with the value for an ideal (non-self-avoiding) chain. Therefore we can see that for low N, the C-C-O backbone behaves as an ideal chain, but as the MW is increased, chain-chain interactions become more prominent and must be taken into account.

Molecular weight-dependent properties

Table 2.2: Table of PEG/PEO MWs and parameters used in this work (†inhibited with 200-500ppm BHT), where **N** is the degree of polymerisation, **r** is the molecular radius, $\mathbf{r_g}$ is the radius of gyration, $\mathbf{c}^*$ is the overlap concentration and l_c is the contour length.

MW	**Sigma Code**	**N**	**r** (nm)	$\mathbf{r_g}$ (nm)	Volume (nm^3)	$\mathbf{c}^*$ (% wt.)	$\mathbf{l_c}$ (nm)
3.35k	P4338-1KG	56	4.34	1.77	23.3	23.86	33.72
8k	P-4463	134	6.70	2.73	86.05	15.44	80.54
20k	Unknown	335	10.6	4.33	340.13	9.77	201.36
100k	181986	1,678	23.71	9.68	3,802	4.37	1,006.8
300k†	182001-250G	5,034	41.07	16.77	19,759	2.52	3,020.4
1M†	372781-250G	16,780	75	30.62	120,255	1.381	10,068
4M†	189464-250G	67,120	150	61.24	962,042	0.691	40,272
8M†	372838-250G	134,240	212.13	86.60	2,721,066	0.488	80,544

Table 2.2 shows some physical parameters for the various MW PEO/PEG used in this work. r_g has been calculated from [78], c^* has been calculated from experimental measurements and l_c is from [79].

In order to show that rheological experiments performed for this work are comparable with the literature [1], Figure 2.13 shows viscosity data for 1,8,10 and 20k MW solutions at a variety of concentrations (scaled by c^*). The general trend is clearly evident, and

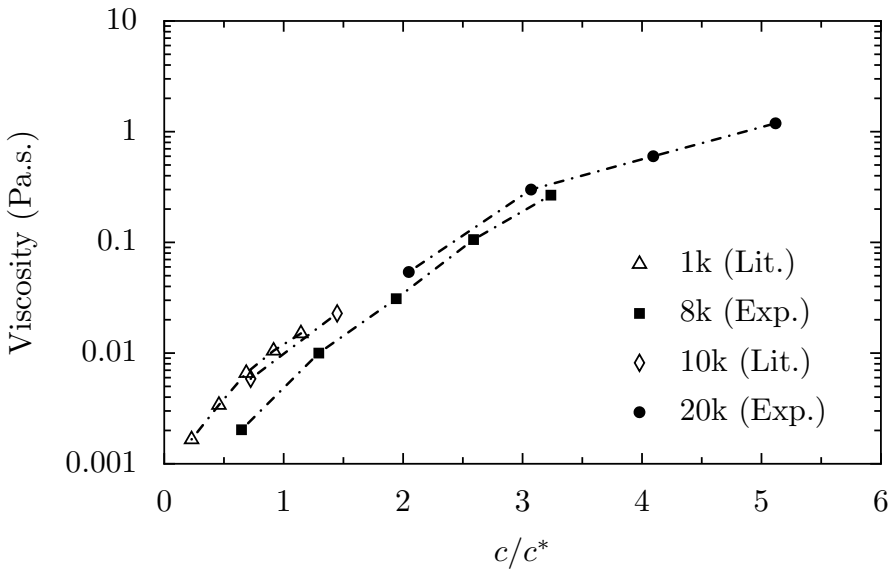

FIGURE 2.13: Viscosity against rescaled concentration $\frac{c}{c^*}$ for various concentrations of 1, 8, 10, and 20k MW PEG/PEO. The hollow symbols represent data from the literature (taken from [1]), and solid symbols show experimental data from this work.

I can be confident that there are no major discrepancies between the samples/protocols used here and those in [1].

2.4.1 Hydration and Solvation of PEO

The hydrophobic nature of CH_2 groups in the PEO/PEG backbone, in combination with the hydrogen bonding with oxygen in aqueous conditions, makes this molecule highly suitable for study as a model biopolymer; the interactions that arise in PEO/water systems may shed light on more complex interactions, such as protein folding and stabilisation, which are driven by the same hydrophobic and hydrogen-bonding forces [80, 81].

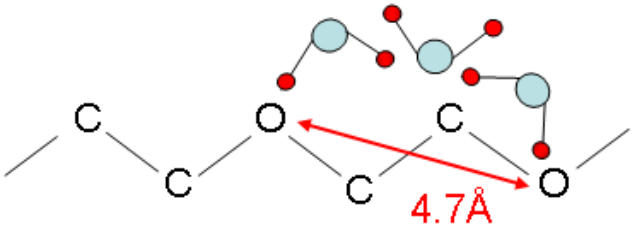

FIGURE 2.14: Schematic showing the likely hydration configuration of a PEO/PEG monomer in aqueous solution.

The solvation characteristics of PEO however are non-standard; if one carbon atom is removed from the repeated monomer unit (-CH_2O-, poly(methylene oxide) (PMO)), the molecule is insoluble in water despite half of the hydrophobic CH_2 groups being removed. Likewise if a CH_2 group is added to the monomer unit (-$CH(CH_3)CH_2O$- poly(propylene oxide) (PPO)), the molecule is also insoluble in water [81, 82]. The solubility of the PEO/PEG molecule arises from the average intermolecular distances between oxygen atoms of ~ 4.7Å, which corresponds with the oxygen-oxygen next-nearest neighbour distance in water [82], as shown in Figure 2.14. Hydrogen-bonding occurs between oxygen atoms in the polymer backbone and the hydrogen atoms in water molecules; this bonding creates a 'dress' of water molecules around each PEO/PEG molecule, effectively shielding the hydrophobic CH_2 groups from the solvent. Each PEO/PEG monomer has 2-3 water molecules in its 'dress', which has been confirmed experimentally [83, 84] and theoretically using electrostatics with Density Functional Theory (DFT) [2]. DFT studies have shown the possibility of 2^{nd} and 3^{rd} order 'dresses' (ie. water molecules hydrogen-bonded to the 'dress' below it) [2], but at the time of writing this has not been confirmed experimentally.

A consequence of PEO/PEG solvation being driven by hydrogen-bonding is that raising the temperature of an aqueous PEO/PEG solution can break the hydrogen bonds, forcing the polymer to come out of solution. PEO/PEG is therefore one of the few molecules for which solubility decreases with increasing temperature (it has an upper critical solubility temperature (UCST)). Branca *et al* have also suggested that the hydration level of the PEO/PEG backbone can be calculated directly from viscosity measurements [85]. They conclude that the number of bound solvent molecules per monomer unit increases with N due to the random walk of the molecule trapping further solvent molecules between adjacent polymer sections. Shikata *et al* have also measured the hydration level of PEO

using dielectric relaxation (introduced earlier as the origin of Cole-Cole plots), which gives an increasing number of hydration water molecules per ethylene oxide monomer upto a MW $\sim$ 1500, above which all MWs have a constant hydration level of 3.7 solvent molecules per monomer [86].

2.4.2 The conformation of a PEO molecule

PEO/PEG have been known to form helices at small length scales in the solid state for some time [87], and it is thought that due to the preferential *trans-gauche-trans* (*tgt*) conformation of the O-C-C-O dihedral the same helicity may occur in dilute aqueous conditions [2, 85, 88].

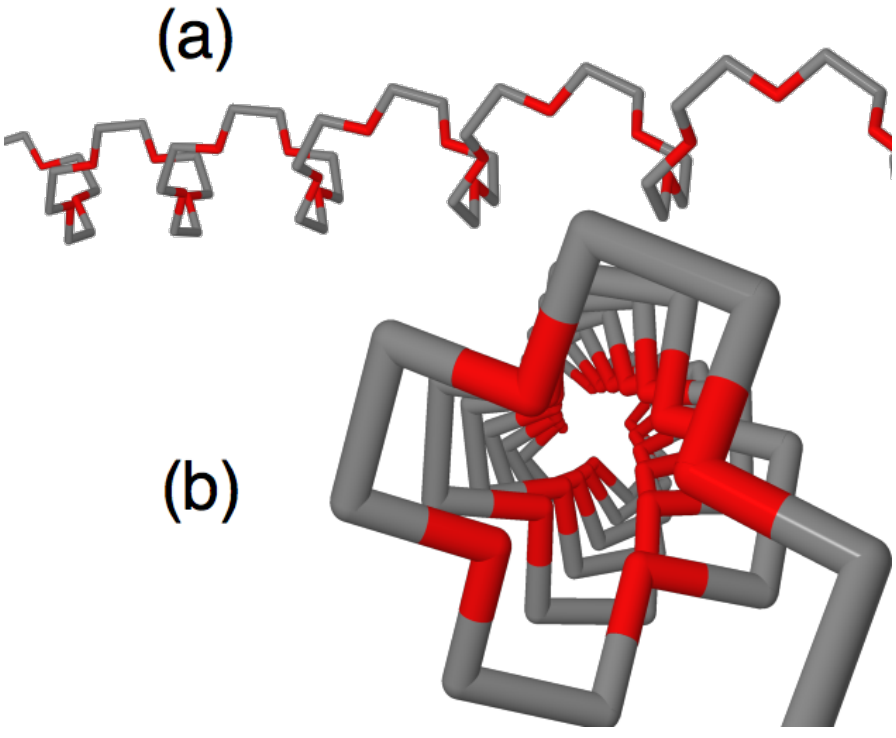

FIGURE 2.15: The conformation of a PEO molecule *in vacuo* showing the helix formed by successive *trans-gauche-trans* bonds. **(a)** Side view and **(b)** end view of same molecule (created using Python, BallVIEW and POV-Ray).

Figure 2.15 shows the result from an electrostatics calculation of PEO *in vacuo* using DMol[3]; one can see that the oxygen atoms are held in the core of the helix by the successive *tgt* conformations, which in solution would force the hydrogen bonding solvent molecules to form a helix rather than a cylinder.

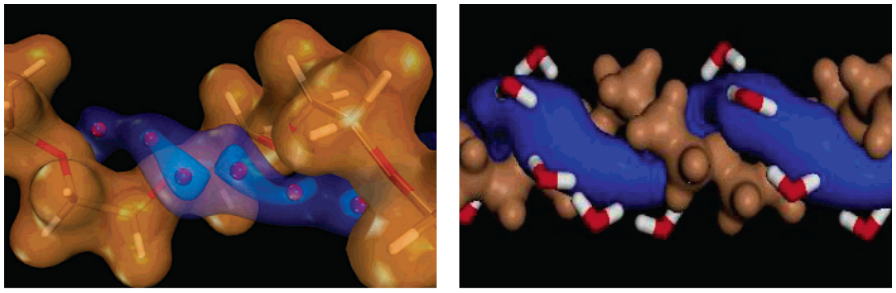

FIGURE 2.16: Figures from [2] showing **(a)** the minima in the topology for hydrogen-bonding to PEO, and **(b)** the simulated 'dress' of water along a PEO helix.

Aray *et al* showed that the dihedral angle is around 85.4° creating a helical revolution every ∼4 monomers, which is corroborated by the calculation performed in this work shown in Figure 2.15. This helix is therefore of sufficient size to encourage hydrogen-bonding from the water molecules along its entire length, as shown in Figure 2.16 (the images in this Figure are taken from [2]). Figure 2.16 **(a)** shows the minima in the topology (red spheres) for hydrogen bonding to the oxygen atoms calculated using DFT, and **(b)** shows the water molecules that are hydrogen-bonded to the polymer after a MD simulation. This work by Aray *et al* can be seen to corroborate the experimental calculations of Branca *et al* [85] by showing that 2−3 water molecules are bound per monomer.

At longer scales ($N \gtrsim 4$ [78]) the polymer follows a random walk as described in §2.3, however the unorthodox helical structure gives PEO/PEG interesting properties, and certainly contributes to its solubility given that $\sim \frac{2}{3}$ of the backbone is a hydrocarbon and therefore hydrophobic.

2.4.3 Clustering

Any hydrophobic molecules in water will aggregate (or go to an interface) if their trajectories meet in order to minimise the surface area in contact with the solvent. Even when shielded from the free solvent, PEO/PEG molecules may form clusters as the hydrogen bonds are easily broken. Aggregates in multi-component systems are known to nucleate around impurities such as dust, and this was originally proposed as the process by which clusters formed in PEO/PEG systems [89]. However PEO clusters have been shown to form even in double-distilled, filtered and de-ionised water [80]. There is therefore currently no consensus opinion on the origin or mechanisms of PEO/PEG cluster formation, and this has been the subject of much research over the last two decades [80, 81, 90, 91].

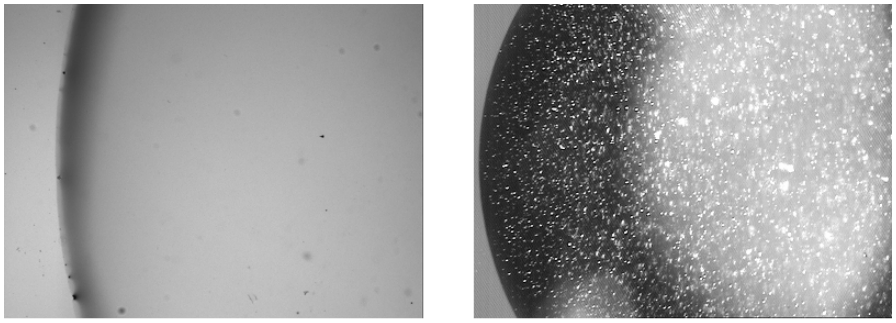

FIGURE 2.17: View from underneath a freshly deposited PEO droplet; **(a)** Filtered through $0.45\mu m$ filter, and **(b)** unfiltered.

Figure 2.17 shows the view from underneath 2 droplets of aqueous PEO solution; **(a)** shows the clear droplet after the clusters have been filtered out using a 0.45μm filter, and **(b)** shows the unfiltered droplet. These images were taken on a Nikon TE-2000 Eclipse microscope with a $2\times$ objective lens. Figure 2.17**(b)** also clearly shows the polydisperse nature of these clusters. After some time, the clusters will reform in the filtered solution, however this can be inhibited with the addition of chloroform [80]. Aggregates of polymeric molecules have also been shown to reduce turbulence in dynamic

systems [92], which could explain the drag reduction effect of high MW PEO in fire hoses discussed previously.

2.5 Concluding Remarks

This chapter has introduced the physical concepts necessary for a full understanding of this work. PEO/PEG features heavily in this research as it is used extensively in the next 3 experimental chapters.

The next chapter presents the optical trapping equipment, theory and calculations that have formed a core part of this research, and concludes with experimental data from aqueous PEO systems as a proof-of-concept for the more in depth studies.

3

Optical Tweezers and their use with Complex Fluids

"The atoms become like a moth, seeking out the region of higher laser intensity."

US Energy Secretary, Nobel Laureate Professor Steven Chu

3.1 The Background and Physics of Optical Tweezers

Ever since Johannes Kepler noticed that the tails of comets always point away from the Sun [93], Western science has been aware of *radiation pressure*; the force exerted on any surface exposed to electromagnetic radiation[1]. The theoretical framework for this force comes from the relativistic energy-momentum tensor [95, 96],

$$E = \sqrt{(\vec{p}c)^2 + (m_0c^2)^2} \tag{3.1}$$

where $\vec{p}$ is the photon momentum, c is the speed of light in a vacuum and m_0 is the rest mass. Using Equation 3.1 we can see that for a photon (where $m_0 = 0$), the momentum is given by

[1]The first observation of the specific direction of comet's tails was by Fracastoro in 1538, however he incorrectly assumed that the comet was a lens focussing the Sun's rays [94].

$$\vec{p} = \frac{E}{c}, \tag{3.2}$$

therefore the momentum imparted on an object by a photon is directly proportional to the photon's energy. Using Maxwell's eponymous equations relating the properties of electric and magnetic fields in combination with the Lorentz force ($\vec{F}_{\text{lorentz}} = q(\vec{E} + \vec{v} \times \vec{B})$), Poynting defined a vector $\vec{S}$ such that

$$\vec{S} = \frac{1}{\mu_0} \vec{E} \times \vec{B}, \tag{3.3}$$

where μ_0 is the magnetic constant, and $\vec{E}$ and $\vec{B}$ represent the electric and magnetic field components, respectively [97]. Equation 3.3 describes the power per unit area through a surface; in conjunction with photon momentum (described above), this can be used to calculate the force on an object from electromagnetic (EM) radiation.

Therefore not only can a force be exerted on an object using photons, but that force can be calculated from first principles.

In reality, using photons to confine particles requires an accurate control of the light beam; it is possible to destroy objects if the intensity is too high, for example. A limiting factor is also that the characteristic refractive index n of any material is dependent on the wavelength of the incident beam; the highest level of control will therefore be attained with a monochromatic EM radiation source. Thus it was not until the invention of the laser (or optical maser) in 1958 [98] that *photonic force traps* became feasible.

The earliest laser traps used pressure from counter-propagating beams in order to hold microscopic particles [99, 100], followed by vertically aligned single-beam lasers using

radiation pressure to counter gravity [101, 102], and resonance radiation pressure to trap atoms [103], work all pioneered by Arthur Ashkin. Later, Ashkin *et al* invented a single-beam gradient trap whereby the conservation of momentum from refracting photons in a focussed laser beam created an harmonic potential for dielectric particles [104]. This is discussed in more detail later.

Hardware to manipulate refractive particles in this way has become known as optical tweezers (OTs), and the use of OTs to trap and cool individual atoms led to the 1997 Nobel Prize being awarded to Steven Chu, one of Ashkin's early collaborators [105].

Optical tweezer setups can generally trap particles from 25nm to 10μm[2], and by performing a force-displacement calibration (discussed in §3.2.4) an OT can measure forces up to ~ 200 pN with sub-pN resolution [104]. As a result OTs are particularly useful for measuring biologically relevant properties; examples being the stretching of DNA [107], elasticity of actin [108, 109] and the force exerted on organelles *in vivo* [110].

Photons incident on a spherical, refractive particle exert both a gradient (trapping) force ($\vec{F}_{\text{grad}}$) and a scattering force ($\vec{F}_{\text{scat}}$). The photons which reflect off the particle's surface will exert a 'forward' force, i.e. one acting in the downstream direction of the incident beam, as shown in Figure 3.1. These photons create $\vec{F}_{\text{scat}}$, which will always act to push the particle away from the light source. Some photons will refract through a dielectric particle; conservation of momentum ensures that the change in direction of a photon exerts a corresponding force in the opposite direction on the particle. Given a spherical particle and a focussed Gaussian beam (discussed later), the particle will feel an overall force in the upstream direction of the incident beam, as shown in Figure 3.1.

[2]Using multiple traps a 300μm cheek cell has been manipulated [106].

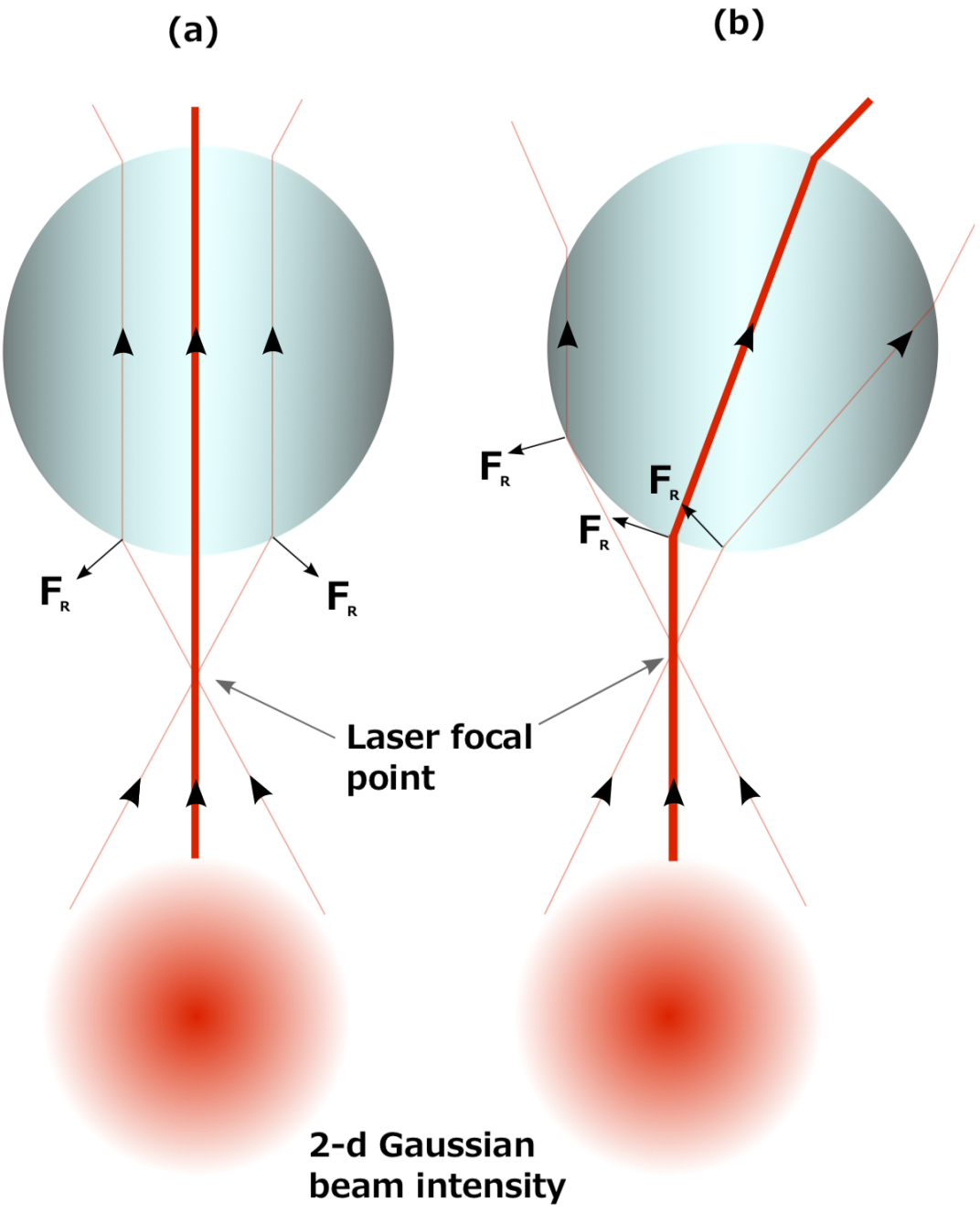

FIGURE 3.1: Schematic showing example photon paths through a trapped particle for **(a)** a central bead and **(b)** an offset bead.

If the gradient force can overcome the scattering force (and any other forces acting on the particle, such as Brownian motion), then the particle will be held in a potential using only a single beam of light.

In the Rayleigh regime where the particle diameter d is much smaller than the wavelength of light λ ($\mathrm{d} \ll \lambda$), $\vec{F}_{\mathrm{grad}}$ and $\vec{F}_{\mathrm{scat}}$ can be calculated using an electric dipole approximation first proposed by Ashkin [104]; the scattering force is given by

$$\vec{F}_{\mathrm{scat}} = n_{\mathrm{b}} \frac{\sigma \langle \vec{S} \rangle}{c} = \frac{I_0}{c} \frac{128\pi^5 r^6}{3\lambda^4} \left(\frac{m^2 - 1}{m^2 + 2} \right)^2 n_{\mathrm{b}} \tag{3.4}$$

where m is the effective refractive index (index of particle / index of medium), n_{b} is the refractive index of the particle, r is the radius of the particle, $\langle \vec{S} \rangle$ is the time-averaged Poynting vector introduced in Equation 3.3, I_0 is the initial intensity of the incident beam and σ is the cross-sectional area of the particle.

The gradient force is given by

$$\vec{F}_{\mathrm{grad}} = -\frac{n_{\mathrm{b}}}{2} \alpha \nabla E^2 = -\frac{n_{\mathrm{b}}^3 r^3}{2} \left(\frac{m^2 - 1}{m^2 - 2} \right) \nabla E^2, \tag{3.5}$$

where α is the polarisability of the Rayleigh particle. Equation 3.5 shows that F_{grad} is proportional to the gradient of electric field magnitude squared (∇E^2); thus the force exerted on a particle is proportional to the gradient of intensity of the beam, in the direction of increasing E, resulting in the particle being attracted to the area with greatest photon flux (ie. the centre of the beam).

Since $\vec{F}_{\mathrm{scat}}$ acts in the direction of the propagation of light and $\vec{F}_{\mathrm{grad}}$ acts in the direction of highest beam intensity, the equilibrium position of a trapped particle is offset

downstream from the focal point of the beam, as shown in Figure 3.1.

If the particle size is increased ($d \gtrsim \lambda$), refraction effects can no longer be ignored so standard ray optics methods are employed to calculate the trapping forces [111]. If the particle diameter d is sufficiently larger than the wavelength λ then diffraction effects become negligible [112], and the forces present can be closely approximated by considering the refraction of individual photon paths through the particle.

In the ray optics regime, each photon path incident on the particle is taken into account; the force exerted on the trapped object is calculated using the momentum change of each photon, calculated using Equation 3.2. Thus, each time the photon is refracted, it imparts momentum to the particle. If the particle is offset in the trap (due to an external force such as Brownian motion), the refractive force $\vec{F}_{\mathrm{R}}$ on the side of the bead closest to the beam centre feels a greater restoring force, creating the potential well. This is shown in Figure 3.1, and since the particles used in this work were between 0.5-10μm, all experimental OT data presented in this work were taken in the ray optics regime.

Experiments have shown that the refractive index of the bead, n_{b}, must be at least $\sim$10% greater than than of the trapping medium in order for the gradient force to dominate [113, 114].

The trapping strength can be increased by using a high numerical aperture (NA) objective lens;

$$NA = n \times sin(\theta) \tag{3.6}$$

where n is the refractive index of the objective lens and θ is the angle from the edge of the lens to the focal point. From Equation 3.6 it can be seen that a larger NA objective results in a tighter focus (increased θ), thus the trapping depth decreases as the NA

increases. However, a tighter focus also increases the gradient force from refraction, therefore in choosing an objective lens a compromise must be made between trap strength and trapping depth. Another aspect of Equation 3.6 is that in raising the NA to increase trapping strength, the limiting factor is n (because $sin(\theta) < 1 \; \forall \; \theta$). Therefore in order to achieve NA > 1, immersion oil must be used on the objective lens so that the refractive index on exiting the lens is as high as possible. In all the work presented here, immersion oil with a refractive index n_{oil} was used, where $1.4 < n_{\text{oil}} < 1.518$, depending on the setup. This work also used objective lenses with 60x (Nikon, NA=1.4), 63x (Leica, NA=1.3) and 100x (Nikon, NA=1.4).

3.1.1 Gaussian Laser Beams

Laser traps have been shown to work with many types of laser beams; Laguerre-Gaussian beams exhibit axial and lateral trapping forces (creating *'Optical spanners'*) [115] and self-interference in Bessel beams can recreate a trapping potential even after the laser is blocked [116], to name just two. In this work all optical traps were created with a TEM_{00} laser mode, which means that the intensity profile shows a single, central maxima that decays radially in a uniform manner.

Ashkin's original work involved high refractive index particles being irradiated with a Gaussian TEM_{00} laser beam [99]; since particles are attracted to regions of higher photon flux, an axisymmetrically focussed Gaussian trapping beam yields a Gaussian distribution for the particle position, with position fluctuations due to thermal Brownian motion (see §3.1.2). Gaussian distributions are given by (ignoring normalisation constants)

$$p(x) \propto e^{-v/k_{\text{B}}T} = e^{-kx^2/k_{\text{B}}T} \tag{3.7}$$

and the energy is governed by Boltzmann statistics [117, 118], where the change in energy between two levels is given by

$$\frac{E_1}{E_2} = \frac{e^{-\frac{\epsilon_1}{k_\mathrm{B}T}}}{e^{-\frac{\epsilon_2}{k_\mathrm{B}T}}} = e^{-\frac{\Delta\epsilon}{k_\mathrm{B}T}} \tag{3.8}$$

and the negative natural log of this gives the system energy, $-\ln\left[e^{-\frac{\Delta\epsilon}{kT}}\right] = \frac{\Delta\epsilon}{kT}$. In a similar manner, taking the negative natural log of the particle displacement histogram yields the effective trap potential:

$$F(x) = -\ln[p(x)] = -\ln\left[e^{-kx^2/k_\mathrm{B}T}\right] = -\frac{kx^2}{k_\mathrm{B}T}. \tag{3.9}$$

Therefore a correctly aligned trap created with a perfectly Gaussian beam creates a Hookean potential, $F(x) \propto kx^2$, where k is the effective spring constant, as shown in Figure 3.2 (p.48).

3.1.2 Brownian motion

Stochastic movements of microscopic particles, labelled *'Brownian motion'*, are present in every material in the known universe; these motions are directly related to temperature, ceasing only at $T = 0K$, and as such they are ubiquitous in many fields of science. Initial observations of this phenomenon were performed by the Scottish biologist/botanist Robert Brown who mistakenly attributed the motions of pollen grains to life at first, before noticing the same behaviour in inorganic materials such as soot, dust and rocks and labelling them *'irritable particles'* [119, 120]. In an ironic twist, modern theories

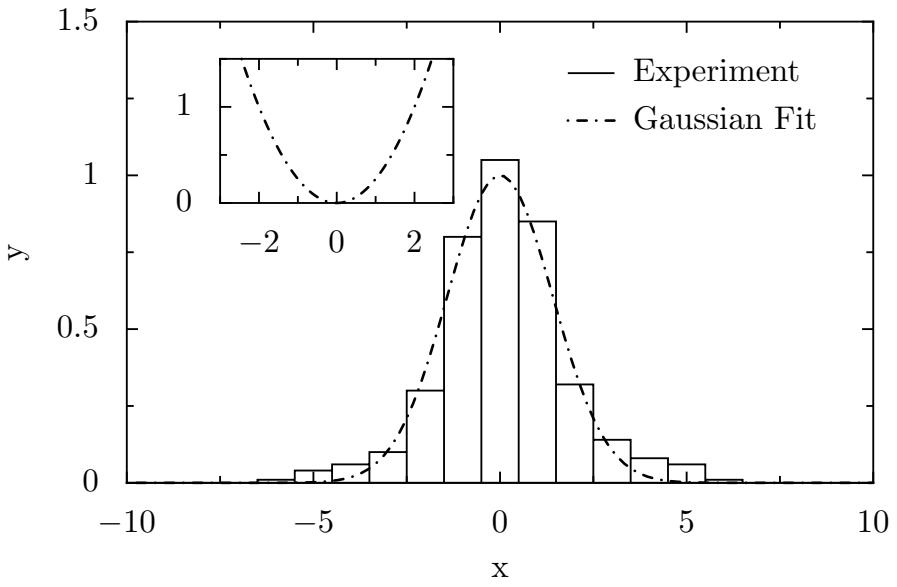

FIGURE 3.2: **Main:** Representative Gaussian curve showing the histogram of particle displacement in an optical trap from a 5μm particle in water, with a theoretical fit. The data has been scaled so that the fit reaches a maxima at $x = 0, y = 1$, and the x-axis represents the histogram 'bin' number with each bin being ≈50nm wide. **Inset:** The effective potential well given by the Gaussian distribution of the Brownian motion displacement.

attribute the emergence of life to Brownian motion [121], rather than *vice versa* as Brown first guessed.

Despite its enormity, the importance of Brown's work was not well understood at the time, thus it was only at the turn of the 20^{th} century that its relevance became apparent. Louis Bachelier's successful defence of his doctoral thesis [122], containing the first theory of Brownian motion, is seen by many as the instigation of stochastic processes relevant to mathematical finance; from a physical point of view Bachelier's work was much more important than that, as it allowed a little known physicist named Albert Einstein to give the molecular-kinetic theory of heat (see §3.1.2.1) an experimental test [123]. Einstein predicted that Brownian motion of visible, microscopic objects was due to the thermal (Brownian) motion of solvent molecules, however his data was inconclusive.

Einstein's prediction was hugely influential; if it failed it also refuted the kinetic theory of heat, if it was successful it would allow the calculation of Avogadro's number [123], which

Einstein achieved in his doctoral research by studying the diffusion of sugar molecules in solution [124]. Rigorous experimental verification of Einstein's ideas was achieved by Jean Perrin [125, 126], who later won the Nobel Prize.

3.1.2.1 Molecular-Kinetic Theory

The first formal formulation of the molecular-kinetic theory, or the 'theory of moving particles', applied to gaseous molecules only and was performed by Clausius in 1857 [127]. Subsequent work on this pioneering research has led to similar theories for matter and heat. The kinetic theory of matter contains 3 postulates [128, 129];

- All matter consists of atoms and molecules.
- All atoms and molecules undergo constant movements.
- Collisions between atoms and molecules are perfectly elastic.

The molecular-kinetic theory of heat consists of 5 accepted postulates [123, 130];

- Heat is a form of energy.
- Molecules can carry potential and kinetic energy.
- Potential energy arises from electric interactions between molecules.
- Kinetic energy gives the molecules their motions.
- Energy can convert between potential and kinetic.

These 8 postulates were used by Einstein in his theoretical formulation of Brownian motion; a consequence being the lowest temperature possible is that with no thermal

motion (absolute zero, 0 Kelvin $\approx -273^\circ$ Celsius), and that at any temperature above absolute zero all atoms and molecules undergo continuous, random movements.

3.1.2.2 Mathematical Description of Brownian Motion

Einstein defined a probability density ρ of a particle being at a certain position x after a given length of time t such that $\rho = \rho(x, t)$. After deriving the diffusion equation

$$\frac{\partial \rho}{\partial t} = D\Delta\rho, \tag{3.10}$$

where D is the diffusion constant, one can take the initial condition $x = 0$ at $t = 0$, yielding

$$\rho(x, t) = \frac{1}{(4\pi Dt)^{3/2}} e^{-\frac{x^2}{4Dt}} \tag{3.11}$$

which is a Gaussian probability distribution [123]. Einstein showed from first physical principles that the diffusion constant

$$D = \frac{k_{\mathrm{B}}T}{\gamma_0}, \tag{3.12}$$

where γ_0 from Stokes' Law is

$$\gamma_0 = 6\pi\eta a v, \tag{3.13}$$

where η is the viscosity, a is the radius of the spherical particle and v is the particle's velocity [123, 124]. Equations 3.12 and 3.13 form the Stokes-Einstein equation, which is related to the Fluctuation-Dissipation Theorem (FDT) [131].

3.1.2.3 Relevance to Studies with Optical Traps

Particles in the size range applicable to OTs ($a \lesssim 20\mu m$) all undergo Brownian motion that can be seen with an optical microscope, with the caveat that when in an optical trap larger displacements are reduced but high frequency movements remain unaffected (this is shown later). A trapped particle in an OT can therefore be considered to undergo 'restricted' Brownian motion, where the magnitude of the imposed potential (introduced in §3.1.1) varies with the square of displacement from the centre.

3.2 Practical Considerations of Optical Tweezer Setups

3.2.1 The Basics

An expanded laser beam is focussed, usually with a microscope objective, creating an area with increased photon flux [104]. Spherical particles up to a few tens of nanometres diameter, with a refractive index at least 10% greater than the solvent, will feel an attractive force towards the laser focal point [113, 114].

It has been shown that the greatest trapping force comes from the outer part of the beam [113], as a result it is preferable to slightly overfill the back aperture (rear opening) of the objective lens. Overfilling ensures the widest possible cone, resulting in a stronger trap.

3.2.2 Experimental Setups for Optical Tweezer Microrheology

The multitude of uses for OTs has led to a variety of experimental setups in use around the world, depending on the quantity being measured - usually a force (instantaneous particle displacement) or brownian motion (particle displacement at longer times). Biologists commonly use a trapping laser (eg. $\lambda = 1064$nm, a wavelength at which most cells are transparent) combined with a shorter wavelength (higher energy) 'cutting' laser (eg. $\lambda = 532$nm) to perform surgery *in vivo* [132, 133], chemists have employed the use of a spectrometer in the detection setup in order to measure the Raman spectra of trapped particles [134, 135] and biophysicists have used multiple-trapping techniques to probe the elasticity of various materials [136, 137, 138], to name just a few.

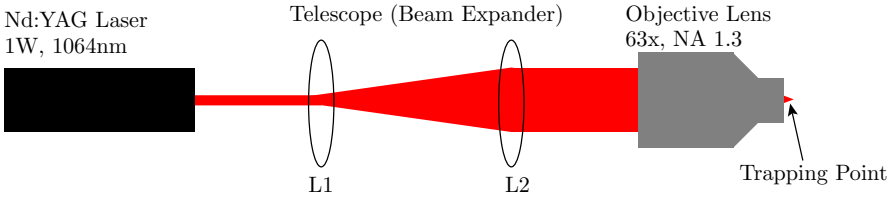

FIGURE 3.3: The simplest setup required for single-beam optical trapping. The example values given are from the NTU single-beam setup.

In this work, I am only measuring the rheological properties of samples, therefore no beam-sharing or holographic techniques are used as they may adversely affect the consistency of the trap. Only one trap is needed in this work, and the repeatability of the potential is of prime importance in order to compare rheological data. The basic concept of microrheology (using Brownian motion to calculate rheological parameters) involves measuring particle displacement, extracting the diffusion co-efficient D, and using the Stokes-Einstein relation to extract the viscosity η from D (the extraction of viscoelastic parameters is discussed later). With this in mind, the experimental hardware was kept as simple as possible in order to perform these experiments. All setups used in this

work consist of a single 1064nm laser used to trap a single silica or polystyrene particle between 0.5-10 microns in diameter, as shown in Figure 3.3.

3.2.2.1 Single-telescope Design

The simplest form of OT, as shown in Figure 3.3, involves using 2 lenses (a telescope) to expand the beam, and a third (objective) lens to focus the expanded beam. Lower numbers of optical components allow for higher beam intensities as less photons are lost in reflection, and simpler alignment than larger setups, however this comes at the expense of flexibility.

The tweezer setup at Nottingham Trent University (NTU), as shown in Figure 3.4 (p.54), is an example of a single-telescope design. The decision to have a single telescope was made for simplicity and safety; the laser fibre enters the custom enclosure at the back of the microscope, and the beam path is completely enclosed in anodised steel until the beam has passed through the sample. A bespoke laser-proof box (for $\lambda = 1064$nm), with electronic interlocks to automatically shut off the laser, was built to fit the microscope stage, the result being that nobody can be exposed to dangerous levels of laser light without completely dismantling the microscope.

The act of focussing a laser is highly dangerous, and therefore safety is a prime concern when designing an OT. This is compounded by the fact that near infra-red (IR) lasers (such as λ=1064nm) do not provoke the blink reflex of the human eye, as they are invisible. As a result, near IR beams have the potential to cause more damage than a higher intensity but visible beam. Another safety factor (particularly relevant to inverted microscopes) is that downstream from the focal point the laser propagates as an inverted cone, with higher magnifications producing larger spreading angles ($\sim 75^\circ$ for a 100$\times$

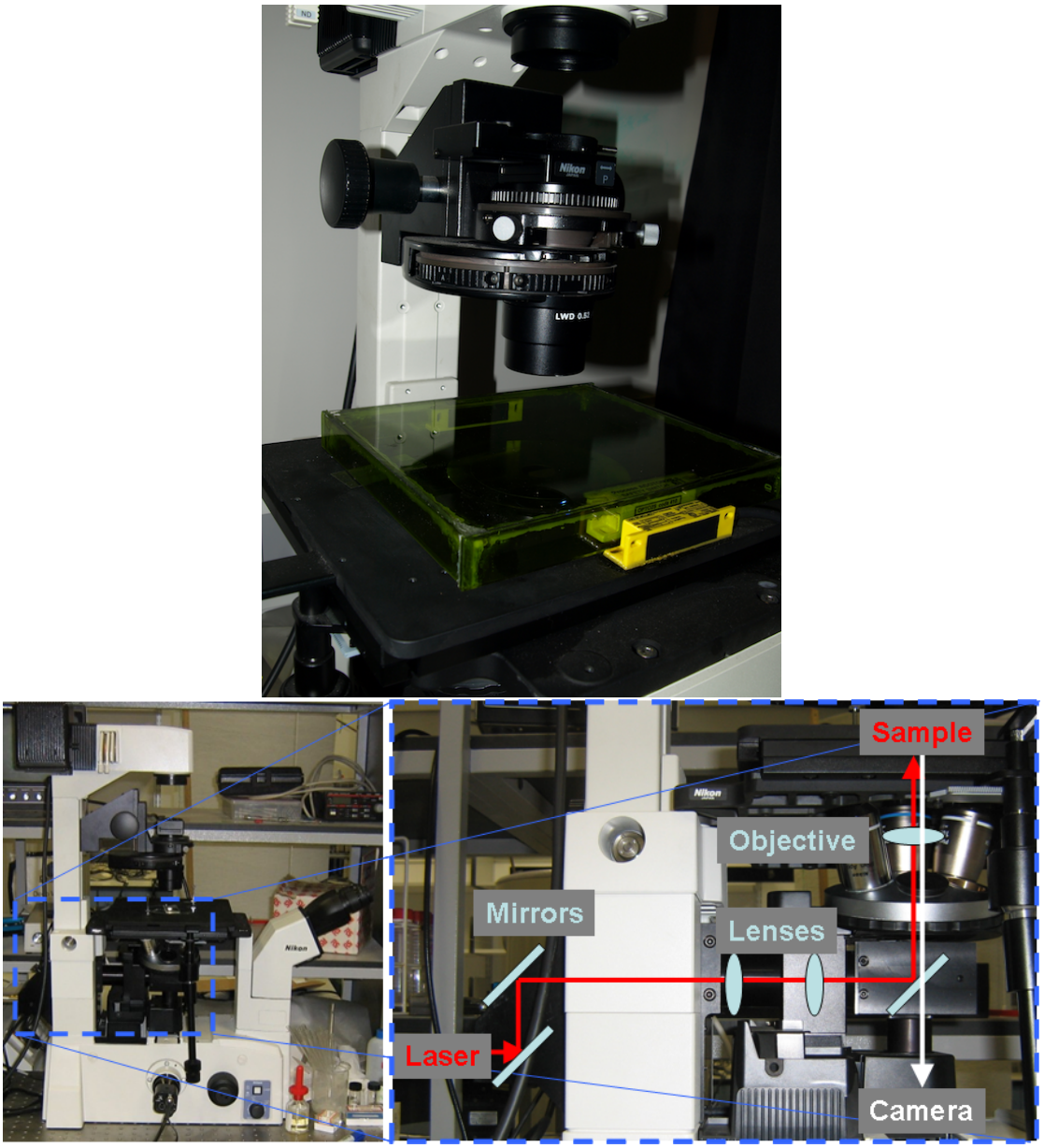

FIGURE 3.4: **Upper:** Close-up of the microscope stage, showing the laser-proof box and interlocks. **Lower:** Optical path for the tweezer setup used at NTU.

Nikon objective, as measured by myself). Despite this, OTs are fairly safe to use as the large spreading angle means the beam rapidly loses intensity per unit area. Using the UK's Health and Safety Executive (HSE) guidelines, I calculated that the dangerous radiation area extended 4.3mm from the focal point for the NTU 100× objective, and 13mm from the focal point for the 60× objective. The laser-proof box was therefore designed primarily to ensure no skin or eye could get within 13mm of the objective lens,

and secondly as a peace of mind guarantee that no laser light is propagating towards the user.

The microscope is a Nikon TE-2000 Eclipse, the anodised steel enclosure was built by Elliot Scientific, the laser-proof box and electronic interlock circuits were designed and built by myself.

This OT setup has an interchangeable detection module, visible in Figure 3.4, allowing either a CCD (for Brightfield Illumination, see §3.2.3.1) or a Quadrant Photo-Diode (QPD, see §3.2.3.2) to be used for particle position measurements, or both with an additional beam-splitter.

3.2.2.2 Dual-telescope Design

Figure 3.5 on page 56 shows the dual-telescope OT setup with Brightfield Illumination detection as used at Rutherford Appleton Laboratory (RAL) for some of the experiments presented in §3.4.

The second telescope in this setup, along with the two extra mirrors (M3 and M4), allow for more precise control and alignment of the laser trap. For example, this layout facilitates fine-tuning of the intensity distribution over the trap, something which cannot be performed on the single-telescope design in §3.2.2.1.

Important experimental notes are the iris/diaphragm around the focus of the 1:1 telescope, designed to remove secondary Bragg reflections from the AOD, and the 1064nm bandpass filter used to remove 800nm noise which was present due to the age of the laser.

This setup was also used to detect backscattered laser light by either turning off the microscope illumination (making experiments more difficult), or by placing a 1064 bandpass

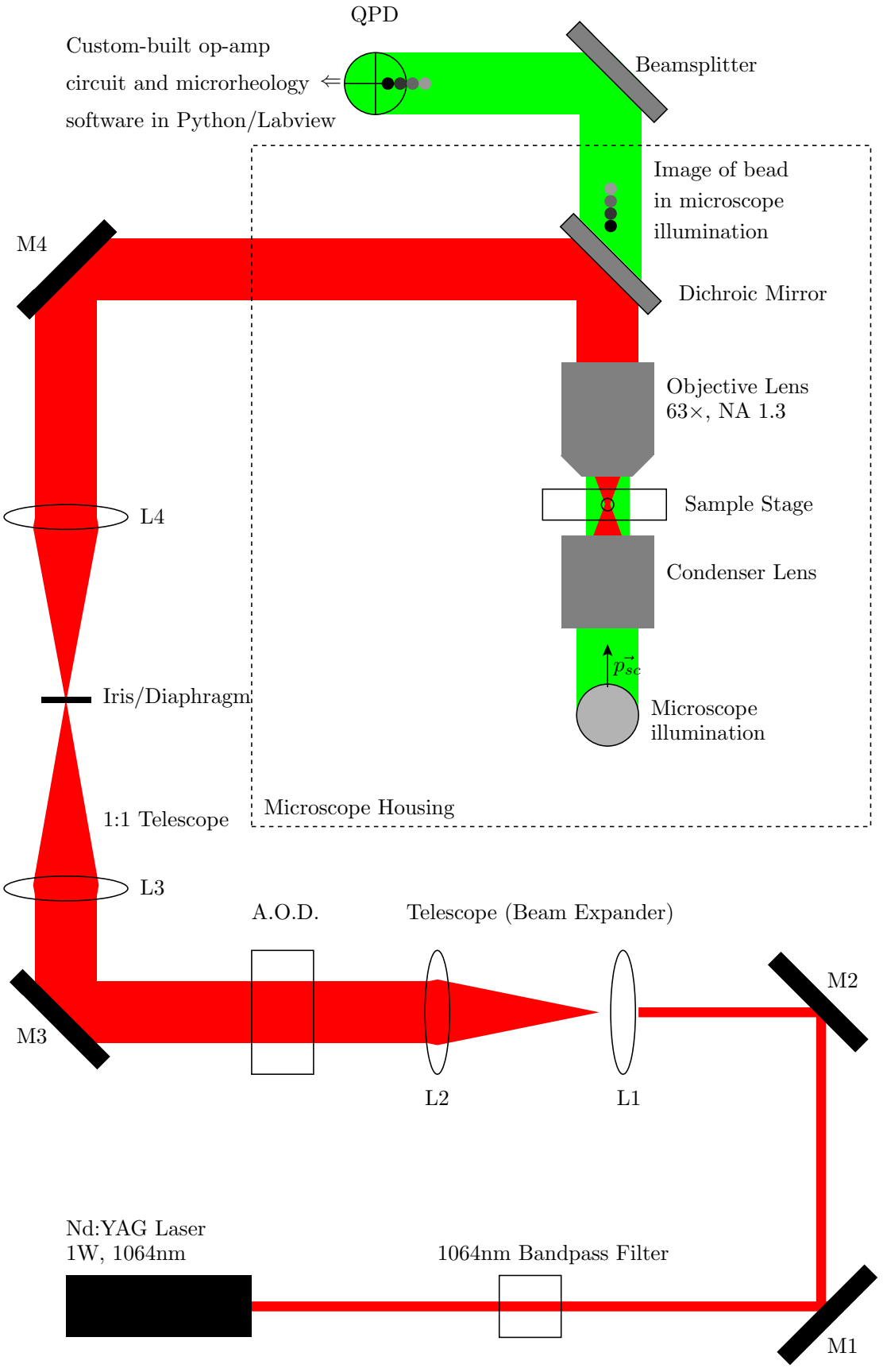

FIGURE 3.5: Optical Tweezer setup used at RAL

filter in front of the QPD. Backscattered laser detection offers slightly higher spatial resolution compared with brightfield illumination, however the lower intensity at the detector increases the relative noise level.

3.2.2.3 Acousto-Optical Deflectors (AODs)

Precise control over the position of the laser focus can be achieved using an acousto-optical deflector (AOD); an AOD uses a crystal, vibrating under pressure from an acoustic transducer, to accurately modify the direction of propagation of the beam. An AOD works by employing Bragg diffraction, described by

$$n\lambda = 2dsin\theta \tag{3.14}$$

where n is an integer representing the order of the diffraction peak, d is the distance between crystal planes and θ is the angle of diffraction.

The resolution of these devices is sufficient in position to allow nanometre control of the trap position, and in time to allow beam-sharing ($\gtrsim$20kHz). Beam-sharing involves sending a periodic signal to the AOD so that the laser switches between 2 or more defined positions, allowing multiple traps to be created. Although beam-sharing was performed on the OT setup at RAL, all experimental data presented here was taken with no beam-sharing, so as to achieve the maximum possible accuracy for the rheological studies (positioning the beam at a constant point increases the consistency of the trap).

It should be noted that due to the multiple orders of Bragg diffraction peaks, a single AOD will give multiple intensity peaks in a plane perpendicular to the beam propagation. Experimentalists must be aware of this, and 'cleaning' the beam by placing an iris around

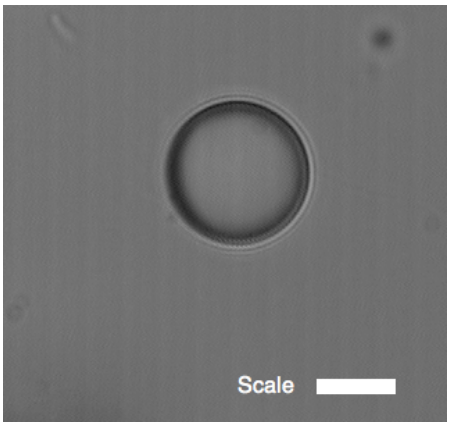

FIGURE 3.6: Image of a trapped 5μm diameter bead. The rings around the circumference are diffraction rings. The scale bar is 2.5μm.

the focal point of a 1:1 telescope removes the extra noise without inhibiting the beam when the position of the AOD crystal is changed.

3.2.3 Particle Displacement Detection

In order to calibrate the trap, it must be possible to quantify the particle displacement in the potential well - this section covers the various experimental methods to achieve this.

3.2.3.1 Brightfield Illumination

In the brightfield illumination technique, the position of the bead, illuminated by the microscope lamp and condenser, is imaged directly onto a detector (either a video camera or a QPD). This is the lowest resolution method to obtain the particle position, as the spatial resolution is usually limited on the order of the wavelength of light[3], and the temporal resolution is ultimately limited by current technology in camera electronics.

[3]This detection method has been used in conjunction with cross-correlation and image processing techniques to yield a nanometre-scale spatial resolution [139], however even two decades later desktop computers cannot perform these calculations in real-time, and more modern techniques give sub-nanometre precision.

For example, a 'standard' camera will record at 25 frames per second (fps), giving a Nyquist sampling frequency on the order of 10Hz, and hence an upper limit to any frequency dependent data. As a result, this method is not widely used for microrheology, but is common in other uses of optical tweezers. A fast camera can be used, however the acquisition rate is limited by the incident light intensity (in practice this was found to be ∼4000fps without additional illumination), therefore this technique was not used in this research.

3.2.3.2 Laser Radiation Detection with Quadrant Photodiode (QPD)

Of the photons incident on the trapped particle, some will refract through the bead and some will be reflected back through the optics. Coated beamsplitters can separate the laser wavelength from microscope illumination wavelengths, allowing visualisation (via a camera) concurrently with nanometre position resolution (via a QPD) in either forward or back-scattered geometries.

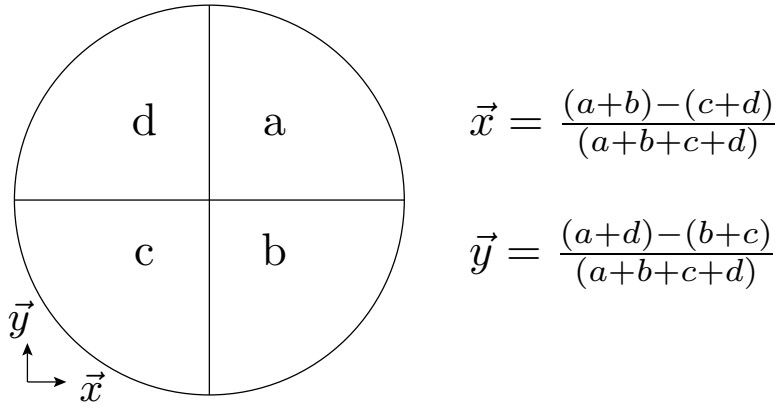

FIGURE 3.7: Diagram showing the setup and calculations when using a QPD to detect bead position.

Figure 3.7 shows a schematic of a QPD along with the calculations used to extract x- and y-position. In order to calculate the x-position, the two left $(a + b)$ and two right $(c+d)$ quadrants are subtracted from each other, this is then normalised by all quadrants

$(a+b+c+d)$ in order to remove any fluctuations in laser intensity (y-position is calculated by upper $(a+d)$ and lower $(b+c)$ quadrants).

QPDs are used for three main reasons; for pre-amplification of weak signals, for current to voltage conversion, and for high temporal resolution processing (>MHz). It is also possible to input the raw quadrant signals into a computer; this method was employed when using the RAL dual-telescope tweezer, which requires software signal processing.

3.2.3.3 True Interferometric Detection

Although laser detection methods with QPDs give better spatial resolution than direct imaging methods, it is possible to achieve high-frequency sub-nanometre accuracy using either Optical Trapping Interferometry (OTI) [114, 140], or Back-Focal-Plane Interferometry (BFPI) [141, 142]. Apart from the improved spatial resolution, inteferometric methods have the added advantage of not requiring the centre of the detector to be aligned with the incident beam.

The main experimental difficulty is that for high accuracy interference fringes, one must ensure that no other light impinges on the detector. It is for this reason that OTI and BFPI were not used extensively in this project, as it was not feasible with either the NTU (Figure 3.4) or RAL (Figure 3.5) tweezer setups to stop all light entering the detection geometry.

3.2.3.4 Circuit for simultaneous pre-amplification and processing of QPD signals

The usual method of collecting data from a QPD involves amplifying/converting the raw signals from current to voltage (1 op-amp per channel), performing the summing

calculation, eg. $(a+b)$, (1 op-amp per channel), and finally performing the differential, eg. $(a+b)-(c+d)$, (1 op-amp per dimension - x and y), yielding a total of 10 op-amps. This method also does not perform the normalising discussed in §3.2.3.2, which requires at least another 3 op-amps.

Each resistor used for amplification across the op-amps must be perfectly matched (ie. the actual resistance values must be as close as possible), otherwise the resulting signals will not be amplified equally. Many components (especially resistors) have a tolerance of between 5 and 20%, and matched components with <1% tolerance are much more expensive, therefore finding matched components is a costly and time-consuming task.

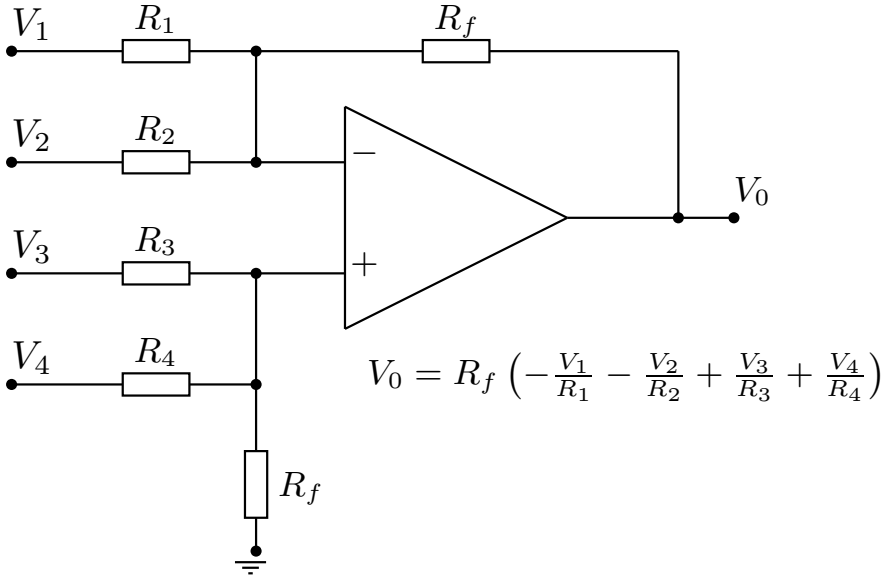

FIGURE 3.8: Circuit schematic used for processing QPD signals on NTU single-telescope optical tweezer. R_f resistors control the amplification, and matched R_{1-4} resistors will give equal amplification to each input.

To solve this, the NTU QPD detection setup employed one op-amp each for the x- and y-dimensions, using the circuit shown in Figure 3.8 (designed by myself). This circuit performs simultaneous summing, differential and amplification requiring only 2 matched feedback resistors and 4 matched input resistors. In this circuit, the op-amps were Texas Instruments THS Series, with an optimum input resistance of 20MΩ (where optimum is the resistance at which the signal to noise ratio is highest). I therefore used 20MΩ

resistors, which were each measured to ensure the resistances were ±0.5% across all components, and the impedance was always matched to the next stage.

This circuit was used in situations where the original signal level was sufficiently low as to cause the data acquisition (DAQ) card resolution to be the bottleneck.

3.2.4 Particle Position Calibration and Optical Tweezer Alignment

Once particle position can be accurately measured, using the techniques discussed in the previous section, the detector response must be calibrated to particle position so that displacement against time can be calculated from QPD voltage data.

This section describes the three methods used in this work to calibrate detector voltage to position with a QPD, and finishes with a brief discussion of experimental considerations when aligning an OT.

3.2.4.1 Particle position calibration with an Acousto-Optical Deflector (AOD)

Using an AOD, discussed in §3.2.2.3, a trapped particle can be moved with nanometre precision, allowing for the QPD signals to be calibrated against position. QPDs in an OT setup have a linear response region inside which any particle movement results in a change in the raw signals which varies linearly with displacement.

Figure 3.9 shows representative data from a calibration I performed using this AOD method at RAL. Before taking this data, the laser power was turned to maximum to reduce the Brownian motion. A 5μm particle was then swept across a range of 3μm in both x- and y-directions in 100nm steps. The fact that both linear regions have the same

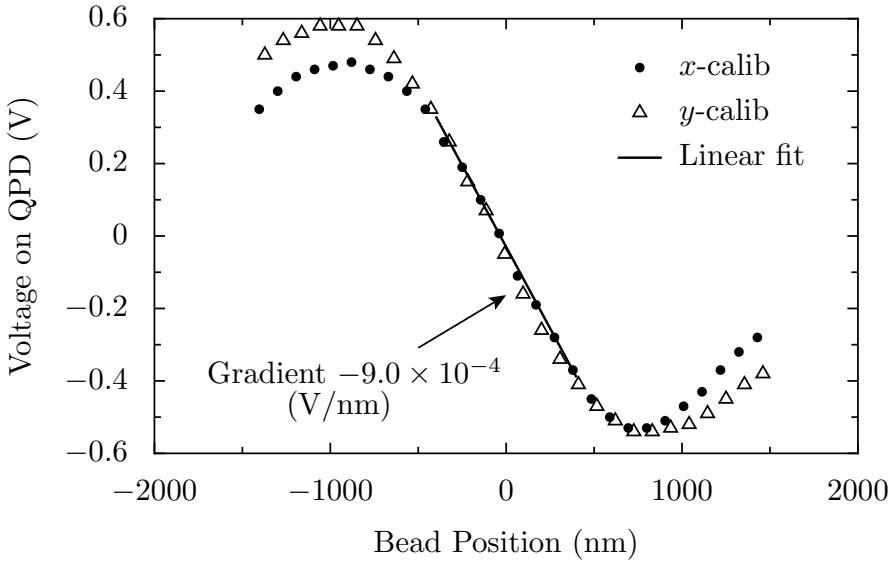

FIGURE 3.9: X- and Y- position calibration using an AOD and QPD

gradient confirms that the QPD response is symmetrical. The gradient is shown on the graph, and using this value all voltage data has been converted to position.

The AOD itself is calibrated by taking images of a trapped particle at the extents of the viewing region, and then dividing by the arbitrary position values shown in the AOD software, thus converting an uncalibrated voltage value into nm. In the RAL system the AOD calibration was on the order of 1nm per AOD step.

It should be noted that although AOD calibration is an accurate method, the process of moving the trap in order to calibrate position means that the relative light intensities on each quadrant are not representative of the equivalent displacement due to Brownian motion when the trap remains fixed. Therefore in this work AOD calibration was used regularly as a way of confirming trap symmetry and alignment, but was ultimately complemented and corroborated with a more accurate technique.

3.2.4.2 Bead position calibration with a Nano-positioning stage

A nano-positioning stage gives nanometre precision when aligning the sample; using a dried sample containing tracer particles, a bead can be swept through the trap whilst keeping the trap stationary. Using a dried sample means that Brownian motion can be ignored.

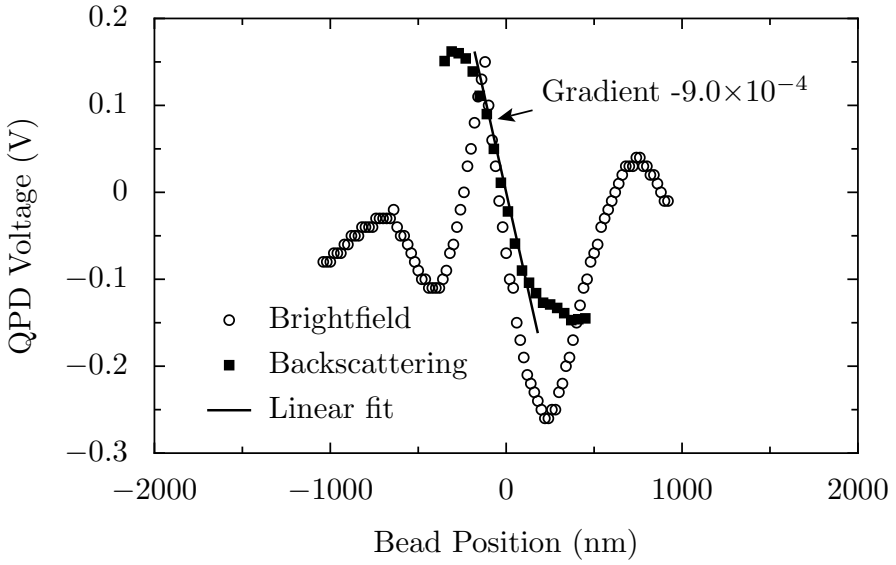

FIGURE 3.10: Nanopositioner calibration data for a 5μm particle trapped in the RAL optical tweezer setup using Brightfield Illumination and Backscattered laser detection geometries.

Representative data for a nano-positioner calibration performed at RAL is shown in Figure 3.10. The circles represent the calibration in brightfield illumination geometry (see §3.2.3.1) and the squares represent the same calibration performed using the backscattered laser light incident on the QPD (see §3.2.3.2). Although the two calibrations do not align perfectly, they confirm the AOD calibration that the linear response region of the QPD gives a calibration constant of around -9.0×10^{-4} V/nm.

Due to the manner in which a spherical particle scatters the incident beam, the QPD response can have multiple minima and maxima given a wide calibration region, as shown in Figure 3.10.

3.2.4.3 Optical Tweezer calibration using a sample of known viscosity

The third, and easiest, method to calibrate an OT setup is to trap a bead in a solution of known viscosity, and by measuring the corner frequency of the PSD (discussed in §3.3.2), one can calculate the trap stiffness α using Equation 3.19 (on page 72). This method does not require a particle to be moved manually in order to calibrate the PSD response, however in order to achieve an accuracy similar to the AOD method, the OT setup must be carefully aligned and have very low noise levels. This method was used to calibrate the NTU tweezer shown in Figure 3.4.

3.2.4.4 Optical Tweezer calibration using the Histogram method

Another way to calibrate a laser trap is to record the position variations due to Brownian motion at a given trap strength, and to plot a histogram of displacement (ie. the probability distribution P). For a Brownian process

$$P(x) = Ae^{-v(x)/k_{\mathrm{B}}T}, \therefore v(x) \propto -k_{\mathrm{B}}T \ln P(x), \tag{3.15}$$

where A is a normalisation constant. As it is based on displacement statistics, the accuracy of this method increases with the amount of data collected, however this method was not used as the calibrations mentioned previously are faster and more accurate.

3.2.4.5 Aligning an Optical Tweezer setup

The series of 8 images in Figure 3.11 show the Newton's rings [143] pattern formed as the objective lens position is moved (i.e. the focus is changed). These images were taken by turning the microscope illumination off and placing a silvered mirror face down on the

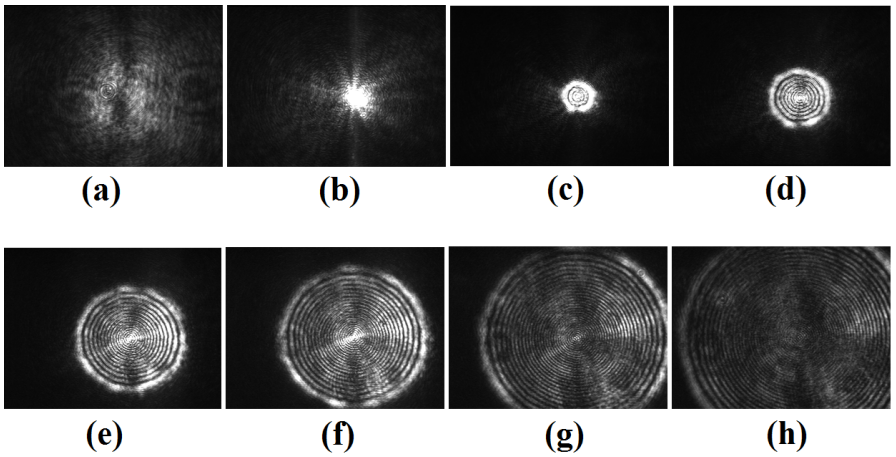

FIGURE 3.11: Images showing the changing Newton's Rings pattern as the trap is focussed. Images **a**-**h** show the trap image as the objective lens is moved closer to the mirror, with **b** showing the point at which the trap is focussed onto the mirror.

microscope sample holder; moving the objective towards the mirror moves the position of the trap focus closer to the mirror. Figure 3.11 (b) is obtained when the trap is focussed directly onto the mirror. This technique visualises the trap is so that the alignment of the beam optics can be checked. Images (c)-(f) in Figure 3.11 show a correctly aligned trap; the points to note are that the Newton's Rings pattern is symmetrical, circular and the intensity is roughly even across the rings (as shown in Figure 3.12).

Interference to cause these rings could occur in many places in an optical system, especially so in this case when the beam is deliberately being reflected back through the same optics. It is worth noting that Figure 3.12 shows a second, much narrower, set of interference fringes which originate from the thin wavelength-dependent coatings on some optics. This was tested by individually replacing components, and it does not affect the operation of the trap.

Figure 3.13 shows a common alignment problem where the laser enters the telescopes or objective at an angle. For a dual-telescope setup as shown in Figure 3.5, adjusting mirrors M1-4 should fix the problem.

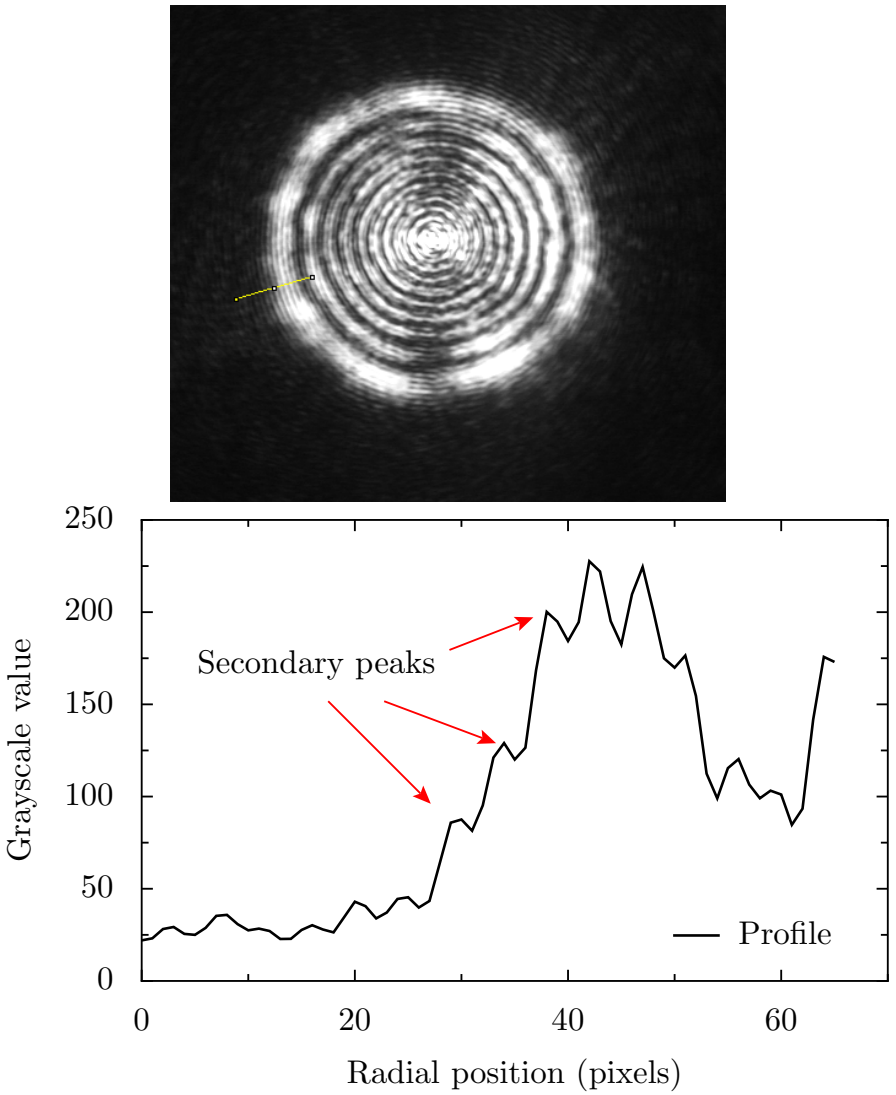

FIGURE 3.12: **Upper:** A CCD Image of a correctly aligned optical trap. The yellow line shows where the profile in the lower graph was performed. **Lower:** A representative profile of the Newton's rings pattern, showing the smaller secondary interference peaks.

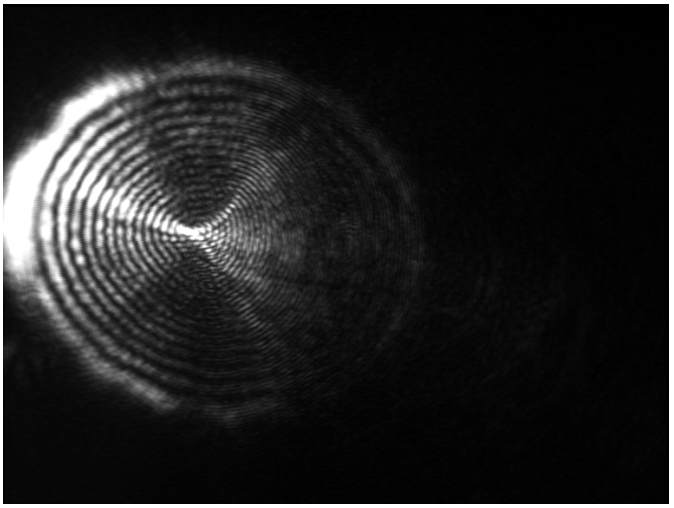

FIGURE 3.13: Incorrect trap alignment - Intensity profile is not symmetrical, adjust mirrors to fix.

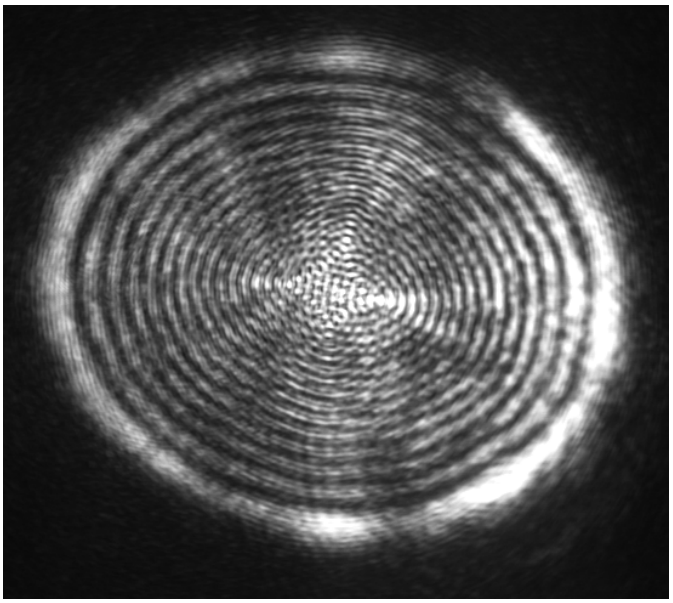

FIGURE 3.14: Incorrect trap alignment - Trap does not come to a clean focus, adjust telescopes or mirrors to fix.

Figure 3.14 shows another incorrectly aligned trap. The central bright spot shown in Figure 3.12 is missing as the laser does not come to a clean focus. The usual cause of this problem is uncollimated light entering the back of the objective, which could be a symptom of misalignment of either the telescopes or the steering mirrors.

3.2.5 Laser-induced Heating

A high-intensity focussed laser beam will impart thermal energy to its surrounding medium, as a result one must be aware of the laser power emerging from the objective lens. It has been shown that if the beam power is less than 50mW at the point where it contacts the sample, then the heating effect due to the trap[4] will be less than 1°C [144].

[4]This heating effect will be sample-dependent, however this rule holds for the typical water-based samples used in this work.

If the sample heating is not calculated and limited (by reducing laser power at the focal point, if needed), the viscosity η and refractive index n of the sample could change during measurements, as both are sensitive to temperature.

3.3 Methods for Rheological Measurements of Complex Fluids with Optical Tweezers

OTs are one of several methods which can be used to measure the viscoelastic properties of a sample [3]; other examples include bulk rheology, Diffusing Wave Spectroscopy (DWS) [145] and video particle tracking [146]. OT microrheology uses small sample volumes (μL) and measures the local microrheology through analysis of an added probe particle undergoing restricted Brownian motion within an optical trap. The temporal resolution is limited by the acquisition rate of the hardware (∼kHz), and spatial resolution is limited by the detection setup used (discussed in Section 3.2.3), but can be ∼nm. High-specification OTs can provide frequency resolution of viscoelastic properties exceeding mechanical rheology and comparable with light scattering methods (f∼100 kHz), and entry level OTs provide frequency resolution comparable with mechanical rheology (f∼kHz).

The main advantage OTs have over DWS and bulk rheology is that the local rheological properties of inhomogeneous samples are measured; these inhomogeneities may either be local variations present in the sample initially, or introduced through a gradient across the sample. Typically only shallow concentration gradients can be used as steeper gradients lead to faster material flow, which can dislodge the particle from the trap. However, in many cases predictions can be extrapolated from the low gradient case assuming linear

diffusion holds, and other forms of gradient (such as temperature or pH) do not suffer from this problem.

It is pertinent here to mention that there is still some debate over whether microrheology measures the same physical properties as bulk rheology [147, 148]. Logically, the Brownian motion of a tracer particle will only be linked to the bulk response if the contour length and mesh size of the network structure are both much smaller than the size of the tracer particle.

Many complex fluids (of commercial, industrial and academic interest) such as emulsions or suspensions contain particles suitable for optical trapping (see §4.11), and therefore they can be easily studied using OTs without modifying the samples with extra components. Polydispersity in some systems means that either particles must be chosen carefully, or multiple calibrations performed.

3.3.1 Measuring the Diffusion Coefficient from Brownian Motion

Raw data from OT experiments is collected in the form of x and y position measurements over time. This can be converted into the power spectral displacement (PSD) using a Fourier transform, or the mean square displacement (MSD, $\langle \Delta r^2 \rangle$), depending on which calculations are required.

The power spectrum is a plot of signal power against frequency; the more movements at a given frequency, the higher the value will be. The diffusion coefficient (D) can be extracted from the region of the power spectrum with negative gradient (on logarithmic axes, due to the power law of -2) by substituting Equation 3.12 ($D = \frac{k_B T}{\gamma_0}$) into

$$PSD(f) \approx \frac{k_{\mathrm{B}}T}{\pi^2 \gamma_0 f^2} = \frac{D}{\pi^2 f^2} \tag{3.16}$$

where γ_0 is from Stokes' Law (Equation 3.13).

The MSD is a plot of $\langle \Delta r^2 \rangle$ against time, and in a similar analysis to the power spectrum the diffusion co-efficient can be extracted from linear regions, which for motion in the x-y plane is

$$\langle \Delta r^2 \rangle = 4Dt, \tag{3.17}$$

where D is the diffusion coefficient.

3.3.2 Converting Brownian Motion to Viscosity

An OT keeps a bead in the trap by radiation pressure which removes the fewer larger and slower movements; this has the effect of creating a plateau (roll off) at low frequencies in the PSD, with the exact roll off frequency determined by the refractive index (of solvent, immersion oil and bead), solvent viscosity (or elasticity), laser wavelength and laser power. An example of this low frequency roll off can be seen in Figure 3.15 below $\sim$55Hz.

In a Newtonian fluid, this roll off means that the power spectrum can be fitted with a Lorentzian,

$$PSD(f) \approx \frac{k_{\mathrm{B}}T}{\pi^2 \gamma_0 (f_{\mathrm{c}}^2 + f^2)}, \tag{3.18}$$

with corner frequency,

$$f_c = \frac{\alpha}{2\pi\gamma_0} \tag{3.19}$$

where α is the trap strength.

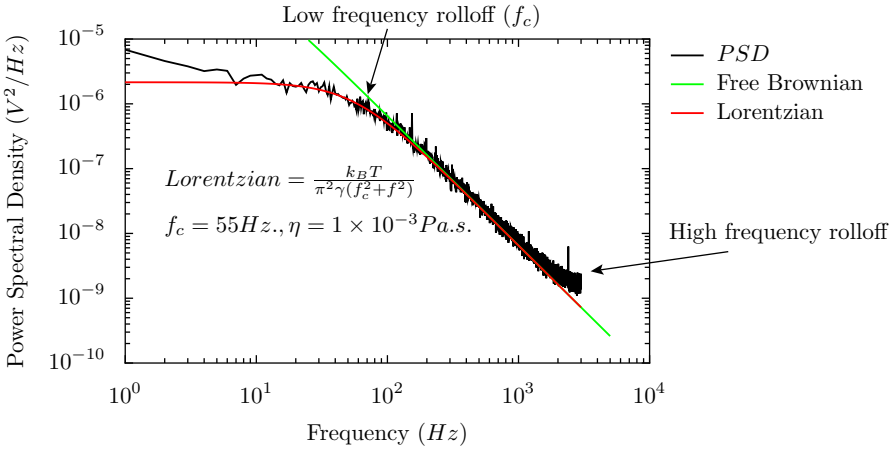

FIGURE 3.15: Power spectrum of bead motion for a trapped 5μm bead in distilled water recorded using the RAL OT setup. The low frequency rolloff is due to the OT, the high frequency rolloff is due to the detector resolution limit. The data is from a calibration with distilled water at 21°C, therefore knowing that the viscosity is $\sim 1 \times 10^{-3}$Pa.s., we would require a roll-off frequency of 55Hz if the system was accurate. The measured rolloff is $\sim$ 60 Hz.

The power spectral density shown in Figure 3.15 is from a calibration performed at RAL using distilled water at 21°C, and a representative calculation showing the conversion of Brownian motion to viscosity is also shown.

3.3.2.1 Mathematical Correction due to Particle-Surface Interactions

Due to the precise control over the position of the probe particle in an OT experiment, it is possible to place the bead (radius R) a given distance from an interface (height h) in order to study the particle surface-interactions. If this is performed, the value for γ from Equation 3.13 must be modified as follows [149],

$$\gamma = \frac{\gamma_0}{1 + \frac{9}{16}\left(\frac{R}{h}\right) + \frac{1}{8}\left(\frac{R}{h}\right)^3 - \frac{45}{256}\left(\frac{R}{h}\right)^4 - \frac{1}{16}\left(\frac{R}{h}\right)^5 + \ldots} \tag{3.20}$$

3.3.2.2 Typical microrheology data for Newtonian Samples

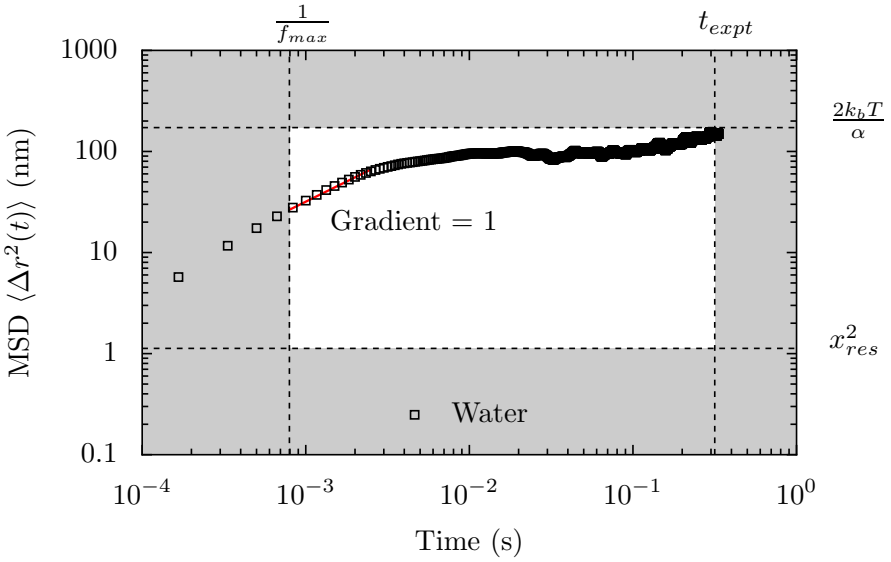

FIGURE 3.16: Representative MSD for a 5μm diameter polystyrene bead in water. The red line indicates where the gradient is unity.

Figure 3.16 shows an example MSD for a 5μm diameter polystyrene particle in water; the particle position was recorded at 6kHz for 2000s., with each 1s. of data being processed (into MSD) individually, and then the average was taken over all MSD files. The data was split every second due to the large volume (4 channels at 6kHz, with 4 channels at 100kHz later), and we could not guarantee that data was not dropped between acquisitions. It would therefore be inappropriate to place the data end-to-end and treat as a single experiment.

Figure 3.16 shows the format in which I will display MSD data, so I will briefly discuss how to read these graphs.

The grey areas represent the limits of experimental reliability, and the labels around the graph represent physical or experimental limits which dictate the usable data. The

TABLE 3.1: Table of limits for OT data, relative to MSD calculations.

Label	Limit	Reason/Fix
$\frac{1}{f_{\max}}$	**Data acquisition frequency**	This equipment acquired data at 6kHz, therefore motion can only be considered below the Nyquist frequency of 3kHz.
t_{expt}	**Experiment time (length)**	Our experiments were run for 1 second, therefore due to the lack of data as $t \to 1$s., data beyond 0.2s has been ignored. At times quicker than this, the data becomes statistically reliable. Running the experiment for longer would extend this limit, as would a greater number of repeats.
$\frac{2k_{\text{B}}T}{\alpha}$	**Trap strength**	The OT removes low frequency, large displacement movements from the particle. There is therefore an upper limit to the displacement of a trapped particle - this can be raised by lowering the laser power whilst ensuring that the particle does not diffuse away.
x^2_{res}	**x-resolution**	This is the resolution of the detection hardware, and represents the smallest motion which can be detected. Displacements below this value will still register a signal on the detector, but they cannot be differentiated from noise. The resolution can be increased by using a true interferometric detection method, discussed in §3.2.3.3.

reasons for these limitations are discussed in Table 3.1. Each limit presented here can be modified experimentally; the white area representing useful data can be maximised using newer hardware/longer experiments, however these limits will always be applicable to some extent. As a result, care was taken to minimise the effects, but for proof-of-concept work I did not spend a significant amount of time attempting to increase the range of available data.

TABLE 3.2: Viscosities of aqueous polymer solutions

Sample	Viscosity (Pa.s.)
Water	0.001
3k 50%	0.03
8k 50%	0.3

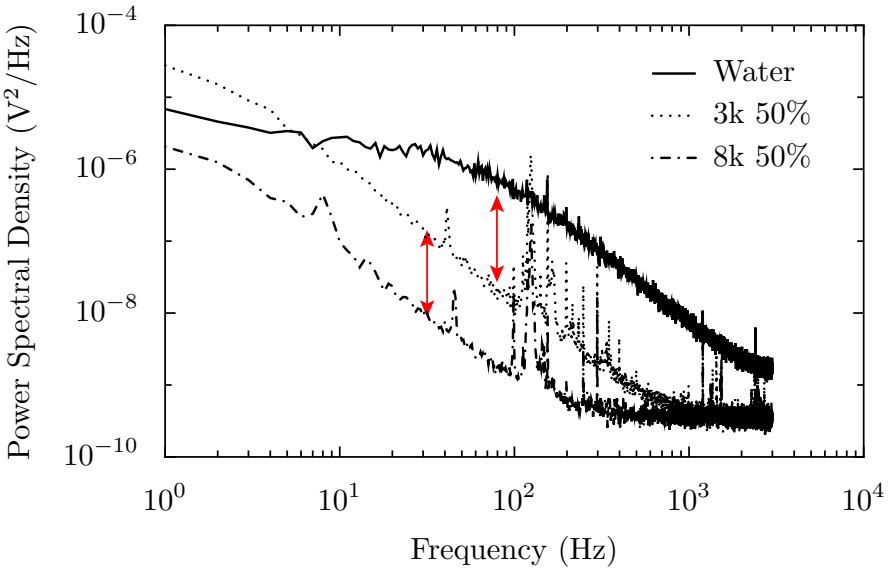

FIGURE 3.17: PSD of 50% wt. 3k MW PEO, 50% wt. 8k MW PEO and water. The red lines indicate one decade differences between the gradients - coinciding with the 1 decade difference between their respective viscosities.

Figure 3.17 shows the PSDs of two low molecular weight aqueous polymer solutions and water. From bulk rheological measurements (performed by myself), their relative viscosities are shown in Table 3.2. There is ∼1 decade between the viscosities of the samples, and this is mirrored in the PSDs in Figure 3.17, where the -2 gradient sections are separated by approximately the same amount, indicated by the red arrows.

3.3.3 Converting Brownian Motion to Viscoelastic Moduli

Data from viscoelastic samples must be treated differently as there is an additional elastic component to the Brownian motion, with the common techniques shown in Figure 3.18 below, reproduced from Reference [3].

Traditionally OT data has been converted into viscoelastic moduli using a Laplace transform method (§3.3.3.1), and the separation of real and complex components can also be achieved using the Kramers-Kronig relations (§3.3.3.2), however a recent theoretical advance [150] has removed the need for Laplace/inverse-Laplace/Fourier conversions

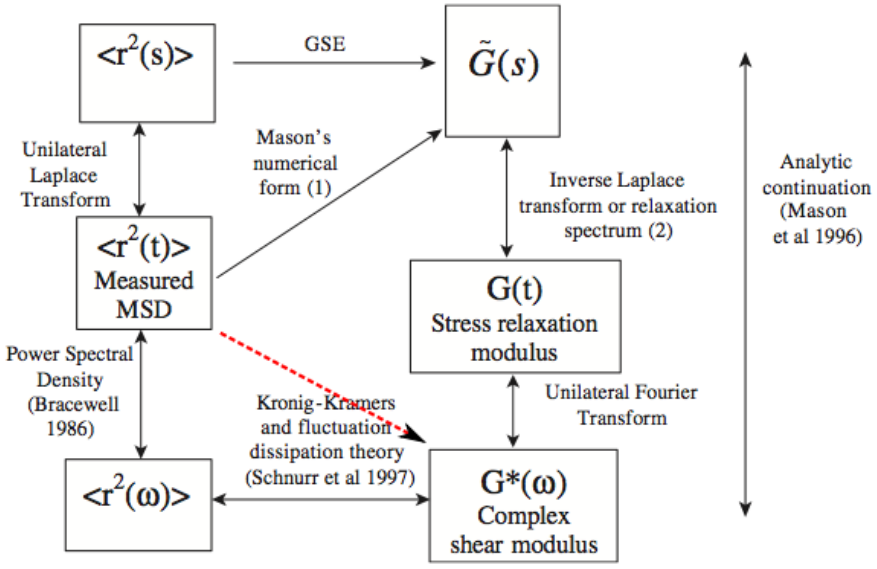

FIGURE 3.18: Diagram from Reference [3] showing the various methods used to convert experimental data into viscoelastic moduli. The dashed red line is an addition I have made showing the theoretical advance made by Evans *et al*, which avoids Laplace/-Fourier transforms and Kramers-Kronig relations.

(§3.3.3.3); this *direct conversion* is shown by the dashed red line in Figure 3.18. These techniques are discussed in detail in this section, along with their relative merits.

3.3.3.1 Laplace Transform Method

Traditionally, x-y position data from OTs has been converted into viscoelastic moduli using a Laplace Transform (LT) method [3, 151, 152]. The generalised Langevin equation (GLE) is used to describe particle displacement in a potential:

$$m\dot{\nu}(t) = f_{\mathrm{R}}(t) - \int_0^t \zeta(t-\tau)\nu(\tau)d\tau, \tag{3.21}$$

where $f_{\mathrm{R}}(t)$ is the restoring force (optical trap), m is the mass and $\nu(t)$ is the velocity of the particle [152]. In terms of the Maxwell model discussed in §2.2.1, the integral over v represents viscosity (dashpot), and the $\zeta(t)$ term is an elastic memory function

(spring). The fluctuation-dissipation theorem [131, 153], which describes the properties of non-equilibrium systems in terms of their equilibrium properties[5], thus becomes

$$\langle f_{\mathrm{R}}(0) f_{\mathrm{R}}(t) \rangle = k_{\mathrm{B}} T \zeta(t), \tag{3.22}$$

and the LT of Equation 3.21, substituting in Equation 3.22, yields

$$\mathcal{L}\left[m\dot{\nu}(t)\right] = \tilde{G}(s) = \frac{s}{6\pi a}\left[\frac{6k_{\mathrm{B}}T}{s^2\langle\Delta\tilde{r}^2(s)\rangle} - ms\right] \tag{3.23}$$

where s is the complex Laplace parameter, when certain assumptions are made [152]. This allows the complex modulus G^* to be found after fitting a polynomial to the MSD, and determining the value of the first and second logarithmic derivatives, which have analytic expressions. The equations for G' and G'' are given in closed analytical form [152, 155], therefore the LT does not need to be calculated numerically, as it has been performed analytically.

Although in widespread use with microrheological data, the LT method is less than ideal as the parametrisation of the MSD means a model is implicitly assumed.

3.3.3.2 Kramers-Kronig Method

The Kramers-Kronig relations [117, 156, 157] connect the real and imaginary parts of some complex functions from frequency-domain data, and have therefore been used to convert Fourier-transformed particle displacement data into viscoelastic moduli [37, 158]. Using the Kramers-Kronig relations is less common than the LT method discussed in

[5]The Stokes-Einstein relation is therefore a type of fluctuation-dissipation theorem as it relates the diffusion coefficient to viscosity [154].

§3.3.3.1, however the equations still contain integrals which must be calculated numerically, resulting in truncation errors.

3.3.3.3 Evans-Tassieri-Auhl-Waigh (ETAW) Method

The truncation errors and model assumption in the Kramers-Kronig and LT methods are avoidable. Evans *et al* recently showed that it is possible to directly convert compliance data into viscoelastic moduli using [150],

$$\frac{i\omega}{G^*\omega} = i\omega J(0) + \left(1 - e^{-i\omega t_1}\right)\frac{(J_1 - J(0))}{t_1} + \frac{e^{-i\omega t_N}}{\eta_\infty} + \sum_{k=2}^{N}\left(\frac{J_k - J_{k-1}}{t_k - t_{k-1}}\right)\left(e^{-i\omega t_{k-1}} - e^{-i\omega t_k}\right) \tag{3.24}$$

where $G^*(\omega)$ is the frequency-dependent complex modulus, J is the compliance and η_∞ represents the infinite viscosity (an extrapolation of the long-time gradient of the compliance to infinity). This closed-form solution means that using only a single experimental parameter η_∞ the storage and loss moduli can be calculated without assuming a model or fit; this is essentially a 'dot-to-dot' treatment of experimental data.

By removing assumed models and truncation errors, the viscoelastic moduli reveal true experimental noise from rheological and microrheological data for the first time. By using

$$J(t) = \frac{3\pi a}{2k_B T}\langle \Delta r^2(t)\rangle \tag{3.25}$$

to relate the MSD to compliance, where a is the radius of the trapped particle, one can use either compliance or MSD for this calculation.

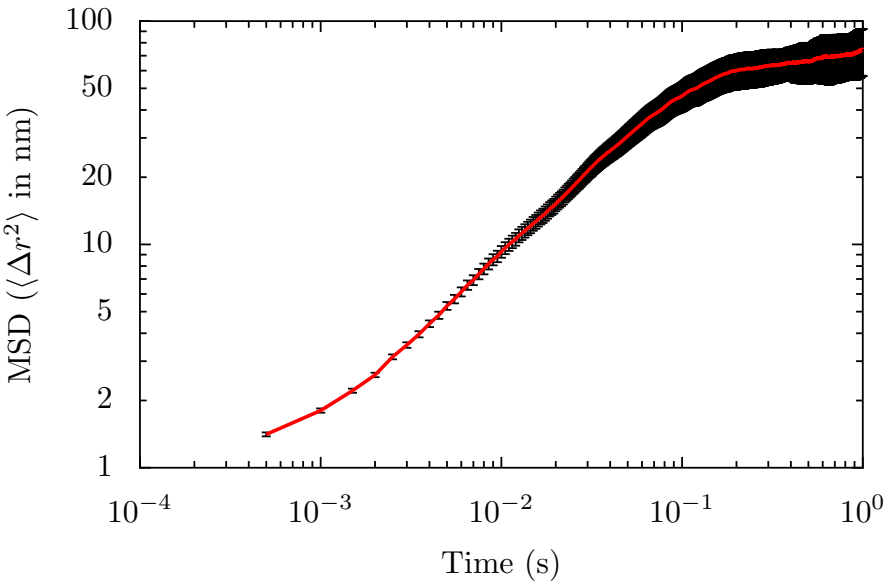

FIGURE 3.19: Representative Mean-Squared Displacement data with error bars showing the statistical uncertainties that arise due to less data being available at longer times.

Figure 3.19 shows a representative MSD plot for a 5μm bead in a viscoelastic system. The increase in errors as $t \to 1$ are statistical errors due to the relative lack of data points at long times. Statistically significant errors due to this can be reduced with longer experimental times, but will always be present.

The method described above removes errors associated with processing and calculations, leaving only statistical uncertainties and experimental noise [150, 159]. This technique is not only more accurate than LT or Kramers-Kronig, but since it is direct conversion, it is as accurate as possible for this calculation. The rheological OT data presented in this work was processed using this method; for completeness the Python code I wrote for this method is in Appendix A, and for brevity I shall eponymously refer to this as the ETAW method.

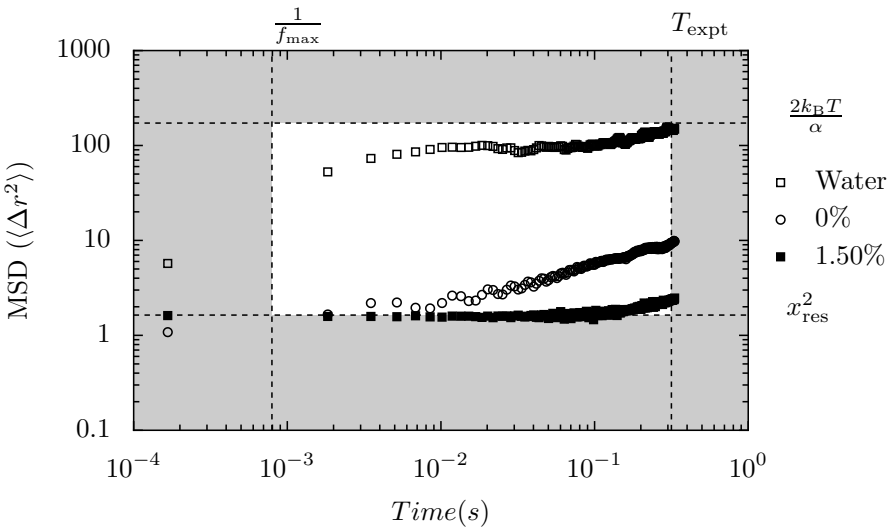

FIGURE 3.20: MSD data for 0.1 equi-Molar SDS:CAPB WLM solutions shown with water. The percentage values in the legend refer to the % wt. NaCl in the WLM samples.

3.3.3.4 Typical microrheology data for Non-Newtonian Samples

Figure 3.20 shows representative MSDs for OT experiments on non-Newtonian systems - entangled wormlike micelles (WLMs). The WLM sample with no additional salt (○) shows much larger particle displacements at longer times than for the same sample with salt (■). However, both samples are still well below the level of water (and close to x_{res}), a common problem encountered due to the high viscosity and elasticity of WLM network structures.

Using an interferometric detection geometry as discussed in §3.2.3.3, the x^2_{res} limit could be lowered, however there is no guarantee that this would yield rheological data from which useful quantities could be extracted, but it would certainly increase the range of data available for the two WLM samples shown here.

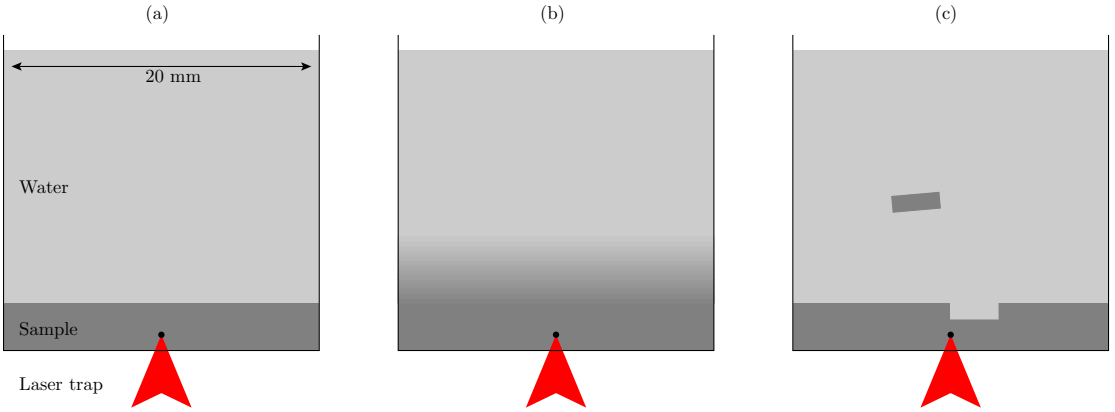

FIGURE 3.21: Schematic showing experimental method for non-equilibrium Optical Tweezer experiments. **(a)** shows the ideal setup for the start of an experiment, **(b)** shows a representation of 'normal' diffusive mixing and **(c)** shows the anomalies that occur predominantly during dilution of living polymer systems, discussed further in Chapter 4.

3.3.4 Method for Performing Non-Equilibrium Experiments with OTs

Non-equilibrium OT experiments were performed using the geometry shown in Figure 3.21, consisting of a 20mm diameter cylinder with a 100μm thick coverslip attached to the base. Small, but known, volumes of samples were placed in the cylinders and left overnight to equilibrate. The viscosity (or elasticity) of some samples was sufficient enough to require being left overnight in order to form an even 2mm thick layer at the base of the cylinders. The cylinders were sealed during this time to prevent evaporation. When ready, the sample holders were carefully placed on the stage of an inverted microscope, and a particle was found, trapped and moved to the optimal distance above the coverslip ($\sim 100\mu m$, the working distance of the objective lens). Water was then carefully placed on top of the sample using a long pipette. As the OT can only exert a force on the order of a few hundred pN, placing water on top typically knocks the particle out of the trap. Despite this I found it simpler to find, trap and move a bead first, quickly recapturing it at the correct height above the coverslip, rather than try to find and move a bead during the dilution process. It should also be noted that for the more viscous samples, the trap strength was not great enough to move a particle, therefore the laser focus is placed over

a particle at the correct height, and the OT is used simply for position measurement until the sample has diluted sufficiently.

3.4 Results from Non-equilibrium experiments with Optical Tweezers

Using the geometry introduced in §3.3.4, non-equilibrium experiments have been performed on a variety of viscous polymer samples in order to investigate changes to η during dilution.

The data shown in this section is representative of various types of samples and processing techniques; §3.4.1 shows the dilution of a Newtonian sample in conjunction with equilibrium sample data in order to calculate the concentration over time, §3.4.2 shows the dilution of a Non-Newtonian sample along with the G' and G'' data over time, and §3.4.3 shows the evaporation of a Newtonian sample over time.

3.4.1 Dilution of 8k MW PEG with MSD Analysis

An 8k MW PEG 50% wt. sample was diluted 20:1 with water, and the particle displacement was monitored over one hour.

Figure 3.22 shows the MSD of particle motion during this experiment, where the grey areas represent unreliable data due to the limits labelled on the graph (discussed in §3.3.2.2). These experiments were performed by recording the x and y motions of the bead for 300 seconds, where each second the latest data is written to a separate file. The MSD is then calculated for each file, and the average is taken giving the results shown above. The times shown on Figure 3.22 signify the difference in time between the

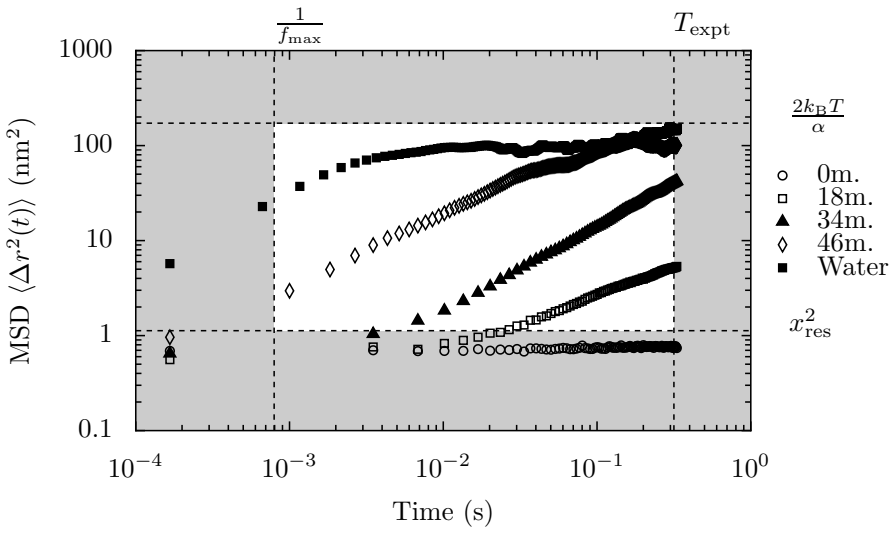

FIGURE 3.22: MSD of a 5μm particle during dilution of 50% wt. 8k PEO solution.

dilution solvent being added and the start of each 300 s. experiment. 5 μm particles were used throughout, with a laser power of 800 mW (corresponding to $<$ 50 mW at the focus) and a 63$\times$ Leica objective lens. Data acquisition was performed with LabView, using a modified RAL script, and all data processing was performed using custom-written Python/numpy programs.

This data shows a steady increase in particle displacement during dilution, as expected, as the sample transforms from a viscous polymer solution to the dilute regime. After only 46 minutes, the 8k PEG MSD was approaching that of water - the y-intercept clearly increases showing a decrease in η over time. From Table 2.2 (p.33) we find that at $t = 0$, c $\approx 3c^*$; taking into account the viscometer data from Figure 2.13, I assume the sample to be purely viscous during this experiment, ie. $c < c^{**}$.

Figure 3.23 shows the MSD of particle motion for pre-diluted 8k PEG samples at equilibrium. Using these in conjunction with the non-equilibrium data shown in Figure 3.22, it is possible to calculate the change in concentration over time. This can either be calibrated and converted to viscosity, or the viscosity can be calculated directly from the MSD data as discussed in §3.3.2.

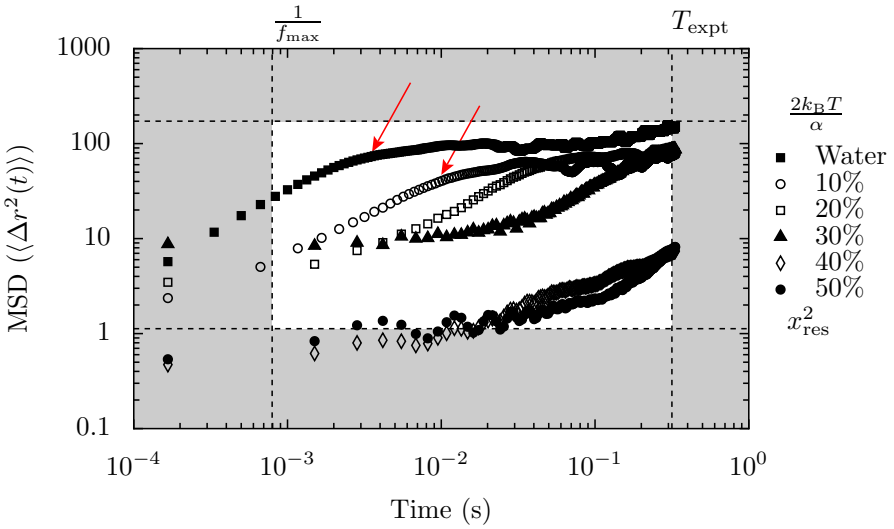

FIGURE 3.23: MSDs of various concentration 8k PEG solutions at equilibrium. The red arrows indicate the places where the OT affects the data (creates a plateau).

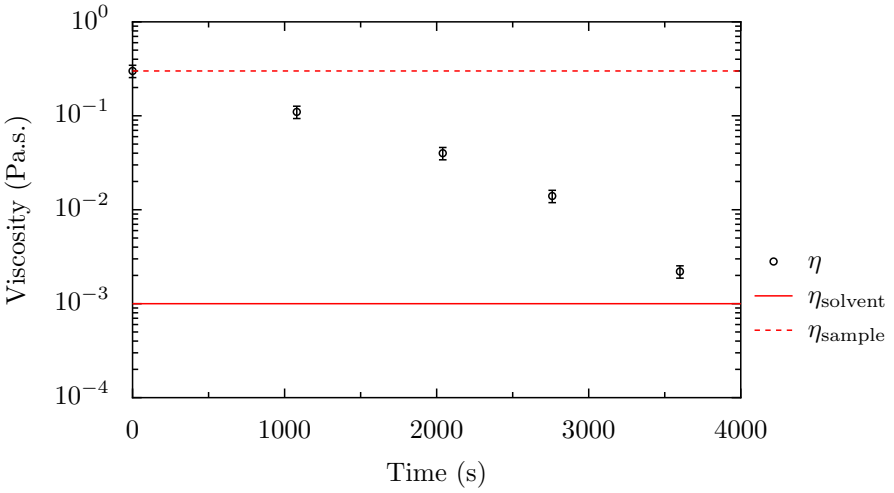

FIGURE 3.24: Viscosity vs. time for the 20:1 dilution of 8k MW PEG 50% wt. with water.

I have converted the MSD data shown in Figure 3.22 to viscosity using the static data in Figure 3.23 as a calibration, this can be seen in Figure 3.24. The dashed red line shows the viscosity of the PEG solution at $t = 0$, and the solid red line represents the literature value for the viscosity of water at 21°C [160]. As with all OT experiments presented here, the trapped particle was held ~100μm from the lower surface, with an overall sample thickness of ~2mm. A distance of 100μm was used as this was the maximum working distance (WD) of the objective lens, and I wanted to minimise particle-surface interactions (described in §3.3.2.1). Substituting the particle radius (5μm) and height

from surface ($100\mu m$) into Equation 3.20 ($\frac{R}{h} = \frac{5}{100} = 0.05$) gives an error due to particle-surface interactions of $\approx 3\%$ for these experiments.

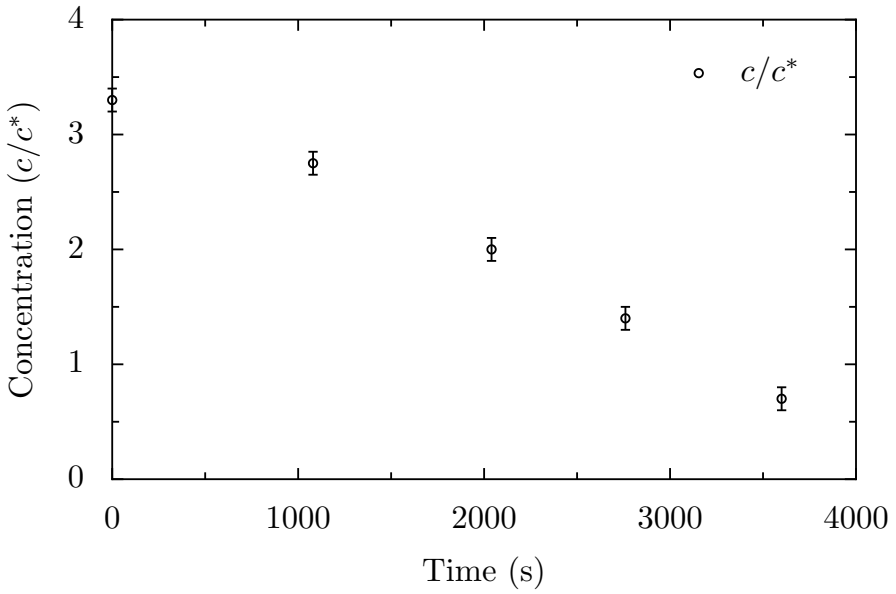

FIGURE 3.25: Concentration (scaled by c^*) against time for the 20:1 dilution of 8k MW PEG 50% wt. with water. The conversion from viscosity to concentration was performed using the experimental data from Figure 2.13.

Figure 3.25 shows the same data as Figure 3.24 with the viscosity values converted to concentration using the experimental data from Figure 2.13 (p.34). This shows the validity of OT equipment for measuring the concentration of a sample during dilution, which is difficult to obtain using bulk rheometry. If this research were to be continued, this data could be corroborated using quantitative phase refractometry (using ultra-violet absorption) during the OT experiments.

When the dilution water is placed on top of the PEG solution, there is obviously a delay before particle displacement changes as the top of the sample dilutes first. If it had been possible to monitor the particle displacement nearer the surface of the sample, the local viscosity would have decreased much faster than shown here. The emphasis in this experiment was on accuracy of the local viscosity measurements in order to validate the technique, however using multiple traps (via beam-sharing, holography or multiple

lasers) the viscosity at a range of locations could be monitored concurrently yielding a more representative picture of the macroscopic dilution gradient evolving over time. These techniques could also probe the homogeneity of the sample during dilution, or to probe the isotropy as the polymers disentangle. It is experimentally challenging however to trap many particles at various heights, and the proximity of the particles may lead to additional interaction effects such as depletion-interaction.

3.4.2 Dilution of 300k MW PEO with PSD Analysis

A sample with 7.8% wt. 300k MW PEO was diluted 20:1 with water, using the same experimental protocol as described in §3.4.1 above; the solvent being placed carefully on top of the polymer solution so as not to induce any artificial mixing. The position of a 5μm particle, placed $\sim$ 100μm from the lower surface, was monitored over $\sim$5 hours, and the power spectral density (PSD) over time is shown below in Figure 3.26 (on page 87). This 300k PEO can be considered to be in a highly entangled state at 7.8% wt., and has viscoelastic properties at this concentration.

The 3d graph (top) is presented here as representative of the noise present in non-equilibrium OT experiments. The 50Hz (mains) and 125Hz (table resonance) marked on the graph are important experimentally as they lower the overall accuracy, and must be removed or accounted for. The 50Hz noise is simply the mains power oscillation being transferred into the laser pumping system, therefore the trap stiffness oscillates, giving the bead a periodic motion on top of its stochastic thermal movements. Noise at $\sim$125Hz is more difficult to find as many modern mechanical components have similar frequencies; in this case, 125Hz was the resonance of the optical table on which the sensitive OT setup was mounted. Small air currents in the interlocked room at RAL blowing over the optical breadboard holes caused vibrations in the table, in a manner conceptually similar to the

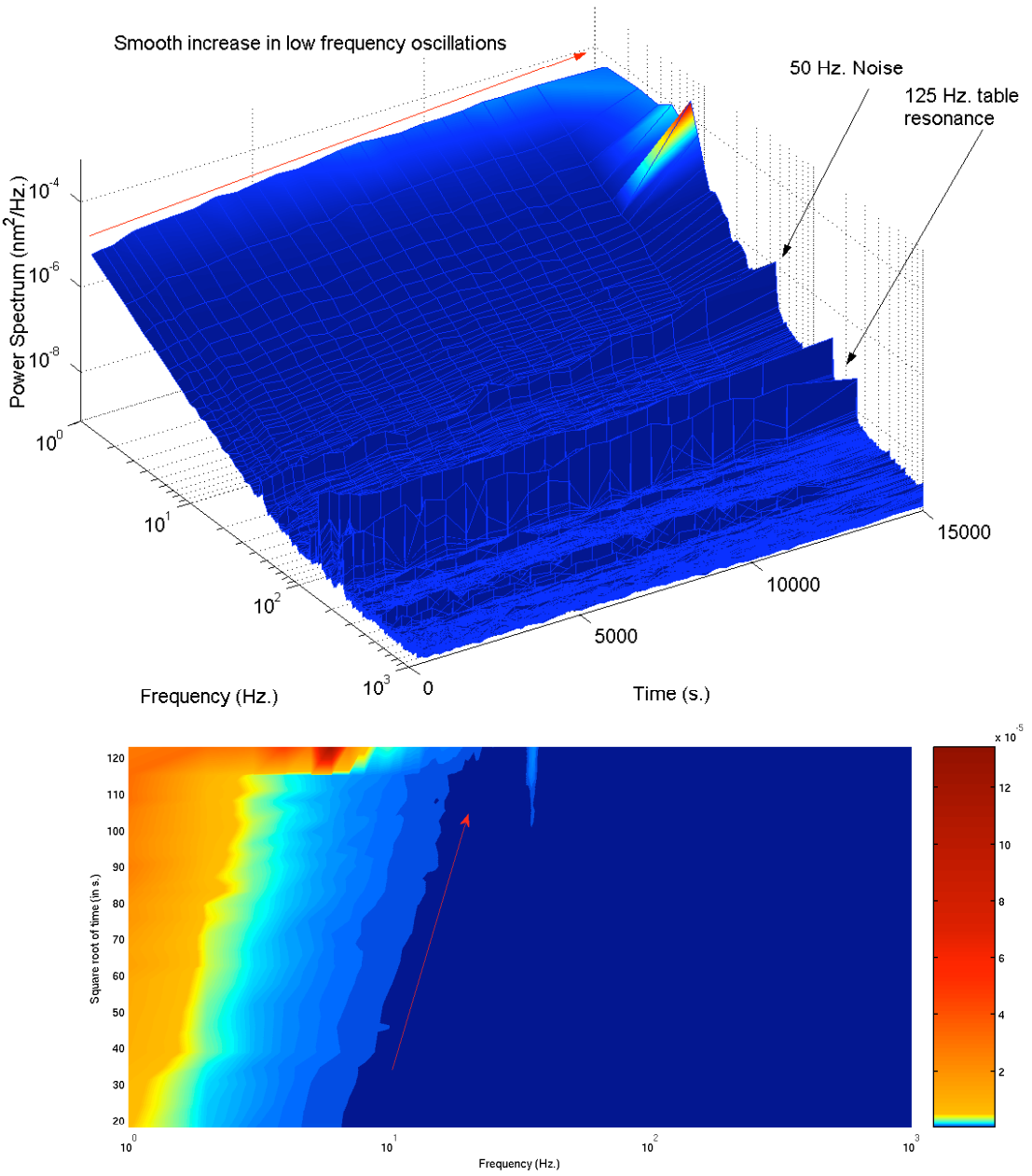

FIGURE 3.26: PSD during dilution of 300k PEO 7.8% wt. solution.

operation of a flute. This could only have been removed by filling the table/holes with sound absorbing foam, or removing the air currents, neither of which was feasible. As a result, where 125Hz was present in our raw data, it was removed via a bandpass filter before data processing (as was the 50Hz mains noise).

It can be seen that the relative intensity of the 50Hz noise increases over the length of the experiment. This can be understood in terms of trap strength relative to sample

viscosity; at t = 0s sample stiffness inhibits particle movement, therefore the weak trap ($\alpha \approx 100$pN) does not have much effect on the bead. We know that the bead is trapped, otherwise the 50Hz from the laser would not be visible, however the OT can be considered to be placed over the bead for detection purposes but without trapping it.

The same principle applies to the decreasing intensity of the 125Hz. table resonance, whereby a 'stiff' sample will transfer a larger proportion of the microscope vibrations to a particle than a more liquid (damped) sample. As further dilution allows larger particle displacements, the relative effect of the laser pumping increases, therefore the 50Hz noise increases and the 125Hz noise decreases over time.

The lower graph in Figure 3.26 shows the same data as the upper one, viewed from above. with the square root dependence of diffusion shown by the red arrow. Lower frequencies show a steady increase in intensity as natural diffusion mixes the polymer solution with solvent over a period of 4-5 hours[6].

Figure 3.27 shows the viscoelastic moduli for the data shown in Figure 3.26; G' and G'' here were calculated using the ETAW Method (§3.3.3.3) from the MSD of particle displacement.

Both G' and G'' show a rapid decrease in the first 1-2 hours, followed by a slow decline until the end of the experiment. It can be concluded that since no rapid change is shown in the power spectral densities (Figure 3.26) over this period, the initial decrease shown here represents the period when this sample can be considered to be viscoelastic. After this time, (t∼6000 s.) the polymers are most likely diluted to the point where they are no longer highly entangled and show only viscous behaviour.

[6]No syneresis was noticed during this or any other polymer dissolution experiment.

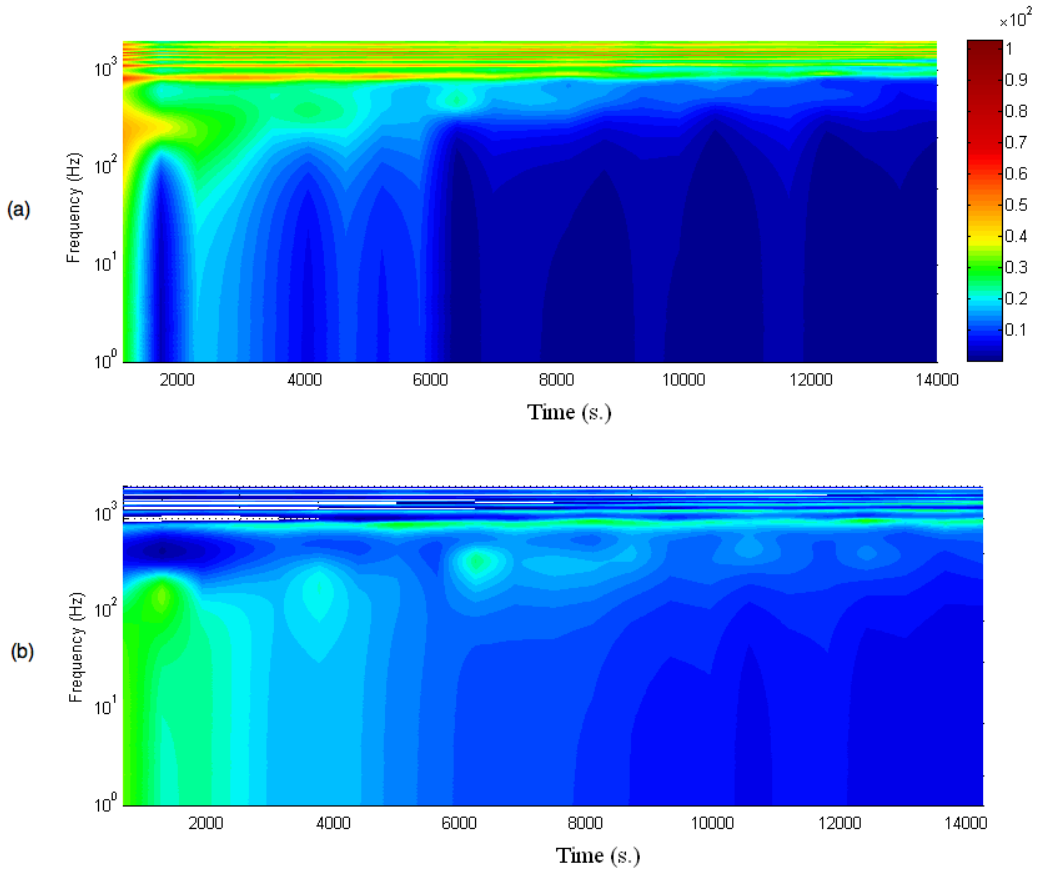

FIGURE 3.27: G' and G'' against ω during dilution for 7.8% wt 300k PEO initial solution. **(a)** Shows G' evolving over time, **(b)** shows G'' evolving over time

G'' clearly shows maxima and minima changing over time, as expected for a Maxwellian system being diluted. It is interesting to note that although G''_{min} occurs at roughly the same frequency over the entire experiment, the value of the minima increases in a stepped fashion. However, the frequency of G''_{max} increases whilst the value decreases over the experiments. To summarise this, the frequency and value of G''_{min} and G''_{max} both converge during the dilution of this viscoelastic sample, but only G''_{max} changes in frequency.

Despite the smooth nature of the PSD in Figure 3.26, the viscoelastic moduli show much variation, possibly due to an accumulation of local inhomogeneities during dilution and the non-smoothed nature of ETAW equation output. Further to this, since the

loss in viscoelasticity is clearly non-linear, the usual parameters for describing a non-Newtonian system such as the relaxation time τ_R and the plateau modulus G_0 are difficult to interpret without a theory encompassing micelle dissolution.

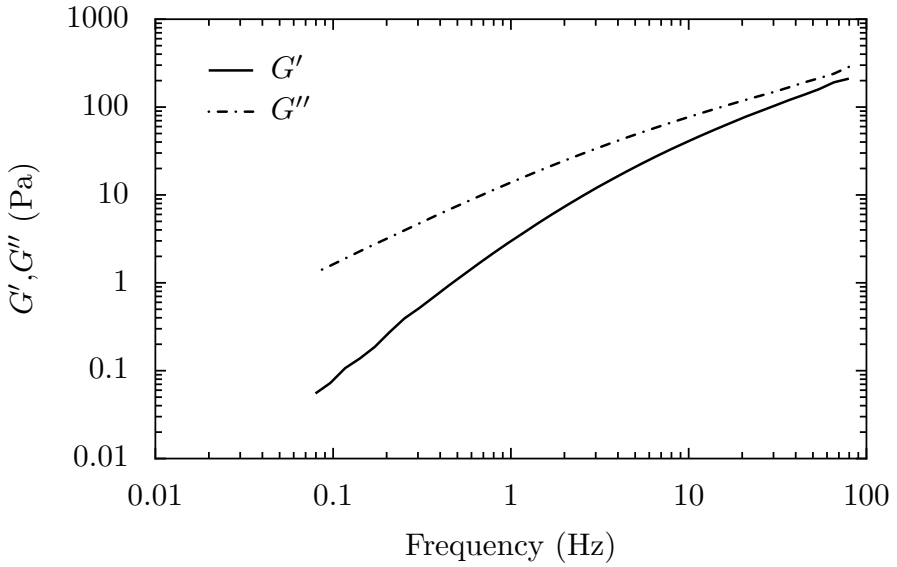

FIGURE 3.28: G',G'' versus frequency for 300k PEO 7.8% wt. aqueous solution, performed on an ARES-LS1 rheometer.

Figure 3.28 shows bulk rheology data performed on the undiluted 300k 7.8% wt. sample used in the dilution experiment above. Here we see that the viscoelastic moduli nearly cross in the range accessible by a cone and plate rheometer, and probably do cross above 100Hz, indicating an element of elasticity will be present at this concentration, but that it is close to being purely viscous, consistent with the dilution experiment above. From Table 2.2 (p.33), we find that the initial concentration $c_0 \approx 3c^*$ for this sample, similar to c_0 for the 8k dilution in the previous section; it is interesting to note that $3c^* > c^{**}$ for 300k, but not for 8k MW, due to increased entanglements from the longer chains.

3.4.3 Evaporative Drying of 100k PEO Solution with MSD Analysis

Figure 3.29 shows the changing MSD for a 5μm particle as 10% wt. 100k MW PEO solution is left to evaporate in ambient conditions. This was a different experimental

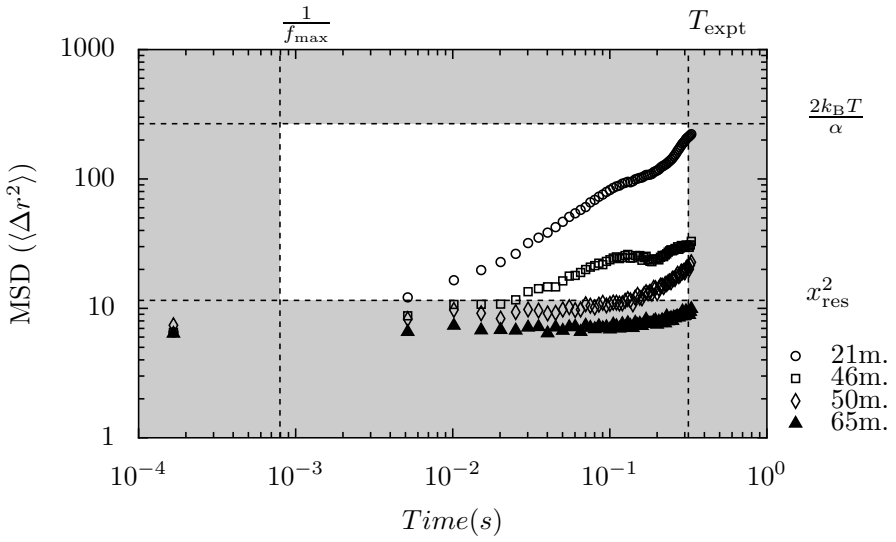

FIGURE 3.29: MSD of a 5μm particle undergoing brownian motion during evaporation of 100k 10% wt solution

alignment as for the dilution studies, resulting in a slightly larger x^2_{res} value, and without the additional water placed on top of the sample.

The MSDs show that rheological measurements during evaporation are viable using OTs, however the available data decreases over time, as opposed to the dilution measurements. This results in any potential phase transitions or new behaviour becoming more difficult to interpret, therefore I concentrated on dilution experiments. However, evaporation is somehow a less violent process than dilution.

3.5 Conclusions and Further Work

3.5.1 Validation and Limitations of the Technique

This chapter has shown that non-equilibrium rheological measurements are possible with an OT, and that the data is reliable within experimental uncertainties.

The dilution of 8k PEG (§3.4.1) shows that the viscosity, and hence concentration, can be easily monitored over time when a shallow gradient is present in the sample, allowing for detailed investigation of the dissolution process.

The dilution of 300k PEO (§3.4.2) has demonstrated the possibility of extracting standard rheological parameters in the presence of a gradient. In conjunction with the ETAW method, this yields *local* rheology data, with experimental noise still present. Using the ETAW method is viable, i.e. the conversion remains valid, as long as the rate at which the moduli change is much longer than the timescale of each experiment [159].

Measurements of rheological parameters have been performed during evaporation of 100k aqueous PEO solution (§3.4.3), demonstrating that different types of gradient can be present during these experiments. With evaporation, less usable data is available during the course of the experiment, therefore either low viscosity samples should be used from the start, or a much higher accuracy detection geometry/OT setup should be used.

3.5.2 Conclusions Drawn on the suitability of OTs for Rheology

None of these experiments can be reliably performed on DWS or mechanical rheometers, as both of these techniques measure the ensemble average, or bulk, rheology. On top of this, most commercial or industrial applications of polymeric complex fluids involve a gradient of some kind being introduced; food is heated, cooled and diluted, hair products are diluted, and micelles used to extract oil are subjected to extremes in temperature and pressure as well as concentration gradients [9]. As a result, OTs are useful for accurately measuring rheological properties of non-equilibrium systems, and equilibrium systems which require very small sample volumes [161]. Magnetic tweezers are a related technique in which carefully aligned magnetic fields are used to control a magnetic particle [162,

163], from which the calculations for viscous or viscoelastic quantities are identical to those for OTs. Magnetic tweezers (MTs) were not used in this study as the large fields required may have aligned the wormlike micelles. This would have been time-consuming to verify, so OTs were used throughout. It would be interesting to verify this, as MTs could also be used for non-equilibrium experiments. Recently surface acoustic wave (SAW) devices have been used to confine cells and particles in a similar manner to OTs and MTs [164]; these acoustic tweezers (ATs) are promising as they can trap multiple particles easily, and are extremely cheap to build.

Although there is no comprehensive theory for the dissolution of polymer/micelle solutions [15, 16], I have shown that qualitative and quantitative conclusions can be drawn from non-equilibrium OT experiments. Some recent advances [165, 166] show that progress is being made in this field, which will hopefully lead to rigorous characterisation and explanations of the effects seen here.

3.5.3 Further Work

Extending the available data in the experiments presented here would make the technique useful to a wider range of samples; the most effective way would be to enclose the OT setup and perform true interferometric detection, in order to lower the x_{res}^2 limits on the graphs shown here.

Another method would be to employ multiple traps to hold a 3-dimensional array of beads that would give a more complete picture of the dissolution dynamics over time.

The simplest option would be to slow the dilution by adding less solvent to a larger sample, and to take individual measurements of more than a second in order to increase the statistical reliability at long times.

It would also be interesting to measure the properties of other important systems, which were previously inaccessible without a non-contact trapping apparatus. Examples include the viscosity change in engine oil as the temperature is increased, monitoring the structural integrity of a living cell as the pH is varied, adding a crosslinker to a polymeric system to monitor the dynamics of gelation and the behaviour of bacteria in the presence of food or light, to name just a few.

3.5.4 Concluding Remarks

This chapter has shown that the viscous and viscoelastic properties of complex fluids in non-equilibrium conditions can be monitored over time, and subsequently quantified, using various OT setups. This work represents the preparatory and proof-of-concept work for an in-depth study on the rheological properties of a commercially-viable model shampoo system (a WLM network structure), in equilibrium and non-equilibrium conditions.

The next chapter presents the results from this shampoo study, and the OT techniques verified here are used in conjunction with bulk rheology and DWS to quantify the physical properties as the system complexity is increased.

4 Wormlike Micelle Rheology and Microrheology

"Chemistry has been termed by the physicist as the messy part of physics, but that is no reason why the physicists should be permitted to make a mess of chemistry when they invade it."

Frederick Soddy, 1877-1956

4.1 Introduction

Wormlike micelles (WLMs) are self-assembled surfactant aggregates introduced in Chapter 2; this chapter represents an investigation performed for Unilever PLC aimed at understanding the rheological behaviour of a 'model' micellar network, and gradually increasing the complexity towards a commercially-viable system.

Many commercial products contain surfactant aggregates for reasons such as controlled deposition [167, 168], conditioning [20, 169, 170] and as a detergent [171, 172], to name just three. Real-world products consist of many individual components; the interactions between these are not always well understood. As a result this work was structured to start with a simple 'ideal' micelle network which forms the basis of many Unilever

products, and to attempt to understand the changes in the rheology caused by each individual additive.

4.1.1 Chapter Layout

TABLE 4.1: Table showing the increasing complexity of the WLM system studied in this work. The left hand column shows the section for each study, and the values in the cells show the range of concentrations for each additive.

Section	SDS	CAPB	NaCl	PEO	Preservative	Jaguar
Equilibrium experiments						
§4.3	0.1-0.2M	0.1-0.2M				
§4.4	0.1-0.2M	0.1-0.2M	0-3%			
§4.6	0.1-0.2M	0.1-0.2M	0-3%	0.1-0.5%		
§4.7	0.1-0.2M	0.1-0.2M	0-1.5%	0.1-0.5%	Glydant/Nipagin	
§4.8	0.1-0.2M	0.1-0.2M	0-3%	0.2-0.4%	Glydant	0.1%
Non-equilibrium experiments						
§4.9	0.1M	0.1M	1.5%			
§4.10	0.2M	0.2M	1.5%	0.5%		
§4.11	N/A	N/A	N/A	N/A	N/A	N/A

Table 4.1 shows the experimental results sections in this chapter, and the components present in each study. This chapter finishes with some non-equilibrium experiments performed using optical tweezers on the initial micelle network, the micelle network with a polymer and finally a real-world product formulation.

4.2 Dual-surfactant SDS:CAPB Wormlike Micelles

Wormlike Micelles (WLMs) have been introduced in §2.3.2, however the micellar systems studied here differ slightly from the standard model. These micelles consist of two different surfactant molecules, each equally weighted with respect to the molar concentration; the two components being Sodium Dodecyl Sulphate (SDS, see §4.2.2.1) and Cocamidopropyl Betaine (CAPB, see §4.2.2.2). The equal molar concentrations are referred to

throughout as *equimolar*, where for example '0.1 eM' refers to 0.1M of each component, 0.2M in total.

Dual-surfactant micelles such as these have been shown to have much more pronounced viscoelastic behaviour at lower concentrations than single-surfactant micelles due to the specific interactions between the components, in this case the electrostatic and steric interactions between the anionic SDS and zwitterionic[1] CAPB.

4.2.1 Experimental Techniques

The experimental techniques used in this chapter include bulk rheology (introduced in Chapter 2), optical tweezer microrheology (introduced in Chapter 3) and Diffusing Wave Spectroscopy (DWS), discussed below.

4.2.1.1 Diffusing Wave Spectroscopy (DWS)

Diffusing Wave Spectroscopy (DWS) is an extension of Dynamic Light Scattering (DLS) to the multiple scattering limit; instead of measuring the photon scatter from single events, the entire sample is made turbid through the addition of tracer particles, forcing the incident beam to scatter over many particles [145, 173], as shown in Figure 4.1. With each individual tracer particle undergoing brownian motion, the 'speckle' arising downstream from the sample contains information on the rheology of the system, but due to the multiple scattering events, the data is inherently more accurate at short times than DLS/OT experiments as it is implicitly averaged over many particles/events. This averaging also presents a problem as any inhomogeneities in the sample will modify the speckle in such a way that it becomes difficult to interpret.

[1] Zwitterionic means to have both positive and negative charges, and comes from the German word *zwitter* meaning hermaphrodite.

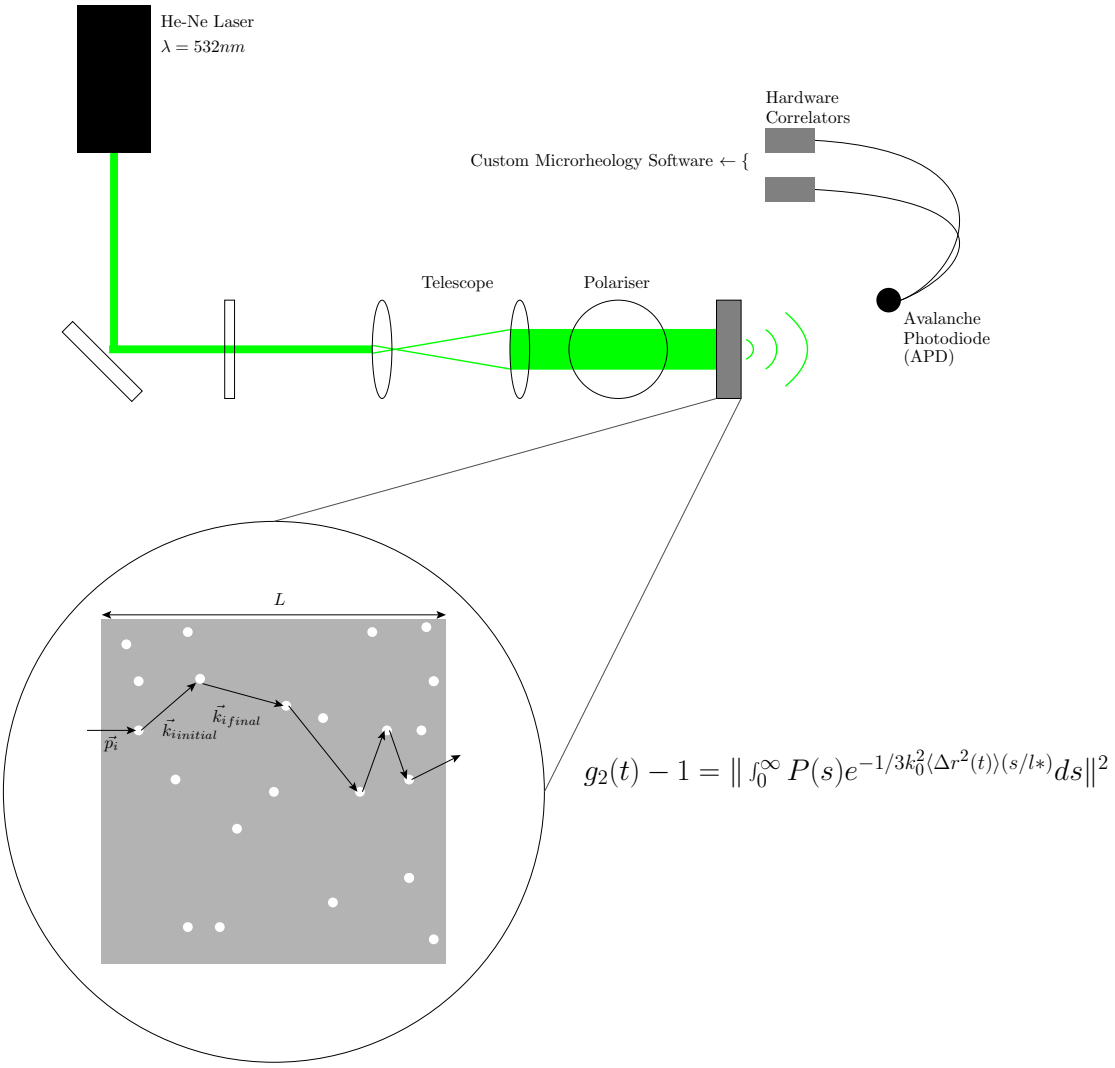

FIGURE 4.1: Ray Diagram and example photon path for Diffusive Wave Spectroscopy (Transmission geometry)

DWS experiments were performed on a custom setup at Unilever R&D, Port Sunlight, with the optical path as shown in Figure 4.1. Samples were made with 1% vol. $0.5\mu m$ diameter silica particles from Fluka (Order No. 95585, standard deviation $\leq 0.05\mu$m), and were then left for 24 hours before being prepared in quartz cells of 2mm and 5mm thickness (a thicker cell implies more scattering events, however the short-time behaviour becomes less distinguishable). The quartz cells were then centrifuged at ∼1000rpm for 5 minutes in order to remove air bubbles, and the samples were left to equilibrate for at least 2 hours. The sample holder was set at 25°C, and samples were left to equilibrate in the holder for 10 minutes before experiments were started. Experiments were run

between 3-5 times for each sample, and back-scattering geometries were tested as well, but the results were not convincing, therefore all data presented here are from forward-scattered DWS.

The experiments measure the speckle intensity I over time giving;

$$g_2(\tau) = \frac{\langle I(t)I(t+\tau)\rangle_t}{\langle I(t)\rangle_t^2} \tag{4.1}$$

where $g_2(\tau) - 1$ is the Intensity Autocorrelation Function (IACF). Using the relation

$$g_2(\tau) - 1 = \left[\int_0^\infty P(s)e^{1/3k_0^2\langle\Delta r^2(t)\rangle(s/l^*)}ds\right]^2 \tag{4.2}$$

where $P(s)$ is the probability density function of the photon path length, the IACF can be converted into mean-square displacement (MSD), which is then converted into G' and G'' (this was performed automatically by the software using the Laplace Transform method discussed in §3.3.3.1).

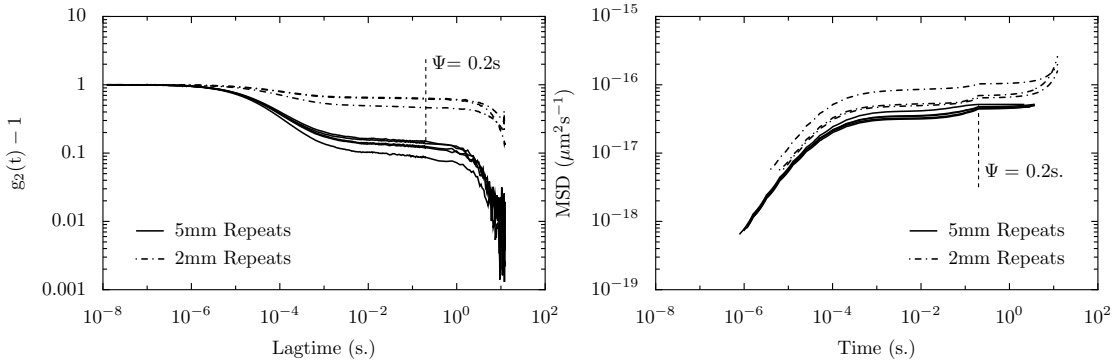

FIGURE 4.2: Representative Intensity Autocorrelation (**left**) and Mean-Square Displacement (**right**) data for 2mm and 5mm DWS sample cells (data are for 0.1 eM SDS:CAPB WLM system with 1.5% wt. additional NaCl). The solid lines show the repeats for the 5mm cells and the dash-dotted lines show the repeats for the 2mm cells . The Ψ point shows where the long-time calculation was fitted incorrectly, and is therefore where the MSD data is truncated before processing.

Figure 4.2 shows representative $g_2 - 1$ and $\langle \Delta r^2(t) \rangle$ data obtained from these DWS experiments. The data acquisition software used an echo technique to deduce the long-time behaviour without the length of experiments increasing too much. This implementation was not quite complete, and therefore a join between 'normal' data and long-time data became apparent in the MSD (although it is present, it is not so obvious in the IACF), as shown by the Ψ points in Figure 4.2. This data was therefore removed from all experiments, leaving just the standard DWS results.

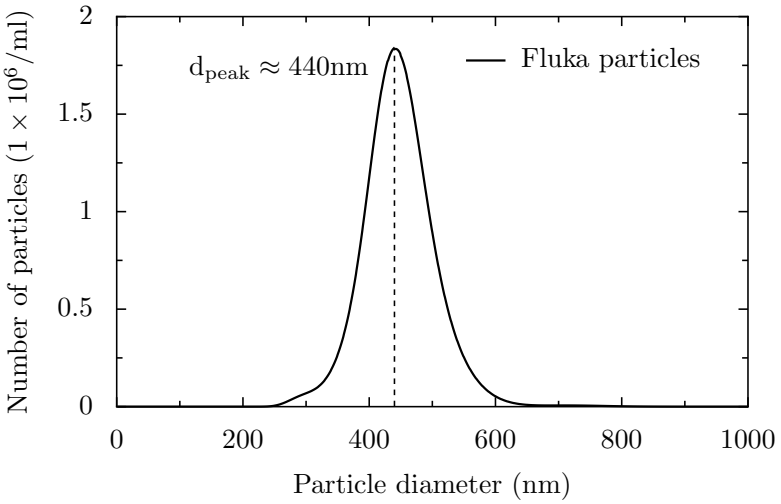

FIGURE 4.3: Particle size distribution as measured on a Nanosight® LM20, showing the '500μm' particles from Fluka were slightly polydisperse with a peak diameter d_{peak} of around 440nm. The DWS data was re-calculated accordingly.

After these DWS experiments were performed, it was noticed in Transmission Electron Microscope (TEM) micrographs that the Fluka particles had a smaller diameter than reported. Since the TEM samples had been dried and sputter-coated, they may misrepresent the true solvated particle size, therefore particle sizing was performed in solution using a Nanosight® LM20. The LM20 measures the brownian motion of particles using reflected laser light, and subsequently calculates the particle size with an error $<$ 1nm. Figure 4.3 shows the results from this experiment; the particles are slightly polydisperse, and the peak diameter $d_{peak} \approx 440$nm. This does not invalidate the DWS experiments as

the IACF was still measured correctly, however the data has been re-processed from the IACF stage into G' and G'' (as described above) with this new value used throughout.

DWS is widely considered to give superior results to other microrheological techniques, however it is not without its pitfalls. Firstly the added tracer particles may modify the rheology of the sample, and secondly the particles may be experiencing 'particle slip' whereby the local area around a particle may become devoid of micelles, resulting in the brownian motion not representing bulk rheological behaviour. Consequently DWS data is usually shifted by a factor of ∼1.5-2 in order to account for particle slip. Since this shift is fairly arbitrary, and the comparisons performed here are concerned primarily with the *change* in behaviour with various additives, the DWS data has not been shifted and is presented separately from other rheological data.

4.2.2 Chemical Components

Poly(ethylene oxide) (PEO) with MW = 4M is used throughout this chapter, the various other components are discussed below. These molecules were chosen by Unilever for this study as they have been shown to be safe for inclusion in personal care products, and have beneficial properties for these products, as discussed previously.

4.2.2.1 Sodium Dodecyl Sulphate (SDS)

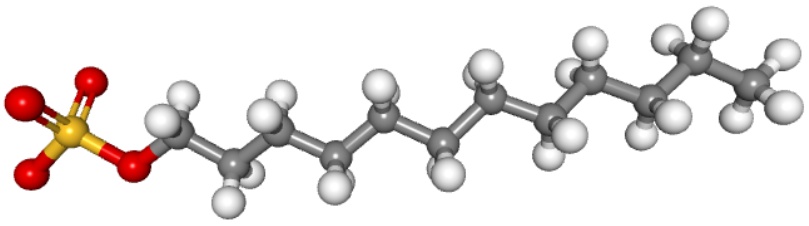

FIGURE 4.4: 3-dimensional rendering of a Sodium Dodecyl Sulphate (SDS) molecule, created using Python, BALLView and POV-Ray.

TABLE 4.2: Properties of Sodium Dodecyl Sulphate

Property	Value
Formula	$NaC_{12}H_{25}SO_4$
Molar Mass	288.38 g mol^{-1}
Density	1.01 g cm^{-3}
Canonical Smiles	[Na+].CCCCCCCCCCCCOS([O-])(=O)=O

Sodium Dodecyl Sulphate (SDS) is an anionic surfactant used in many personal and household care products - a 3d rendering is shown in Figure 4.4 and some of its properties are shown in Table 4.2. In aqueous solution at 25°C, SDS has been shown to have a critical micelle concentration (CMC) ≈ 0.0082M [174].

4.2.2.2 Cocamidopropyl Betaine (CAPB)

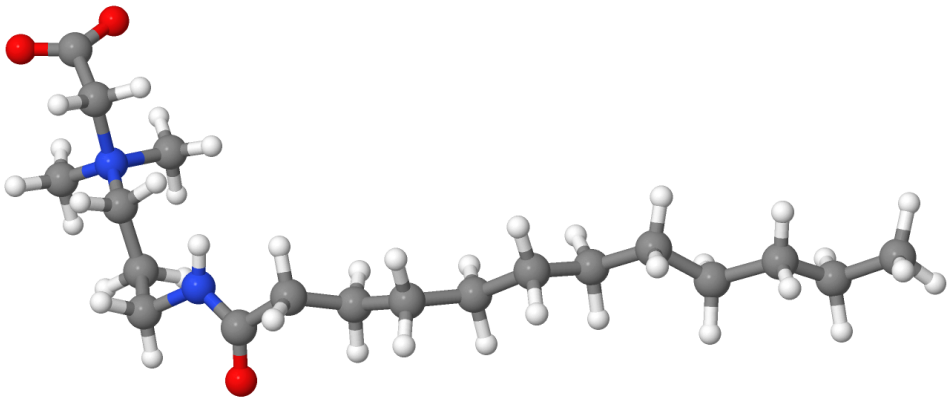

FIGURE 4.5: 3-dimensional rendering of a Cocamidopropyl Betaine (CAPB) molecule, created using Python, BALLView and POV-Ray.

TABLE 4.3: Properties of Cocamidopropyl Betaine

Property	Value
Formula	$C_{19}H_{38}N_2O_3$
Molar Mass	342.52 g mol^{-1}
Density	1.043 g cm^{-3} at 25°C
Canonical Smiles	CCCCCCCCCCCC(=O)NCCC[N+](C)(C)CC(=O)[O-]

Cocamidopropyl Betaine (CAPB), a rendering of which is shown in Figure 4.5, is a surfactant widely used in personal care products [175, 176], and which is derived from coconut oil; some physico-chemical properties are shown in Table 4.3. Cocamides are

coconut oil extracts with an even-number of carbons in their tail, and the head group of CAPB is trimethylglycine which was historically called 'betaine'. Trimethylglycine has the ionic state of $(CH_3)_3N^+CH_2CO_2^-$ between pH ∼2-8 [177], therefore giving CAPB its zwitterionic properties.

CAPB is used extensively in this work as it has been shown to have beneficial properties for personal care products such as moisturising and low allergy rates [178], and thus along with SDS forms the basic micellar system studied here. CAPB is usually provided as a solution, for all of the work presented here the initial product was an aqueous solution of which 30% by volume was CAPB. These solutions also ship with ∼2-3% NaCl, and therefore in every sample there is a small amount of extra ionic strength.

4.2.2.3 Glydant

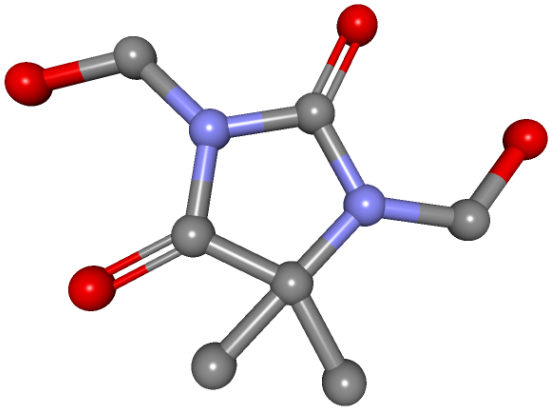

FIGURE 4.6: Computer rendering of a Glydant molecule, created using Python, BallVIEW and POV-Ray.

TABLE 4.4: Properties of Glydant

Property	Value
Chemical Name	1,3-bis(hydroxymethyl)-5,5-dimethyl-imidazolidine-2,4-dione
Formula	$C_7H_{12}N_2O_4$
Molar Mass	188.18 g mol^{-1}
Density	1.349 g cm^{-3}
Canonical Smiles	CC1(C(=O)N(C(=O)N1CO)CO)C

Glydant® by Lonza is the trademarked name of a preservative, shown in Figure 4.6 and some properties are given in Table 4.4, which is used in many personal care products.

As Glydant® is designed to kill living organisms, it can be toxic to humans in high concentrations (yet is perfectly safe in the low concentrations found in commercial products), therefore when this preservative was measured out, all work was performed in a fume cupboard.

4.2.2.4 Nipagin M

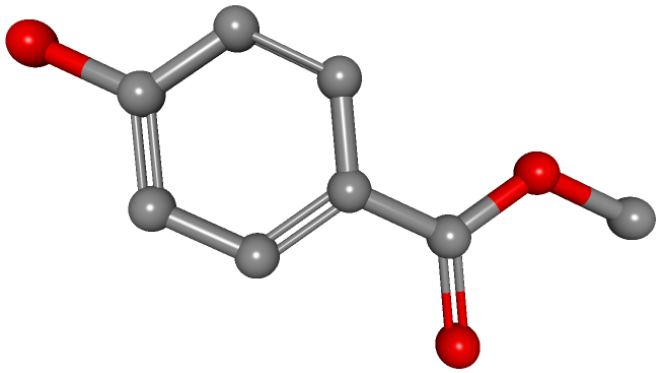

FIGURE 4.7: Computer rendering of a Nipagin M molecule, created using Python, BallVIEW and POV-Ray.

TABLE 4.5: Properties of Nipagin M

Property	**Value**
Chemical Name	methyl 4-hydroxybenzoate
Formula	$C_8H_8O_3$
Molar Mass	152.14732 g mol^{-1}
Density	1.36 g cm^{-3}
Canonical Smiles	COC(=O)C1=CC=C(C=C1)O

The other preservative studied in §4.7 is Nipagin M® by Clariant, shown in Figure 4.7 and details in Table 4.5. The same precautions were taken as for Glydant.

4.2.2.5 'Jaguar' Guar Gum Derivative

The polyelectrolyte under investigation in §4.8 is guar hydroxypropyltrimonium chloride (trade-marked as 'Jaguar' by Rhodia), at two different charge densities (CD); Jaguar C-13-S (CD $\sim$ 0.8 mEq g^{-1} [179]), and Jaguar C-17 (CD $\sim$ 1.6 mEq g^{-1} [179]). This polycation is a quaternary derivative of guar gum, and has been shown to have properties beneficial in hair products such as thickening and conditioning [180, 181, 182].

Due to experimental difficulties in measuring the molecular weight of Jaguar, we are assuming a value of 1-2M MW from previous experiments performed by Unilever [183].

4.2.3 Sample Preparation

Bulk rheological measurements were made at 20±3°C using ARES and G2 rheometers from TA Instruments, fitted with a 2° 50mm diameter cone-plate geometry. Experiments were performed using the protocol described in §2.2.3.

The water soluble polymer poly(ethylene oxide) (PEO) was supplied by Sigma with mean molecular weight 4×10^6 amu. Assuming ideal solvent conditions we see from Table 2.2 (p.33) that the radius of gyration $r_g \approx 60$nm and the overlap concentration $c^* \approx 0.7\%$. At the concentrations used in this study, the pure polymer solution is Newtonian with effective viscosity of 1.64mPa.s. at 0.1% and 1.64mPa.s. at 0.5% (measured using 50mm 2° cone-plate and double-gap geometry on an Anton Paar MCR101 and MCR301 at 20°C).

The surfactant solutions were prepared by dissolving measured masses of both commercial-quality surfactants (SDS and CAPB) in distilled water. Mixing was accelerated using

gentle centrifugation before being left for at least 48 hours to equilibrate. Two eM surfactant concentrations were studied, [SDS] = [CAPB] = 0.1M and 0.2M at three salt concentrations, [NaCl] = 0.0, 1.5 and 3.0% wt. Each of these six combinations were repeated at three polymer concentrations, [PEO] = 0.0, 0.1 and 0.5% wt. SDS:CAPB micelles have been studied previously, but at lower concentrations when the micelles are spherical/rodlike [184].

Table 4.6 (on p.107) shows the extracted and calculated properties of all the measurements performed in this chapter on samples without polyelectrolyte (the polyelectrolyte results table is in §4.8.3). Here, c_{surf} is the eM surfactant concentration, and c_{NaCl} is the additional NaCl combined with the ionic strength from the CAPB. These values are discussed in §2.3.2 (p.26).

4.3 Study: Effect of surfactant concentration on WLM Rheology

For this study the 0.1eM surfactant solution with 0% additional NaCl and 0% PEO is compared with the corresponding 0.2eM system, using bulk rheology, DWS and Optical Tweezer (OT) setups.

TABLE 4.6: Summary of results, where c_{salt} is the additional NaCl concentration, c_{NaCl} is the total NaCl concentration (including the component from the CAPB solution), τ_R is the relaxation time where $\omega_{G'=G''}$ in rad/s

c_{surf}	c_{salt}	c_{NaCl}	c_{PEO}	ω	G	ω	G'	G''	DFS	ratio	τ_R	τ_{br}	τ_{rep}	$\frac{G'_{min}}{G''_{min}}$	l_e	$\bar{L}$	ξ
eM	%	%	%	rad/s	Pa	rad/s	Pa	Pa			s.	s.	s.		nm	nm	nm
				$\vert_{G'=G''}$			$\vert_{G''_{min}}$										
0.06	1.5	1.94	0	0.08	11	12.6	30	2	0.73	1	12.5	12.5	12.5	0.066	117	1761	57.2
0.06	1.5	1.94	0.2	0.03	11	1.3	25	3	0.88	0.3	33.33	10	111	0.12	130	1083	57.2
0.06	1.5	1.94	0.4	0.04	8.5	0.44	18	5	0.94	0.17	25	4.25	147	0.277	156	561	62.3
0.1	0	0.74	0	5	10						0.2						59
0.1	0	0.74	0.1	5	10						0.2						59
0.1	0	0.74	0.5	0.2	11	70	105	20	0.21		5			0.19	58.5	307	57.2
0.1	1.5	2.24	0	0.063	33	12.6	70	2	0.94	0.17	15.87	2.69	93.3	0.025	73.3	2852	39.6
0.1	1.5	2.24	0.1	0.094	30	15.7	70	4	0.86	0.4	10.64	4.25	26.5	0.057	73.3	1283	40.9
0.1	1.5	2.24	0.5	0.25	10	44	60	13	0.33		4		11.3	0.216	79.9	368	59
0.1	3.0	3.74	0	0.44	46	125	100	6	0.92	0.2	2.27	0.45		0.06	60.16	1002	35.5
0.1	3.0	3.74	0.1	0.44	45	56.5	90	3	1	0	2.27			0.033	63.8	1913	35.8
0.1	3.0	3.74	0.5	0.5	14	4	20	10	1.4	0	2			0.5	147	294	52.8
0.11	0.0	0.82	0.0	0.57	10	30	40	14	0.5		1.754			0.35	100	285	59
0.11	0.0	0.82	0.2	1.3	13						0.769						54.1
0.11	0.0	0.82	0.4	0.9	13						1.11						54.1
0.15	0.0	1.11	0.0	0.03	42	31	150	10	0.56		33.33			0.066	48	720	36.6
0.15	0.0	1.11	0.2	0.05	43	31	155	14	0.55		20			0.09	47.1	522	36.3
0.15	0.0	1.11	0.4	0.04	50	31	170	20	0.59	2.6	25	65	9.61	0.11	44.8	380	34.5
0.2	0.0	1.48	0.0	0.05	100	12.5	200	6	1	0.1	20	2	200	0.03	40.9	1364	27.4
0.2	0.0	1.48	0.1	0.063	50	19	140	10	0.71	1.1	15.87	17.5	14.4	0.071	49.9	698	34.5
0.2	0.0	1.48	0.5	0.06	80	63	200	8	0.8	0.6	16.67	10	27.7	0.04	40.9	1023	29.5
0.2	1.5	2.98	0.0	0.25	100	50	230	7	0.87	0.35	4	1.4	11.4	0.03	37.8	1244	27.4
0.2	1.5	2.98	0.1	0.09	65	13	166	4	0.78	0.7	11.11	7.77	15.9	0.024	45.4	1884	31.6
0.2	1.5	2.98	0.5	0.31	76	25	200	33	0.76	0.8	3.22	2.58	4.03	0.165	40.9	248	30
0.2	3.0	4.48	0.0	0.5	80	125	200	10	0.8	0.6	2	1.2	3.33	0.05	40.9	818	29.5
0.2	3.0	4.48	0.1	1.9	100	94	300	30	0.67	1.5	0.52	0.79	0.35	0.1	32.7	326	27.4
0.2	3.0	4.48	0.5	45	90						0.022						

4.3.1 Results from bulk rheology

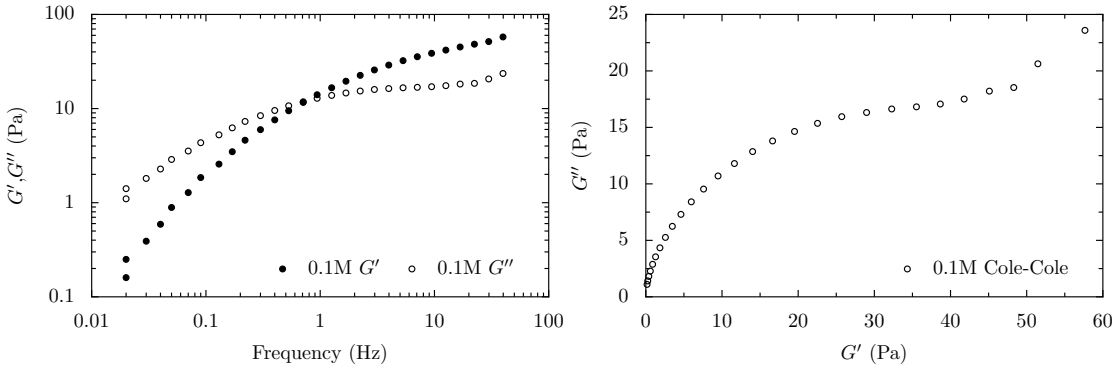

FIGURE 4.8: **Left:** G' and G'' against Frequency for a SDS:CAPB WLM sample at 0.1 eM surfactant concentration. **Right:** Cole-Cole plot for the same data

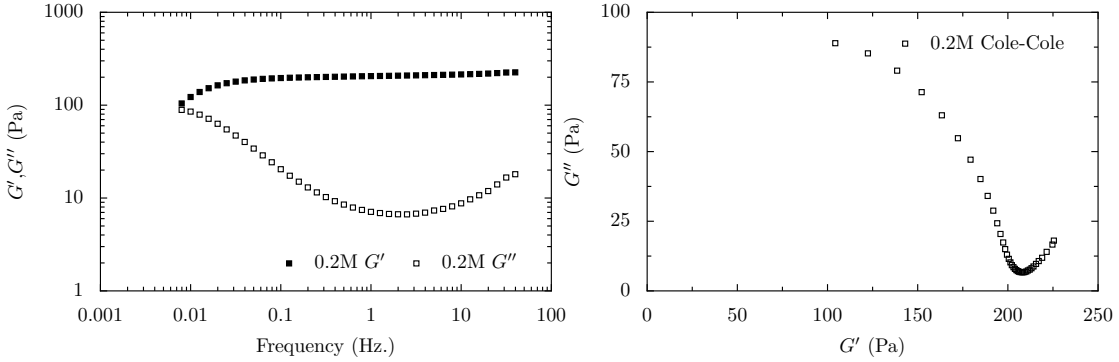

FIGURE 4.9: **Left:** G' and G'' against frequency for a SDS:CAPB WLM sample at 0.2 eM surfactant concentration. **Right:** Cole-Cole plot for the same data

4.3.2 Results from DWS

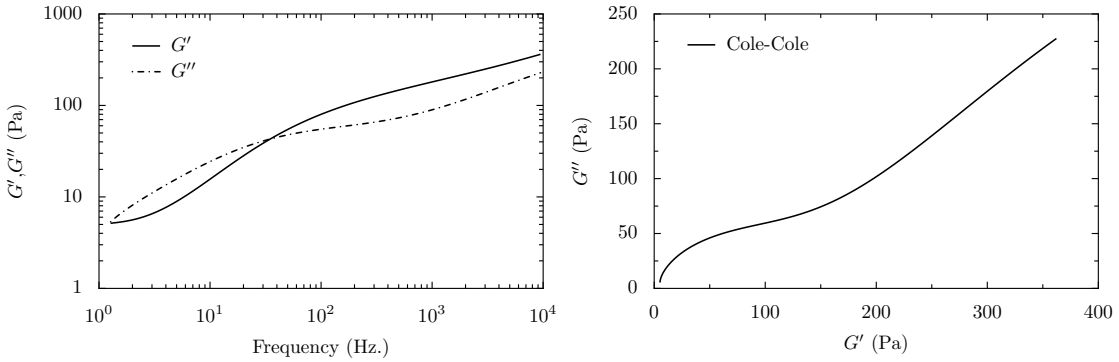

FIGURE 4.10: G' and G'' against Frequency for a 0.1eM SDS:CAPB WLM sample using DWS.

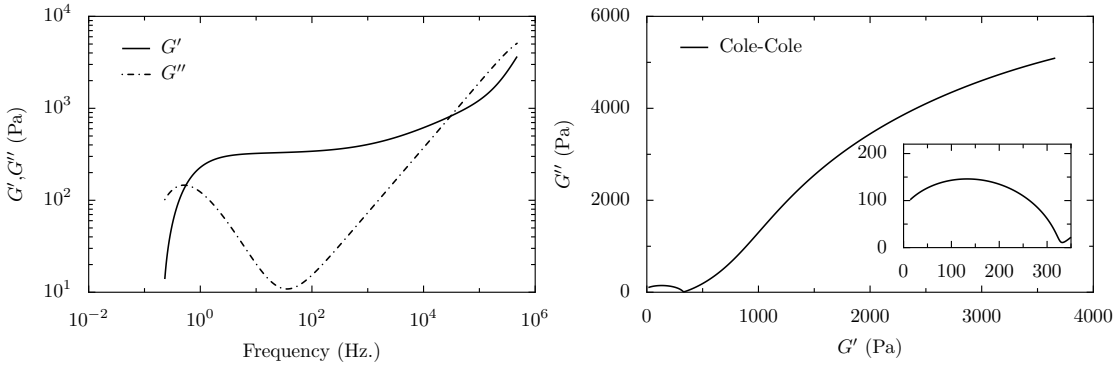

FIGURE 4.11: **Left:** G' and G'' against Frequency for a 0.2eM SDS:CAPB WLM sample using DWS. **Right:** Cole-Cole plot for the same data (**Inset:** Close-up of the terminal region for the same data).

4.3.3 Results from Optical Tweezers

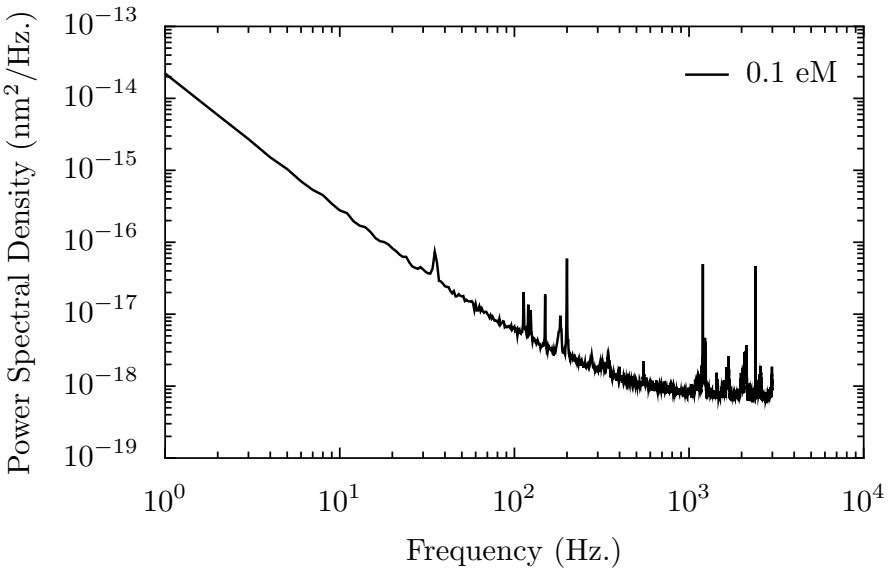

FIGURE 4.12: Optical Tweezer PSD for a SDS:CAPB WLM sample at 0.1 eM surfactant concentration.

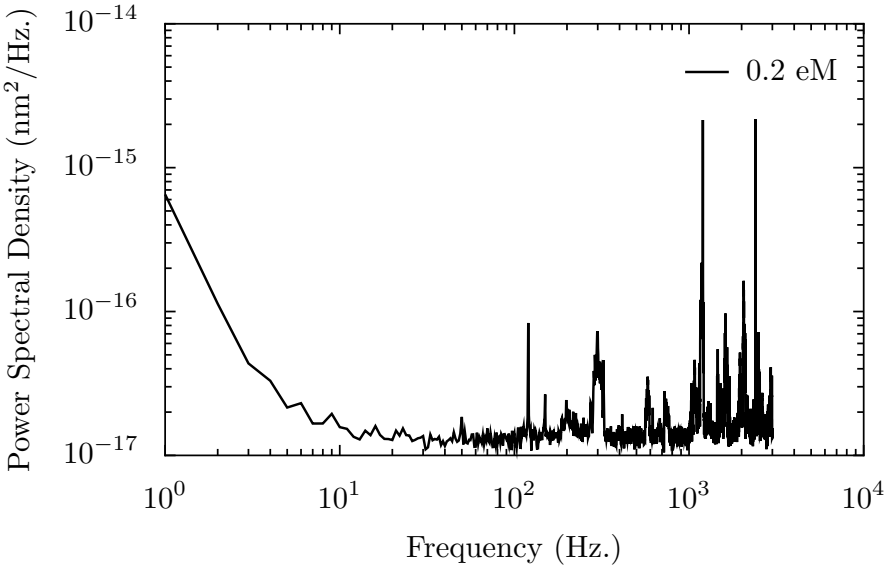

FIGURE 4.13: Optical Tweezer PSD for a SDS:CAPB WLM sample at 0.2 eM surfactant concentration.

PHYSICAL INTERPRETATION AND IMPLICATIONS

At low surfactant concentration (0.1eM, Figures 4.8 and 4.10) there is a crossover in G' and G'' signifying an element of elasticity from entanglements. However the monotonic increase in both G' and G'' means there is a lack of a defined G' plateau or G'' minima

showing that the system has a range of relaxation times due to a broad distribution of rod-like micellar lengths. We therefore have $\frac{\tau_{\text{break}}}{\tau_{\text{rep}}} \gg 1$, which implies effectively unbreakable, polydisperse micelles which relax via curvilinear reptation rather than through micelle scission. In essence, additional surfactant or electrolyte is required to encourage sufficient micellar growth (with a corresponding increase in the density of entanglements) for this system to become highly entangled, or even Maxwellian.

On doubling the surfactant molar fractions we find exactly this behaviour (0.2 eM, Figures 4.8 and 4.11); the plateau in G' extends over 3 decades, and there is a well-defined minima in G'' at $f \approx 2$Hz (in the bulk rheology data). The Cole-Cole plots in Figures 4.8 also show evidence of semi-circular behaviour, showing a transformation to a Maxwellian system. This conversion to an entangled state without added electrolyte could be due to both the NaCl present in the liquid form of CAPB and the higher concentration of surfactant.

These surfactant-only solutions show behaviour expected of a model WLM system with increasing surfactant concentration, providing evidence that despite using industrial components the system in this study can be regarded as a 'model' WLM system.

Optical Tweezer data from this system is disappointing, however. Even at the lowest surfactant concentration with no further additives (Figure 4.12) there is no lower 'roll-off' frequency present, and the upper 'roll-off' frequency limits the data to ∼2-300Hz., below which there is still considerable noise. As expected, the usable frequency range decreases as the surfactant concentration is increased (Figure 4.13), and it is therefore inappropriate to use the OT experimental data in a rheological comparison. This shows that given the equipment and budget constraints of this project, the network structures used in some of Unilever's products are sufficiently viscous as to render OT microrheology

less useful than either bulk rheology or DWS. However as discussed in Chapter 3, OTs allow the possibility of studying non-equilibrium behaviour, whereas bulk rheology and DWS do not. All subsequent studies where the samples are in equilibrium will therefore concentrate on bulk rheological and DWS microrheological data.

4.4 Study: Effect of NaCl concentration on WLM Rheology

For this study the 0.1 and 0.2eM systems with varying NaCl concentrations are compared using bulk rheology and DWS.

4.4.1 Results from bulk rheology

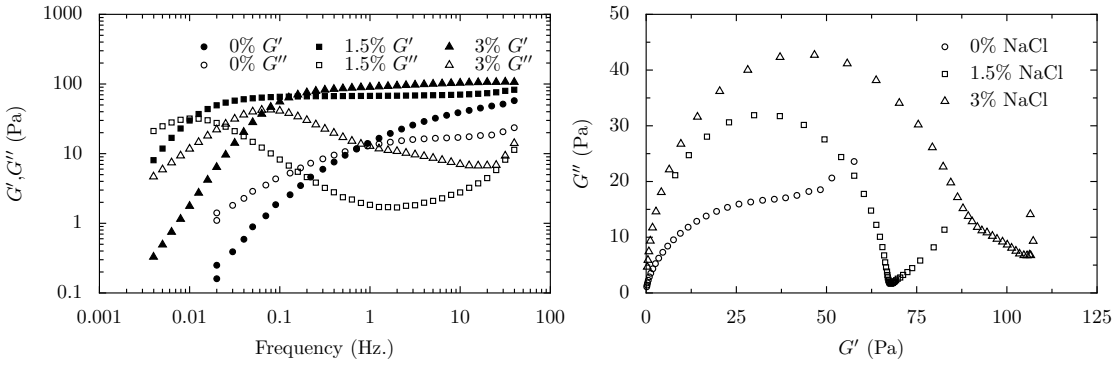

FIGURE 4.14: Graphs showing the rheological changes in a 0.1 eM SDS:CAPB WLM system with additional NaCl at 0,1.5 and 3% wt. **Left:** G' and G'' against Frequency. **Right:** Cole-Cole plots for the same data

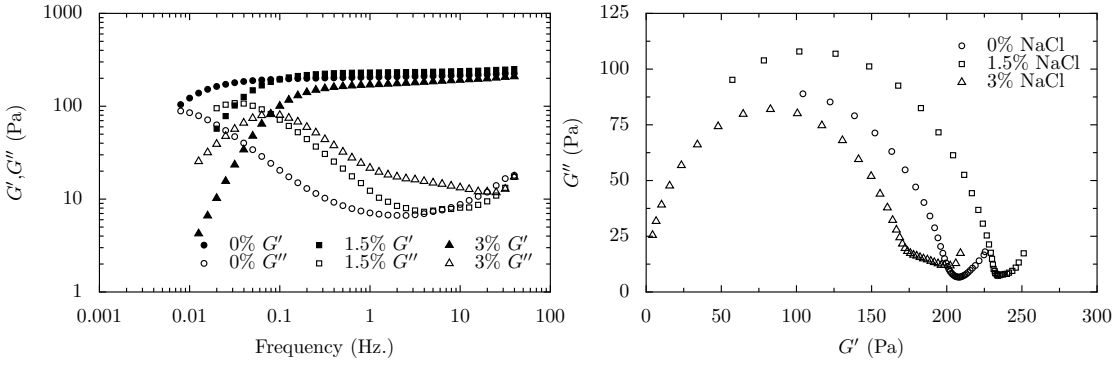

FIGURE 4.15: Graphs showing the rheological changes in a 0.2 eM SDS:CAPB WLM system with additional NaCl at 0,1.5 and 3% wt. **Left:** G' and G'' against Frequency. **Right:** Cole-Cole plots for the same data

4.4.2 Results from DWS

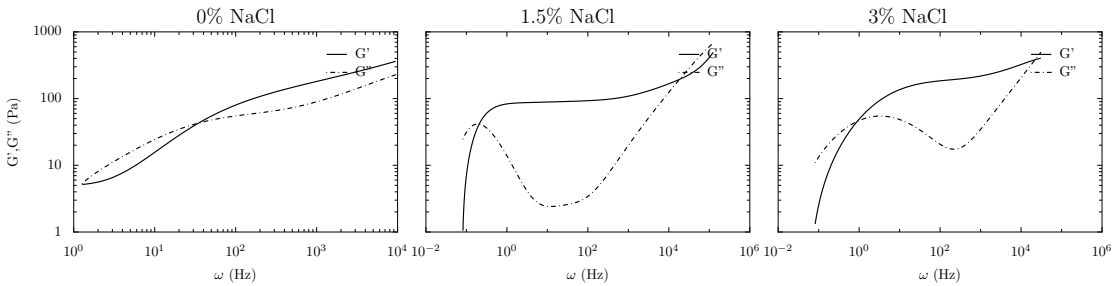

FIGURE 4.16: G', G" vs. ω for 0.1 eM SDS:CAPB, 0% PEO, graphs shown with increasing concentration of NaCl

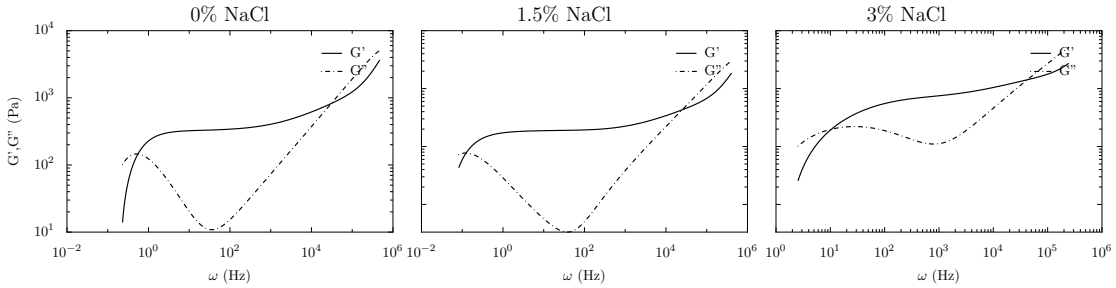

FIGURE 4.17: G',G" vs. ω for 0.2 eM SDS:CAPB, 0% PEO, graphs shown with increasing concentration of NaCl

PHYSICAL INTERPRETATION AND IMPLICATIONS

For the 0.1eM system (Figures 4.14 and 4.16) we see that the NaCl = 0% system shown previously transforms into a classic, highly entangled Maxwellian fluid on the addition of 1.5% NaCl. The crossing point at 0.008Hz (squares in Figure 4.14) gives a single relaxation time $\tau_R \approx 125$s, and the Cole-Cole plot shows perfect semi-circular behaviour.

At NaCl = 3% (triangles in Figure 4.14) the Cole-Cole plot indicates a slightly higher plateau modulus and a slight 'flick' deviation from a semi-circle for $G' > 85$Pa, which could indicate small amounts of micellar branching. At this level of ionic strength τ_R has also decreased to ≈ 2.3s, which could be due to branches sliding down the micelle core.

For the 0.2eM system (Figure 4.15), where the NaCl =0% sample already shows entangled Maxwellian behaviour, we find a maximum in G' with increasing salt concentration, as predicted by Dreiss [56]. However, we also find that τ_R decreases monotonically from

20s to 4s to 2s with increasing ionic strength. Branching would explain this behaviour, however the clear semi-circular Cole-Cole plots for NaCl = 0% and 1.5% indicate that branching has probably not occurred at these concentrations.

With NaCl = 3% both 0.1eM and 0.2eM samples show the flick mentioned above, therefore although the number of samples is small here, we see evidence of branching at electrolyte concentrations above that of the G' maxima. We can therefore be confident that this system shows behaviour similar to the literature when increasing the ionic strength of the solutions.

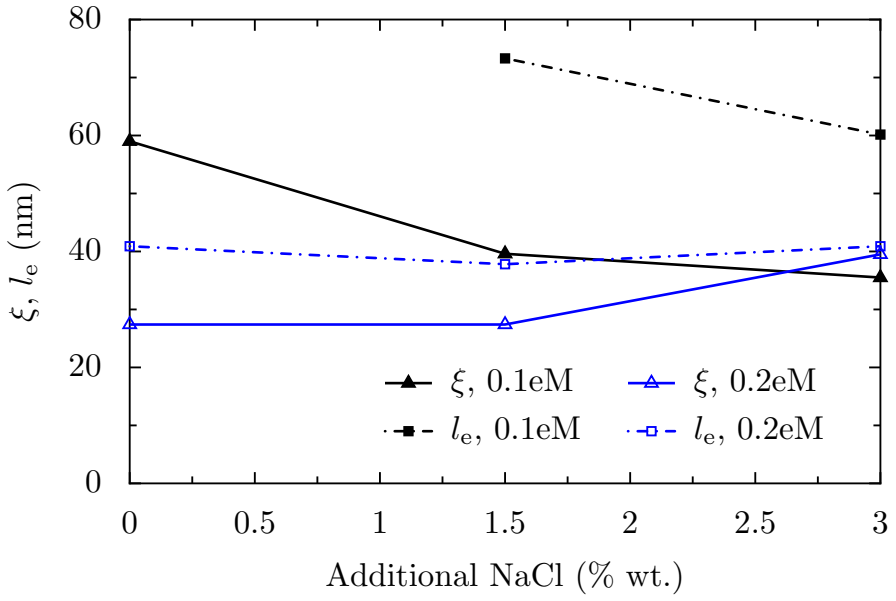

FIGURE 4.18: ξ and l_e for 0.1 and 0.2eM SDS:CAPB WLM solutions with 0% PEO, data from Table 4.6

Figure 4.18 shows the correlation length ξ and entanglement length l_e for 0.1 and 0.2eM SDS:CAPB WLMs with no additional NaCl (these two quantities are discussed in §2.3.2, p.26 onwards) - the data is from Table 4.6. This data shows that at 0.1eM both the entanglement length and the average mesh size of the network structure decrease with additional ionic strength upto 3% wt NaCl, yet both increase at 0.2eM above $\sim$ 1.5% wt. This increase in ξ and l_e is consistent with the onset of branching discussed above, and the decrease is a sign that the micelles are lengthening and becoming more entangled.

4.5 Study: Effect of PEO concentration on WLM Rheology

In this study the 0.1eM and 0.2eM systems with 0% additional NaCl and varying PEO concentrations are compared using bulk rheology and DWS. As described previously, the PEO used here has mean MW = 4×10^6 amu, $r_g \approx 60$nm and $c^* \approx 0.7\%$ (values from Table 2.2, p.33).

4.5.1 Results from bulk rheology

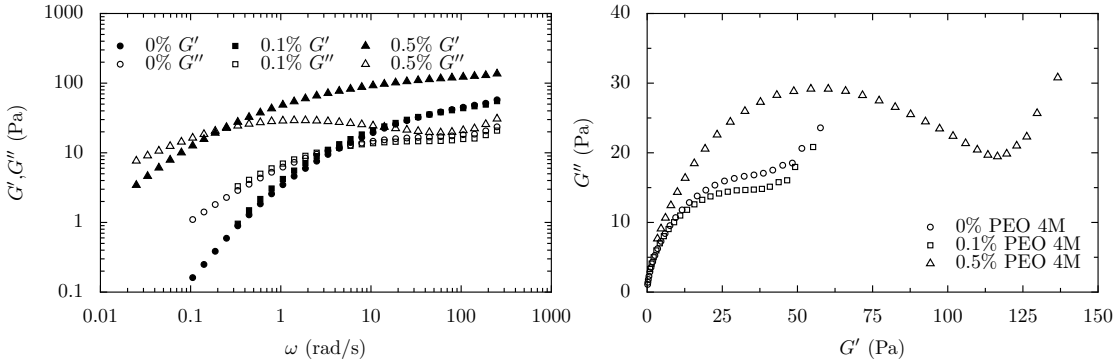

FIGURE 4.19: Graphs showing the rheological changes in a 0.1 eM SDS:CAPB WLM system with additional PEO at 0,0.1 and 0.5% wt. and no additional NaCl **Left:** G' and G'' against Frequency. **Right:** Cole-Cole plots for the same data

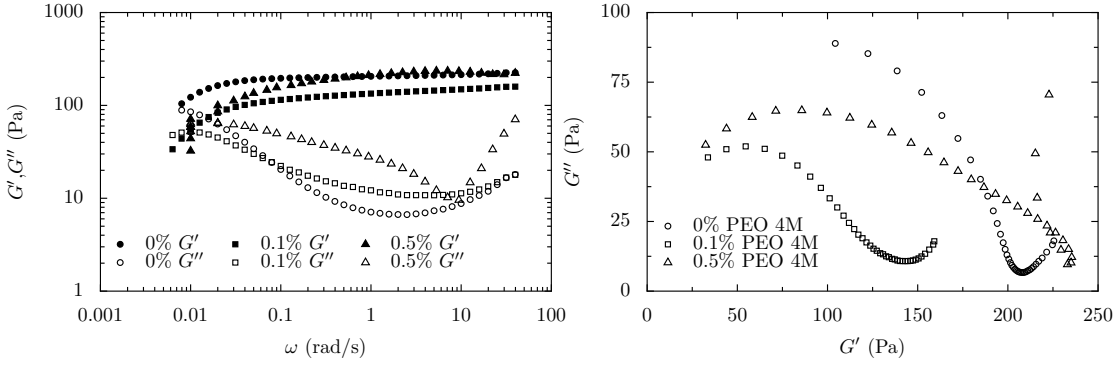

FIGURE 4.20: Graphs showing the rheological changes in a 0.2 eM SDS:CAPB WLM system with additional PEO at 0,0.1 and 0.5% wt. and no additional NaCl **Left:** G' and G'' against Frequency. **Right:** Cole-Cole plots for the same data

4.5.2 Results from DWS

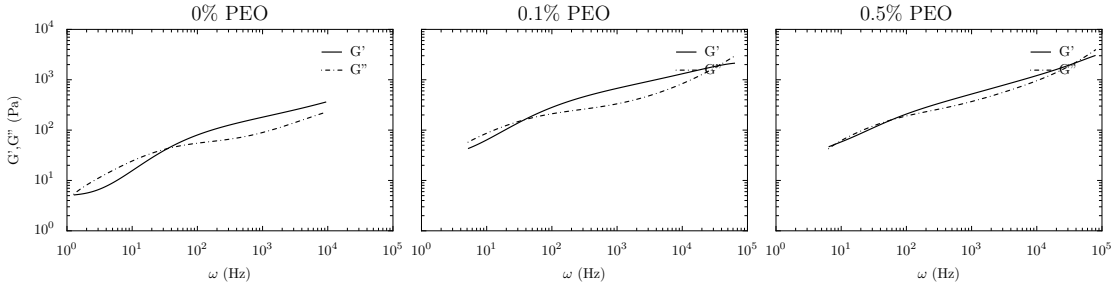

FIGURE 4.21: G',G'' vs. ω for 0.1 eM SDS:CAPB, 0% NaCl, graphs shown with increasing concentration of PEO

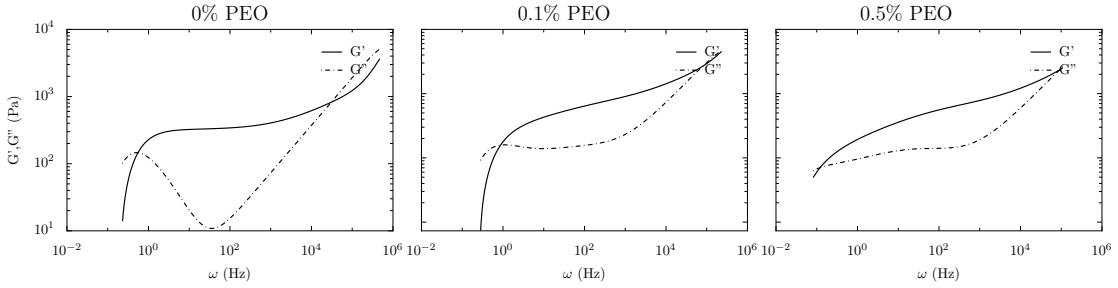

FIGURE 4.22: G',G'' vs ω for 0.2 eM SDS:CAPB, 0% NaCl, graphs shown with increasing concentration of PEO.

PHYSICAL INTERPRETATION AND IMPLICATIONS

For the bulk rheology of the 0.1eM system (Figure 4.19) we see that PEO = 0.1% ($\frac{c}{c^*}$ = 0.14) makes negligible change to the rheological behaviour of the WLM network, from which I conclude that there is no strong chemical interaction between the polymer and the other components, and that the existing network is not disrupted. When the polymer concentration is increased to PEO = 0.5% ($\frac{c}{c^*}$ = 0.71), τ_R increases by more than an order of magnitude (0.2s to 5s) and an accompanying increase is seen in G_0, ie. an increase in elasticity.

It is interesting to note that the corresponding DWS samples (Figure 4.21) do not show the increase in τ_R with PEO = 0.5%, or the minima in G'', with both G' and G'' increasing monotonically at this polymer concentration. I can only assume that the tracer particles

added for the DWS measurements are interacting with the PEO, possibly disrupting the PEO network structure, which has shown an increase in elasticity in Figure 4.19.

Unlike the 0.1eM results, additional PEO = 0.1% at 0.2eM results in significant rheological changes (Figure 4.20); τ_R decreases from ≈ 20s to 16s, G' decreases from ≈ 200Pa to 140Pa, and G''_{min} increases slightly. This implies that the WLMs become less entangled and/or shorter - $\frac{l_e}{L}$ increases by a factor of 3. As the rheological properties of the PEO at this concentration are not significant enough to account for the changes in behaviour alone, there must be interactions between the PEO and surfactant molecules. Surprisingly, the effect seen here is opposite to that for the 0.1eM system, and may indicate that some surfactant is condensing along the polymer backbone, thereby reducing the free surfactant molecules that can contribute to the WLM network.

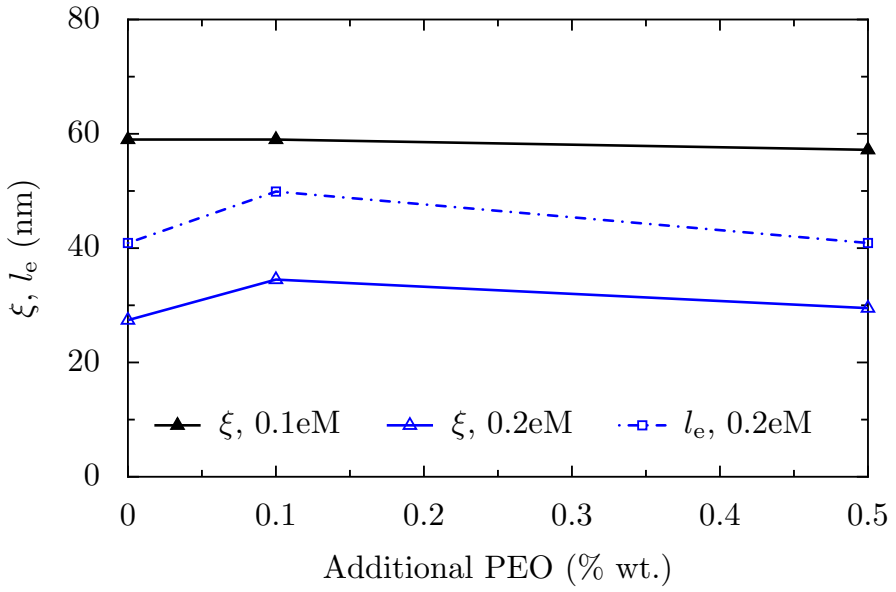

FIGURE 4.23: ξ and l_e for 0.1 and 0.2eM SDS:CAPB WLM solutions with 0% additional NaCl and 0,0.1 or 0.5% additional PEO 4M. Data from Table 4.6.

Figure 4.23 shows ξ for 0.1 and 0.2eM and l_e for 0.2eM SDS:CAPB WLMs; in comparison with Figure 4.18 (p.114), the PEO has a much smaller effect on the mesh size and entanglement length than the NaCl. This indicates that the WLMs are probably becoming shorter, rather than less entangled as discussed above, on the addition of PEO.

A less entangled system would show a large increase in both ξ and l_e; the small changes shown here show that the surfactant molecules condensing along the polymer backbone is a more likely explanation for the rheological changes shown in Figures 4.19 and 4.20. This results in shorter micelles with the network structure maintaining its correlation length and mesh size.

4.6 Study: Effect of PEO, NaCl and surfactant concentration on WLM Rheology

In this study the changing rheology of the SDS:CAPB system is investigated using bulk rheology and DWS whilst varying the NaCl, PEO and surfactant concentrations.

4.6.1 Results from bulk rheology

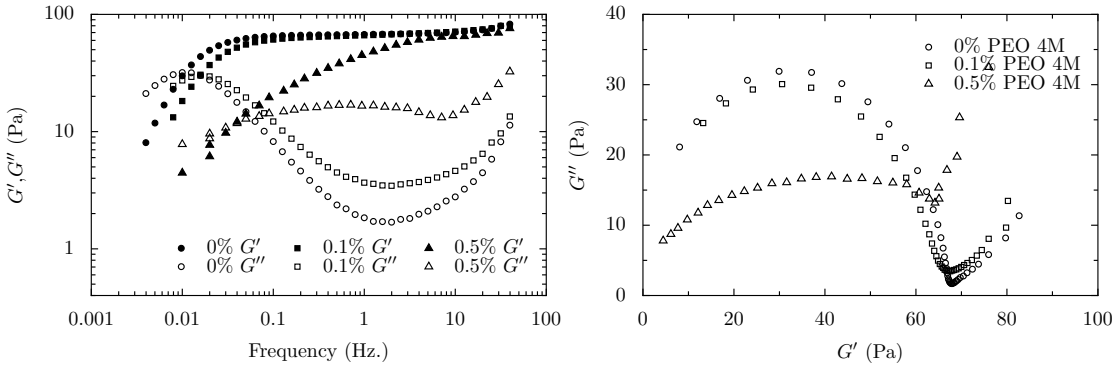

FIGURE 4.24: Graphs showing the rheological changes in a 0.1 eM SDS:CAPB WLM system with additional PEO at 0, 0.1 and 0.5% wt. and 1.5% wt. additional NaCl. **Left:** G' and G'' against Frequency. **Right:** Cole-Cole plots for the same data.

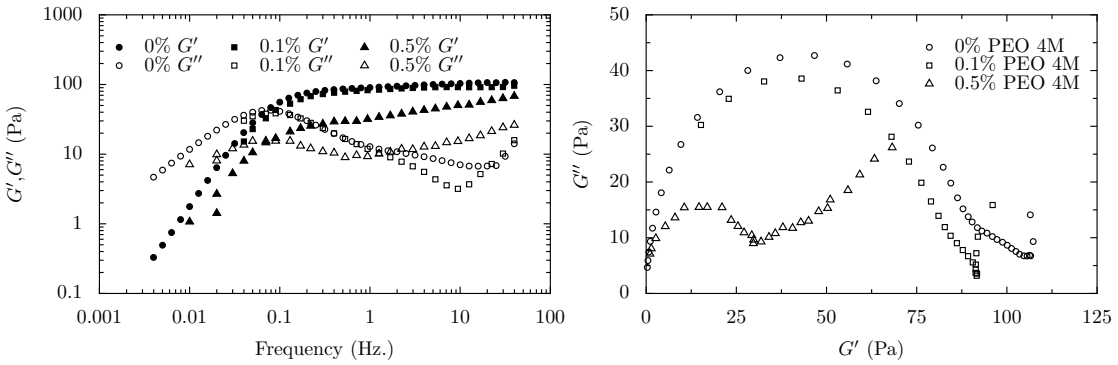

FIGURE 4.25: Graphs showing the rheological changes in a 0.1 eM SDS:CAPB WLM system with additional PEO at 0, 0.1 and 0.5% wt. and 3% wt. additional NaCl. **Left:** G' and G'' against Frequency. **Right:** Cole-Cole plots for the same data.

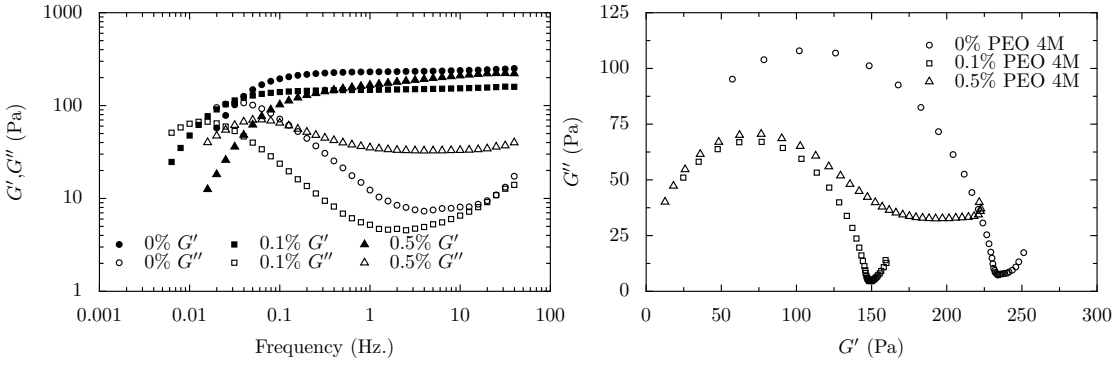

FIGURE 4.26: Graphs showing the rheological changes in a 0.2 eM SDS:CAPB WLM system with additional PEO at 0, 0.1 and 0.5% wt. and 1.5% wt. additional NaCl. **Left:** G' and G'' against Frequency. **Right:** Cole-Cole plots for the same data.

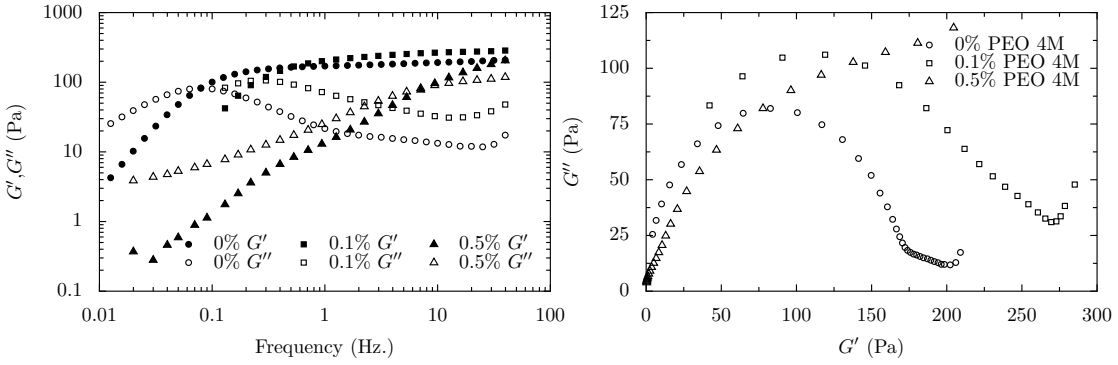

FIGURE 4.27: Graphs showing the rheological changes in a 0.2 eM SDS:CAPB WLM system with additional PEO at 0, 0.1 and 0.5% wt. and 3% wt. additional NaCl. **Left:** G' and G'' against frequency. **Right:** Cole-Cole plots for the same data.

4.6.2 Results from DWS

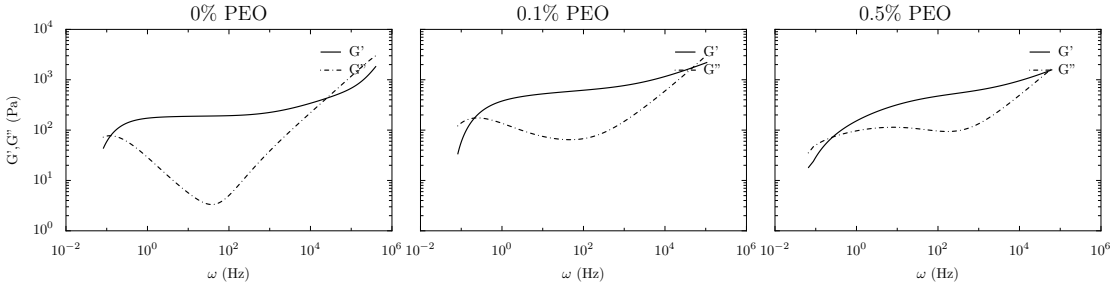

FIGURE 4.28: G',G'' against frequency for 0.2 eM SDS:CAPB, 1.5% NaCl, graphs shown with increasing concentration of PEO.

PHYSICAL INTERPRETATION AND IMPLICATIONS

0.5% PEO completely changes the rheological behaviour of these samples, which are already in a highly entangled state due to the additional 1.5% wt. NaCl. Since G_0 is seen to increase along with τ_R, the modifications to the network structures could be bridging [185], and therefore a full analysis requires a model which also accounts for the relaxation time of the transient network. This can be implemented by adding a second term into Equations 2.11 and 2.12 yielding:

$$G'(\omega) = G_{\text{micelle}} \frac{\tau_{\text{micelle}}^2 \omega^2}{1 + \tau_{\text{micelle}}^2 \omega^2} + G_{\text{transient}} \frac{\tau_{\text{transient}}^2 \omega^2}{1 + \tau_{\text{transient}}^2 \omega^2} \tag{4.3}$$

$$G''(\omega) = G_{\text{micelle}} \frac{\tau_{\text{micelle}} \omega}{1 + \tau_{\text{micelle}}^2 \omega^2} + G_{\text{transient}} \frac{\tau_{\text{transient}} \omega}{1 + \tau_{\text{transient}}^2 \omega^2} \tag{4.4}$$

which in the spring/dashpot analogy introduced in §2.1 equates to a second spring/dashpot pair in parallel with the first.

Figure 4.29 shows the Cole-Cole plots with double-Maxwell fits for the non-Maxwellian data from Figures 4.25 and 4.27. These fits were made by using the Levenburg-Marquardt algorithm to apply a least squares fit to Equations 4.3 and 4.4, the code for which is in

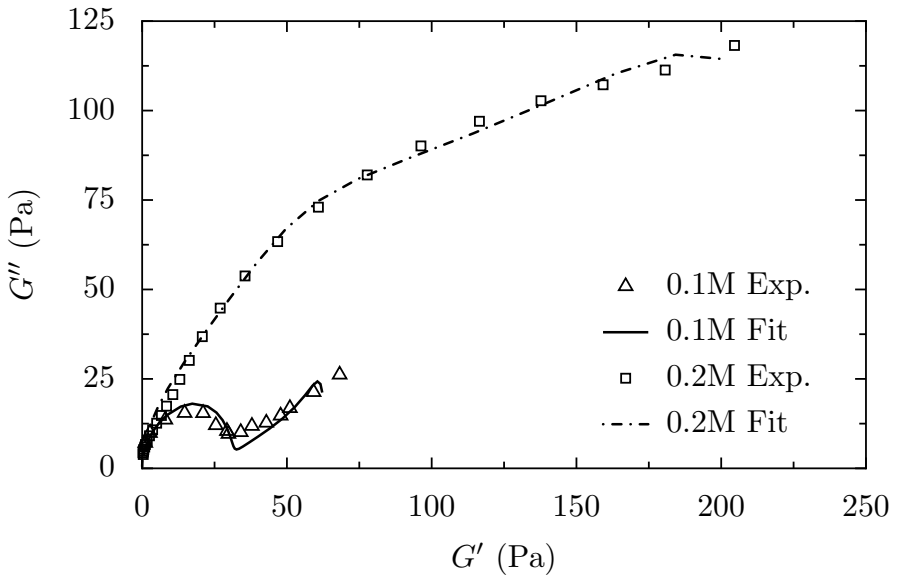

FIGURE 4.29: Cole-Cole plot showing Experimental data and double Maxwell fit using Equations 4.3 and 4.4. Both samples are SDS:CAPB micelles with 3% wt. NaCl and 0.5% PEO 4M; the 0.1M data (△) is from Figure 4.25 and the 0.2M data (□) is from Figure 4.27.

Appendix C. As we can see, the addition of a second relaxation time to the model gives a good fit to the experimental data, implying that these systems may have a transient network structure created by the PEO.

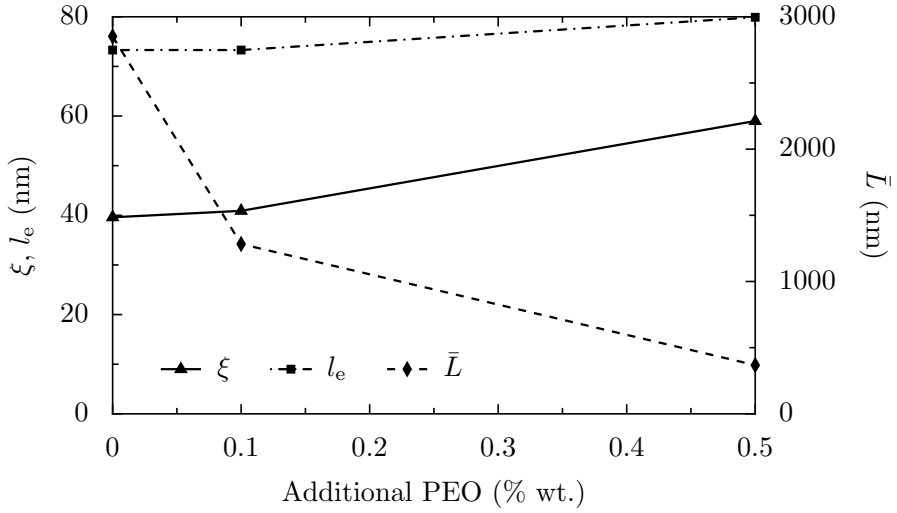

FIGURE 4.30: ξ, l_e and $\bar{L}$ for 0.1eM SDS:CAPB WLMs with 1.5% NaCl and increasing PEO concentration.

Figure 4.30 shows ξ, l_e and $\bar{L}$ for the 0.1 eM WLMs with 1.5% NaCl shown previously in Figure 4.24. Here we see that the mesh size and entanglement length both increase, whilst the average length of the micelles $\bar{L}$ decreases from ∼2800→1200nm with 0.1%

PEO 4M, and down to ∼380nm with 0.5% PEO 4M. These effects are consistent with surfactant material condensing onto the polymer backbone, shortening the micelles, and disrupting the network structure at 0.5% as seen in Figure 4.24.

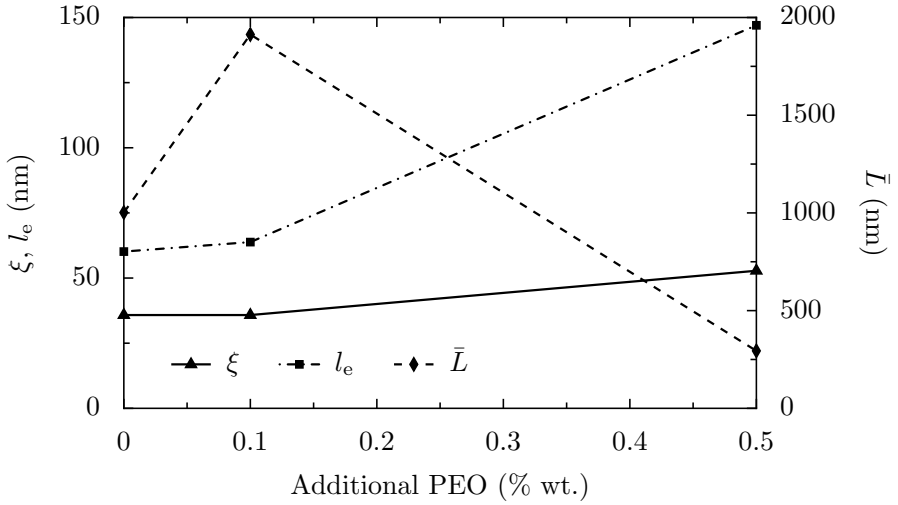

FIGURE 4.31: ξ, l_e and $\bar{L}$ for 0.1eM SDS:CAPB WLMs with 3% NaCl and increasing PEO concentration.

Figure 4.31 shows ξ, l_e and $\bar{L}$ for the 0.1eM SDS:CAPB WLMs with 3% additional NaCl shown previously in Figure 4.25. In contrast to the 1.5% NaCl samples shown above, the mean micellar length $\bar{L}$ shows a maxima before decreasing to ∼300nm with 0.5% PEO, whilst ξ and l_e both increase. The increase in l_e is much larger here than seen previously, showing a higher level of disruption to the micellar network, also shown in the Cole-Cole plots in Figure 4.25. However, the maxima in $\bar{L}$ implies that the polymers may be wrapping around the micelles, encouraging them to lengthen, but as polymer concentration $c \rightarrow c^*$, the network structure is disrupted in much the same way as for the 1.5% samples.

Figure 4.32 shows ξ, l_e and $\bar{L}$ for the 0.2eM WLMs with 1.5% NaCl and increasing PEO concentration shown previously in Figure 4.26. Here we see a maxima in $\bar{L}$, first seen in the 0.1eM 3% NaCl samples in Figure 4.31, however in this case l_e decreases slightly and ξ remains roughly constant as the polymer concentration is raised from 0.1→0.5% wt. This

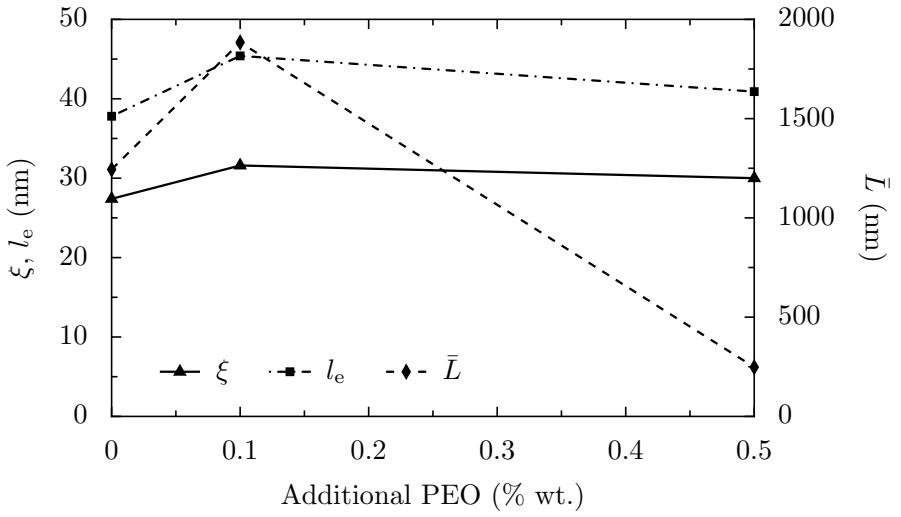

FIGURE 4.32: ξ, l_e and $\bar{L}$ for 0.2eM SDS:CAPB WLMs with 1.5% NaCl and increasing PEO concentration.

implies that the micelles are becoming much shorter (to ∼250nm as seen previously), yet the properties of the network structure appear to be maintained. This is interesting as in Figure 4.26 we see that G_0 decreases by ∼100Pa with 0.1% PEO; this loss of elasticity would be explained by surfactant material condensing onto the polymer, however the constant ξ as $c \to c^*$ (for the PEO) suggests that the polymer may be embedding itself in the micelles, or wrapping around them, with the corresponding increase in micellar diameter accounting for the constant mesh size.

4.7 Study: Effect of preservatives on WLM Rheology

Formulations which use biological extracts are prone to encouraging the growth of organisms; common examples of polymeric extracts are Dextran (a branched polysaccharide) and guar gums such as Jaguar. As a result, many commercial products contain small amounts of preservative in order to maintain sterility.

In §4.8 a polyelectrolyte derived from guar gum (Jaguar) is added to the micelle network, and therefore a preservative is required; in order to ascertain the effect of the preservative

on the micelle network, this section shows the results from a precursor study in which the rheological changes brought about by Glydant and Nipagin are investigated. The Nipagin was used at 0.2% wt. and the Glydant was used at 0.06% wt. throughout - these concentrations were pre-determined by Unilever. These results were all obtained using an Anton Paar MCR101 rheometer at Nottingham University Sutton Bonington campus.

4.7.1 Results from bulk rheology

4.7.1.1 Glydant Results

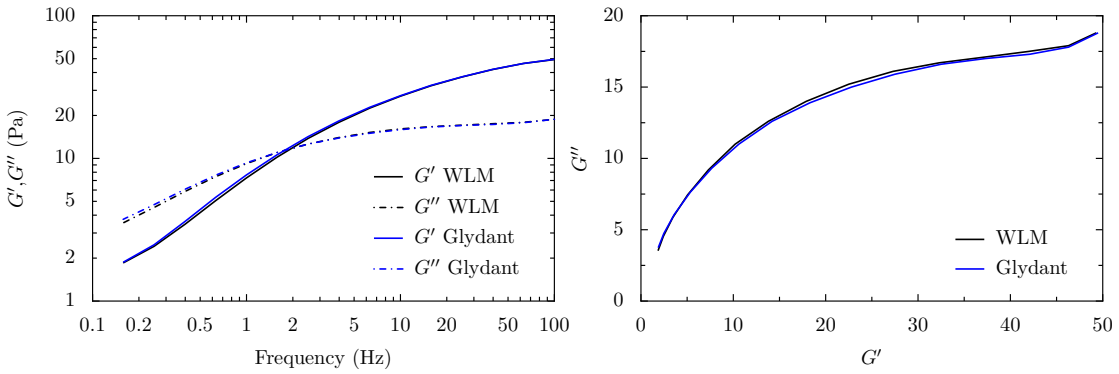

FIGURE 4.33: Comparison of 0.1M SDS:CAPB, 0% NaCl WLM with and without Glydant preservative; **Left:** G',G'' vs Frequency, **Right:** Cole-Cole plot for the same data.

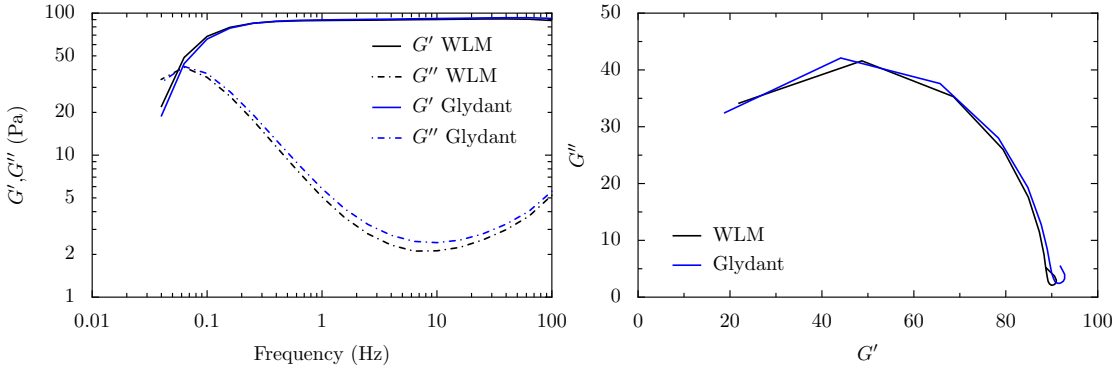

FIGURE 4.34: Comparison of 0.1M SDS:CAPB, 1.5% NaCl WLM with and without Glydant preservative; **Left:** G',G'' vs Frequency, **Right:** Cole-Cole plot for the same data.

4.7.1.2 Nipagin M Results

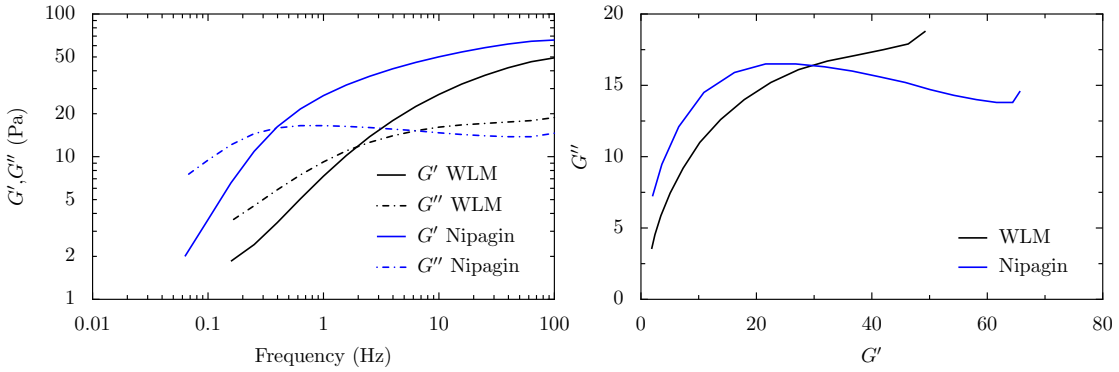

FIGURE 4.35: Comparison of 0.1M SDS:CAPB, 0% NaCl WLM with and without Glydant preservative; **Left:** G',G'' vs Frequency, **Right:** Cole-Cole plot for the same data.

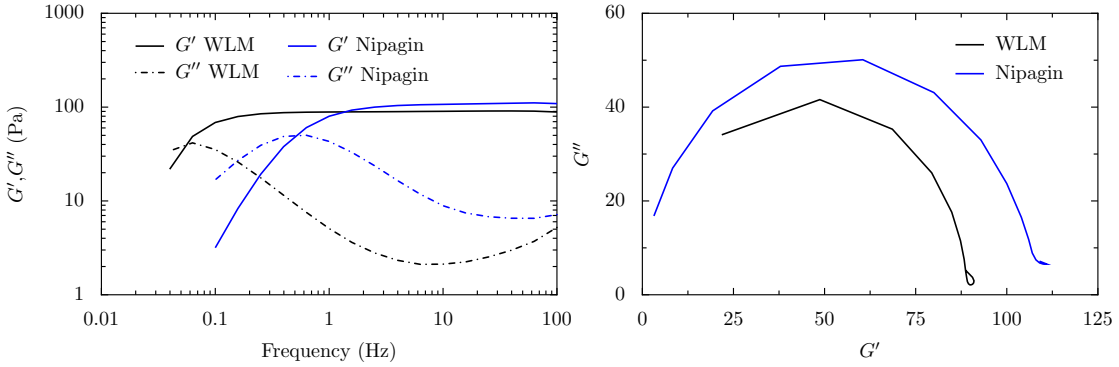

FIGURE 4.36: Comparison of 0.1M SDS:CAPB, 1.5% NaCl WLM with and without Glydant preservative; **Left:** G',G'' vs Frequency, **Right:** Cole-Cole plot for the same data.

PHYSICAL INTERPRETATION AND IMPLICATIONS

Figures 4.33 and 4.34 show that at both 0.1 and 0.2eM surfactant concentrations, the additional Glydant has negligible effect on the WLM network structure. Conversely, Figures 4.35 and 4.36 show that Nipagin M significantly modifies the WLM rheology, with the relaxation time τ_R increasing by an order of magnitude in the 0.1eM sample and decreasing by an order of magnitude in the 0.2eM system.

This is interesting behaviour in itself, however for the purposes of determining the most appropriate preservative these results are sufficient to choose Glydant as the preservative in the polyelectrolyte study.

4.8 Study: Effect of a polyelectrolyte on WLM Rheology

The microstructures and interactions present in polymer-surfactant systems play an important role in fields such as personal care products [180, 186], paints [187] and oil recovery [188]. In personal care products, polymers have traditionally been used as thickening agents, however the properties of polymers and polyelectrolytes have proven to be beneficial in other ways, for example as deposition enhancers [189, 190] and to reduce skin irritation [186, 191].

In polyelectrolyte-WLM systems such as hair products, where dilution during use will reduce the overall surfactant concentration, a complexation process can occur in which the system moves from a single-phase into a two-phase region on the phase diagram, so the product phase separates. This flocculation point is when the active material (silicone, alcohol or polymer, for example) is most readily adsorbed onto the keratin substrate (hair fibres), usually with the cationic polyelectrolyte as an adsorption agent [180].

Presented here are the results of investigations into the phase behaviour and rheology of wormlike micelle (WLM) solutions made from eM mixtures of the surfactants sodium dodecyl sulphate (SDS) and cocamidopropyl betaine (CAPB) in the presence of either charged or uncharged polymers; Jaguar and poly(ethylene oxide) (PEO) respectively. There are two phase boundaries for the polyelectrolyte systems (see Section 4.8.1 below), above the higher phase boundary the sample is a single phase. This phase boundary is found for the WLM with Jaguar system for a range of polymer and NaCl concentrations, and the bulk rheology is compared with samples of WLMs with PEO at similar molar concentrations to the Jaguar.

4.8.1 Background

Self-assembled structures of SDS and CAPB have been shown to undergo a sphere-to-rod transition at low concentrations (∼10mM) [184]. On increasing the surfactant concentration or on the addition of electrolyte the system becomes Maxwellian, showing a well-defined plateau in G' and a defined minima in G'', whilst at high concentrations (>3% wt. NaCl), behaviour indicative of branching has been seen [62], this is also shown in the previous section.

The combination used here of anionic (SDS) and zwitterionic (CAPB) surfactants with a cationic polyelectrolyte (Jaguar) can be regarded as a model shampoo system [11, 12, 180]. In these model systems, three distinct regions have been observed due to the strong associative-binding of a polyelectrolyte with an oppositely-charged surfactant [180, 192]:

- At low surfactant concentrations the system remains in a single phase. At a given surfactant concentration, the reduction in the overall polyelectrolyte charge due to surfactant-binding will encourage the polymer to form particles (∼100nm [192]), with a net positive charge.
- At intermediate surfactant concentrations the particles aggregate due to further surfactant-induced charge reduction and the system phase separates.
- At higher surfactant concentrations, the surfactant-binding reverses the net charge on the particles, converting the system to a single-phase.

Although the phase separation region has useful properties for hair products, flocculation increases the turbidity, which is undesirable for commercial shampoo systems. A fine tuning of the parameters can lead to a system which has desirable properties for the consumer (rheology, turbidity, foaming), and which, on dilution, performs the required actions (cleansing, depositing material).

The aims of this study are as follows:

- To determine the upper phase boundary region of SDS:CAPB with Jaguar for various surfactant, polyelectrolyte and salt concentrations.

- To measure the changes in the rheological properties of the single-phase system as the concentration of each component is varied.
- To understand the changes in rheology and network structure present in this WLM system on the addition of a charged or uncharged polymer.

4.8.2 Methods and Mixing Protocol

4.8.2.1 Sample Preparation

Various mixing protocols were tried until a suitable one was found; all the samples presented in this work were mixed using the following three-stage process:

- The Jaguar (or PEO, depending on the sample[2]) was mixed on its own with around half of the required water. The Jaguar requires around 24-48 hours of low-shear mixing ($\ll$1000rpm) at 50°C in order to fully dissolve. Low-shear rates were used so as not to damage the polymer, and this mixing was performed in 50mL centrifuge tubes with a magnetic stirrer. On contact with water, the slight hydrophobicity of the Jaguar means that the powder disperses, and requires mechanical mixing along with heat to dissolve. In the protocols where Jaguar powder was added to a pre-formed micelle network structure, the polyelectrolyte never fully dissolved, remaining in visible 'flocs'.
- The WLM system (SDS, CAPB and Glydant) was mixed separately with the remaining water.
- Once both samples had cleared, they were combined and salt was added last, if required.

[2] A further set of experiments were also performed which showed that pre-dissolving the PEO in water before addition to the WLM structure results in no rheological change to the system compared with the PEO being added later. This pre-dissolving is necessary for the Jaguar, however.

All samples were centrifuged at 2000rpm for 300 seconds, then left to equilibrate for at least 24 hours before experiments were performed. Small amounts of the more turbid samples were taken and centrifuged at 12,500 rpm for 10 minutes. On finding two samples, one which phase separates and one which remains in a single phase after high-speed centrifuging, we know the limits of the phase boundary for this system. The phase boundaries were calculated to 2 d.p. of surfactant concentration.

It should be noted that in previous work using Jaguar [192] the polyelectrolyte was purified before mixing, however Unilever do not intend to further purify the raw ingredients, so in this work the Jaguar was used as it came from Rhodia.

4.8.2.2 Rheology Protocol

All rheological measurements were made on an Anton Paar MCR 301 with Peltier Hood. Oscillatory rheology measurements were performed using the protocol described in §2.2.3.

4.8.2.3 Spectrophotometer Protocol

Spectrophotometer measurements were made on a Beckman Coulter DU Series machine. A WLM formulation without any additional polymer or salt was used as the calibration sample for the measurements. Experiments were taken with wavelength $\lambda = 600$nm, and the sample absorption relative to the calibration sample is reported.

4.8.3 Results, Discussion and Implications

SDS:CAPB (eM)	Symbol	Jaguar (% wt.)	PEO 4M (% wt.)	c_{salt} (% wt.)	Absorp.	Flocculated	G_0 (Pa.s.)	τ_R (s.)	Maxwellian
0.01	○	0.1 (13)	0	1.5	0.049	×	N/A	N/A	N/A
0.02	○	0.1 (13)	0	1.5	0.020	×	N/A	N/A	N/A
0.05	●	0.1 (17)	0	1.5	0.158	✓	N/A	N/A	N/A
0.06	●	0.1 (17)	0	1.5	0.049	×	41	7.69	✓
0.06	●	0	0	1.5	0.0	×	30	12.5	✓
0.06	●	0	0.2	1.5	0.0	×	30	28.5	✓
0.06	●	0	0.4	1.5	0.0	×	N/A	25.0	×
0.07	●	0.1 (17)	0	1.5	0.044	×	45	5.0	✓
0.08	●	0.1 (17)	0	1.5	0.030	×	60	5.26	✓
0.10	●	0.1 (17)	0	1.5	0.01	×	100	10.0	✓
0.10	△	0.1 (13)	0	0	0.150	✓	N/A	N/A	N/A
0.11	△	0.1 (13)	0	0	0.045	×	N/A	1.42	×
0.11	△	0	0	0	0.0	×	N/A	1.66	×
0.11	△	0	0.2	0	0.0	×	N/A	1.0	×
0.11	△	0	0.4	0	0.0	×	N/A	1.11	×
0.12	△	0.1 (13)	0	0	0.031	×	N/A	2.85	×
0.13	△	0.1 (13)	0	0	0.017	×	N/A	4.0	×
0.15	△	0.1 (13)	0	0	0.02	×	105	9.09	✓
0.14	▲	0.1 (17)	0	0	0.162	✓	N/A	N/A	N/A
0.15	▲	0.1 (17)	0	0	0.110	×	150	8.0	✓
0.15	▲	0	0	0	0.0	×	130	33.3	✓
0.15	▲	0	0.2	0	0.0	×	140	20	✓
0.15	▲	0	0.4	0	0.0	×	170	22.2	✓
0.16	▲	0.1 (17)	0	0	0.051	×	180	10.0	✓
0.17	▲	0.1 (17)	0	0	0.035	×	190	13.3	✓
0.18	▲	0.1 (17)	0	0	0.013	×	210	15.87	✓

TABLE 4.7: Results from rheology and spectrophotometry for all samples. The bolder colours represent those samples which phase separated. c_{salt} is the additional salt concentration in each sample, excluding the component from the CAPB solution.

Jaguar C-13-S, 1.5% NaCl

Jaguar C-17, 1.5% NaCl

Jaguar C-13-S, 0% NaCl

Jaguar C-17, 0% NaCl

Figure 4.37 shows the flocculation regions specified in Table 4.8.3. Jaguar C-13-S samples with 1.5% wt. additional NaCl remained clear and colourless down to 0.01 eM surfactant concentration, and therefore the flocculation region is not specified. These regions are

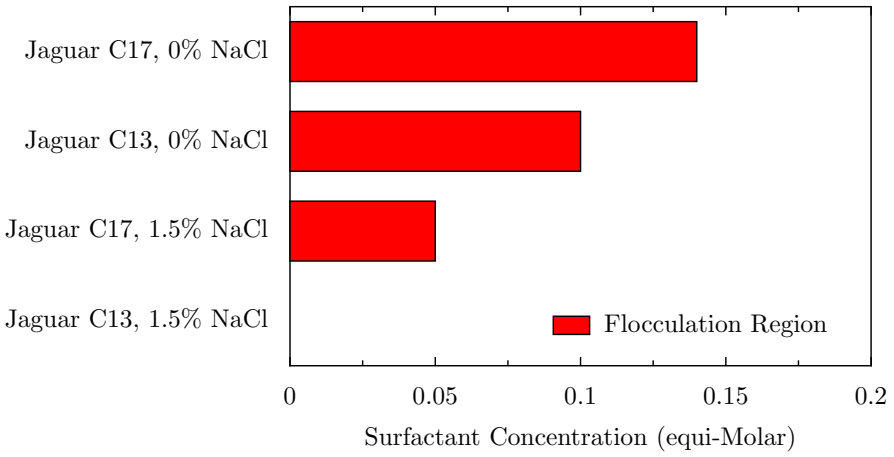

FIGURE 4.37: Phase diagram for SDS:CAPB micelles with and without additional NaCl. The red regions indicate surfactant and salt combinations in which the Jaguar polyelectrolyte flocculates.

defined by the upper phase boundaries, and there may exist lower phase boundaries as described in §4.8.1 but these are not relevant to this study.

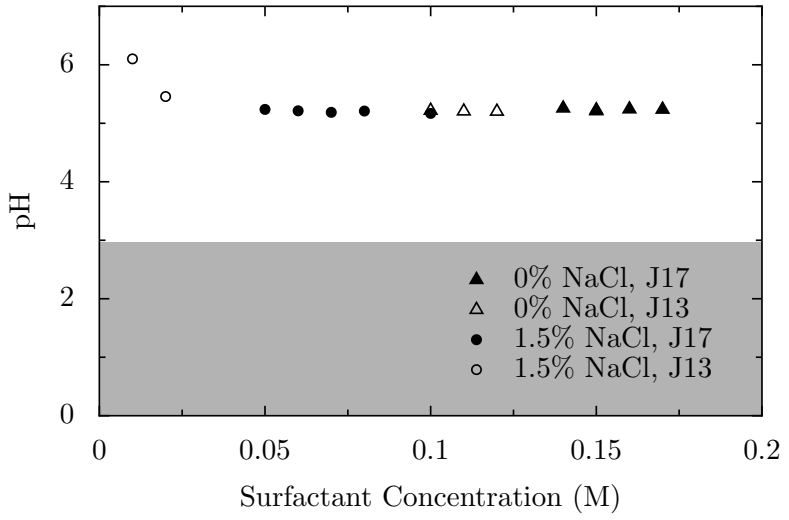

FIGURE 4.38: Variation of pH with SDS:CAPB surfactant concentration. The white area represents the pH levels for which CAPB can be considered to have one negative charge. No buffering agent (such as citric acid) was used in this work in order to avoid possible effects from the buffer on the WLM network.

Figure 4.38 shows that for all of the rheology data presented here, we can consider CAPB to be negatively charged.

Figure 4.39 shows the absorption of each sample at a wavelength $\lambda = 600$nm, relative to the absorption of a WLM formulation without Jaguar; the higher the value, the greater

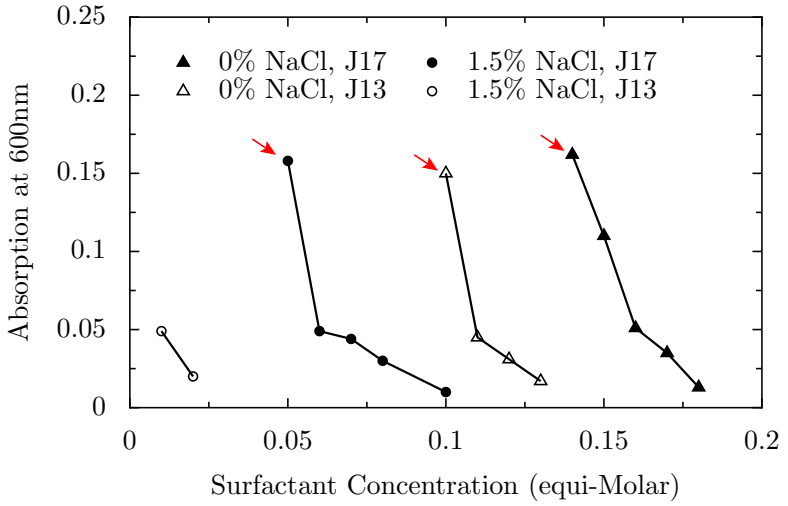

FIGURE 4.39: Absorption versus surfactant concentration at 600nm. The red arrows signify the samples which phase separated.

the turbidity. Samples which phase separated after high-speed centrifuging (12.5k RPM) are labelled with red arrows. These mark the phase boundary of each system, indicating that absorption could be used as a quick test of phase behaviour.

4.8.3.1 Phase Boundary: Jaguar C-17 with Salt

Figure 4.40 shows the changing rheology of 0.06M SDS:CAPB with 1.5% wt. NaCl with additional Jaguar or PEO. This system shows highly entangled viscoelastic behaviour at these surfactant concentrations; the semi-circular Cole-Cole plots are indicative of a well-developed Maxwellian system. On the addition of Jaguar C-17, the relaxation time shortens and the elastic modulus (G_0) increases dramatically, however when the Jaguar is replaced with PEO 4M MW, the modulus remains roughly constant but the Cole-Cole plots show deviation from Maxwellian behaviour. This is not a disruption to the micellar network, otherwise G_0 would decrease dramatically, so we can assume that at the higher PEO concentration we have extra relaxation times arising.

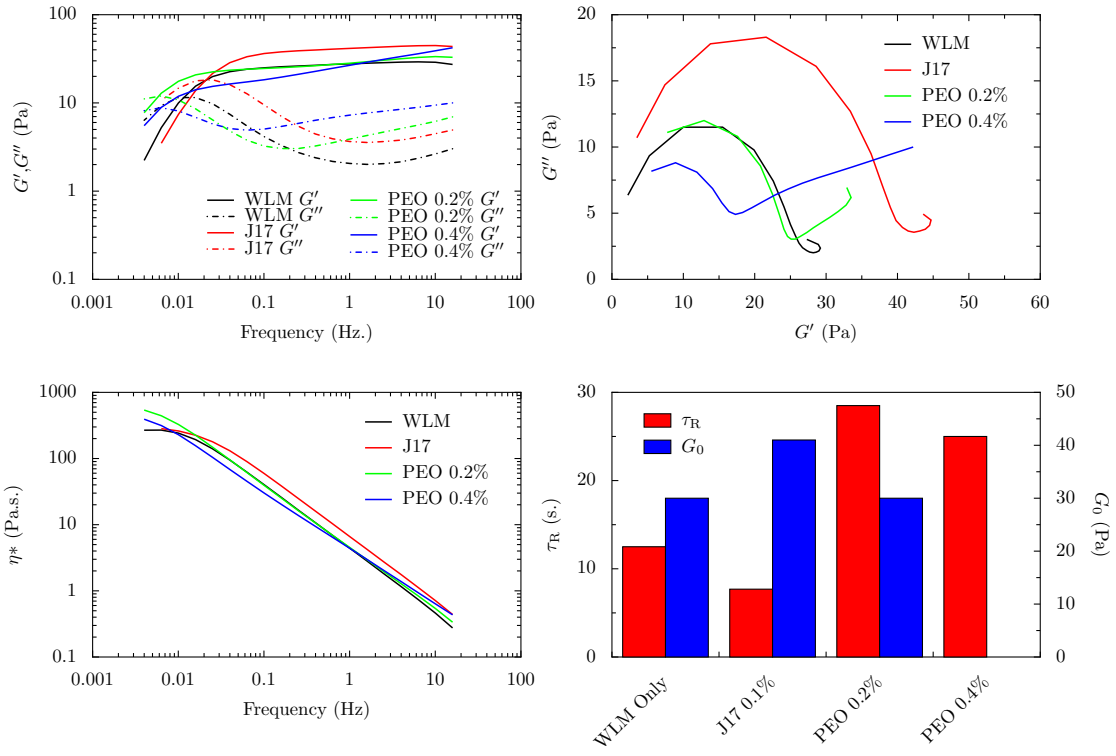

FIGURE 4.40: **Top left:** G',G'' vs ω, **Top right:** Cole-Cole plot, **Bottom left:** Complex viscosity vs ω. All graphs are for 0.06 eM SDS:CAPB with 1.5% wt. additional salt. **WLM** refers to the pure SDS:CAPB micelle system with additional salt only, **J17** refers to the samples with 0.1% wt. Jaguar C-17 and the PEO is 4M MW.

The higher PEO concentration sample (blue lines) also becomes gel-like at higher frequencies; the two-decade region where G' and G'' are nearly parallel is classic gel-like behaviour, again indicating a spread of relaxation times.

PHYSICAL INTERPRETATION AND IMPLICATIONS

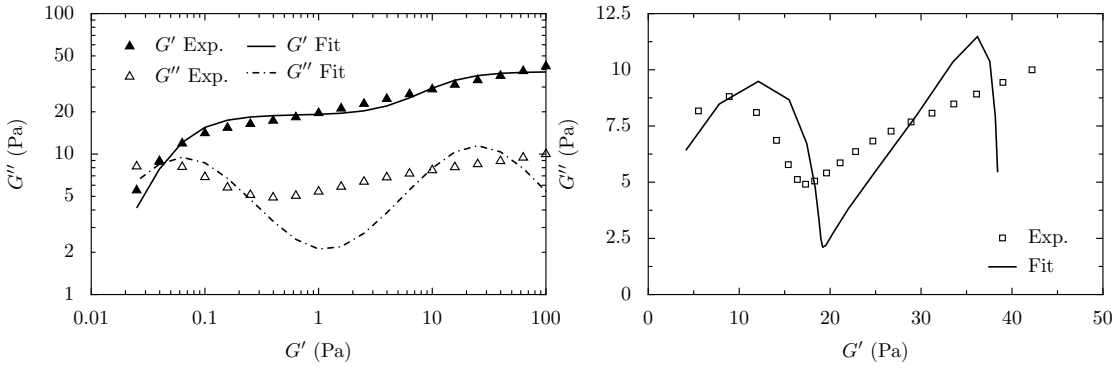

FIGURE 4.41: **Left:** Data and Fit for G' and G'' against Frequency, **Right:** The same data in Cole-Cole form, showing the inappropriate nature of a double Maxwell model for this sample.

Figure 4.41 shows an application of the double Maxwell model (introduced in §4.6) to the PEO 0.4% wt. data shown in Figure 4.40. A comparison with the double Maxwell fits shown in §4.6 shows that this is not an appropriate model for this particular gel-like sample as a small, discrete number of τ_R values (in this case two) is far too simplistic for a gel which is better modelled with a continuous spectrum of relaxations. I can therefore conclude that in this case the deviation from Maxwellian behaviour is not an indication of a transient network as shown previously.

Current models for the interaction of surfactant micelles with a polymer additive point to two behavioural regimes; *bridging* [185, 193] and *mopping-up* [11, 12, 180, 194]. Bridging is defined as the polymer embedding parts of itself in the cores of multiple micelles; this creates a *transient* network structure which acts to increase the elasticity of the system [180]. Mopping-up is when the polymer chains are separate to the micelles, but accrete surfactant from the micellar network, which acts to shorten the micelles, resulting in decreased τ_R and decreased G_0.

We can see from the changing rheological behaviour in Figure 4.40 that there is a major interaction with the PEO, we also know that the PEO is not 'mopping-up' the surfactant, else the behaviour would not resemble an entangled state. We can therefore say with some certainty that the PEO has formed part of the network structure, most probably through bridging, therefore maintaining the elasticity whilst creating a spread of relaxation times.

The behaviour of the Jaguar is more difficult to ascertain; Jaguar brings additional ionic strength (much like the NaCl and CAPB discussed previously), but τ_R decreases whilst G_0 increases, which is not covered by current theories. One would expect the relaxation time to decrease along with a corresponding increase in the elasticity if the micelles were

branching due to the branches 'sliding' down the micellar length, but there are currently no experimental results showing that a polyelectrolyte can initiate branching in micelles.

The Jaguar is positively charged, and we know that this system is around pH 5 (see Figure 4.38), therefore the CAPB is slightly positively charged. If the Jaguar were mopping-up the surfactant it would therefore mop-up the SDS preferentially over the CAPB; this would result in τ_R and G_0 both decreasing, which we can see is not the case as G_0 increases substantially. From Equations 2.31 and 2.32, we know that G_0 is dominated by the entanglement lengths; subtracting the SDS would make the micelles charged, and therefore less flexible, however the entanglement length would increase slightly due to the extra length of CAPB compared with SDS molecules. If the number of entanglements remained constant, but the micelles became thicker through CAPB-domination, then the density of entanglements would decrease. This would result in a corresponding decrease in the plateau modulus as G_0 is proportional to the density of entanglements.

We can therefore be confident that the Jaguar is not mopping-up or bridging, and as a consequence its effect is not clear, although these results do hint at previously unseen behaviour in a WLM system with polyelectrolyte.

4.8.3.2 Phase Boundary: Jaguar C-13-S without Salt

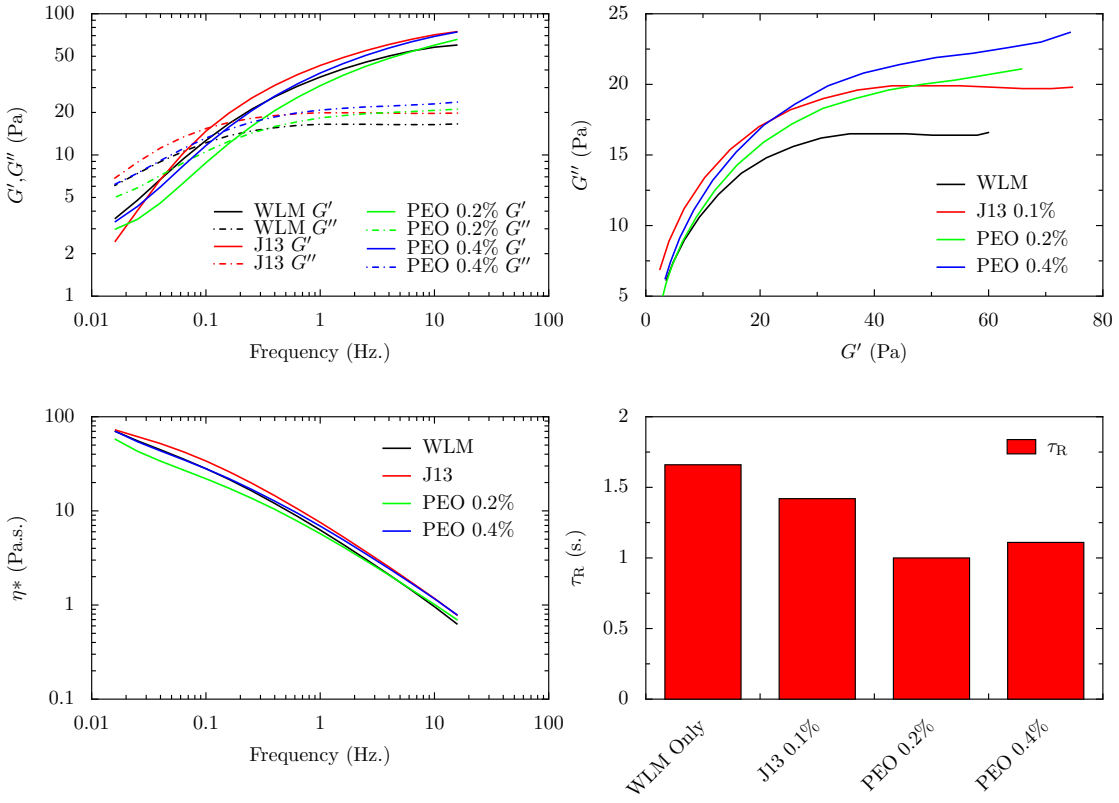

FIGURE 4.42: **Top left:** G',G'' vs ω, **Top right:** Cole-Cole plot, **Bottom left:** Complex viscosity vs ω. All graphs are for 0.11 eM SDS:CAPB with no additional salt.

Figure 4.42 shows the rheology of the 0.11 eM SDS:CAPB WLM system with 0.1% additional Jaguar C-13-S, and additional PEO at 0.2 and 0.4% wt. The 0.11eM SDS:CAPB samples do not show a highly entangled system; the lack of a plateau in G' or a well-defined minima in G'' shows that the system consists of rod-like micelles rather than worm-like. It is therefore difficult to discuss relaxation times when there is a lack of entanglements, but we can see that neither PEO nor Jaguar has a significant effect on this system.

In previous studies (§4.6,§4.8.3.1) we have shown that polymer bridging between micelles strengthens the micellar network and therefore increases the elasticity. In this case there is no network structure to reinforce, and therefore all samples show similar, but not identical, rheological behaviour.

4.8.3.3 Phase Boundary: Jaguar C-17 without Salt

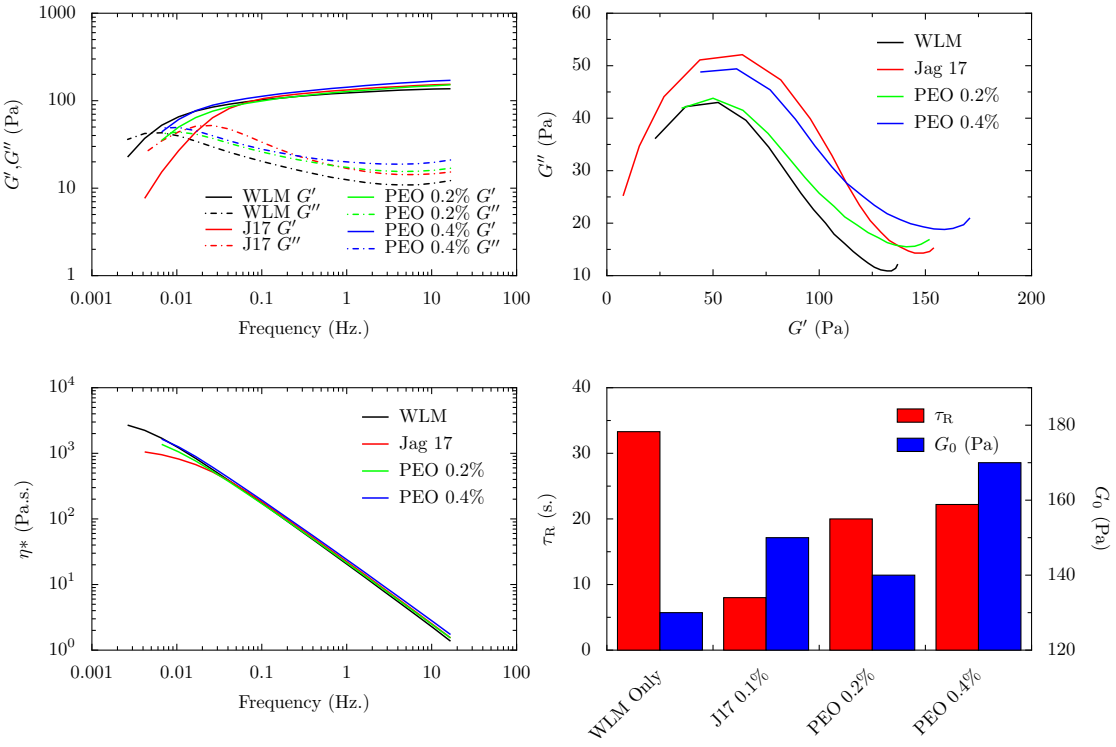

FIGURE 4.43: **Top left:** G',G'' vs ω, **Top right:** Cole-Cole plot, **Bottom left:** Complex viscosity vs ω. All graphs are for 0.15 eM SDS:CAPB with no additional salt.

Figure 4.43 shows the rheological properties of 0.15 eM SDS:CAPB wormlike micelles with the same polymer additions as before, with no additional salt. We can see that even without the extra ionic strength from the NaCl, this system forms an entangled network structure at these concentrations, signified by the large plateaus in G', minimas in G'' and the semi-circular Cole-Cole plots.

The behaviour is akin to the lower concentration system presented in §4.8.3.1 with G_0 increasing slightly, yet τ_R decreasing significantly on the addition of either polymer. This effect is most marked with the Jaguar, which reduces τ_R to $\frac{1}{4}$ of its initial value, and therefore has a stronger influence on the system than the PEO at either concentration.

We know that the WLM-only system is not branched at 0.15 eM surfactant concentration, firstly because the same system is not branched at 0.2 eM (§4.3), and secondly because

the Cole-Cole plots do not show deviations indicative of branching. As a result we can assume that there is no branching in the systems with polymer, however branching is the only known mechanism by which G_0 can increase whilst τ_R decreases. We therefore cannot interpret this reliably, but again this hints at previously unseen behaviour.

4.8.3.4 Jaguar C-13-S with increasing surfactant Concentration

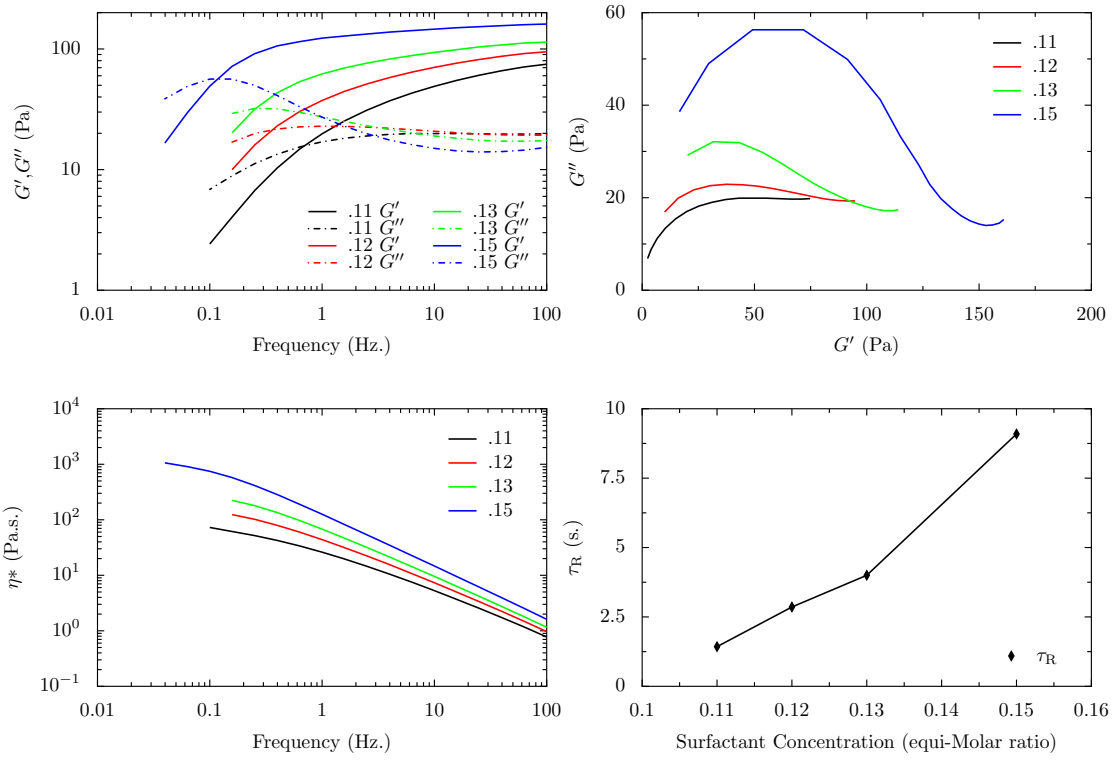

FIGURE 4.44: **Top left:** G',G'' vs ω, **Top right:** Cole-Cole plot, **Bottom left:** Complex viscosity vs ω, **Bottom right:** Relaxation time vs. Surfactant Conc.. All graphs are for 0.1% Jaguar C-13-S with no additional salt, and the number in the graph keys show the equimolar surfactant concentration.

Figure 4.44 shows the transition into a highly entangled WLM system as the relative surfactant concentration is increased from 0.11 to 0.15 eM SDS:CAPB, but with no additional NaCl and the polyelectrolyte concentration held constant at 0.1% wt. Only at 0.15 eM SDS:CAPB does the system show Maxwellian behaviour; between 0.11 and 0.15 eM τ_R increases roughly linearly with surfactant concentration, however G_0 is ambiguous for all samples except 0.15 eM as there is no well-defined G' plateau or G'' minima.

4.8.3.5 Jaguar C-17 with Increasing Surfactant Concentration

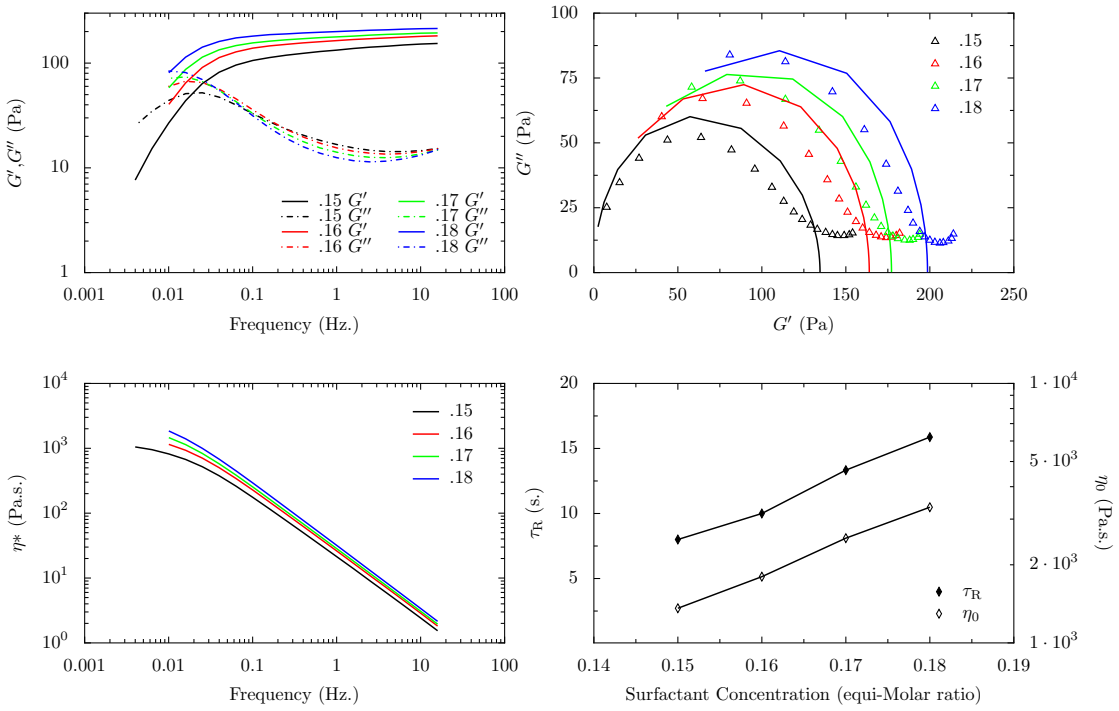

FIGURE 4.45: **Top left:** G',G'' vs ω, **Top right:** Cole-Cole plot, **Bottom left:** Complex viscosity vs ω, **Bottom right:** Relaxation time vs. Surfactant Conc.. All graphs are for 0.1% Jaguar C-17 with no additional salt, and the number in the graph keys show the equimolar surfactant concentration.

Figure 4.45 shows the same behaviour as the Jag-13-S system without salt (Figure 4.44); relaxation time and G_0 both increase along with the surfactant concentration. Unlike the C-13-S system, these samples show an entangled network structure even at the lowest surfactant concentration.

4.8.3.6 Jaguar C-17 with NaCl and Increasing Surfactant Concentration

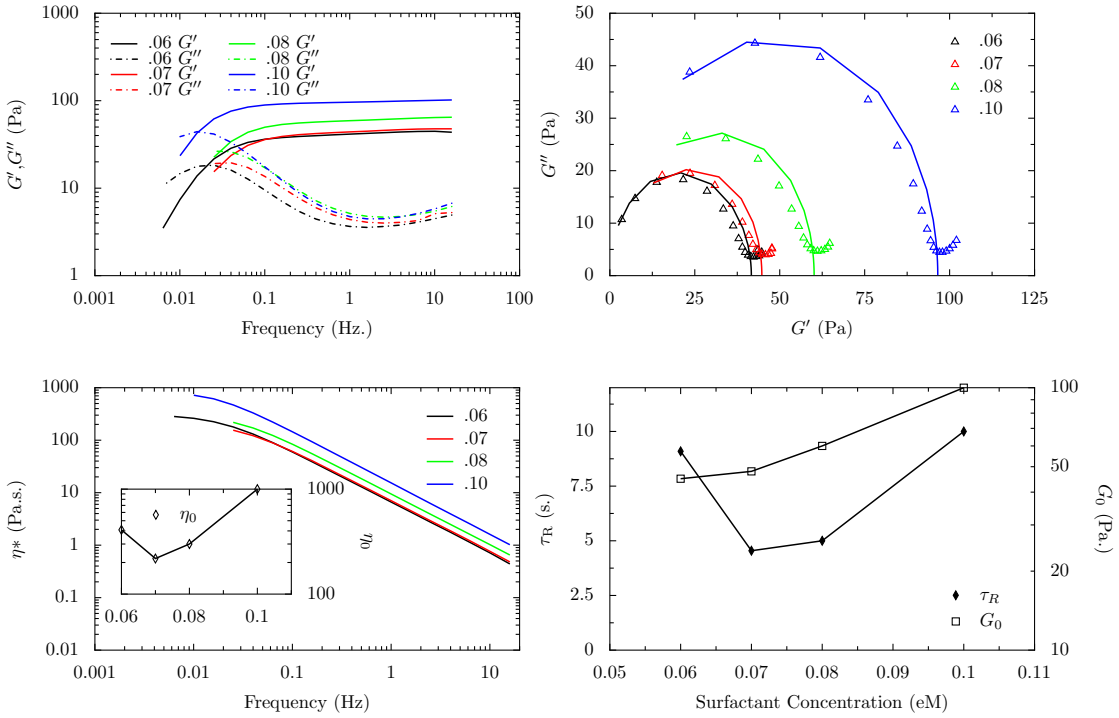

FIGURE 4.46: **Top left:** G',G'' vs ω, **Top right:** Cole-Cole plots of experimental data (symbols) and single-exponential Maxwell fits (solid lines). **Bottom left:** Complex viscosity against Frequency, **Inset:** Zero-shear viscosity against surfactant concentration. **Bottom right:** Relaxation time and plateau modulus against eM surfactant concentration. All graphs are for 0.1% Jaguar C-17 with 1.5% additional salt, and the number in the graph keys shows the eM surfactant concentration.

Figure 4.46 shows the rheological changes in a SDS:CAPB WLM system with 1.5% wt. NaCl and 0.1% wt. Jaguar C-17 when the eM surfactant concentration is varied from 0.06 to 0.10. All samples show a highly entangled Maxwellian system with well-defined G' plateaus over 2-3 decades and semi-circular Cole-Cole plots. Compared with Figures 4.44 and 4.45, the extra ionic strength in this system screens the charges along the micelles allowing them to elongate and therefore entangle at such a low surfactant concentration.

The top-right graph in Figure 4.46 shows the Cole-Cole experimental data (symbols) and single-exponential Maxwellian fits (solid lines) - the fitting code can be found in Appendix B (p.214). All samples show themselves to be very close approximations to an ideal Maxwell fluid, with only small deviations from the ideal semi-circular fit.

The behaviour here is abnormal however, as τ_R and η_0 both show a minima with increasing surfactant concentration. A maximum in η_0 has been witnessed and explained in this context as a change from entangled to branched dynamics, whereby the increase in the end-cap energy E_C is counter-balanced by the opposite curvature created during micellar branching [56]. A minimum however shows exactly the opposite behaviour; on increasing the surfactant concentration with 0.1% wt. Jaguar C-17 the system initially loses viscosity before gaining it again, whilst maintaining a highly entangled, Maxwellian network structure at all times.

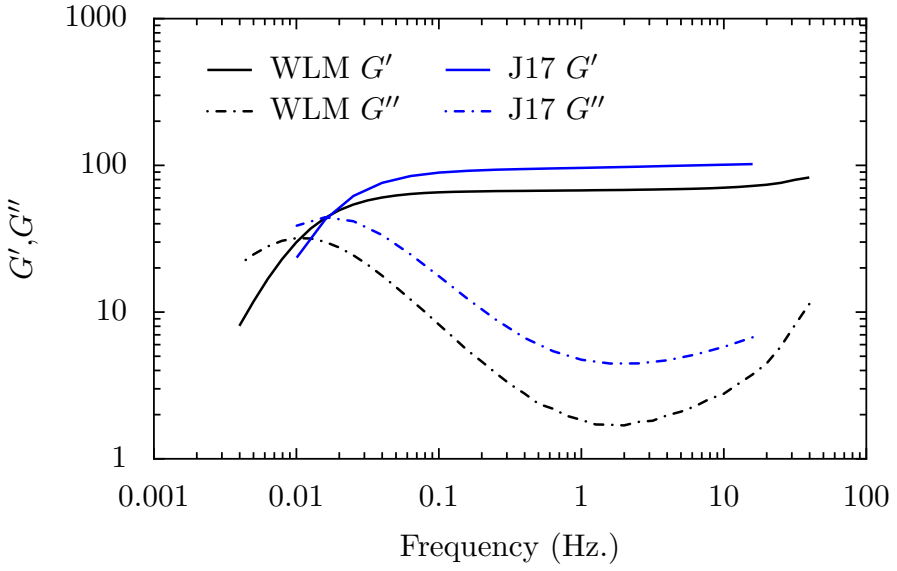

FIGURE 4.47: Comparison of 0.1M SDS:CAPB WLM 1.5% NaCl with and without 0.1% wt. Jaguar C-17. The WLM only data (black lines) are from a previous WLM study (Figure 4.24, p.118) and the Jaguar data (blue lines) are the same data from Figure 4.46 above.

In order to distinguish the polymeric from the micellar effects, we must look at the rheology of this system alongside that of a pure WLM system, shown in Figure 4.47. Here we see that 0.1% Jaguar C-17 decreases τ_R and increases G_0, yet G''_{min} remains roughly constant. This behaviour could be indicative of branching, however as mentioned previously there is currently no literature to suggest that a polyelectrolyte could initiate branching. Flood [195] has reported growth of spherical into rod-like micelles on the addition of a polyelectrolyte, experiments performed using small-angle neutron scattering

(SANS) and confirmed using cryo-TEM. This is important as it shows a movement on the phase diagram, on the addition of a polyelectrolyte, in the same direction as required for a transition to branching. Khokhlov *et al* [196] have also speculated that a polyelectrolyte network could collapse on the addition of an oppositely charged surfactant, exhibiting 3 distinct regimes;

- Low surfactant concentration - no micelles formed, polymer network dominates.
- Intermediate surfactant concentration - micelles form ($c >$ CMC), and the polymer network collapses due to the loss of osmotic pressure from the surfactant molecules.
- High surfactant concentration - Micelle network dominates.

These regimes result in a minima in viscosity with increasing surfactant concentration, however we know from Lips *et al* [184] that eM solutions of SDS and CAPB form rodlike micelles at ∼0.015 eM, therefore it is unlikely that the minima in τ_R at ∼0.07 eM is due to polyelectrolyte network collapse.

It is therefore possible that these results show an entangled WLM system branching on the addition of a polyelectrolyte, however this would need to be confirmed using cryo-TEM, and this still does not explain how increasing the eM surfactant concentration from 0.06 to 0.07 causes τ_R and η_0 to decrease.

4.8.3.7 Jaguar Charge Density Comparison

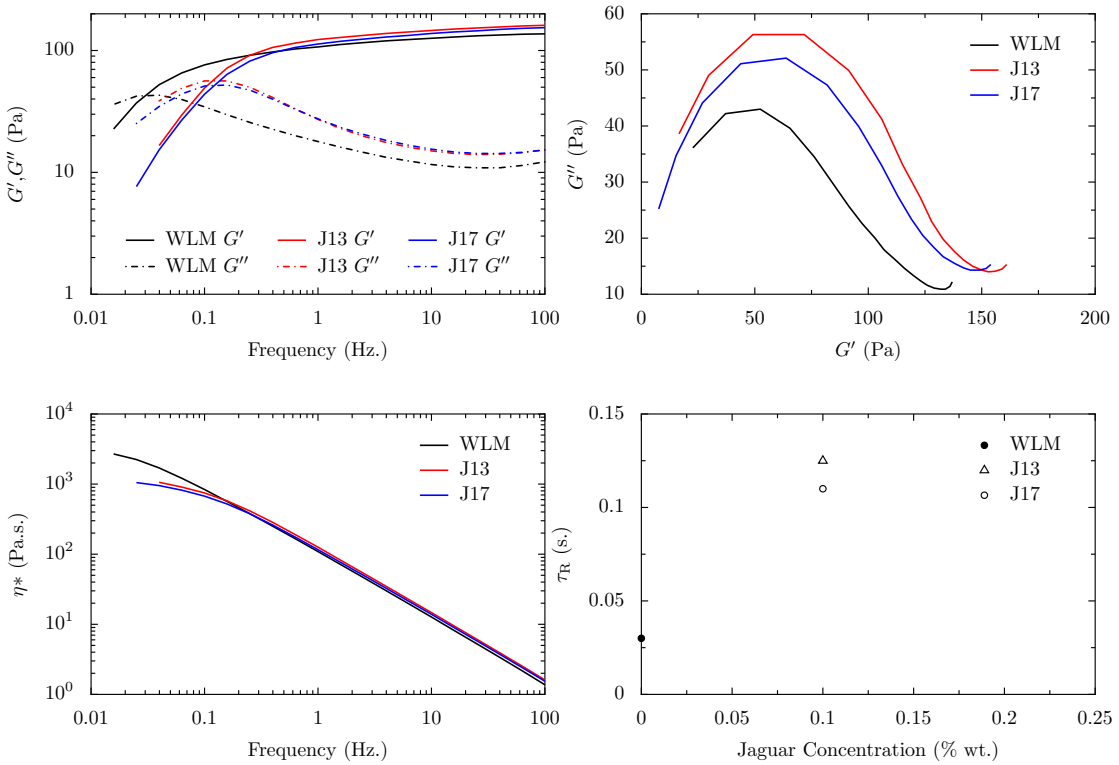

FIGURE 4.48: **Top left:** G',G'' vs ω, **Top right:** Cole-Cole plot, **Bottom left:** Complex viscosity vs ω, **Bottom right:** Relaxation time vs. Polymer Conc.. All graphs are for 0.15 eM SDS:CAPB with no additional salt, and 0.1% Polymer

Figure 4.48 shows the effect that the different charge densities have on a Maxwellian WLM system; both Jaguars decrease the relaxation time and increase the plateau modulus. It is interesting to note that the extra charge density of the C-17 Jaguar results in a lower G_0 than the lower charge density C-13-S, yet G''_{min} remains constant regardless of Jaguar concentration or charge density. This could also point to polyelectrolyte-induced branching, as the extra charge density induces more branches, reducing G_0 further.

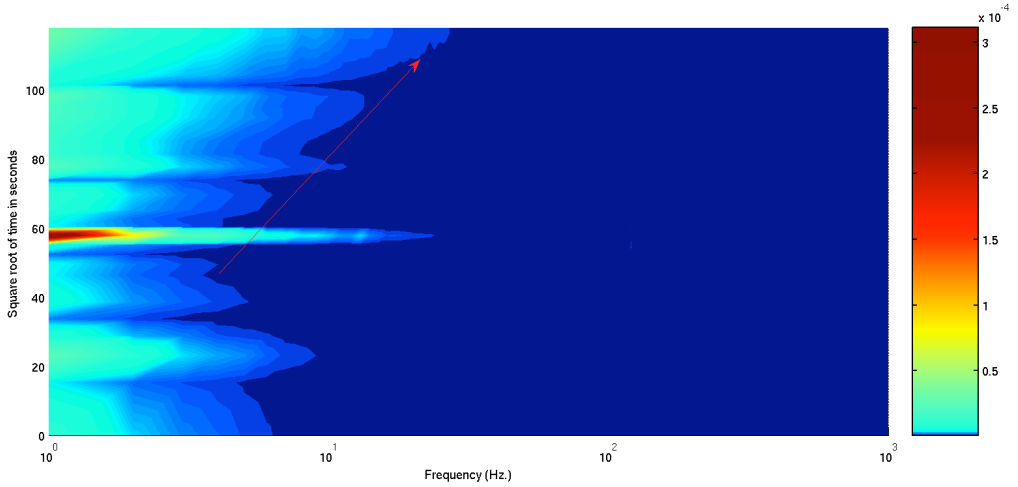

FIGURE 4.49: The dynamic power spectrum of 0.1 eM SDS:CAPB, 0% PEO, 1.5%NaCl. The red arrows shows increased particle movements due to the dissolution.

4.9 Non-equilibrium Optical Tweezer experiment on a model micelle system

Figure 4.49 shows the evolution of the power spectrum during a 20:1 dilution experiment of 0.1 eM SDS:CAPB, 0% PEO, 1.5% wt. NaCl. The geometry and experimental protocol was the same as described in §3.3.4; in Chapter 3 the solutions were semi-dilute aqueous polymer samples, here the sample being diluted is a living polymer system with extra ionic strength to create an entangled, Maxwellian system. The bulk rheology of this pre-diluted sample is shown by the squares in Figure 4.14, and the DWS microrheology of this pre-diluted sample is shown by the central graph in Figure 4.16. Both of these techniques show this system to have a highly entangled, viscoelastic network structure, with no signs of any branching, mopping up or any other deviation from the Maxwell model.

The shift towards higher frequencies over time, shown by the red arrow on Figure 4.49, indicates an overall trend towards a less entangled, more fluid state as the sample dilutes. The most interesting observation about this data is the quasi-regular appearance of

'jumps' in the data, roughly every 20 minutes. These jumps occur much more frequently that in the dilution of a pure polymer solution (see §3.4.1 and §3.4.2), but are likewise attributed to local flaking events. The flaking can be seen by eye as small portions of material detach from the interface, and is presumed to be part of the dissolution process of wormlike micelles.

Physical interpretation and implications

This flaking raises interesting questions about the use of a WLM network structure in commercial products. When introduced in Chapter 2, these micelles were called 'living' polymers due to their constant scission and recombination processes which continue even when the bulk system is at rest. When applying a dilution to these micelles, it is easy to image the scission processes outnumbering recombinations as the extra solvent pervades the network structure, causing local sections to break from the bulk material. Although the system must undergo phase changes as it dilutes (these can be visualised in Figure 2.11 on p.27 as being transitions from **(c)** to **(b)** and finally **(b)** to **(a)**), the results above suggest that the dilution gradient is not uniform across the sample plane as it appears to be in polymer solutions.

4.10 Non-equilibrium Optical Tweezer experiment on a micelle and polymer system

Figure 4.50 shows the PSD evolving over time for a 0.2 eM SDS:CAPB WLM sample with 1.5% NaCl and 0.5% PEO 4M, diluted 20:1 with water with the same geometry and protocol as before. This sample has twice the surfactant concentration as the previous

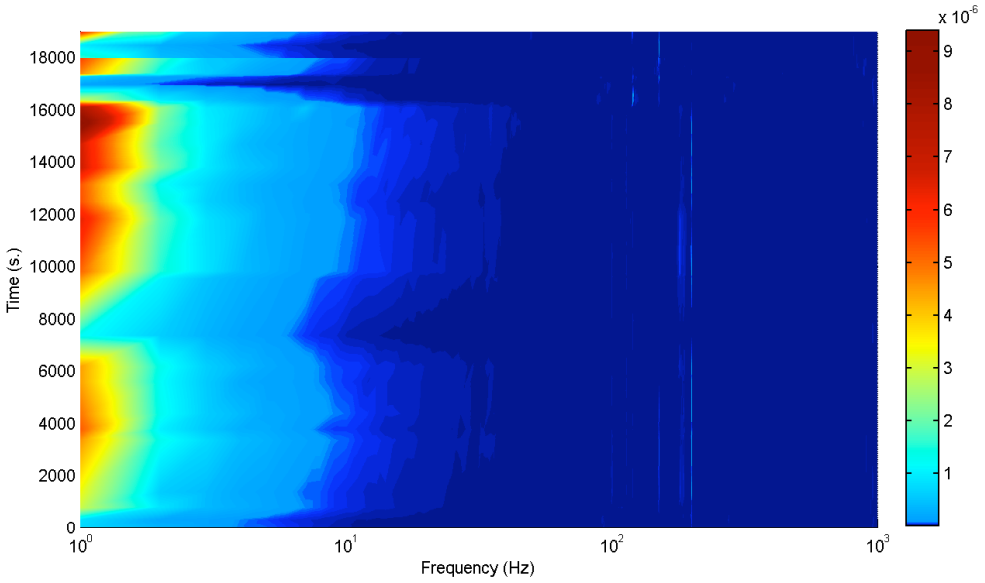

FIGURE 4.50: The dynamic power spectrum of 0.2 eM SDS:CAPB, 0.5% PEO 4M, 1.5% NaCl.

dilution study (§4.9) along with a long chain polymer at just under the overlap concentration c^*. The combination of higher surfactant concentration and polymer at $\sim c^*$ introduces the possibility of bridging, and also means that this sample has the slowest dissolution rate of all the non-equilibrium OT experiments presented in this work.

As expected, there is a general trend towards a lower level of entanglement, however the jumps in the data are less severe and less frequent than reported in §4.9 with a lower surfactant concentration and without additional polymer.

PHYSICAL INTERPRETATION AND IMPLICATIONS

The non-equilibrium data shown in Figure 4.50 shows dynamics with characteristics of both micelles (frequent jumps) and polymers (long periods of stable dissolution). The bulk rheology for this pre-diluted sample (Figure 4.26) and the DWS microrheology (Figure 4.28) both show an entangled system where the behaviour deviates from Maxwellian, presumably through bridging/branching.

This data in conjunction with the WLM dilution without polymer (§4.9) shows that either extra surfactant or additional polymer goes some way towards removing the erratic dissolution behaviour seen previously.

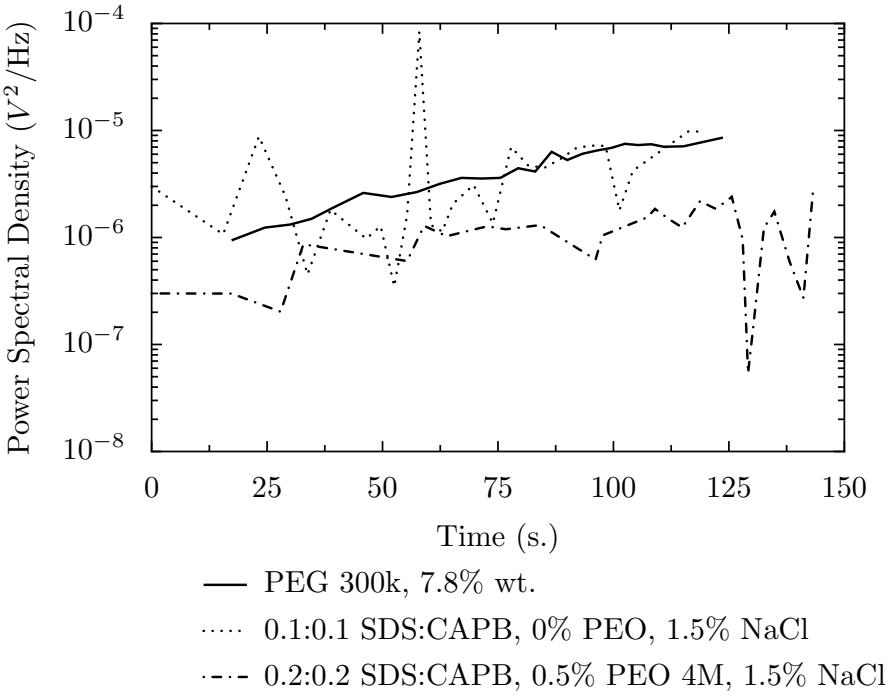

FIGURE 4.51: Comparison of the low-frequency (1 Hz.) dynamics for the 300k PEO (§3.4.2), WLM (§4.9) and WLM w/PEO 4M non-equilibrium OT experiments.

Although a quantitative comparison is difficult due to the apparently stochastic nature of the jumps and the absence of repeat experiments, a preliminary attempt at comparing the various non-equilibrium behaviours is shown in Figure 4.51. The PSD value at 1Hz is plotted over time for the PEO 300k (§3.4.2), WLM only (§4.9) and WLM with PEO 4M non-equilibrium experiments. The aqueous polymer sample clearly shows very little in the way of anomalous behaviour in comparison with the 2 micellar samples; its dilution shows an even upward trend (towards lower viscosity/higher fluidity).

4.11 Experimental Study on the Dilution of a prototype Hair Conditioner using Optical Tweezers

After studies in §4.9 and §4.10 showed the ability of OTs to study the rheology of a WLM and WLM with polymer system in non-equilibrium conditions, a further investigation was performed using a prototype Unilever conditioner codename HU25.

As a prototype conditioner, it has some additives on top of the surfactants, salt and polymers studied so far, most notably polydisperse silicone oil droplets which are traditionally added to hair products to enhance shine. As a result, no tracer particles were added during this investigation, and the OT was used to trap an oil droplet, for which the size was determined later. The dilution protocol and equipment was the same as in all previous non-equilibrium studies.

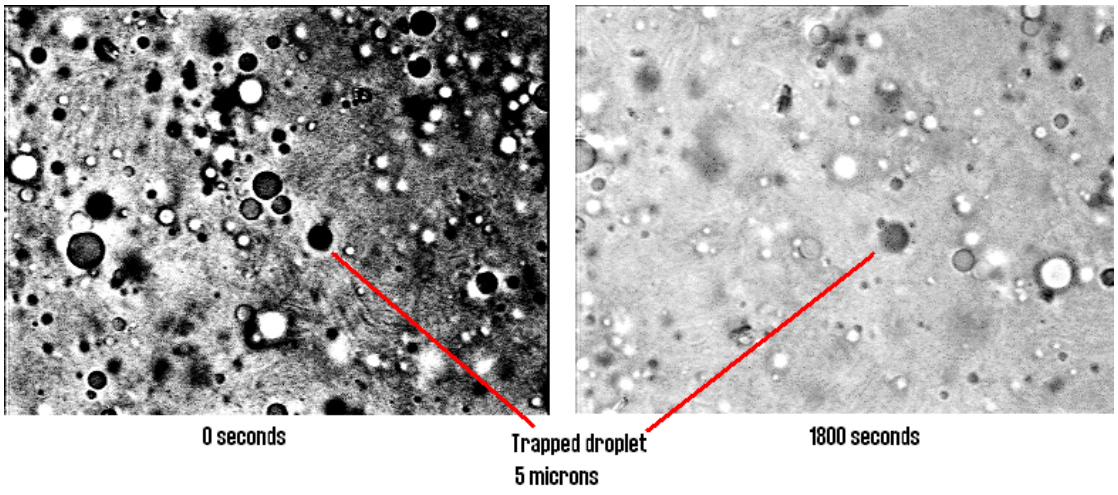

FIGURE 4.52: Prototype Hair Conditioner (HU25) before and during dilution

Figure 4.11 shows two screenshots from this investigation; *left:* at $t = 0$s. and *right:* at $t = 1800$s. At $t = 0$ we see that there is a very high concentration of silicone droplets, which are highly polydisperse, presumably a result of the mixing protocol. For these

images the exposure level of the camera was fixed, therefore the increased brightness of the $t = 1800$ is a qualitative measure of the sample dilution.

Unfortunately these experiments on HU25 did not yield usable data as the high concentration of silicone oil droplets resulted in many particles rapidly becoming trapped in the potential well, and therefore disrupting the Brownian movements of the primary particle. These secondary droplets can be seen in the $t = 1800$s image. Any attempt to reduce the amount of silicone in this sample would modify both the system rheology and the efficacy of the final product, therefore in order to obtain usable data, I suggest that a multiple-trap system such as holographic tweezers or AOD-based time-sharing could be implemented to remove any secondary droplets from the local area.

4.12 Conclusions and Further Work

These results clearly show for the first time that dual-surfactant SDS:CAPB systems form highly entangled wormlike micellar networks above ∼0.1 eM surfactant concentration, and that this level can be reduced considerably (to $\sim$ 0.06 eM) when extra ionic strength is added, in the form of NaCl, to screen the charges. With saline concentrations above 1.5% wt. some samples show evidence of branching in their rheological behaviour, however rheology data on its own cannot distinguish between branching and other behaviours, therefore cryo-TEM experiments [197, 198] must be performed in order to determine the exact behavioural regime. Increasing the number of samples for each system would also make it easier to draw firm conclusions as to the behaviour of this system.

The fact that the OT hardware could not provide reliable micro-rheological data is disappointing, however one goal of this research project was to determine the applicability

of OTs to Unilever's rheological studies, to which I can conclude that bulk rheology yields the most reliable data compared with DWS and OT systems. DWS is a promising technology, and significantly reduces the experimental time, however the necessary monodisperse scattering particles are expensive, and may modify the system rheology. On top of this, due to particle slip the Brownian motion of these additional particles may not represent the bulk rheological properties [199], which is the fundamental assumption of microrheology. The particle slip 'correction' that is usually applied is somewhat arbitrary, and therefore I feel that bulk rheology provides the most reliable data for quantitative comparisons.

With a true interferometric detection setup for the OTs one could improve the temporal and spatial resolution, however given that DWS covers a much larger frequency range, and bulk rheology provides reliable data at frequencies which cover τ_R for all samples, I feel that the strength of OTs in studies relevant to Unilever is in the ability to study rheology in non-equilibrium conditions - something which cannot be achieved reliably with DWS or bulk rheology.

The non-equilibrium experiments performed in §4.9 and §4.10 show that these OT experiments yield interesting results, however the data is difficult to interpret when the dilution gradient is nonmonotonic. The prototype conditioner study in §4.11 also raises questions as to the usefulness of these OT hardware setups in studying complete systems; I conclude that OTs are potentially extremely useful at studying the non-equilibrium rheology of certain systems, however where there is a high concentration of droplets (such as in HU25), high-speed video particle tracking microrheology will yield more reliable data, and in not using a laser is inherently safer than OT experiments.

Table 4.8 shows the conclusions that can reliably be made from the equilibrium studies

TABLE 4.8: Conclusions relating to SDS:CAPB micelles with various concentrations of PEO 4M MW.

PEO Conc. % wt.	Behaviour	Supporting Figures
0.1	No significant changes to rheology of system unless the sample is on the verge of branching (0.2eM SDS:CAPB, 1.5%NaCl), in which case it lowers G_0 considerably.	4.19,4.24,4.25,4.26
0.2	Has a small effect on the sample rheology at all surfactant concentrations, but shows no sign of gel-like behaviour.	4.40,4.42
0.4	In a low surfactant concentration system (0.06eM), shows evidence of gel-like behaviour (spread of multiple τ_R values). In all other concentrations, G_0 always increases showing an increase in elasticity consistent with a transient network.	4.40,4.41,4.42,4.43
0.5	Can completely disrupt the micellar network, yielding a gel-like system which shows evidence of multiple relaxation. times	4.19,4.20,4.24,4.25

performed in this chapter. From Table 2.2 we find that the overlap concentration c^* of PEO 4M MW is ∼0.7%, and therefore aqueous PEO 4M solutions show entangled viscoelastic behaviour when the concentration approaches this level. It is therefore not surprising that a Maxwellian micelle network with additional 0.5% PEO 4M ($\frac{c}{c^*} \rightarrow 1$) shows evidence of having at least one fast and one slow relaxation time (Figure 4.29), consistent with current bridging theories [185, 193].

A further investigation to study the cause of the Nipagin phenomena may also yield previously unseen results; Figure 4.35 shows an increase in τ_R by an order of magnitude, however with double the surfactant concentration Figure 4.36 shows a decrease in τ_R of a similar level. This hints at a strong interaction between Nipagin and either SDS and/or CAPB, further investigation of which could lead to additional methods of controlling the viscosity of personal care products.

Anomalous Jaguar Behaviour - Physical Interpretation and Implications

§4.8.3.6 shows the truly surprising behaviour of a minima in τ_R and η_0 as the surfactant concentration is increased. A maxima in these values has been witnessed elsewhere [56], which can be explained by the onset of branching, however from Figure 4.14 we know that even the highest surfactant concentration sample in §4.8.3.6 shows no evidence of branching, only classic Maxwellian behaviour. It is interesting to note that even though τ_R and η_0 show a minima, G_0 increases throughout and all samples show well-defined G' plateaus, G'' minimas and Maxwellian Cole-Cole plots. We can therefore say with some certainty that whatever underlying mechanism is causing this behaviour, it is not disrupting the network or adding extra relaxation times. We can also rule out the Khokhlov polyelectrolyte network collapse regime [196], as the minima in η_0 is at $\sim 7\times$ the critical micelle concentration.

It would be extremely interesting to perform cryo-TEM or fluorescence microscopy experiments to confirm whether the polyelectrolyte is inducing branching, something hinted at by Flood's work [195], but previously unseen.

5 Bootstrap Droplets

"If your result needs a statistician then you should design a better experiment."

Nobel Laureate Ernest Rutherford (1871 - 1937)

5.1 Introduction and Chapter Layout

Many important processes require the controlled evaporation of droplets, from ink-jet printing (drying of sessile colloidal suspensions) [7, 8] to spray cooling [200] and rocket propulsion engines (combustion of a fine spray) [201, 202] to name just three. The understanding of physical processes leading to evaporation is therefore of direct industrial and commercial relevance as well as being of academic interest.

This chapter presents work performed on sessile droplets of various complex fluid systems during controlled evaporation. Many fields of scientific research form through serendipity, and this is no exception. Preliminary work in this area was performed by myself in an attempt to corroborate the skin-buckling theory of Pauchard and Allain [203] (discussed in §5.1 below) by studying similar systems, and as a simple non-equilibrium system to study before moving onto dilution. It soon became apparent that the structures created

in these systems did not conform to any previous droplet evaporation theory, and more in-depth investigations were undertaken.

A variety of aqueous droplets were studied in this work, and a wide range of analytic techniques were used to measure their physical quantities; this chapter has been ordered such that all experimental equipment and techniques are introduced first, and the results from each droplet system are presented second (an overview is shown in Table 5.1). A theory accounting for the previously unseen results is also presented, and finally plans for future work and recent developments by the Fairhurst group.

TABLE 5.1: Results sections in this chapter. Properties for the PEO/PEG at each MW can be found in Table 2.2 (p.33), and the *Experiments* column shows the number of droplet evaporation experiments performed for each system. This indicates the systems which showed the most novel behaviour, were investigated further, and therefore have been given the most attention in this chapter.

Section	System	MW	Experiments
§5.3.1	PEO	100,000	>100
§5.3.2	PEG	20,000	>40
§5.3.3	PEG	8,000	4
§5.3.4	PEG	3,350	5
§5.3.5	PEO	300,000	3

5.1.1 Droplet Evaporation Theory

Various model systems have been used in the experimental study of the drying of complex fluid droplets. Deegan *et al* investigated the formation of the familiar 'coffee-ring stain' using a model of very dilute micro-spheres suspended in water [204]. They concluded that enhanced evaporation along the contact line, due to a contact angle $\theta \leq 90°$, must be fed by outward flow from the centre of the droplet. Suspended particles are carried to the periphery in the flow, and deposited at the edge leading to the familiar ring-like pattern. As well as material transport, this replenishment of solvent at the contact ring forces the droplet contact line to stay pinned; the result being that deposition occurs

primarily in a narrow band around the droplet edge. Recently, Hu and Larson showed that this ring-formation can be disrupted in the presence of recirculating currents caused by Marangoni flow [205, 206].

Parisse and Allain investigated the changing profile of droplets of concentrated suspensions as they dry [207], observing a gelled 'foot' near the drop edge which progressively grows inwards. Allain and Pauchard used the model system of the aqueous polymer dextran to investigate the additional complexities that arise as polymer solutions evaporate [203]. In this case, the increase in polymer concentration at the droplet's edge, due again to the outward flux of water, resulted in a phase change; on the surface of the liquid droplet a glassy skin formed which was flexible and permeable, but also incompressible. Further evaporation of water within the droplet led to the glassy skin deforming and buckling, the various shapes of which have been analysed theoretically [208]. Another model system is that of a mixture of a hydrophobic and a hydrophilic liquid, investigated by Rowan *et al* [209]. These droplets initially dried to a flat puddle with a contact line that was pinned but that rapidly retreated later causing a nearly spherical droplet to spring from the puddle - an effect driven by an increase in the surface tension as the hydrophilic component evaporated first, increasing the contact angle.

5.2 Experimental Methods

Experiments were performed using droplets of aqueous solutions of poly(ethylene oxide) (PEO) / poly(ethylene glycol) (PEG) with average molecular weight (MW) 3,350 - 300k as detailed in Table 2.2 (p.33).

All samples were mixed carefully by hand in quantities large enough to negate measurement errors ($\gtrsim$50mL); mechanical mixing methods were not used (vortex mixer,

centrifuge or sonicator) to avoid damaging the polymers. Samples were left to equilibrate for at least 24 hours before use. The droplets were dispensed extremely slowly using a Hamilton 710 microlitre syringe onto an isopropanol-cleaned TABA 24mm × 24mm glass slide, and were left to evaporate in ambient conditions. The needle on the Hamilton syringe was ∼0.2mm internal diameter, which could potentially lead to high shear rates during dispensation; droplets from the same sample were tested against ones dispensed using much wider needles, and there were no major differences observed in the behaviour. I can therefore conclude that this experimental protocol does not damage the polymers.

5.2.1 Drop Shape Analysis (DSA)

The contact angle, droplet height and base diameter for each droplet were measured during evaporation using the Krüss DSA system (DSA Model 10 Mk 2). For each measurement, a droplet was dispensed using a Hamilton 710 microlitre syringe onto a glass microscope slide, previously cleaned with isopropanol to remove dust and grease. The droplet was then left to evaporate in an observation chamber (measuring 0.6m by 0.75m by 0.94m) at ambient conditions where the temperature was monitored to within 0.5°C. The chamber was sufficiently large that droplet evaporation did not saturate the local atmosphere. A digital camera and light source placed either side of the droplet in the chamber were used to record the drying process. Care was taken to place the slide horizontally and to reduce convective air currents around the droplet due to the light source; two effects which can interfere with the deposition process.

Images of the drying droplet were recorded at 10 second intervals using Krüss Drop Shape Analysis (DSA) hardware, and analysed using DSA software. At early times when the droplet is smooth, the profile is fitted using the Young-Laplace equation [210], and values

for the droplet base diameter, height, volume and contact angle are calculated. Once deposition has started, this equation no longer describes the surface so only the total height and maximum width are extracted reliably. In experiments where the mass was measured, this was performed using a KERN ALJ160-4NM analytic balance and the values logged using LabView.

The raw images were converted to binary using ImageJ, and profiles were extracted using the code in Appendix D which was implemented as an ImageJ macro (this code was written by Kyle Baldwin and is reproduced here for completeness). This code outputs the x, y co-ordinates for each profile into a series of text files, which were then processed using the Python code in Appendix E to obtain volume and surface area with calculated errors. The code in Appendix E performs an implicit numerical integration over the droplet surface, calculated from the profile, and therefore makes the assumption that the droplet is axisymmetric at all times, around the highest point. The errors come from comparing the area or volume contribution from each side of the central axis, eg. $\Delta A = A_{\mathrm{LHS}} - A_{\mathrm{RHS}}$.

5.2.2 Optical Coherence Tomography

Optical Coherence Tomography (OCT) is an optical imaging technique which uses the magnitude and time delay of backscattered photons to construct $2d/3d$ sub-surface images of objects, even where the sample is visually opaque. OCT has its foundations in biomedical imaging, as the resolution (on the order of 1-10μm), and ability to non-invasively image biological tissue *in vivo* has led to a variety of specialist uses, such as ocular [211, 212] and arterial [213] to name just two. Tomographs are easily calculated in real-time and therefore in terms of resolution and penetration, OCT fills a useful gap between ultrasound and confocal microscopy [214, 215].

An OCT image (a 'tomogram') will visualise differences in refractive index, therefore in this work OCT is used to show density fluctuations inside the droplet deposits. The OCT used in this work has a central wavelength of 1325 nm, with a spectral bandwidth of 100 nm (full-width half-maximum (FWHM)).

5.2.3 Interferometric Surface Profiling

Nanometre precision profilometry studies were performed using a Taicaan® Xyris 4000 WL (white light) surface profiler. This allowed visualisation of droplet and deposit surfaces at nm to μm resolution [216, 217]. The Xyris uses an interferometric technique to vary the position of a lens required to keep the sample in focus at that point. The system therefore holds the calibration required to convert the lens height into sample height.

Although the highest spatial resolution is on the order of a nanometre, this level of precision increases the experimental time considerably, and is therefore inappropriate for studying the systems during evaporation, but has been used to image the final deposits. The experiments performed during evaporation were run at a much lower resolution in order to achieve as many scans as possible in a given time frame.

5.2.4 Particle Tracking Analysis

For some droplet evaporation experiments the glass slides were placed on an inverted microscope (Nikon TE-2000 S, as used for the OT experiments in §3.2.2.1, with a Nikon 10× objective lens), in order to magnify and image the droplet from below over time. The clusters present in PEO systems, discussed in §2.4.3, were used as tracer particles and therefore these experiments required no modifications to the system under study.

The positions of these clusters were recorded over time using the tracking algorithm by Sbalzarini [218], implemented as an ImageJ plugin, yielding velocity profiles across a 2d slice of the droplet over time[1]. Where velocity profiles are shown in this work, they always represent the slice closest to the substrate.

5.2.5 Magnetic Resonance Imaging

Magnetic Resonance Imaging (MRI) involves measuring the spin relaxation of atoms to determine the sample composition. A full description of magnetic resonance techniques is outside the scope of this work, but can be found in references [219] and [220]. MRI is used here solely as a means of qualitatively comparing concentration fluctuations.

5.2.6 Scanning Electron Microscopy (SEM)

Scanning Electron Microscopy (SEM) involves targeting a focussed beam of high-energy electrons at a sample; using the secondary electrons created via electron-sample interactions, the nanoscale structure of the sample can be visualised with resolution on the order of 10nm. Samples must be prepared so that sufficient secondary electrons are produced in the SEM chamber, which usually involves 'sputter-coating' the samples by depositing a thin layer of fine metallic particles (diameter $\approx$ 1nm) onto the surface. Many other measurements other than imaging can be performed by SEM, for example crystal structure and chemical analysis [221, 222], however in this work SEM is used solely as a visualisation tool for the droplet deposits.

A JEOL JSM-480A Scanning Electron Microscope was used along with the JEOL software for image capture and calibration.

[1] The depth-of-field of the Nikon 10$\times$ objective was $\sim$10-20μm, with a field of view $\sim$3mm $\times$ 3mm, therefore although this is a volume it is sufficiently thin to be considered 2-dimensional.

5.3 Experimental Data of poly(ethylene oxide) (PEO) Droplets

This section reports the results from evaporative drying experiments of PEG/PEO droplets from 3.35-300k MW; as shown in Table 5.1 the majority of the research time was spent on the 100k system as this MW showed the most unusual behaviour, the other MWs are reported here for a slightly wider perspective and to give some qualitative insights into various unreported drying regimes. I will now show representative data from an evaporating 100k 10% initial weight droplet in order to clarify the terminology used in this section.

Figure 5.1 shows the droplet profiles on the right, dissected into the four regimes seen in many of the 20k and 100k MW droplets presented later. Stage 1 is a 'standard' pinned drying regime, where the diameter d remains constant and the loss of solvent is compensated by the contact angle θ and drop height h decreasing linearly with time. Stage 2 is a 'de-wetting' regime in which the contact line de-pins and recedes, leaving behind a thin film deposit, whilst θ and h both increase - the start of this stage is signalled by the increase in h and θ. Stage 3 is a 'bootstrap' growth stage in which the droplet appears to lift itself on top of its deposit, forming a conical shape, until the entire structure is encased in PEO crystals. Stage 4 is the final shrinking stage, where the conical deposit loses volume from the remaining liquid evaporating away; this is signified by a constant d and decreasing h.

When the droplet de-pins at the end of Stage 1, the deposit left behind the receding contact line means that θ and d are no longer defined unambiguously, and therefore on the lower graph in Figure 5.1 they are shown in red. Where θ and d are shown in this chapter beyond the end of Stage 1, I have always ignored the thin deposit, and measured the remaining droplet or bootstrap structure. It should be noted that for some droplets

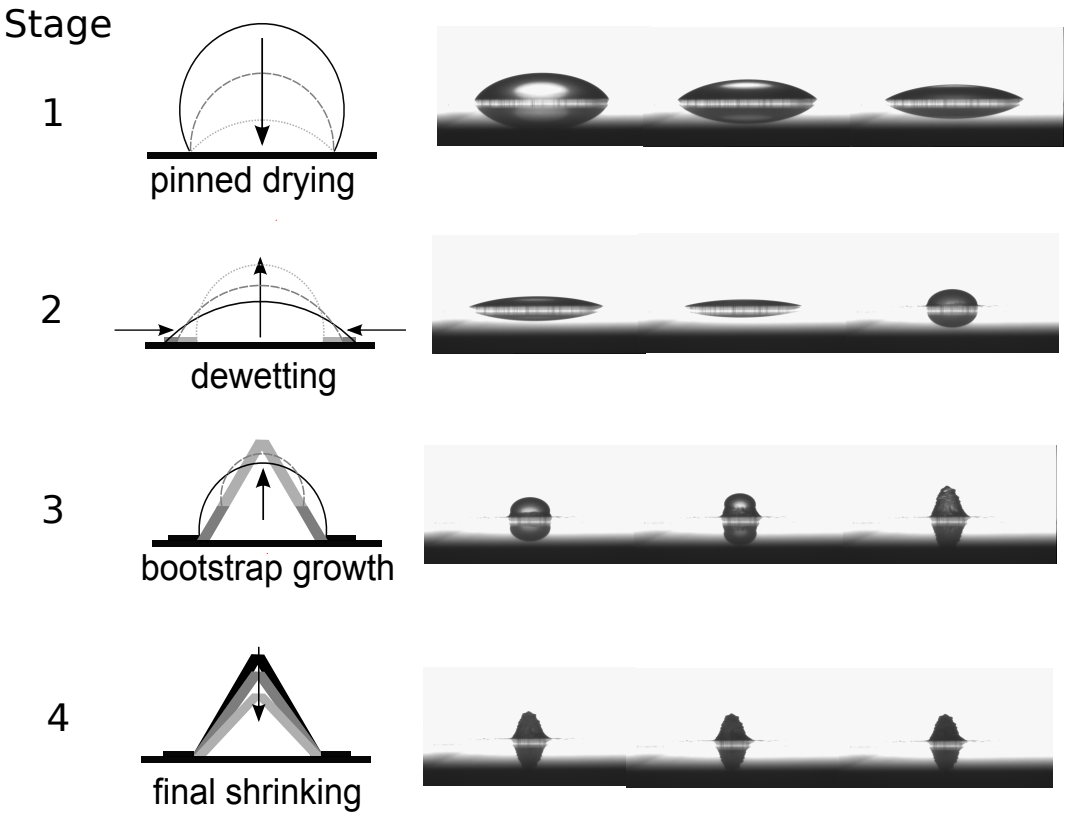

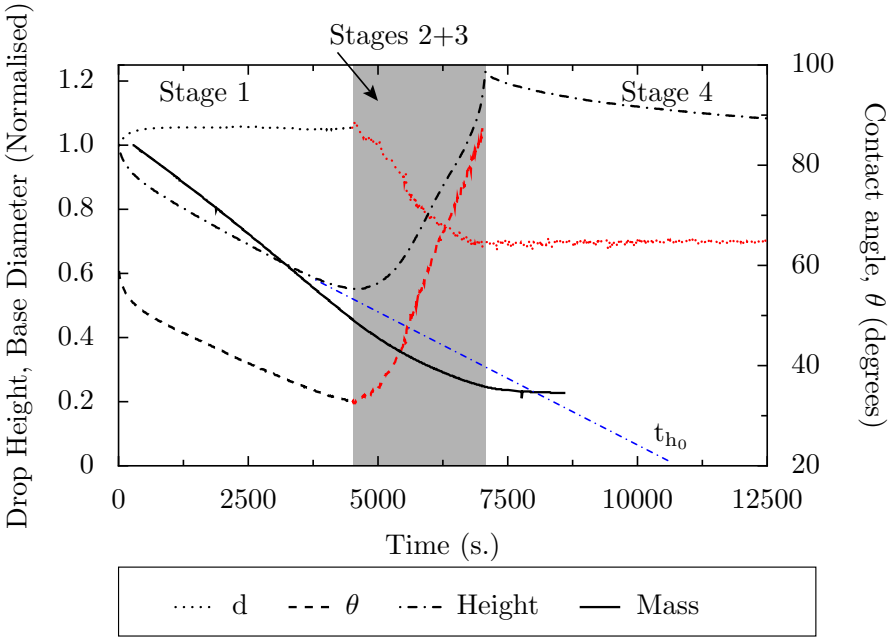

FIGURE 5.1: Drop Height (DH), Base Diameter (BD), contact angle (θ) and mass over time for a $75 \pm 5\mu L$ 100k MW PEO 10% wt. initial concentration droplet. The red data shows θ and BD after the droplet has de-pinned; after Stage 1 the droplet shape means that these quantities are ambiguous. The blue line shows the definition of t_{h_0} - it is the time at which an extrapolation of the initial decay reaches $h = 0$. The solid black line represents the mass of the droplet.

Stages 2 and 3 can merge together, ie. the de-pinning is not obvious or non-existent, and therefore in all figures which show droplet height, the grey area represents increasing h which is Stages 2 and 3 combined.

As in Pauchard's work, I extrapolate the linear portion of V to intercept the time axis, and use this as the time the droplet would have taken to reach zero volume t_0, had the growth phenomena not occurred;

$$t_0 = -\frac{V_0}{\left(\frac{\partial V}{\partial t}\right)_{\mathrm{t=0}}} \tag{5.1}$$

This t_0 value is used to normalise experimental times, thereby compensating for uncontrolled variations in temperature and humidity.

5.3.1 Results from 100,000 MW PEO

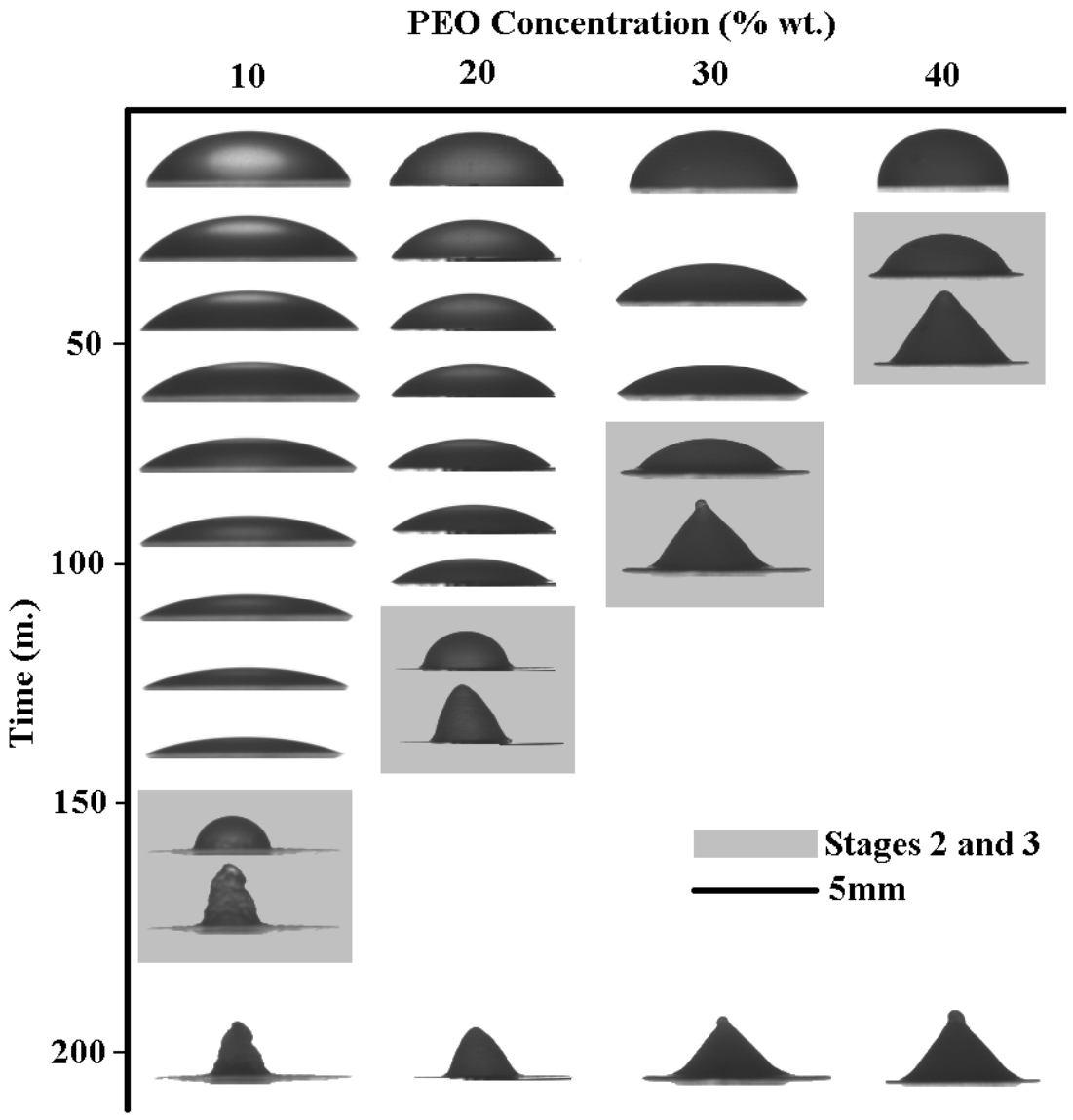

FIGURE 5.2: PEO Concentration against time for 100k MW $75 \pm 5\mu$L droplets

Figure 5.2 shows series of DSA images for various initial concentrations of $75 \pm 5 \mu L$ PEO 100k MW droplets over time. The top row shows the droplets at time $t = 0$; a point to notice here is that the contact angle increases with concentration. Moving down each column, the images show the same droplets evolving over time. Where the droplet profile deviates from standard 'pinned' drying, the backgrounds have been coloured grey, and follow the 4 stage drying process described above.

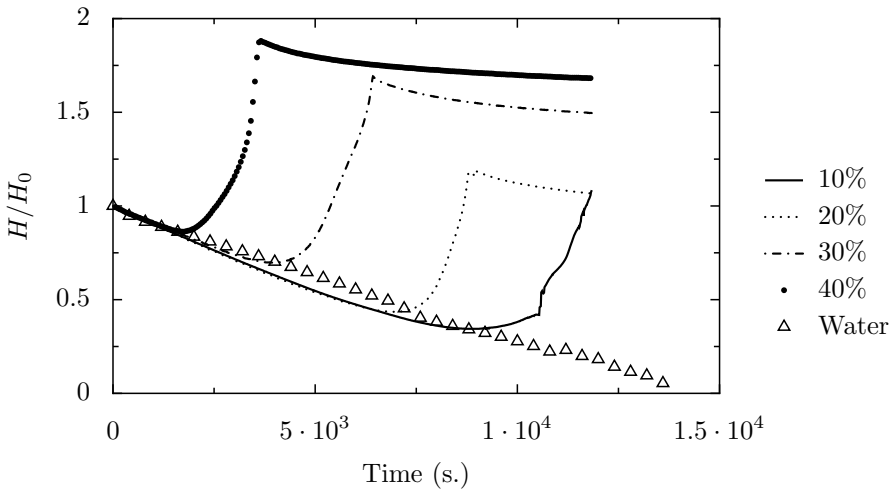

FIGURE 5.3: Evolution of droplet height over time for the droplets shown in Figure 5.2, with the height of an equal volume pure water droplet shown for comparison.

Figure 5.3 shows the normalised droplet height evolving over time for the same droplets as shown in Figure 5.2. It is interesting to note that the initial decays of the droplets with PEO are linear, and almost identical once the initial heights have been normalised, yet the height decay of the pure water droplet varies around the same gradient - this is likely due to the 'slip-stick' process [223].

FIGURE 5.4: Filmstrip showing the evolution of a $75 \pm 5\mu L$ 100k MW PEO 40% wt. initial concentration droplet during Stage 4 final drying. The shrinking of the constant surface area polymer skin due to evaporation causes the internal pressure to increase. In some cases this can lead to some liquid phase being expelled from the droplet summit, which is the weakest/thinnest part of the skin (as it dries last).

Figure 5.4 shows a late time 'spurting' effect for the $c_0 = 40\%$ droplet shown in the previous two Figures. As the deposit forms during stages 2 and 3, evaporative drying causes the base structure to shrink which can only add to the growth during stage 3, and also causes the glass coverslip to bend. During stage 4 when crystals have dried over the entire surface, this final-stage shrinking will increase the internal pressure which in some circumstances can lead to this bursting effect at the weakest point. Similar behaviour

can be seen in the $c_0 = 30\%$ droplet in Figures 5.26 and 5.2, however the bursting in Figure 5.26 usually occurs much later in Stage 4. We therefore know that the structures encapsulate a liquid phase at t_{max}, and that the structure shrinks during stages 3 and 4. This brings us onto the physical structure of the deposits.

Physical Properties of the Conical Deposits

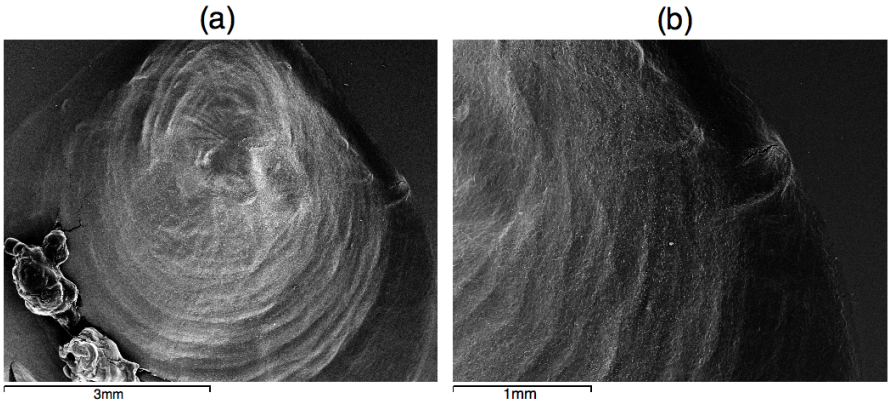

Figure 5.5: Low-magnification SEM image of 100k MW $c_0 = 30\%$ wt droplet deposit. The concentric rings show that formation of the thin film deposit (Stage 2) occurs in discrete steps.

Figure 5.5 **(a)** shows a low magnification SEM image of a $c_0 = 30\%$ droplet deposit. Solid PEO is a white powder (or white structure in this case), and therefore imaging surface details is difficult with optical components; the electron microscope is used here simply as a visualisation tool, rather than for any magnification or chemical analysis. The peak of the deposit is towards the top of the image where some lines are seen moving radially outwards. The prominent concentric rings evident in the lower half of the photo are predominantly in the thin-film deposit left during Stage 2. This shows that the film is created and/or deposited in discrete steps, rather than one continuous motion as one might infer from the DSA data. Figure 5.5 **(b)** shows a close-up of the side of the conical deposit on the same droplet. Here we see that the concentric rings continue throughout the thin film and the deposit structure.

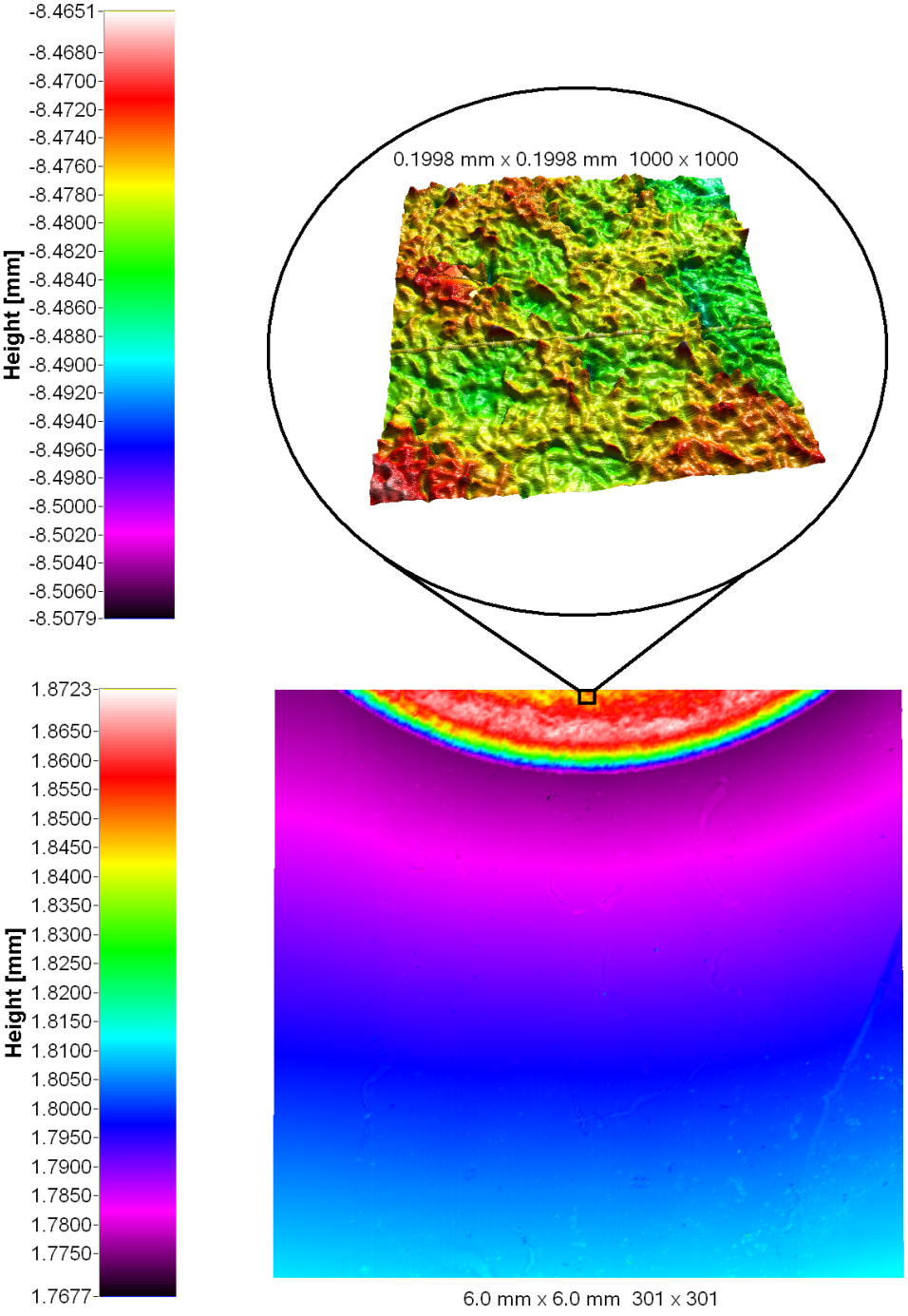

FIGURE 5.6: Surface profiler scans of a 100k 30% wt. droplet residue

Figure 5.6 shows a high- (upper image) and low-resolution (lower image) surface profile of a $c_0 = 30\%$ droplet residue taken on a Taicaan® interferometric profiler. The bottom image shows a 6mm × 6mm section (at 19μm resolution) of the thin film stage 2 residue and glass coverslip. The droplet residue is the circular section towards the top of the image, and the remaining ∼90% of the image shows the glass coverslip. This coverslip was imaged for two reasons; firstly to ensure that the profilometer gave reasonable results, and secondly to show the curvature of the coverslip observed for higher concentration droplets ($c_0 \gtrsim 20\%$). The onset of this curvature occurs during stages 2 and 3, and can be seen in the purple and blue bands around the middle of the lower image. The high-resolution (upper) image shows a 0.1998mm × 0.1998mm section from the lower image (magnified ∼100× at 199nm resolution) .

The fact that the evaporative drying can create a deposit which bends the coverslip shows that the PEO residue binds strongly to this substrate, yet the onset of the buckling during Stage 2 shows that it is not driven by the change in shape of the final deposit once the complete polymer 'skin' has formed. In fact, from the instant of deposition, the PEO crystals shrink in size which not only bends the coverslip, but also acts to squeeze the remaining liquid phase vertically upwards, enhancing, or possibly creating the growth mechanism.

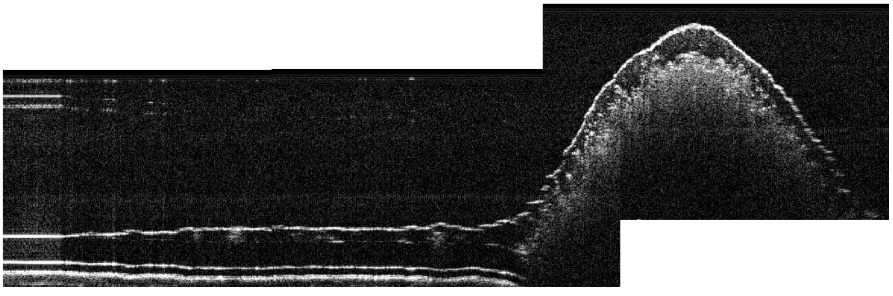

FIGURE 5.7: OCT images of a 100k 20% wt droplet residue.

Figure 5.7 shows an OCT tomograph of a $c_0 = 20\%$ droplet deposit (>72 hours after Stage 4), created by 'stitching' together multiple images. The solid white line on the far left shows the glass coverslip, and the white hazy area on the right-hand side indicates a change in refractive index inside the droplet. From this we see that the deposit forms a thin solid polymer skin, and that the inside of the deposit is hollow.

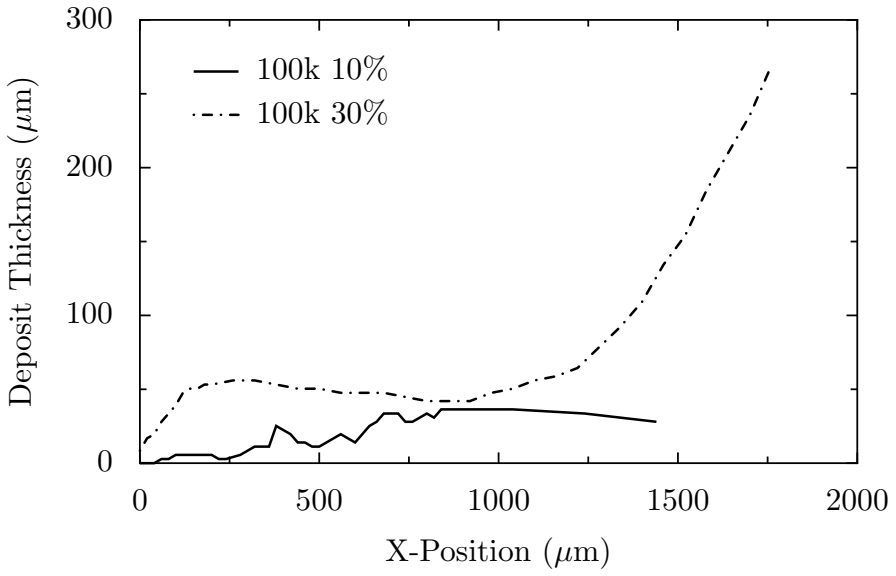

FIGURE 5.8: Deposit thickness measured from OCT images

Figure 5.8 shows the thickness of representative $c_0 = 10\%$ and 30% droplet deposits measured using OCT images as shown above. This shows that the Stage 2 deposition leaves a film $\sim 50\mu$m thick, however this can increase significantly inside the conical deposit.

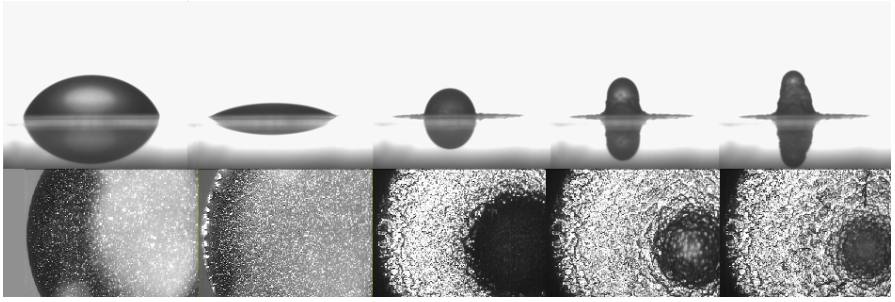

FIGURE 5.9: Filmstrip showing the droplet profile and view from underneath taken concurrently for a $c_0 = 10\%$ wt droplet. The images from underneath were taken using a Nikon TE-2000 Eclipse inverted telescope with a 2× objective lens.

Figure 5.9 shows the profile and view from underneath the droplet concurrently during evaporation. Here we confirm that the final deposit is indeed hollow, and that the deposition does start at the contact line and progress radially inwards.

This section has discussed physical properties of the conical structures; the images in Figure 5.9 from underneath the droplets show the four distinct stages mentioned throughout this chapter for a 100k $c_0 = 10\%$ droplet. Using videos from underneath droplets during multiple repeats of this experiment (100k MW PEO, $c_0 = 10\%$, $V_0 = 75\mu L$), the discussion will now move onto the hydrodynamic flow during evaporation.

Hydrodynamic Flow

Hydrodynamic Flow - Stage 1. During the pinned drying the PEO clusters are carried by internal currents; the clusters have been tracked using the ImageJ particle tracking plugin [218].

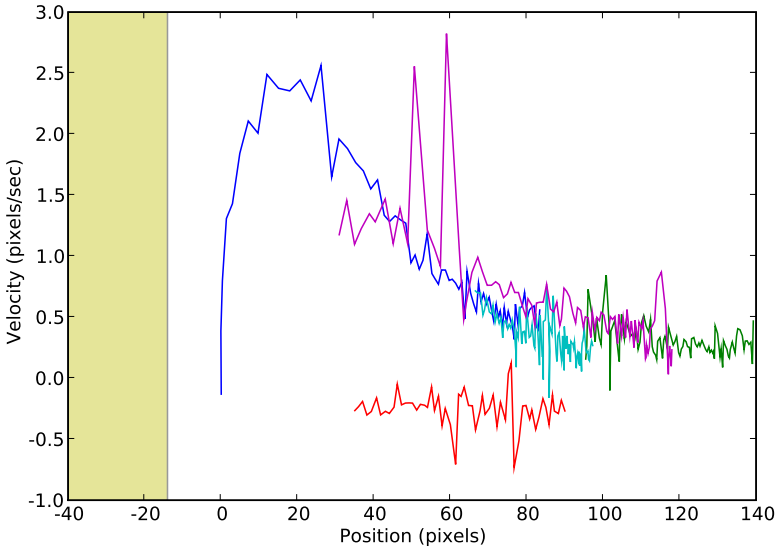

Figure 5.10: Particle velocities during Stage 1 pinned drying. The colours represent different particles which were tracked using ImageJ, and the velocity over a 3-frame average (0.1 s. averaging time) is shown against the position inside the droplet. The coloured region on the left represents the area outside the droplet.

Figure 5.10 shows the 3-frame average velocities of 5 particles near the contact line (shown by the yellow-green region). The velocities of these particles increase quadratically as they approach the contact region, but instead of depositing at the contact line, they 're-circulate', implying the existence of a current with similar flux in the direction away from the droplet edge. This re-circulation has been seen in various sessile droplet systems before [224, 225], however the similar fluxes in the counter-propagating currents shows that the evaporation dynamics are not as simple as the Deegan model in this case.

In order for material to be deposited at the contact line there must be a net flux radially outwards, therefore any inbound flow must exert a lower force on a given particle because some solvent is lost due to higher evaporation at the contact region. The similar inward and outward flow velocities of the particles therefore calls into question the applicability of the Deegan model during Stage 1. In order to confirm whether the concentration increased at the contact line, an MRI experiment was performed on a 100k $c_0 = 10\%$ droplet, in order to visualise the water concentration over time.

Figure 5.11 shows data from this MRI experiment; MRI hardware is typically highly sensitive to protons, and therefore water molecules are easily studied - the fact that our bodies are $\approx \frac{2}{3}$ water has therefore made MRI useful in many medical applications. In order to quantify the water concentration, a complex calibration must be undertaken, which was not performed here for the following reasons:

- The aim of this experiment was only to assert that the polymer concentration increases at the droplet edge.
- Local atmosphere inside the narrow MRI sample tube will have quickly saturated during evaporation, and therefore any quantitative results are not comparable with other droplet studies.

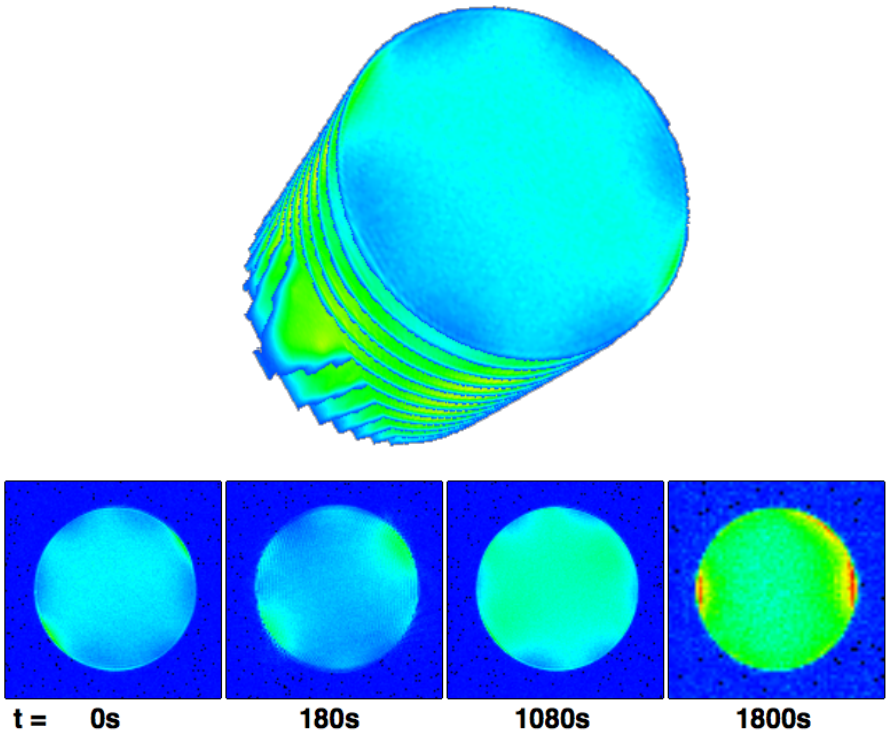

FIGURE 5.11: Images from an MRI experiment on a 100k PEO $c_0 = 10\%$ wt droplet; UPPER: 3-dimensional droplet section at time t = 0, showing the slices taken by the equipment, LOWER: 2-dimensional images of the same droplet slice ($\approx 40\mu$m above the coverslip) over time.

- The calibration is time-consuming and outside the scope of this experiment.

The upper image in Figure 5.11 indicates how this hardware performs the experiment - multiple 2d slices are stacked together to form a 3d volume. The lower image shows the top slice at four times during this experiment - the experimental volume is approximately 6mm $\times$ 6mm $\times$ 40μm, therefore in the 3d image the z-axes has been exaggerated. The gradual change of the 2d slices over time from blue to green to red shows a decrease in water concentration over time, as expected from evaporation. We can also see that the water concentration at the edge is slightly lower than in the centre at most times during evaporation. Unfortunately the closed nature of this MRI system made it impossible to determine the four stages discussed previously, however this data does show qualitatively

that the relative polymer concentration increases towards the droplet edge, as would be expected from material transport as per the Deegan model.

Hydrodynamic Flow - Stage 2. As the contact line recedes during Stage 2 ($t_{\min}$ onwards) the internal flow must change, as the recession will either be caused by circulation reversal 'pulling' solvent away from the edge, or the deposition 'squeezing' any remaining aqueous phase inwards.

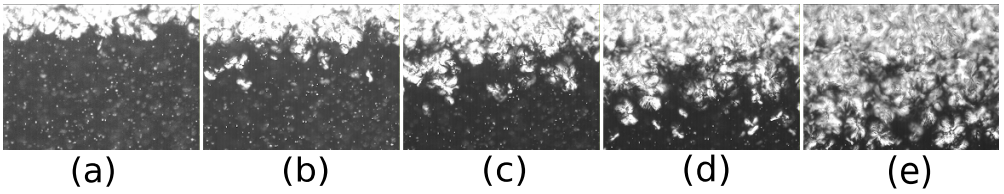

FIGURE 5.12: Images from underneath a 100k $c_0 = 10\%$ droplet at **(a)** $t = t_{\min}$, **(b)** $t = t_{\min}+$ 45s, **(c)** $t = t_{\min}+$ 90s, **(d)** $t = t_{\min}+$ 135s, **(e)** $t = t_{\min}+$ 180s. These images were taken using a Nikon TE-2000 Eclipse inverted telescope with a 10× objective lens.

Figure 5.12 shows the polymer deposit left behind the receding contact ring during Stage 2. The objective lens was placed at the droplet edge and these images show 45 second intervals from when deposition first takes place. From the raw video of the entire droplet evaporation, it is obvious that the re-circulatory flow present in Stage 1 ceases at $t_{\min}$, however the liquid phase must have some flow present in order to de-pin and increase the contact angle as shown in the transition from **(b)**→**(c)** in Figure 5.9. In order to investigate the origin of this de-pinning, particle tracking analyses have been performed.

Figure 5.13 shows the raw particle trajectories from an analysis of the video corresponding with Figure 5.12. Four tracks were chosen due to their consistency (no missing points or collisions) for further analysis, shown below, labelled $\alpha \rightarrow \delta$. An interesting point about Figure 5.13 is that there were very few tracks picked up in the top half of the video, and the trajectories which are present are short in comparison with the lower half. We know from Figure 5.12 that the deposition region moves vertically downwards, and these short trajectories in the upper half are a sign that the clusters are not moving with sufficient

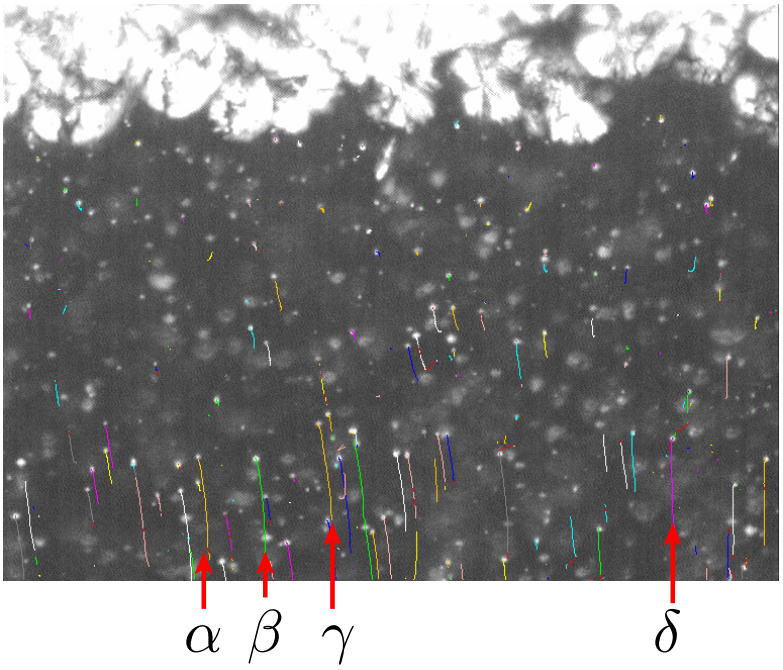

FIGURE 5.13: Image from Figure 5.12**(a)** with particle trajectories overlaid. α, β, γ and δ show the tracks which were chosen for further analysis.

velocity away from the contact line to escape the crystallisation region, presumably due to an increased viscosity near the contact line.

Figure 5.14 shows the 3-frame mean velocities for the four tracks labelled above as α, β, γ and δ during the first 80-90 seconds of Stage 3; using raw images such as that in Figure 3.6 (p.58), a pixel-to-metres calibration was performed to allow calculation of particle positions and velocities. In all four cases the velocity starts at $\sim$0.05-0.1μm s^{-1} and increases in a linear fashion to $\sim$0.6μm s^{-1} over the first 60 seconds before the velocity drops sharply. This rapid decline in the velocity occurs as the crystallisation region 'sweeps up' the particles, as can be seen by the spherulitic shapes present in the 5^{th} image of each particle track in Figure 5.14. This shows that the particles shown here were accelerating inwards radially at $\sim$0.01μm s^{-2} due to the contact line de-pinning, however this acceleration was not sufficient to 'out-run' the receding contact line. I presume that either these particles were caught in a turbulent boundary layer near the coverslip, or there exists a region of higher polymer concentration near the coverslip due

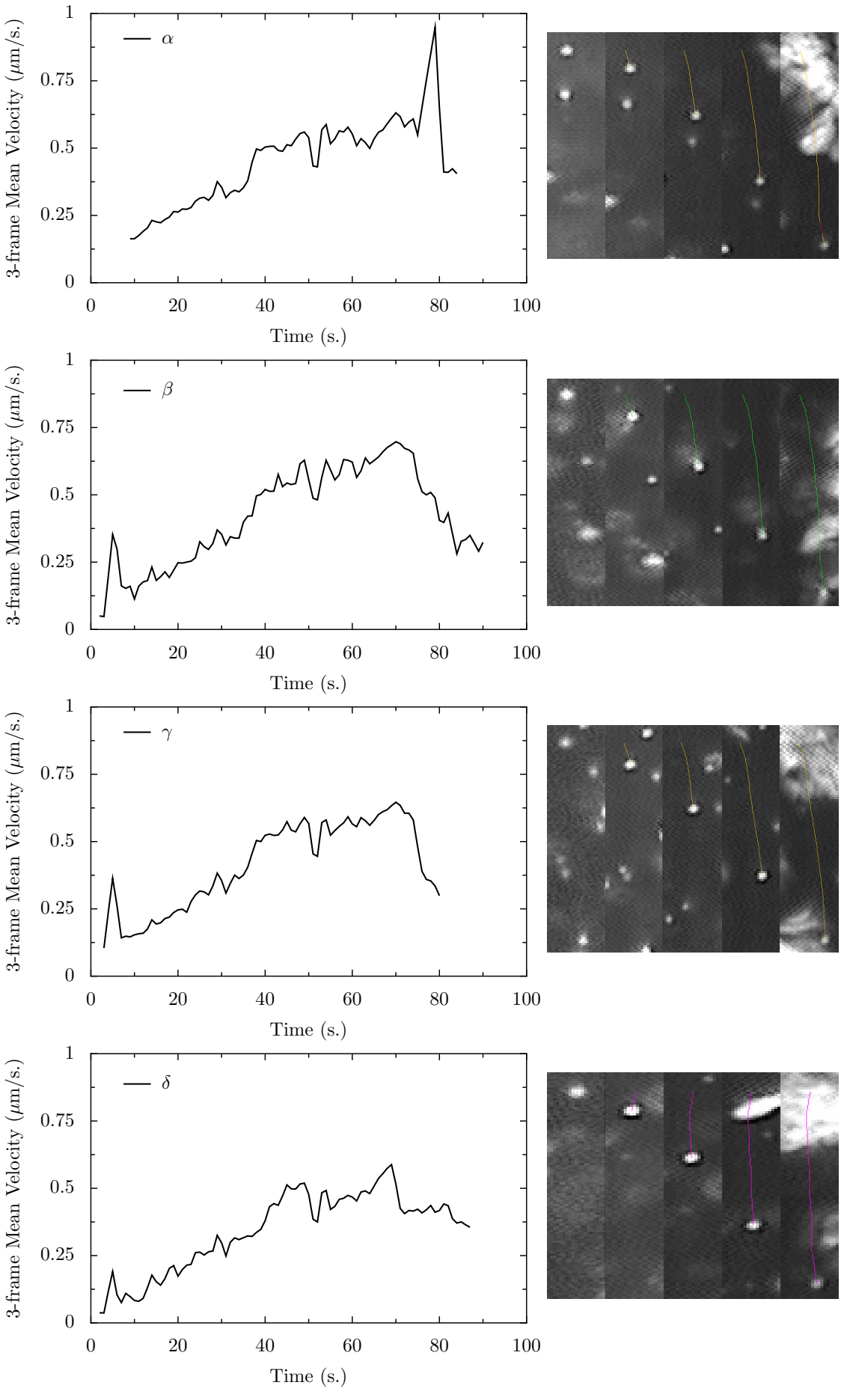

FIGURE 5.14: Graphs of particle tracks and images

to the outwards transport of material in a similar manner to the Deegan model.

Unfortunately for this particle tracking data, η varies with position in the sample (due to concentration gradients) as well as with time (due to evaporation), and therefore analysing the drag force on the particles using Stokes' Law (Equation 3.13) is inappropriate.

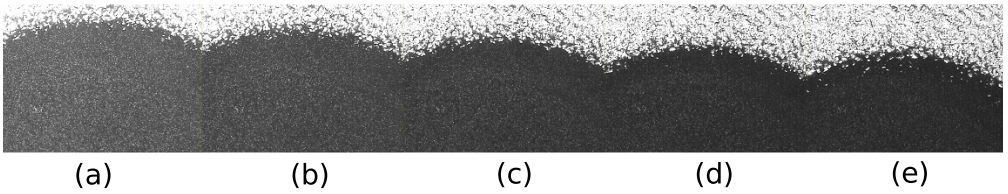

FIGURE 5.15: A series of images taken from underneath a 100k MW PEO, $c_0 = 10\%$ wt droplet during Stage 2. The decrease in transmission makes the clusters less well-defined, and given sufficient attenuation particle tracking becomes unfeasible.

Figure 5.15 shows the view from underneath a 100k $c_0 = 10\%$ droplet during the later parts of Stage 2 using a 2× objective lens. The loss of transmission as the liquid phase de-wets (ie. θ increases) makes particle tracking difficult, but qualitatively-speaking the same general trend of a slow, viscous flow towards the centre is evident, as seen in Figures 5.12 and 5.14. A potential solution for this would be to 'seed' the droplets with fluorescent particles, thus allowing particle tracking at later stages.

Hydrodynamic flow - Stage 3. Figure 5.16 shows the evolution of an evaporating 100k MW $c_0 = 10\%$ droplet during Stage 3. Images **(a)**→**(e)** are taken at 150s intervals starting when the PEO crystals are no longer being deposited on the substrate. This series displays many interesting features; **a1** shows the faint ring that appears around the clusters, **b1** shows the increase in transmission throughout the droplet during this growth phase, and **e1** shows the increase in clarity of the conical deposit at long times.

a1 shows the surprising behaviour of a circular (possibly spherical) artefact which originates from the receding contact line. This artefact then rises as the droplet height

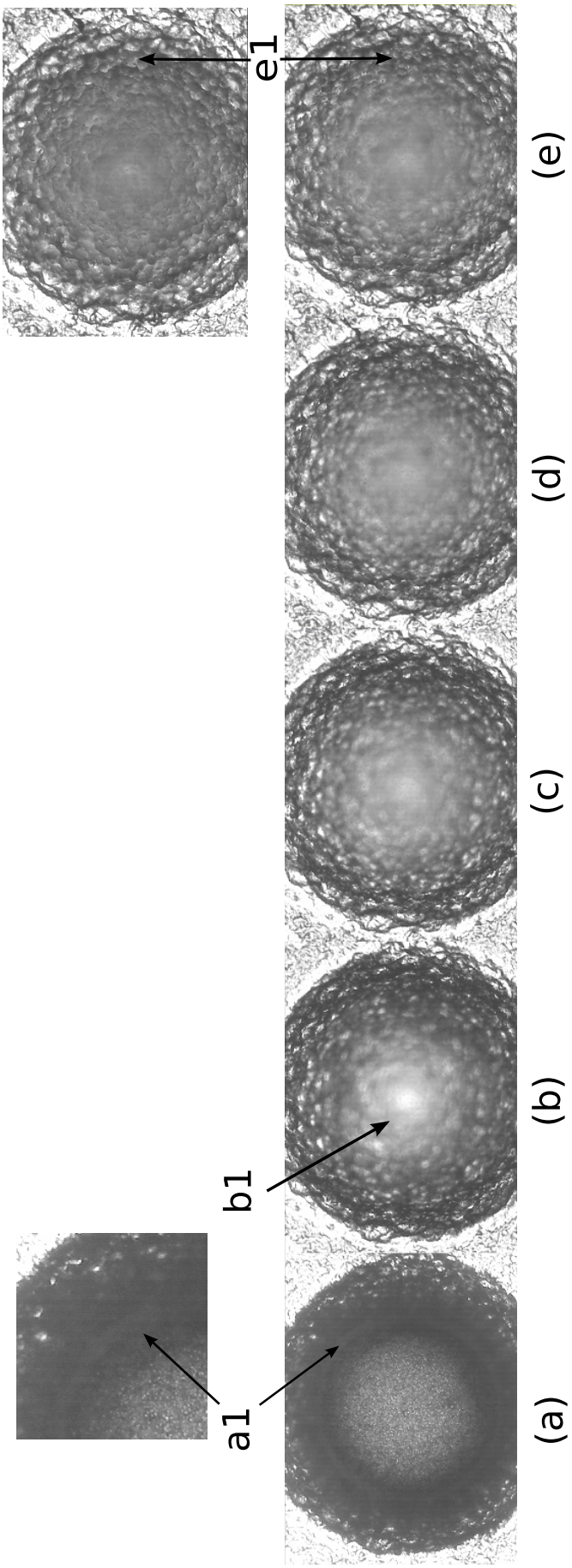

FIGURE 5.16: Images showing the droplet evolution during Stage 3.

increases, taking with it the PEO clusters and leaving behind a clear aqueous phase. This phenomena acts to filter the remaining liquid phase during the Stage 3 growth, evident from the lack of clusters in **(b)**→**(e)**.

The increase in transmission from **(a)**→**(b)** is difficult to quantify due to natural variation between experiments, however the peak in transmission coincides with $t_{\max}$, implying that the decay in transmission occurs due to crystallisation closing over the top of the deposit.

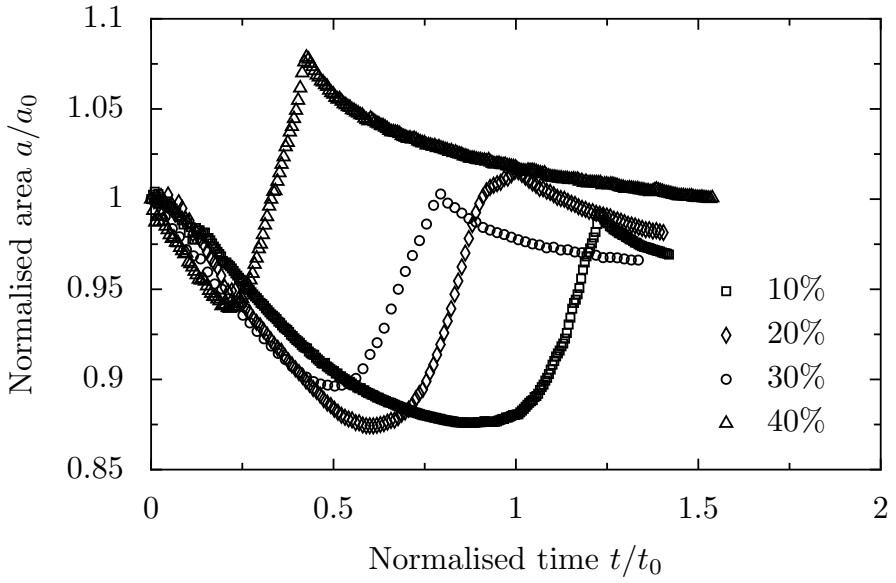

FIGURE 5.17: Normalised area $\frac{a}{a_0}$ against normalised time $\frac{t}{t_0}$ for 100k PEO droplets c_0 = 10-40% wt

Figure 5.17 shows the normalised area $\frac{a}{a_0}$ for four 100k PEO droplets c_0 = 10-40%, calculated by integrating around the droplet profile using the code in Appendix E. This confirms that the growth phenomenon in these droplets is different from the Pauchard model, as a buckling skin model requires a permeable, but *constant surface area* skin.

Figure 5.18 shows the normalised $t_{\min}$ and Δt values for some 100k PEO droplets plotted against c_0, and shows that the concentration at $t_{\min}$ can be considered to be c_{sat} for all droplets [226]. It is also interesting to note that Δt is approximately constant, regardless

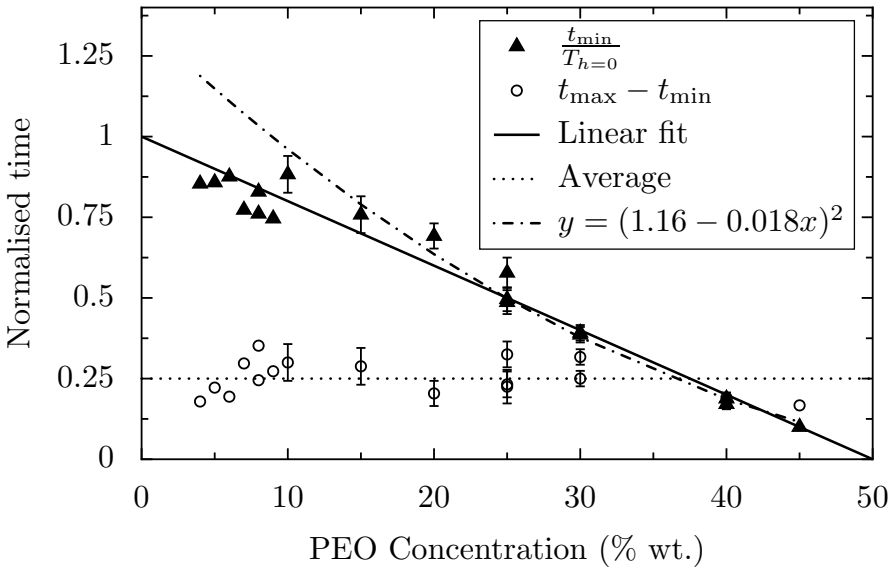

FIGURE 5.18: Normalised values of t_{min} and Δt (ie. $t_{max} - t_{min}$). The error bars are due to uncertainties in the exact time of the extrema and in the extrapolation to determine t_0. The straight line fit through the t_{min} data has y-intercept fixed at 1 and gives a c_0-intercept of 50% wt (Equation 5.3).

of c_0, in contrast to the 8k droplets shown previously, where Δt showed a maxima with increasing c_0.

Physical Interpretation and Implications

Figures 5.2 and 5.4 show 'spurts' from the top of the conical deposits where $c_0 \gtrsim 30\%$. As mentioned previously, this shows that the internal phase remains liquid after the structure has completely formed, however the shrinking that causes this behaviour cannot be from evaporative loss of this internally-contained fluid. If the loss of volume was from the encapsulated liquid, then the shrinking would be a reaction to maintain equilibrium pressure. The fact that the shrinking raises internal pressure sufficiently to induce late time spurts shows that the volume of trapped liquid must decrease more slowly than the solid deposit volume.

This raises the question as to what causes the solid deposit to lose volume so quickly. The spherulites that form these structures contain hydrogen-bound water molecules [227, 228], which will be lost over time as the spherulites become a pure PEO deposit. We know from

§2.4 that hydrated PEO can form helices with a corresponding water helix, which acts to shield the CH_2 groups from the solvent. From the MD simulation shown in Figure 2.16 (from [2]) we see that this hydration shield adds considerable volume to each effective cylinder created by the PEO helix. I therefore hypothesise that the initial spherulitic structure is a swollen structure which loses volume as the water shield evaporates. In contrast to the flexible, permeable skins in the Pauchard model [203], as this spherulite-to-solid transition occurs the overall deposit structure must maintain a lower level of permeability in order for the internal pressure to rise. Perhaps the evaporation of solvent occurs from the top layers of the cone first, causing the initial shrinking and increased pressure, and then diffusive motion of the remaining solvent through the structure causes the final drying.

Physical Interpretation - Four-stage deposition model.

In §5.3 the four observed stages were introduced to clarify the terminology; these Stages will now be described more thoroughly in terms of the PEO behaviour, followed by a discussion of specific predictions.

Stage 1. During this pinned stage the droplet volume, h and θ decrease, however θ typically remains above the receding contact angle, which was measured to be $\approx 5°$ in separate experiments. $\theta < 90° \; \forall \; c_0$ during this stage, therefore we can be confident that evaporation is greatest at the contact line and is sustained by solvent within the droplet flowing radially outwards as per the Deegan model [204]. This is confirmed experimentally with the particle tracking of clusters shown in Figures 5.10. This outward solvent flow must also carry dissolved polymers to the periphery in order for the concentration there to increase, which is where the similarities with the Deegan model end; both Deegan and Popov [229] assume that the build up of material at the contact ring does not inhibit

solvent flow. When the droplet concentration reaches c_{sat}, semi-crystalline spherulites precipitate, inside of which the water molecules are bound through hydrogen-bonding to the oxygens in the PEO backbone, and therefore are not able to participate in the outward flow. As a result, the increased contact ring evaporation is unsustainable as the solvent cannot be replenished, so the contact line de-pins; at this time the droplet has reached its minimum height h_{min} with concentration c_{sat}.

Stage 2. During Stage 2 the contact line of the remaining liquid retracts, but the specific reason for this retraction is unclear. It could be driven by the actual contact angle being less than the equilibrium contact angle θ_{e} at c_{sat} (we know from Figure 5.2 that θ_0 varies with c for some droplets). However, this raises the question of how θ can decrease past θ_{e} during Stage 1 (whilst c is increasing). This retraction could equally be driven by Marangoni convection; the concentration gradient across the sample at t_{min} could easily form a surface tension gradient across the droplet. It has been shown that Marangoni effects can initiate a re-circulative hydrodynamic flow inside sessile droplets [205, 206, 225], which would explain how the solvent flow towards the contact ring stops causing the de-pinning. Unfortunately we have to rule out the Marangoni effect as the particle tracking experiments show that *all* flow inside the liquid phase stops at t_{min}, presumably due to the viscosity at c_{sat}.

Another possibility is that the hydrophobicity of the PEO spherulites, which form at the contact ring, 'squeezes' the remaining liquid phase into a ball. I hypothesise that this is the method by which the Stage 2 de-pinning occurs, because the thin film deposit left behind the receding contact line actually forms in a layer above the contact ring as it is deposited as the liquid retreats from beneath it, as shown in Figure 5.19.

The final possibility for the de-pinning in Stage 2 comes from the increasing surface

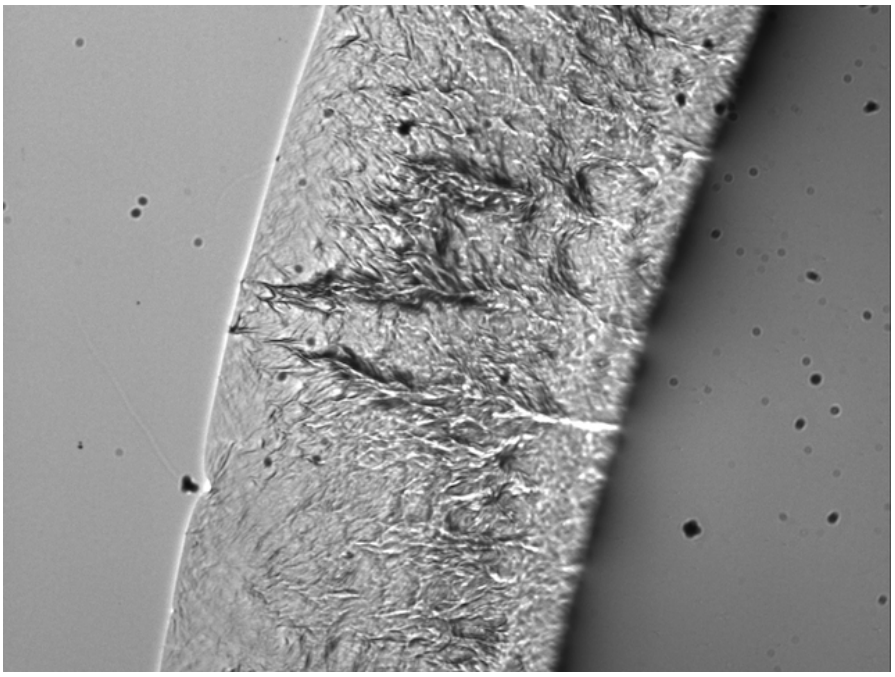

FIGURE 5.19: Image of a filtered droplet during Stage 2 de-pinning. Here it is interesting to note that the thin deposit in contact with the coverslip is in focus, yet the crystallisation region is out of focus. This shows that the spherulitic film forms above the coverslip and either drops down as the aqueous phase retreats, or 'squeezes' the aqueous phase inwards. Causation is difficult to prove in this case.

area A during this stage; an increase in A will have a corresponding increase in the surface energy. In fact, the hydrophilic/hydrophobic state of PEO means that it can be considered a surfactant as it will try to aggregate at interfaces, which in turn acts to lower the surface tension. Measurements to quantify the surface tension lowering properties of PEO by Cao and Kim [230] showed a maximal reduction for polymers with MW = 80k; which is close to the MW of the droplets which exhibit Stage 2 behaviour.

The receding contact line leaves behind a thin layer of dry polymer, similar to the gelled foot reported in previous studies of dense particle suspensions [207], and is seen to finish receding when $\theta \approx 80°$.

Stage 3. Once θ has reached $\approx 80°$, the spherulites that form at the contact ring (see Figure 5.19) will be placed on top of the previous deposits because θ is nearly perpendicular to the substrate. Being hydrophobic, they will repel the remaining liquid phase; this

process continues and the liquid can completely lose contact with the substrate, leaving behind a solid, hollow structure, as shown in Figure 5.20 below.

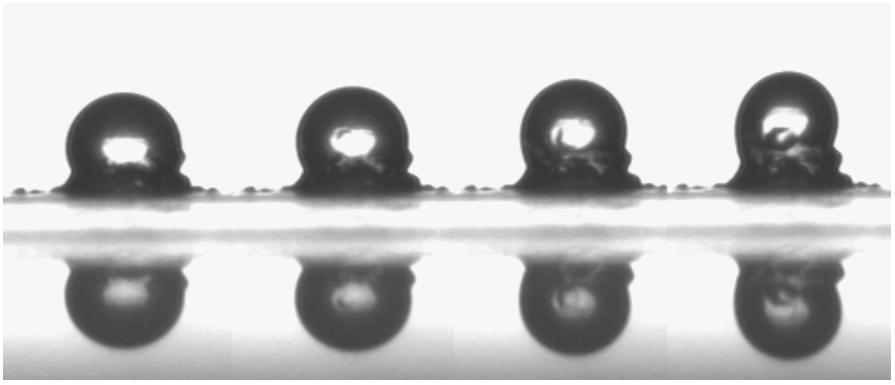

FIGURE 5.20: Filmstrip showing a liquid ball rising up on top of the deposit during the evaporation of a $75 \pm 5\mu L$ 100k MW 10% PEO droplet. The frames were taken 20s apart.

We know the structures are hollow from the images taken from underneath, the OCT tomographs and from carefully cutting them open once dried. Stage 3 ends when the spherulites have completely encapsulated the deposit, halting any further growth, at time $t_{\max}$.

The filtering effect seen in Figure 5.16 shows some similarities to the Pauchard skin model. In order for this filtering phenomena to occur, there must be a permeable, flexible membrane formed during Stage 2/3 which removes all objects as effectively as a 0.45μm filter (see Figure 2.17 on p.38).

We know from Figure 5.14 that hydrodynamic flow close to the substrate is slower than the Stage 2 de-wetting transition (ie. the clusters get caught by the deposition region), which has previously been attributed to inhibition of boundary-layer flow. I hypothesise that there may be another effect, caused by the flow during Stage 1; the internal flow according to the Deegan model states that material is transported to the contact region, however Deegan's model did not account for the material build-up inhibiting solvent flow. I suggest that rather than *all* the polymers being transported to the contact

region, there is a gradient of deposition occurring whereby a gel phase forms across the substrate, which acts to slow the clusters in an identical manner to boundary-layer flow discussed previously. If this occurs, then as $\theta \to 90°$ during Stage 2, this gel phase could form a complete encapsulation of the liquid phase (assuming a similar gel-like skin develops on the surface) which is pulled upwards by further deposition at the contact line. Thus Stage 3 may involve the formation of a permeable skin, as per the Pauchard model. That this skin is of the correct size to filter out PEO clusters is a fortuitous coincidence.

Stage 4. During Stage 4, the solid structure formed during Stage 3 shrinks slowly by up to 10% in height as the remaining water within the spherulites evaporates. From $t_{\max}$ onwards the remaining enclosed liquid phase must either evaporate slowly through the porous spherulite skin, causing a buckling along the lines of the Pauchard model [203], or will be forced out if the pressure is sufficiently high given the strength of the skin. Stage 4 ends when the droplet is completely dry. During this stage the forces generated by the shrinking structure stuck to the coverslip can be strong enough to cause the glass coverslip to bend upwards, in a similar process to Francis *et al* [231].

Implications - Predictions of the four-stage deposition model.

The model presented above lends itself to various experimental verifications [226], details of which are discussed below.

Prediction - Value at minimum height. This model allows for the prediction of several parameters, such as de-pinning time $t_{\min}$, bootstrap time $t_{\max}$, $h_{\max}$ and concentration. First of all, since the de-pinning signifying the start of Stage 2 occurs when the first deposition takes place, the model predicts that the minimum height should occur

at the same concentration for all c_0, labelled previously as the saturation concentration c_{sat}.

The linear fit through the normalised t_{min} data shown in Figure 5.18 gives a c_{sat} value (x-intercept) of 50%, identical to the literature value [81].

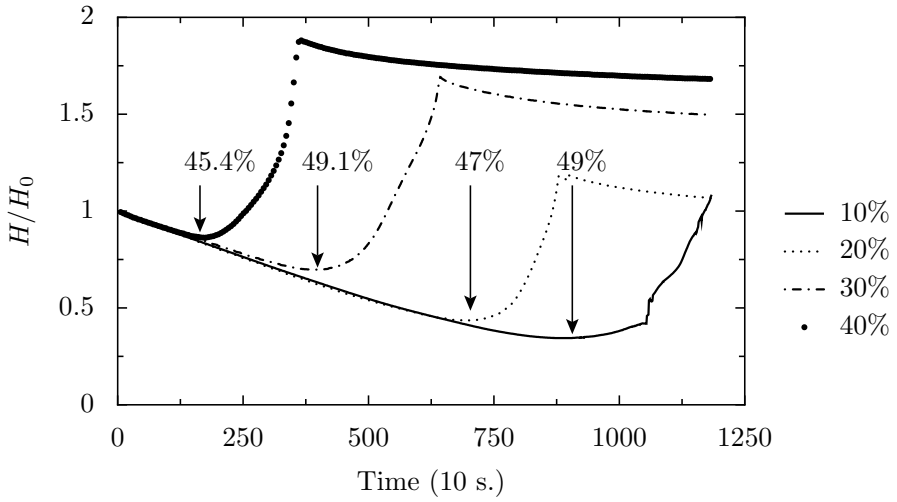

FIGURE 5.21: Normalised droplet height over time with the calculated droplet concentrations at t_{min} labelled.

Figure 5.21 shows the same data as Figure 5.3 with the concentration at t_{min} labelled, calculated from the volume difference $\Delta v = v_0 - v_{\text{min}}$. Therefore the measured c_{sat} at t_{min} (from Δv), the implied c_{sat} (from a fit to t_{min}) and the literature all corroborate the first prediction.

PREDICTION - VALUE AT MAXIMUM HEIGHT. The model also predicts that the concentration at the maximum height c_{max} should be independent of c_0. Since the Stage 3 growth is highly asymmetric, and the profile at h_{max} does not fit any accepted model, an accurate measurement of c_{max} is difficult. The concept of c_{max} is also slightly ambiguous as the droplet has started precipitating and is therefore in 2 phases. Here I define c_{max} as the theoretical concentration if all of the polymer (dissolved and deposited) were in solution with the remaining solvent (the water held in the conical structure).

Figure 5.18 (p.178) shows a linear regression fit to the $t_{\min}$ data; by performing the same fit to the $t_{\max}$ data we can make a prediction for this concept of $c_{\max}$, from which we obtain $c_{\max} \approx 70\%$.

PREDICTION - NORMALISED $t_{\min}$ VALUES. Assuming that volume loss continues at its initial rate, which appears to be valid from Figure 5.1, the normalised $t_{\min}$ values can be calculated by integrating Equation 5.1 to obtain $V(t)$, and combining with material conservation:

$$c_{\min} = \frac{c_0 V_0}{V_{\min}} \tag{5.2}$$

to give

$$\frac{t_{\min}}{t_0} = 1 - \frac{c_0}{c_{\min}}. \tag{5.3}$$

Figure 5.18 shows that this equation fits the $t_{\min}$ data well, and re-inforces the first prediction that $c_{\min} = c_{\text{sat}}$. A similar analysis for $t_{\max}$ is inappropriate however because the assumption about volume loss is no longer valid, as shown in Figure 5.1.

PREDICTION - $h_{\min}(c_0)$. With the single assumption that the droplet always takes the shape of a spherical cap during Stage 1, its volume V can be written as

$$V = \frac{1}{6}\pi r^3 \left[\zeta^3 + 3\zeta\right] \tag{5.4}$$

where $r = \frac{d}{2}$ is the base radius and the ratio

$$\zeta = \frac{h}{r} = \frac{\tan\theta}{2}. \tag{5.5}$$

Using Equations 5.2 and 5.5 we can formulate $\zeta_{\min}$ in terms of known parameters;

$$\zeta_{\min}^3 + 3\zeta_{\min} = \frac{c_0}{c_{\text{sat}}}\left(\zeta_0^3 + 3\zeta_0\right) = 2D \tag{5.6}$$

where D is constant and the r-terms cancel due to the pinned contact line during Stage 1. The solution to this depressed cubic is shown in Appendix F; ignoring negative square roots and normalising by ζ_0 we obtain an analytical expression for $h_{\min}(c_0)$:

$$\begin{aligned} \frac{h_{\min}}{h_0} &= \frac{\zeta_{\min}}{\zeta_0} \\ &= \frac{1}{\zeta_0}\left[\frac{1}{t} - t\right] \end{aligned} \tag{5.7}$$

where $t = \sqrt[3]{-D + \sqrt{D^2+1}}$.

Taking $\theta_0 = 70°$ and $c_{\text{sat}} = 50\%$ we obtain the dashed line in Figure 5.22 (p.187), showing good agreement with experimental results.

Prediction - Deposit Growth Boundary. Here an argument is made to predict whether the droplets undergo Stages 2 and 3. Not all droplets form conical structures; if the receding contact angle θ_{r}, measured to be around 5° for $c_0 = 15\%$, is reached before c_{sat} then the droplet will de-pin without depositing a polymer film. In this case the final residue is a thin flat disk around the centre of the original droplet footprint. A critical

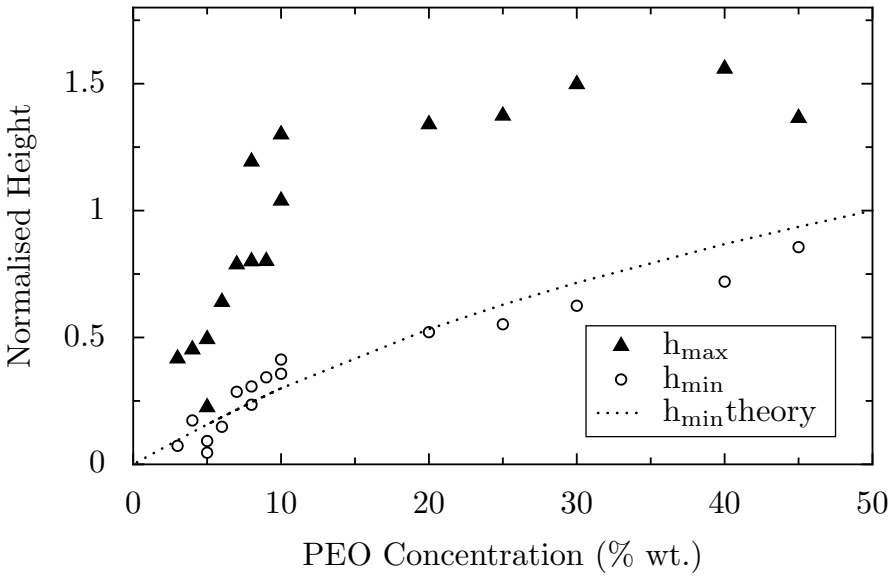

FIGURE 5.22: Normalised $h_{\min}$ and $h_{\max}$ values for a range of initial concentration values c_0. The $h_{\min}$ theory line $(\cdots)$ is a prediction for $h_{\min}$ using Equation 5.7 where $c_{\text{sat}} = 50\%$ wt.

concentration c_{crit} can be defined, below which no growth phase is seen, using Equation 5.5 to write θ in terms of ζ :

$$c_{\text{crit}} = c_{\text{sat}} \left(\frac{\zeta_{\text{r}}^3 + 3\zeta}{\zeta_0^3 + 3\zeta} \right) \tag{5.8}$$

where $\zeta_{\text{r}} = \tan \theta_{\text{r}}/2$. The initial contact angle θ_0 of a droplet can be artificially lowered by allowing the droplet to equilibrate (and 'pin' itself), and then using a pipette to remove a known volume. On performing this, θ will decrease but d will remain constant.

Where $c_0 < c_{\text{crit}}$ the deposit is a thin film/disk and conversely where $c_0 > c_{\text{crit}}$ the deposit is conical after undergoing the four stage growth phenomena described previously, as indicated in Figure 5.23. This graph shows the results for multiple experiments both with and without artificial θ reduction. The solid line shows Equation 5.8 using the previously found values of $c_{\text{sat}} = 50\%$ and $\theta_{\text{r}} = 3°$, which shows good agreement with experimental data.

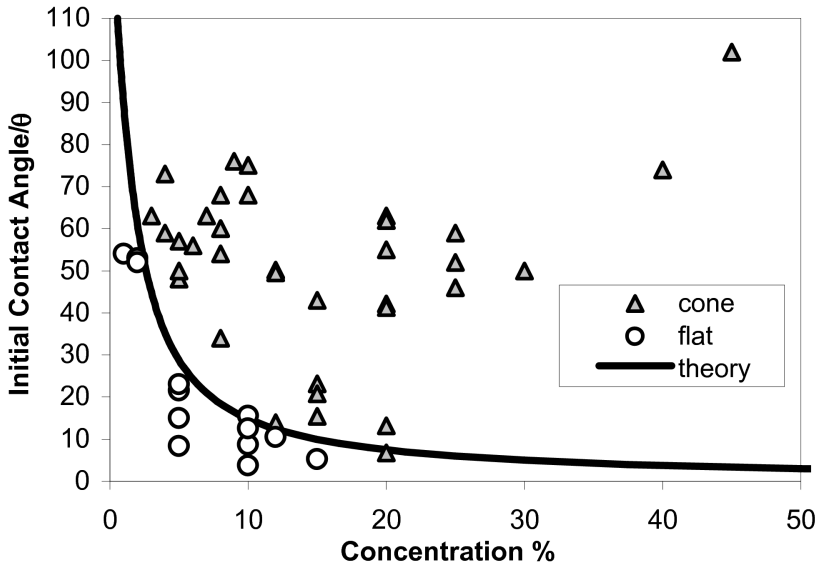

FIGURE 5.23: 'Phase diagram' showing whether the final deposit was a flat disk or conical structure for a range of initial concentrations c_0 and initial contact angles θ_0. The solid line shows the theoretical separation of the two behaviours (Equation 5.8).

5.3.2 Results from 20,000 MW PEO

Figure 5.24 shows the evolution of 20k MW PEO droplets at 10-40% wt over time; the grey areas signify times when the deposition and growth phenomena are apparent - labelled Sections 2 and 3, discussed below.

Figure 5.25 shows a phenomenon seen occasionally in high concentration ($\gtrsim$ 50% wt. PEO) 20k MW droplets; the droplet can form a solid 'cap' as well as a solid deposit around the contact ring, whilst maintaining a liquid phase in the rest of the droplet.

PHYSICAL INTERPRETATION AND IMPLICATIONS

With regards to the simultaneous solidification at the contact ring and the cap shown in Figure 5.25; deposition at the contact line is fully described by the Deegan model [204], however both Deegan and Popov [229] assume that material build-up does not inhibit solvent flow. In fact this assumption is valid in the case of coffee-stains as the deposited colloidal particles are limited to a small band around the periphery. In the systems presented in this section, however, this assumption is clearly invalid as evaporation occurs

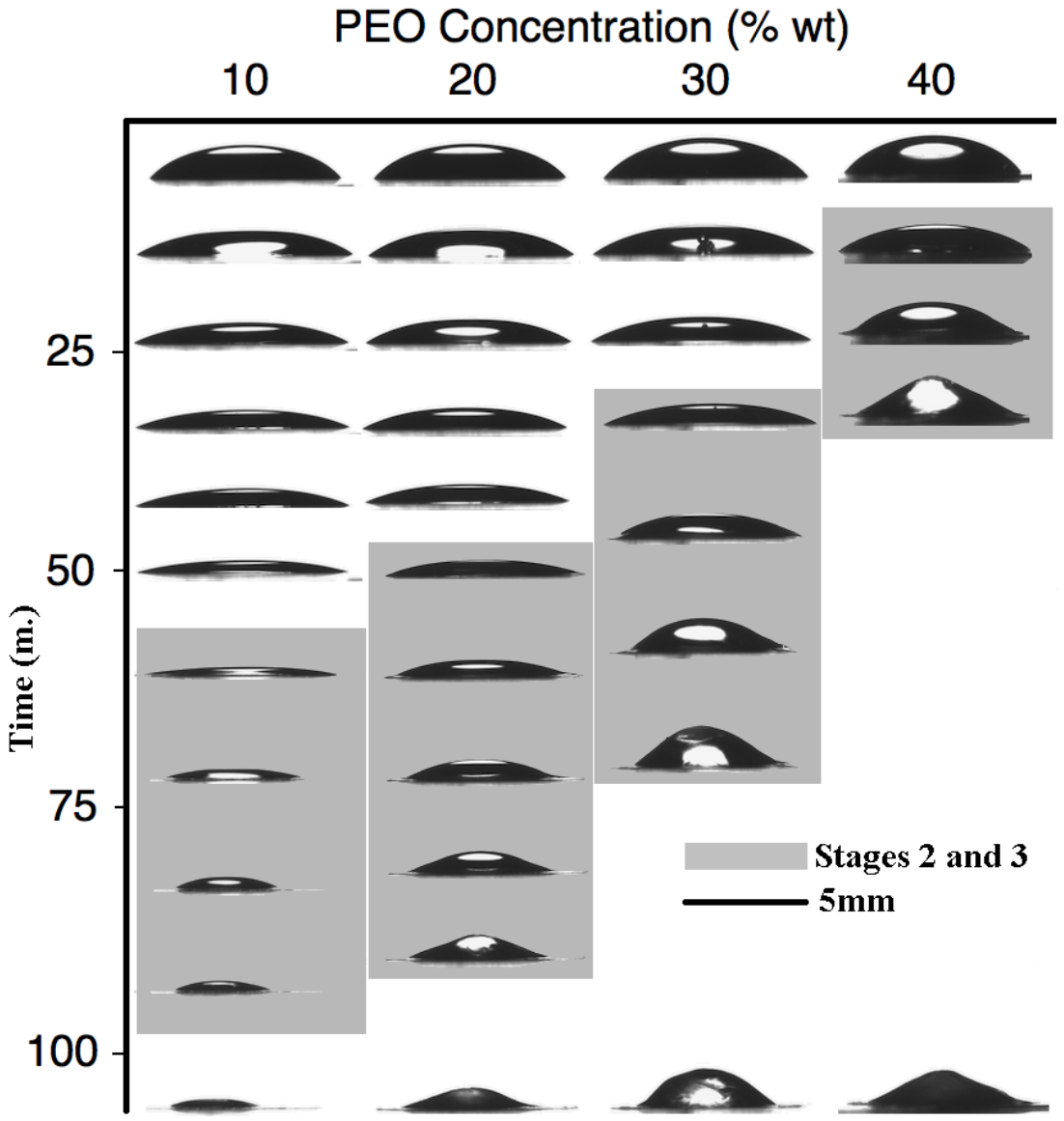

FIGURE 5.24: An image chart showing the profiles of various concentration droplets over time.

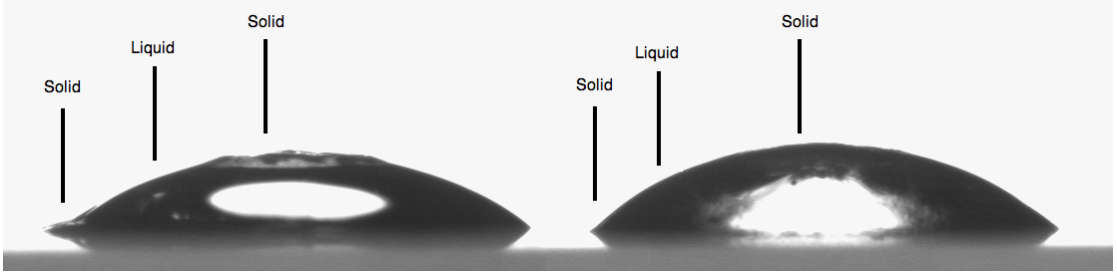

FIGURE 5.25: DSA images from different experiments showing the solid 'cap' which can form during the evaporation of high concentration ($\gtrsim$50% wt) 20k PEO droplets. Both of these droplets had an initial volume of 75 $\pm 5\mu$L.

whilst the contact line recedes, leaving a thin-film deposit. In this case, the build-up of polymer material at the contact ring does not allow the solvent lost through evaporation to be replenished, and therefore undergoes a glass/gel to solid phase transition before deposition[2]. As discussed in §2.4.1, PEO/PEG which is not fully dissolved can be hydrophobic, therefore a build up in gel or glass phase around the contact ring could easily prevent solvent flow due to its hydrophobic nature. A second solidification region on the droplet summit as shown is an extension to the PEO drying mechanism discussed by myself [226]. To explain this phenomenon, one can resurrect the Deegan model [204] which describes the radially outward convection of water inside a sessile drop due to enhanced evaporation at the contact ring. If this flow should occur in a high-concentration, viscous system, the replenishment of solvent at the summit due to concentration gradient-driven diffusion (slow) or hydrodynamic re-circulation (fast) may be less than the rate of solvent transport radially outwards in accordance with the Deegan model. This could lead to deposition at the receding contact line in conjunction with phase transitions in the summit region as shown in Figure 5.25. This hypothesis is difficult to prove using particle tracking as the droplet must necessarily be viscous enough to be close to crystallisation, however a sensitive MRI or OCT machine may be able to measure solvent flow in these conditions.

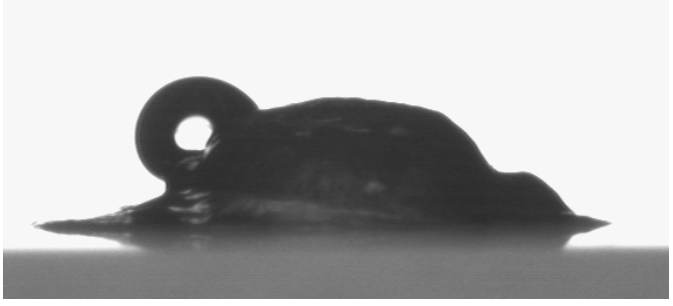

FIGURE 5.26: An representative screenshot from a 60% wt. 20k MW PEO droplet showing the 'high-pressure bursting' effect which can occur in droplets which have solidification regions at the base and summit.

[2]Although this shows similarities to the buckling skin model, a precursor film was only found in higher concentration droplets ($c_0 \gtrsim 20\%$ wt.).

The implications of this are that the droplet growth will be inhibited as the remaining liquid cannot be supported by the contact ring deposit. Solidification from the top and base of the same droplet also implies that in comparison to the lower concentration droplets ($\leq$40% PEO) the remaining liquid phase will not only be completely contained earlier in the evaporation process, but will be under greater pressure when the deposits go through the final shrinking phase, discussed above. This increased pressure could explain the occasional 'burst droplet' seen during evaporation, as shown in Figure 5.26.

Finally, this bursting can only occur in these systems as a result of a constant surface area, yet permeable, skin attempting to lose volume faster than the equivalent volume of solvent can evaporate. If the skin volume loss is driven by solvent evaporation, then internal pressure would be at equilibrium, which does not allow for the bursting shown above. Thus the fluids studied here show aspects of both the Deegan model (deposition at contact ring) as well as the Pauchard and Allain model (buckling polymer skin), yet neither fully describes these results. This is not a trivial problem to solve theoretically as a complete model must account for the high-viscosity contact ring inhibiting solvent flow towards the evaporation region, and must also account for the permeability of the same polymer skin which drives the buckling.

5.3.3 Results from 8,000 MW PEG

Figure 5.27 shows PEG 8k c_0 = 30-60% wt droplets evolving over time. Each column shows images of a single droplet evolving over time, with the y-position of the image representing the time t since deposition. The grey areas represent regions of time when the droplet height was increasing - Stages 2 and 3.

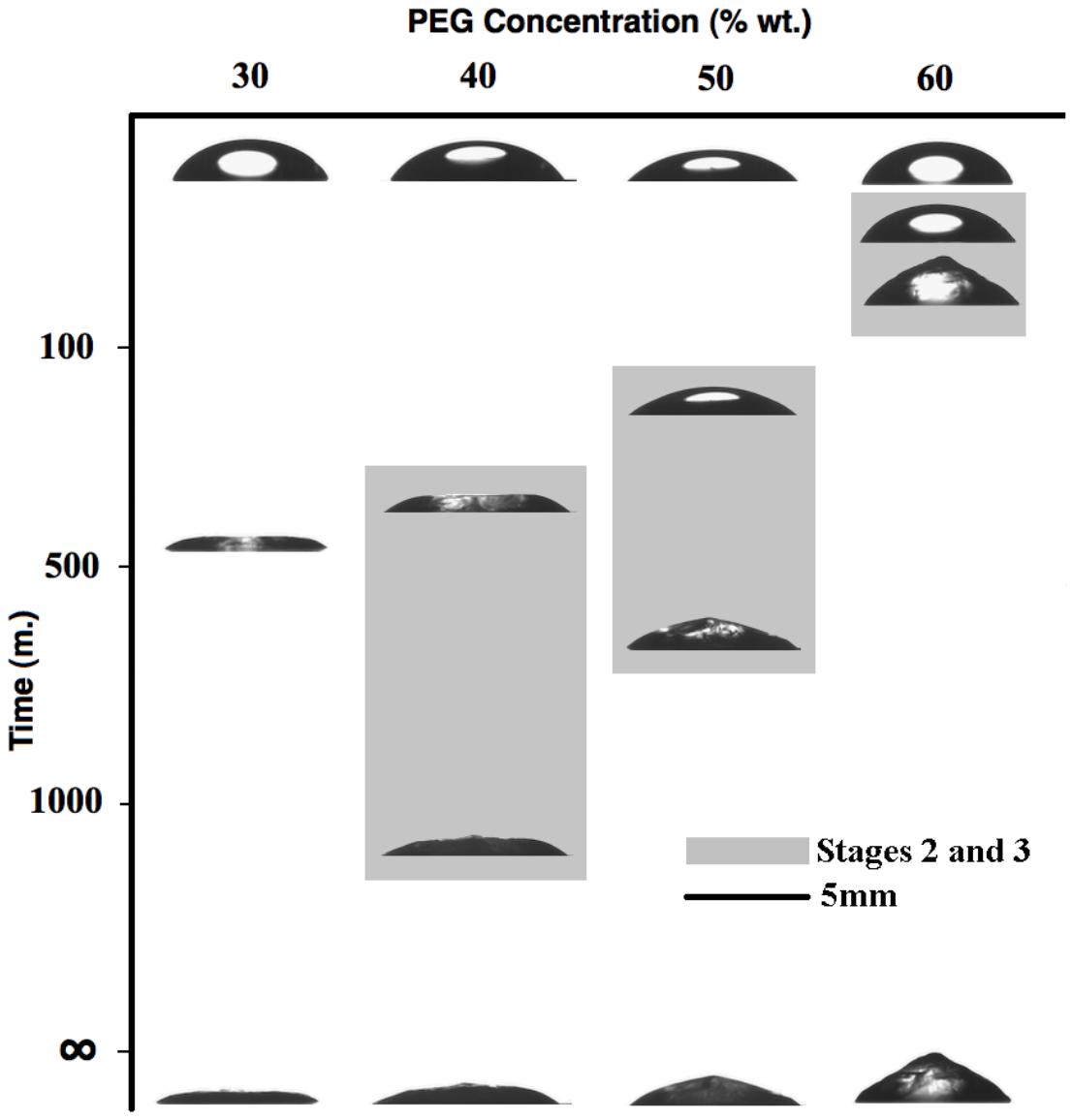

FIGURE 5.27: An image chart showing the profiles of 30-60% wt c_0 droplets evolving over time in ambient conditions. All images were taken on the Krüss DSA system discussed in §5.2.1.

At $c_0 = 30\%$ wt. this system shows standard droplet drying behaviour with an initial spherical cap gradually losing solvent through evaporation leaving behind a flat polymer film. The polymer concentration is sufficient to keep the contact line pinned, and therefore the base diameter remains constant throughout, except for an initial 'equilibration' period at the start. For $c_0 \gtrsim 40\%$, the droplet height shows a minima, presumably as a certain concentration/contact angle is reached, after which the growth continues until only a solid deposit surface remains. After this growth phenomena, the droplet height

decreases slightly over time as the final trapped solvent is lost.

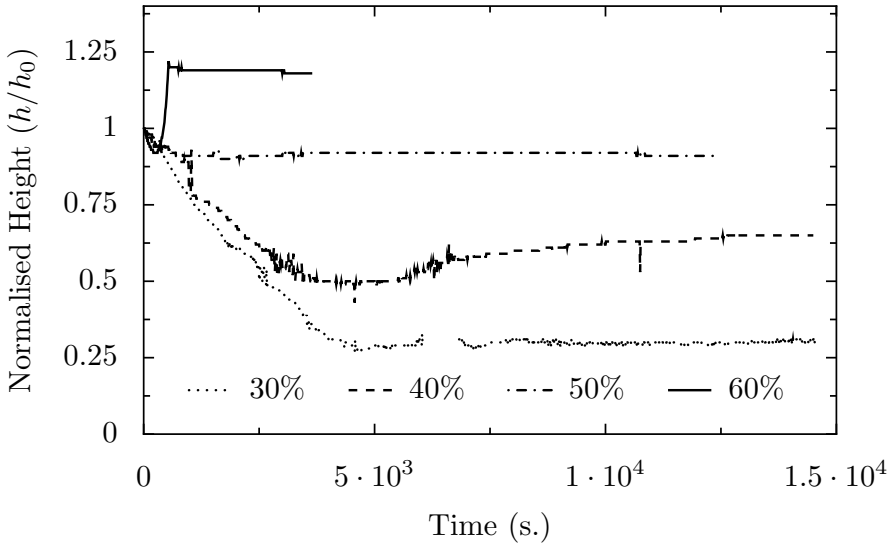

FIGURE 5.28: Normalised height against time for 8k 30-60% c_0 droplets.

Figure 5.28 shows the height data against time for the same droplets shown in Figure 5.27 previously. The small amount of noise in these data sets is caused by reflections from the droplet/deposit surface confusing the height/width algorithm in the DSA software. Despite the noise there are clear trends evident, discussed in Table 5.2:

TABLE 5.2: Table explaining the parameters and quantities discussed in this section.

Property	Behaviour
$h(t)$	The heights show an initial decrease for all c_0, and for $c_0 \gtrsim$ 40% an increase in the height is seen after time $t_{\min}$.
$t_{\min}$	For droplets where $t_{\min}$ is defined, it is inversely proportional to c_0, ie. less concentrated solutions take longer to reach this critical point.
$t_{\max}$	The time to reach maximum height after a minima is also inversely proportional to c_0.
$h_{\min}$	The height of the droplet at $t_{\min}$ is proportional to c_0.
$h_{\max}$	The height of the droplet at $t_{\max}$ is also proportional to c_0, with $c_0 = 60\%$ the only droplet which goes above its starting height h_0.

Figure 5.29 shows $h_{\min}$ and $h_{\max}$ against c_0 for the PEG 8k MW droplets discussed previously, normalised by h_0. All data shows a linear upwards trend, indicating that although the growth phenomena is likely to start at a given concentration or contact

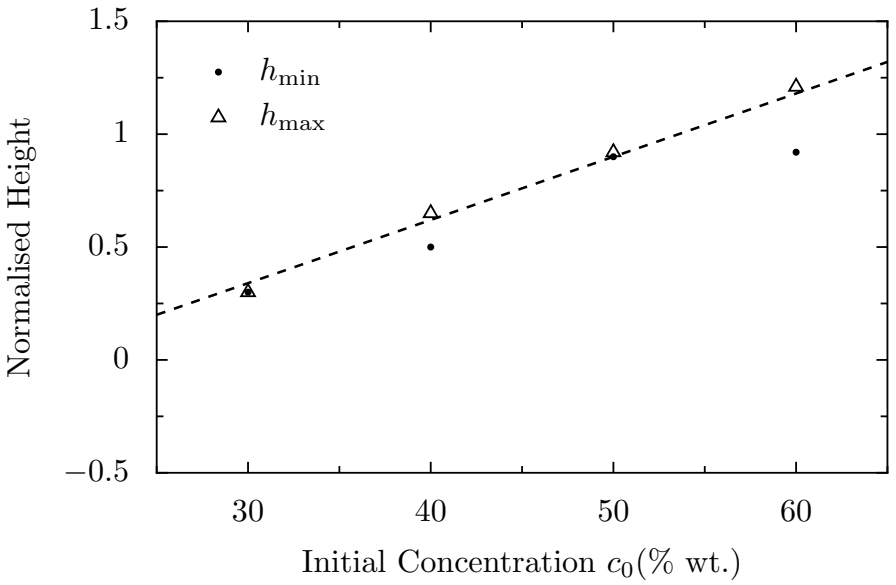

FIGURE 5.29: Graph showing normalised $h_{\min}$ and $h_{\max}$ against initial droplet concentration c_0. The general trend is of an increase in both $h_{\min}$ and $h_{\max}$ with concentration, but with the change in height $\Delta h = h_{\max} - h_{\min}$ showing no discernible trend with this small dataset.

angle, $h_{\max}$ appears to be linearly proportional to c_0, although further experiments are needed to confirm this.

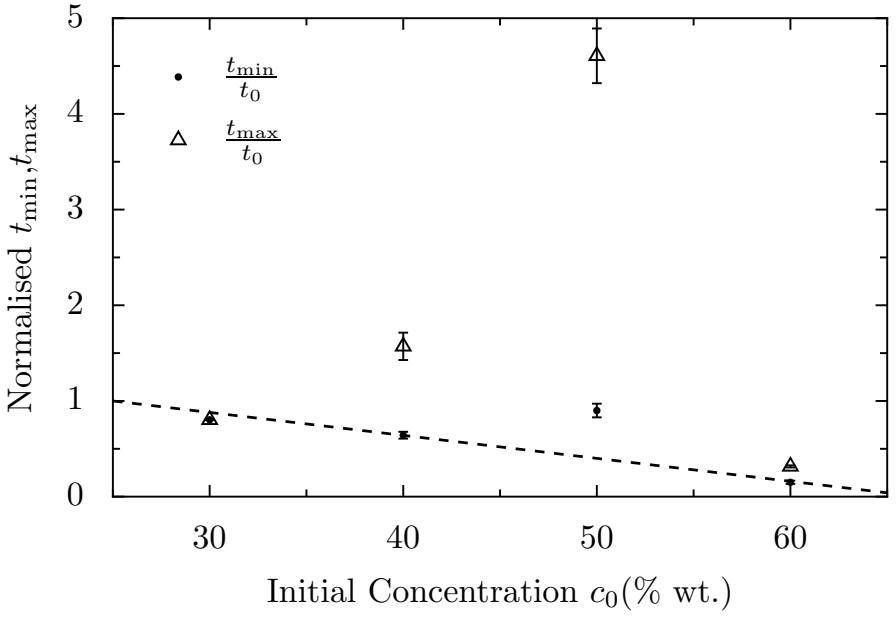

FIGURE 5.30: Normalised $t_{\min}$ and $t_{\max}$ values against c_0 for the 8k PEG droplets.

Figure 5.30 shows the $t_{\min}$ and $t_{\max}$ values from the 8k PEG droplets shown previously, normalised by t_0 as performed by Pauchard and Allain [203]. Here we see that when the

slope of the initial decay is taken into account (to remove slight variations in droplet size and humidity), the $t_{\min}$ values remain in a downward trend with the exception of $c_0 = 50\%$, however $t_{\max}$ shows a distinct maxima. This shows that at low concentrations ($c_0 \lesssim 30\%$), the lack of a growth mechanism means $t_{\max}$ is undefined, yet between 30-40% a critical point is reached at which the growth can start, signified by the separation of $t_{\min}$ and $t_{\max}$ values. As c_0 is increased further, the gap between $t_{\min}$ and $t_{\max}$ widens, showing a peak (in this small sample set) at $c_0 = 50\%$, yet this gap reduces considerably as $c_0 \to 60\%$.

Physical Interpretation and Implications

Although the sample set is small for this 8k MW study, making quantitative analysis difficult, there are some interesting behaviours present; the maxima in $\frac{t_{\max}}{t_0}$ is counter-intuitive, for example. One would expect the droplet growth to be initiated by a concentration level c_{growth} being reached, therefore droplets with a larger c_0 will have a greater volume at c_{growth}. One would therefore expect $h_{\min}$ to be proportional to c_0, as shown in Figure 5.29. This would explain how the 60% droplet grows higher than the others, however if the growth is solely dependent on concentration, it would be logical to expect a constant growth rate across all droplet growth regimes. This would result in the larger growth in the higher c_0 droplets taking longer, and $t_{\max} - t_{\min}$ being proportional to c_0, neither of which is seen.

The initial contact angle θ_0 could influence the growth, however the variation does not appear to be significant. I therefore hypothesize that the contact angle at $t_{\min}$ (i.e. θ_{growth}) must play a part; the pinned contact line discussed previously implies that a larger θ value converts into a larger volume, which is necessary for significant growth. A more in depth experimental study at this MW is necessary to make any firm conclusions.

It is interesting to note the growth behaviour at $c_0 = 10\%$ for the 20k MW droplets, in comparison with the 8k MW data shown in Figures 5.27 and 5.30. From Table 2.1 (p.32) we find that 8k PEG has an overlap concentration c^* of 15.44%, whereas for 20k PEG $c^* = 9.77\%$. Therefore with the 8k droplets, no growth phenomena are seen at $c_0 \approx 2c^*$, yet for 20k droplets growth is seen at $c_0 \approx c^*$.

This is highly counter-intuitive as c_0 clearly affects the drying behaviour, with larger c_0 values leading to higher and faster growth in both 8k and 20k MW droplets. It is therefore sensible to assume that the concentration at which the polymer coils begin to overlap would play a part in determining the size and structural integrity of the deposit. One can only surmise that there are one or more polymer attributes which influence the growth more strongly than c^*.

The qualitative difference between the image graphs (Figures 5.27, 5.24 and 5.2) are also notable; as the MW is increased (c^* decreased) the transmission of the backlight drops considerably as the clusters scatter more light. This is difficult to quantify from these pictures as refraction will fluctuate with the spherical or elliptical cap shape, however this could be performed using a spectrophotometer as in §4.8.2.3. The initial contact angle θ_0 also remains roughly even for the lower MW systems, yet shows a clear dependence on c_0 for 100k MW, indicating the increased hydrophobicity of the 100k systems.

5.3.4 Results from 3,350 MW PEG

Figure 5.31 shows a 75μL 3k MW PEG, $c_0 = 70\%$ droplet evolving over time, along with an image of the final dried deposit. The deposit is distinctly heptagonal with a concave region at the top - in the filmstrip images above you can clearly see the spherical cap profile evolving into a polyhedral profile.

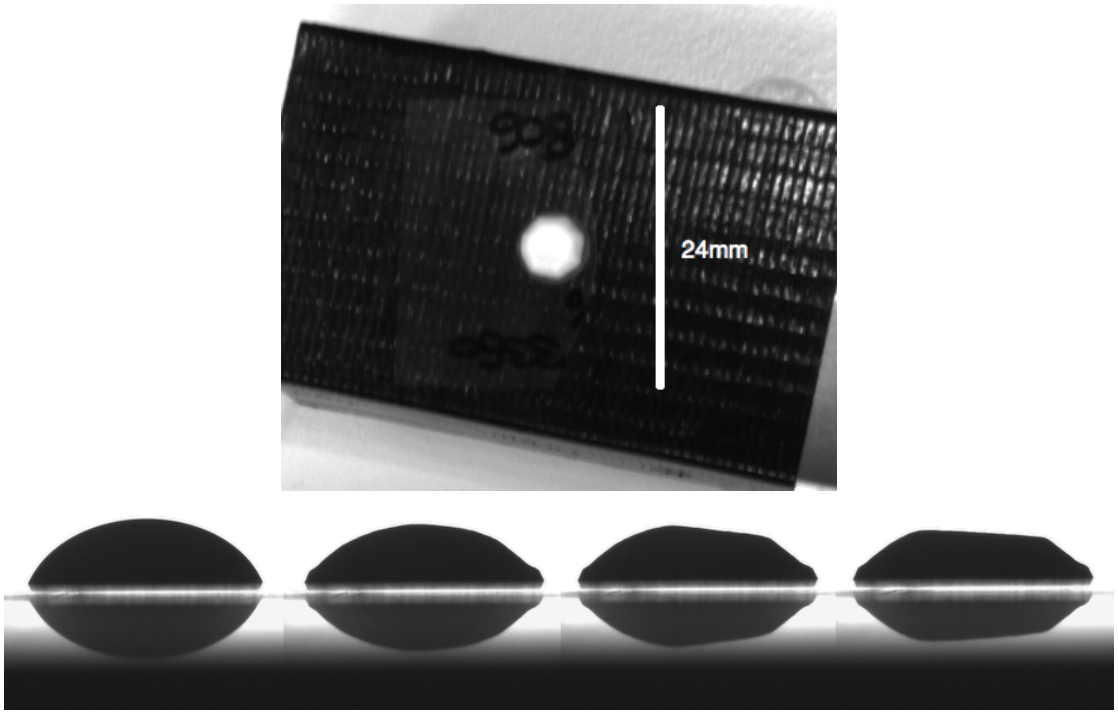

FIGURE 5.31: **Upper:** Image of the dried droplet deposit from above. **Lower:** Film-strip of the 75μL 3k MW PEG droplet, $c_0 = 70\%$ wt, evolving over time.

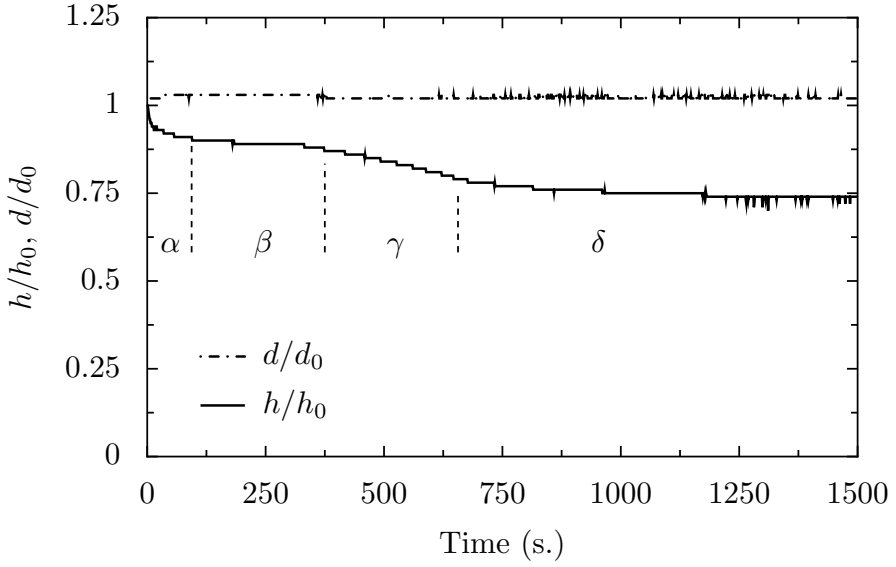

FIGURE 5.32: Normalised height h and base diameter d for a 3,350 MW PEG, $c_0 = 70\%$ wt droplet. α, β, γ and δ show the four observed stages during the evolution of this droplet (these stages are distinct from stages 1-4 mentioned previously).

Figure 5.32 shows the normalised height $\frac{h}{h_0}$ and diameter $\frac{d}{d_0}$ evolving over time for a representative 3.35k MW PEG droplet, with $c_0 = 70\%$. The base diameter remains almost constant for the entire experiment, except for a short period at the start where the viscous droplet is settling into its equilibrium position for the given substrate. This equilibration period is shown as α, during which the height h decreases rapidly and the base diameter d increases rapidly. The next section (labelled β) where $\frac{h}{h_0}$ shows a plateau, as does the diameter, is where the step around the contact ring forms (visible in the second filmstrip image in Figure 5.31) and is indicative of enhanced deposition at the contact line similar to the Deegan model. γ shows the time period where the droplet loses height - in this region the droplet buckles into the polyhedral shape shown above. In contrast to the Pauchard and Allain model of buckling dextran droplets, the concave region seen in Figure 5.31 means that the droplet loses height during the buckling process. δ is the final drying regime where the residue shape no longer changes, but the droplet loses mass as the remaining solvent evaporates.

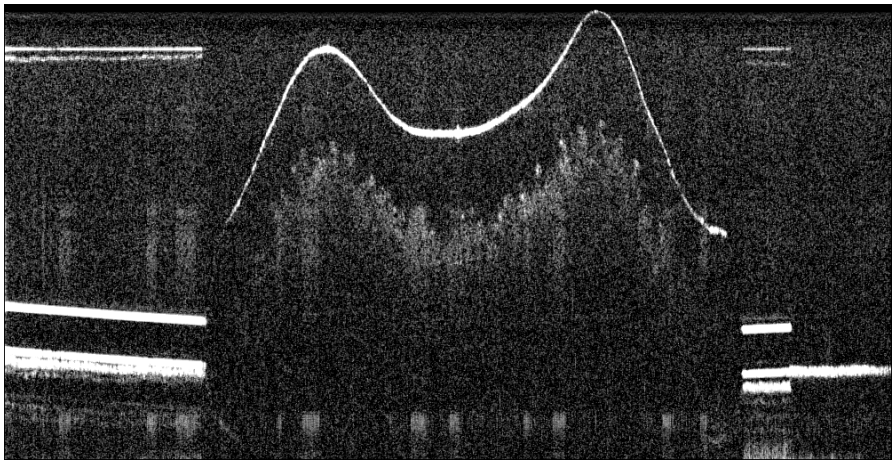

FIGURE 5.33: OCT image of 3.35k MW, 60% wt. heptagonal droplet residue

Figure 5.33 shows an OCT image of a 75μL 3k MW $c_0 = 70\%$ heptagonal-based droplet residue. The bright white lines towards the lower edges are reflections from the glass slide, and the twin-peaked white line in the centre indicates the droplet surface in this

cross-section. The wider grey area below the droplet surface shows where the deposit is hollow, and therefore shows the thickness of the skin. There is also an obvious 'step' between the droplet edge and the glass slide, also visible in the filmstrip in Figure 5.31, where the polymer has created a thick wall at the contact ring. In this image the concave region at the top of the droplet is clearly shown, and it is interesting to note that the deposit is thickest in this region and thinnest towards the sides.

Physical Interpretation and Implications

I postulate that in order for the β plateau phase to occur, the spherulites must have already formed a layer covering the droplet surface, and that the evaporation continues throughout this phase. Thus the β phase is similar to the skin buckling model of Pauchard and Allain [203], whereby a constant surface area skin tries to lose volume due to continued evaporation. The difference is that in Pauchard's work the polymer was dextran, which forms a glassy phase as many sugars do (dextran is a branched polysaccharide), yet PEG is known to crystallise [232, 233, 234]. These spherulite crystals that form often have regular polygonal shapes, and therefore in large numbers could induce macroscopic buckling into a polyhedron such as that shown in Figure 5.31, as opposed to the axisymmetric cones seen with dextran [203] and modelled numerically [208]. This could certainly lead to straight edges forming, as seen in various droplets throughout this chapter.

I see this as analogous to the way in which the $\sim 104.5 - 109.5°$ angle in a water molecule directly leads to the macroscopic hexagonal patterns in snowflakes[3] [236]; the heptagonal base pattern seen here may ultimately be an indicator of the physical structure of clusters (see §2.4.3) or crystals of 3,350 MW PEG. If the specific shape of the spherulites

[3]Not only was Johannes Kepler the first person to correctly deduce the forces creating a comet's tail (see §3.1), but by comtemplating the origin of a snowflake's shape he pioneered the study of crystal structure [235].

is dictated by the clusters, rather than crystals, then the solvation of PEG through hydrogen-bonding would make the shape highly temperature-dependent. As discussed previously, there is also evidence that the hydration level (number of bound solvent molecules per monomer) depends on the degree of polymerisation N [85], therefore the exact polyhedral-shape may also be MW-dependent.

This behaviour is subtly different from the growth phenomena exhibited previously, but more experiments are necessary in order to form any conclusions.

5.3.5 Results from 300k MW PEO Droplets

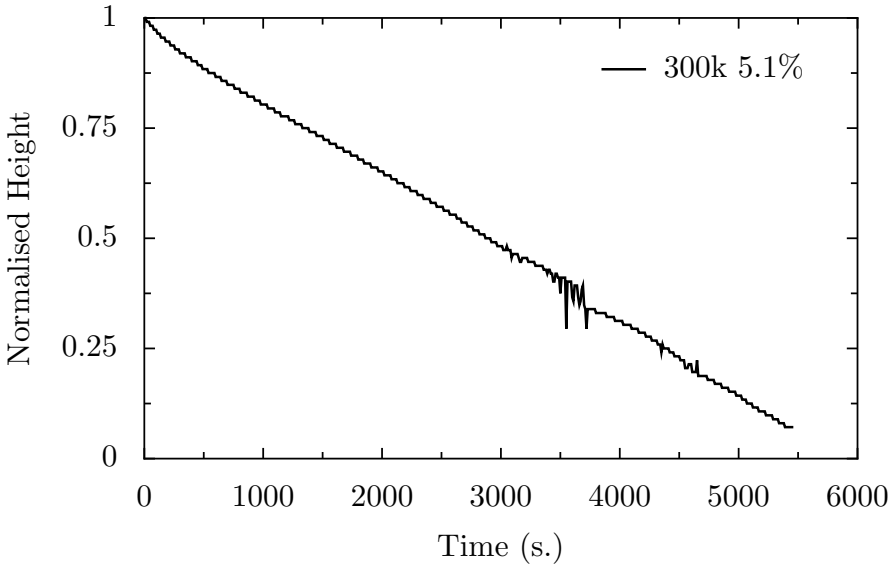

FIGURE 5.34: The height of a 75μL 300k PEO $c_0 = 5.1\%$ wt droplet evolving over time.

Figure 5.34 shows h/h_0 against time for a 300k $c_0 = 5.1\%$ droplet. This is representative of all 300k data, as no growth regime was observed for all $c_0 < 8\%$ (above this value, the solutions were too viscous to pipette accurately). Thus 300k MW droplets can be classed under 'standard' pinned drying, leaving a thin residue . This is unexpected as (from Table 2.1) r_g is 9.68 for 100k and 16.77 for 300k, and c^* is 4.37% for 100k and

2.52% for 300k; these are relatively small changes to the solution properties, yet the phenomenological growth has completely disappeared at 300k MW.

I hypothesise that the longer chains of 300k MW are less readily carried to the contact ring by the evaporative flow, therefore the increase in viscosity at the contact line is much lower, and cannot inhibit the flow to initiate Stage 2.

5.3.6 Other Droplet Systems

During the course of this work, various other droplet systems were studied during evaporation, some of which are outlined below.

PEO with Starch

Starch is known to form extremely hard, yet brittle, structures as it dries. In an attempt to increase the structural integrity of the PEO deposits 1-4% wt. starch solution (stored chilled in chloroform) was added to 100k PEO solutions between 10-30% wt. The additional starch did not disrupt the growth mechanism, however the late drying (Stage 4) resulted in macroscopic buckling and wrinkling at all concentrations. I assume that extra structural strength from the starch meant that the Stage 4 shrinking had to induce buckling or fracture.

PEO with Laponite

Laponite is a clay consisting of thin discs $\sim$ 1nm $\times$ 20nm, which is known to create 'shake-gels' whereby the discs form a 'house of cards' structure under shear with a relaxation time that can be measured in hours or days. Laponite is known to interact with PEO by encouraging the polymer to wrap around the clay discs, creating desirable commercial properties for these shake-gels [237].

100k MW PEO droplets with $10\% < c_0 < 35\%$ and 0.05-10% wt. Laponite were investigated; at *all* concentrations of Laponite the growth phenomena were completely disrupted, and the final deposit was an even, thin polymer film. Further investigation into this may give the ability to control the deposits more accurately, yet it is interesting that even at such low relative Laponite concentrations (0.05% wt, with 10-35% wt. PEO) the highly repeatable growth mechanism is foiled.

Dextran at 70k and 500k MW

Pauchard and Allain originally used Dextran, a branched polysaccharide, at 35k and 70k MW when investigating the buckling phenomena [203], and so some experiments were performed to corroborate their results. In many situations the droplets showed evidence of Pauchard's buckling theory, however with higher MW and concentrations some behaviour similar to the PEO growth presented here was found. It should be noted that the droplets which buckled exerted significant forces on the coverslips, and at higher concentrations they can bend the glass sufficiently to break it. This preliminary work has led to further investigations into the internal forces present during Dextran evaporation [238].

Polystyrene

Polystyrene droplets[4] were investigated at 35k - 200k MW at 10-30% wt. The polystyrene formed glassy deposits, typically with a small 'spike' at the centre, reminiscent of the Dextran buckling on a much smaller scale. These glassy deposits were clear, and accurate control of the residue shape, using pressure, temperature or another polymer, could lead to polystyrene being used as a cheap replacement for glass in small lenses.

[4]The polystyrene was dissolved in toluene for this work as it is insoluble in water.

5.4 Conclusions and Further Work

I conclude that the previously unseen droplet growth phenomena presented in this chapter are likely to be driven by the hydrogen bonding-driven solvation discussed in §2.4.1; in particular the deposit at the contact ring may repel the remaining aqueous phase (due to its hydrophobicity), resulting in the receding contact line seen in Stage 2 being 'squeezed' in by the spherulitic crystals which start to form at $t_{\min}$. This is supported by the raw videos which show circulatory flow ceasing at $t_{\min}$, and by Figure 5.19 which shows that the crystallisation region exists above the substrate (ie. out of focus) in conjunction with the particle tracking in Figure 5.14 which shows that the particles are not moving fast enough to escape the receding contact line. If the receding contact line is driven by circulation reversal (ie. Marangoni flow), one would expect the particles to move faster than the contact line - ie. the effect must follow the cause. Even assuming the existence of a viscous or turbulent boundary layer in the particle tracking experiments, the videos clearly show re-circulatory flow halting at $t_{\min}$, therefore I conclude that it is the receding contact line which 'squeezes' the remaining aqueous phase causing θ and h to increase in Stage 2. In a similar manner, the shrinking deposit causes the buckling shown in Figure 5.6, however this shrinking could also be responsible for 'squeezing' the Stage 2 droplet vertically upwards as deposition continues at the solid-liquid phase boundary, causing the Stage 3 vertical growth.

Whether this Stage 3 squeezing is sufficient to create all of the growth remains unclear - one can assert that a contact angle $\gtrsim 90°$ as found at late times in Stage 2 would encourage any deposition at the contact line to occur on top of previous deposits. This would naturally lead to a droplet with large θ being raised on top of its own deposit, and the continual loss of volume would reduce the contact line diameter - these two effects

occurring simultaneously would logically lead to a conical shape being formed, as has been seen throughout this chapter.

I feel that a combination of the deposit shrinking, and new deposits being placed on top of previous ones due to $\theta \gtrsim 90°$ is the most likely explanation, and is what leads to a Stage 3 growth which can reach $\approx 1.8 \times h_0$.

The test for this hypothesis is to find an alternative polymer which is predominantly hydrophobic (or which repels an alternative solvent), but which dissolves due to the physical properties of the chain facilitating hydrogen-bonding, and subsequently shielding the hydrophobic sections until the UCST is reached or deposition occurs at c_{sat}.

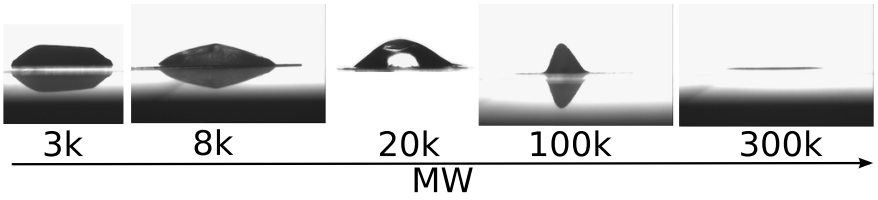

FIGURE 5.35: Final droplet deposits with increasing MW for initial concentration $c_0 \approx 3c^*$. As the MW is increased, the Stage 2 de-pinning becomes more pronounced, resulting in a narrower 'cone', but the growth regime stops abruptly at $\approx$ 300k MW for all concentrations.

Figure 5.35 shows the final deposit shapes for 3-300k MW droplets, where $c_0 \approx 3c^*$ (the overlap concentrations can be found in Table 2.2, p.33). A value of $3c^*$ was chosen arbitrarily for this comparison as I had results for a variety of MWs at this value. Here we see that as the MW is increased, the Stage 2 de-pinning becomes more pronounced, which leads to higher θ values, encouraging more vertical growth during the deposition stage. It is interesting to note that the growth phenomena is not present at 300k MW for $c_0 \lesssim 8\%$, resulting in an even, flat disk of polymer deposit. For the growth phenomena to be driven by evaporation the polymer chains must be easily transported by the internal flow, therefore one can see how the longer chains (with a corresponding lower diffusion constant D) will be harder to move. However, this does not explain how the lower MW

droplets fail to de-pin. To account for this, I propose that this growth mechanism may also be dependent on a trade-off between particle advection due to flux and brownian motion-driven diffusion, referred to as the Péclet number:

$$Pe = \frac{Jx}{D} \tag{5.9}$$

where J is the flux, x is a characteristic length of the system and D is the diffusion constant. Widjaja and Harris showed using numerical simulations that in systems with low Péclet numbers, the concentration of suspended particles was greatest at the apex and lowest at the contact ring [239]. From Equation 5.9, a lower Péclet number could arise from a higher diffusion constant D, which we would expect from shorter, more mobile chains. In Figure 5.35 we see that the 3k and 8k MW droplets do not de-pin, leaving a deposit with approximately the same base diameter as the original droplet. In the OCT image of a 3k deposit (Figure 5.33) we also see that the deposit is thickest at the centre and thinnest at the edge - consistent with Widjaja and Harris' results.

I therefore conclude that the growth mechanism seen here in 20k and 100k MW droplets is driven by the unusual hydrogen-bonding-driven solvation of the PEG/PEO molecule, yet the growth is most apparent in systems with larger Péclet numbers, where material is transported to the contact ring as per the Deegan model. In systems such as the 300k MW PEO shown here, I propose that either the Péclet number is too large due to the lower diffusivity of longer chains, or the elasticity present from entanglements between these polymers (shown in Figures 3.27 and 3.28, p.89-90) lowers the mobility of the molecules sufficiently to prevent the growth phenomena.

Linear versus Branched polymers

Pauchard's original work with Dextran showed a permeable, constant surface area skin forming and buckling as solvent evaporated; although Dextran is a polysaccharide which undergoes a phase transition into a glassy state, it is possible that this behaviour occurs due to the different entanglement properties of a branched polymer (Dextran) to a linear polymer (ie. PEO). It would therefore be interesting to create branched PEO and compare evaporation regimes for droplets with similar molar concentrations. Branched PEO can be created by chemical processes or by subjecting the linear sample to high velocity neutrons to initiate cross-linking, both of which were outside the scope of this research.

Taicaan Interferometric Profiler

The high-resolution scan shown in Figure 5.6 clearly shows the deposit structure, shape and substrate buckling mentioned previously - the Taicaan® profiler used for this allowed for simple and accurate data acquisition, however the z-axis range was too low for most of the droplets and the high-resolution scans took too long to visualise the growth phenomena. With future hardware and software advances this equipment may become invaluable for droplet evaporation studies, and an investigation into the substrate bending whilst monitoring the droplet and deposit shapes may yield further information as to the internal processes during these phenomena.

Currently, I feel that further study of the changing droplet properties during Stages 2 and 3 would be best served using OCT hardware. Although the spatial resolution cannot match the interferometric profiler, the temporal resolution is $\approx$ 30Hz for current commercial systems, and one can visualise the PEO clusters in certain situations [240], thereby allowing the internal flow to be measured simultaneously, which cannot be performed with the Taicaan profiler.

Theoretical Advances

As the experimental results in this chapter and Reference [226] are the first reports of this PEO droplet evaporation phenomena, there is currently no supporting theory for this work. It would be useful to extend the theories of Popov [229] and Deegan [204, 241, 242] to account for a reduction in the evaporative flux J due to increased concentration at the contact line as a result of material transport. This would have to account for the fact that a colloidal system such as coffee does not experience reduced J, but some PEO droplets do. It is also possible that viscoelasticity plays a role in determining the final structure, especially considering the reduction of the bootstrap effect in higher MW systems.

6

Conclusions and Further Work

"Conclusions arrived at through reasoning have very little or no influence in altering the course of our lives."

Carlos Casteneda, 1925-1998

"Enough research will tend to support your conclusions."

Arthur Bloch

"I am turned into a sort of machine for observing facts and grinding out conclusions."

Charles Darwin, 1809-1882

6.1 Conclusions

In the course of this research the non-equilibrium behaviour of various polymeric complex fluid systems (through evaporation and dilution) has been investigated, with an emphasis on poly(ethylene oxide) due to its commercially-desirable properties.

A safe and easy to use optical tweezer (OT) apparatus has been developed (§3) in order to facilitate the investigation of various systems during dilution or drying. This OT hardware has been shown to yield information about the non-equilibrium rheology of single-component polymeric systems (§3.4.1,§3.4.2,§3.4.3), and more complex 'living' polymer samples (§4.9,§4.10), which is unobtainable using traditional bulk rheology or Diffusing Wave Spectroscopy (DWS). This information is difficult to interpret in the case of the wormlike micelle (WLM) system as the dilution gradient is inhomogeneous, however this in itself allows a qualitative comparison to be made between systems which is unfeasible using other methods. Further investigation of WLM and WLM with polymer systems may explain the origin of the WLM dilution behaviour discussed in §4.9 and §4.10, which is crucial to the more commercially-relevant task of controlling and exploiting the dilution behaviour to improve the efficacy of products.

The advantages of OT systems are limited in scope however, as I have shown that in equilibrium conditions both bulk rheology and DWS yield more reliable data than the OT apparatus (§4.3) developed in Chapter 3. Further to this, the arbitrary nature of corrections to DWS data (§4.2.1.1) leads me to conclude that bulk rheology is still the most reliable and useful method to study rheological behaviour, although this may change as microrheological methods are refined.

In the course of comparing equilibrium data from various systems using bulk rheology, OTs and DWS, I have undertaken an investigation into the changing rheology of a 'model' WLM network structure as various components are added with a view to understanding the behaviour of commercially-viable systems. I have shown that a dual-surfactant (SDS and CAPB) system will form WLMs given sufficient surfactant concentration, or additional ionic strength, however CAPB contains a small percentage of NaCl, and therefore

one must keep in mind that increasing the eM surfactant concentration will simultaneously increase the electrolyte level. With 1.5% wt additional NaCl, these WLM systems show increased elasticity and entanglements consistent with micelle lengthening due to charge screening; on the addition of 3% wt NaCl, this system shows behaviour indicative of branching at both 0.1 and 0.2 eM surfactant concentrations. These results show that SDS:CAPB eM samples can be considered 'model' WLM systems, and close approximations of Maxwellian systems on the addition of extra salt or surfactant above 0.1eM.

The effect of an uncharged polymer (PEO 4M MW) on the WLM network structure was subsequently investigated, and at low concentrations ($\lesssim$0.2% wt. PEO) there was little to no effect, at intermediate concentrations ($\lesssim$0.4% wt. PEO) there was evidence of a transient network structure forming, giving a secondary relaxation time, and at high concentrations (0.5% wt. PEO) a gel-like system was created with behaviour indicative of multiple relaxation times, although the exact effect was dependent on the surfactant concentration c_{surf}. PEO is used extensively in home and personal care products as a viscosifier, so it is important to quantify its effect on a system, and this data gives a product designer the ability to modify a product's feel simply by altering the concentration of a single, safe component between $0-0.5$% wt.

Further to this, the effect of a conditioning polyelectrolyte on the network structure was studied; its effect was highly dependent on surfactant and electrolyte concentration, but also hinted at the previously unreported behaviour of the polyelectrolyte initiating micellar branching. It would be extremely interesting to verify this using cryo-TEM as described in Chapter 4, as this would lead to a new technique to control the rheology of commercial products.

These are useful results for product designers as the samples studied in this work are close to commercial systems, yet I have shown that they have properties close to 'model' systems. Typically commercial products are 'messy', due to the multiple components interacting in ways which are not well understood; this study into SDS:CAPB WLMs provides evidence that products can be developed whilst maintaining 'ideal' rheological properties.

Droplet Evaporation Investigation

Drying experiments have been performed using the OT apparatus mentioned above (eg. §3.4.3), however I decided to concentrate on the simpler experimental technique of monitoring sessile droplets in ambient conditions. This investigation has led to us reporting a droplet evaporation regime in which the overall surface area increases through a four-stage deposition process [226], with behavioural elements similar to Deegan's [204], Pauchard's [203] and Widjaja's [239] models.

In Chapter 5 I hypothesise that the concurrent solidification regions that occur in some droplets may be due to the lack of re-circulation as a result of their high viscosity. It would be interesting to measure the flow in these droplets using NMR/MRI to attempt to determine the underlying reasons why viscosity increases sufficiently to inhibit solvent replenishment in some systems but not others. This could also be performed by seeding the droplets with fluorescent spheres to allow for particle tracking over the entire experimental time (for the evaporating droplets). At the moment, particle tracking becomes unreliable during Stage 2, however adding sufficient spheres to visualise the flow at later times may affect the behaviour, so magnetic resonance techniques are preferable.

Poly(ethylene oxide)

Poly(ethylene oxide) (PEO) has been used extensively in this work, and has shown various behavioural regimes, including the possibility that it makes WLM dilution more uniform, and that it can make the evaporation of a sessile droplet less uniform. In Chapter 1 it is mentioned that PEO has apparently contradictory behaviours - this work has found more behavioural regimes of this molecule which exhibit behaviour not covered by current theories.

The non-standard solvation mechanism for this droplet certainly gives it unusual properties, such as an upper critical solubility temperature (UCST), and this hydrogen-bonding solvation may be the reason for the droplet growth phenomena. Whether this solvation process is important in the many other properties of PEO remains to be seen, however it can be concluded that the non-equilibrium behaviour of this one molecule is wide and varied, and can give apparently contradictory results, therefore a complete theory of non-equilibrium complex fluids will require extensive further research at the intersection of physics, chemistry and engineering.

A

Python Code for ETAW Method

```
# Author: Dave Willmer, 2008, MIT Licence
from __future__ import with_statement
import os
from numpy import array, polyfit, zeros, logspace, power, exp, diff
from pylab import loglog, show

def directConversion(J, t, linear_t, data_points, fn="convdata"):
    J, t, storage, loss = array(J), array(t), list(), list()
    n0 = 1./polyfit(x=t[linear_t:], y=J[linear_t:], deg=1)
    gdata = zeros( (data_points+1, 3) )
    frange = logspace(start=-3, stop=3, num=data_points)

    for omega in range(1,data_points+1):
        w = power(10, (frange[0]+(omega*frange[1])) )
        g_star = 1j*w / (( J[0]*1j*w + exp(-1j*w*t[-1])/n0[0]) + \
            sum( diff(J)/diff(t) * ( exp(-1j*w*(t[:-1]-t[0])) - \
            exp(-1j*w*(t[1:]-t[0])))))
        storage.append( (omega,g_star.real) )
        loss.append( (omega, g_star.imag) )

    gp = zip(*storage)
    gdp = zip(*loss)
    #loglog(gp[0][1:],gp[1][1:])
    #loglog(gdp[0][1:],gdp[1][1:])
    #show()
    f = open(fn+".MODULI.csv",'w')
    for each in range(len(gp[0])):
        f.write(str(gp[0][each])+','+str(gp[1][each])+ \
                ','+str(gdp[1][each])+'\n')
    f.close()

if __name__ == '__main__':
    folder = '071218_T2C2_water_on_top_0.8W_AOD65.5k'
    files = [x for x in os.listdir(folder) if x.endswith('STD.dat')]

    for fn in files:
        with open(os.path.join(folder,fn),'r') as f:
            d = zip(*[x.rstrip('\n').split('\t') for x in f.readlines()])
            d_0, d_1 = map(float,d[0]), map(float,d[1])
            directConversion(array(d_1),array(d_0),int(1900),int(2000), fn)
```

Python Code for Maxwellian Single-Exponential Fit

```
# Author: Dave Willmer, MIT Licence 2009
from scipy import optimize
from numpy import power
import pylab as p

b06 = r"jaguar/data/jag17-beta.06-jaguar-study.txt"
b07 = r"jaguar/data/jag17-beta.07-jaguar-study.txt"
b08 = r"jaguar/data/jag17-beta.08-jaguar-study.txt"
b10 = r"jaguar/data/jag17-beta.10-jaguar-study.txt"

def select_columns(fn, x_col, y_col, headers=1):
        data = zip(*[q.rstrip('\n').rstrip('\r').split('\t')
                                for q in open(fn,'r').readlines()[headers:]])
        return (map(float,data[x_col]), map(float,data[y_col]))

def fit_g_prime(x, Gm, Tm, Gt, Tt):
        return Gm * ( (Tm*Tm*power(x,2)) / (1+(Tm*Tm*power(x,2))) )

def fit_g_double_prime(x, Gm, Tm, Gt, Tt):
        return Gm * ( (Tm*power(x,1)) / (1+ (Tm*Tm*power(x,2))) )

gp_x, gp_y   = select_columns(b10, 1, 2, headers=2)
gdp_x, gdp_y = select_columns(b10, 1, 3, headers=2)

gss = [1,1,1,1]
gp_fit, gp_cov   = optimize.curve_fit(fit_g_prime, gp_x, gp_y, p0=gss)
gdp_fit, gdp_cov = optimize.curve_fit(fit_g_double_prime, gdp_x, gdp_y, p0=gss)

Gm, Tm, Gt, Tt = gp_fit
gp_fit_vals  = [fit_g_prime(val, Gm, Tm, Gt, Tt) for val in gp_x]
Gm, Tm, Gt, Tt = gdp_fit
gdp_fit_vals = [fit_g_double_prime(val, Gm, Tm, Gt, Tt) for val in gdp_x]
```

C

Python Code for Double-Maxwell Fit

```
#Author: Dave Willmer, MIT Licence 2009
from scipy import optimize
from numpy import power
import pylab as p

gel_fit = "jaguar/data/peo4x-beta.06-jaguar-study.txt"

def select_columns(fn, x_col, y_col, headers=1):
    data = zip(*[q.rstrip('\n').rstrip('\r').split('\t')
                 for q in open(fn,'r').readlines()[headers:]])
    return (map(float,data[x_col]), map(float,data[y_col]))

def fit_g_prime(x, Gm, Tm, Gt, Tt):
    return Gm * ( (Tm*Tm*power(x,2)) / (1+(Tm*Tm*power(x,2))) ) + \
        Gt * ( (Tt*Tt*power(x,2)) / (1+(Tt*Tt*power(x,2))) )

def fit_g_double_prime(x, Gm, Tm, Gt, Tt):
    return Gm * ( (Tm*power(x,1)) / (1+ (Tm*Tm*power(x,2))) ) + \
        Gt * ( (Tt*power(x,1)) / (1+ (Tt*Tt*power(x,2))) )

gp_x, gp_y   = select_columns(gel_fit, 1, 2, headers=2)
gdp_x, gdp_y = select_columns(gel_fit, 1, 3, headers=2)

gss = [1,1,10,10]
gp_fit, gp_cov   = optimize.curve_fit(fit_g_prime, gp_x, gp_y, p0=gss)
gdp_fit, gdp_cov = optimize.curve_fit(fit_g_double_prime, gdp_x, gdp_y)

gp_fit_vals  = [fit_g_prime(val, *gp_fit) for val in gp_x]
gdp_fit_vals = [fit_g_double_prime(val, *gdp_fit) for val in gdp_x]
```

ImageJ Macro for Droplet Profile Extraction

```
34 base_file_name = "./8k/macrod";
35 setSlice(1);
36
37 for (i=1;i <= nSlices; i++)
38 {
39     file_name=base_file_name+i+".txt";
40     doWand(1,1);
41     getSelectionCoordinates(x, y);
42     for (j=5; j<x.length-5; j++)
43     {
44         xave = (x[j]+x[j-1])/2;
45         yave = (y[j]+y[j-1])/2;
46         File.append(xave+","+yave,file_name);
47     }
48
49     run("Next Slice [>]");
50     run("Select None");
51 }
```

E

Python Code for Droplet Profile Calculations

```
1
2  import os
3  import numpy as n
4  import pylab as p
5
6  from numpy import array as n_array, min as n_min, max as n_max, \
7          power as n_power, abs as n_abs, polyval, polyfit, \
8          sum as n_sum, sqrt as n_sqrt, pi as n_pi
9
10 ######## USER DEFINITIONS BELOW ######
11
12 directory = '/Users/dave/Desktop/image_j_procd/8k60pc/'
13 prefix = 'macrod'
14
15 ########################################
16
17 '''
18
19 Data storage class
20
21 '''
22
23 class Profile( object ):
24         ''' Class to store profile data and info. '''
25         def __init__(self, number):
26                 self.number = number
27                 self._data = dict()
28
29         def __getitem__(self, item):
30                 return self._data[item]
31
32         def set_data(self, data):
33                 for k, v in data.items():
34                         self._data[k] = v
35
36
37 '''
38
39 Data processing code.
40
41 '''
42
43 list_of_profiles = list()
44 fnames = [x for x in os.listdir(directory) if x.startswith(prefix)]
45
```

```
46 p.subplot(221)
47 p.title('Profiles')
48 for i in range(1,len(fnames)):
49
50         fn = 'macrod'+str(i)+'.txt'
51
52         # read data into array
53         with open(os.path.join(directory,fn),'r') as f:
54             rawdata = f.readlines()
55
56         # split rawdata into x- and y-arrays
57         x_data, y_data = zip(*[line.rstrip('\n').split(',') \
58             for line in rawdata])
59
60         # convert all data in float (is read in as string)
61         x_data = map(float, x_data)
62         y_data = map(float, y_data)
63
64         # reverse y-array as imageJ has 0,0 in top-left
65         max_y = max(y_data)
66         y_data_reverse = [max_y-y for y in y_data]
67
68         # convert to numpy arrays
69         x_array = n_array( x_data )
70         y_array = n_array( y_data_reverse )
71
72         # get 8th order polynomial fit values
73         fit_coeffs = polyfit( x_array, y_array, 8 )
74         fit_values = polyval( fit_coeffs, x_array )
75
76         # get min + max values with indices of polynomial fit
77         temp_values = fit_values.tolist()
78         max_y, min_y = n_max( fit_values ), n_min( fit_values )
79         max_y_index = temp_values.index( max_y )
80         min_y_index = temp_values.index( min_y )
81
82         # recentre data with max in middle
83         x_array -= x_array[max_y_index]
84
85         if not i % 100:
86                 p.plot(x_array, y_array)
87                 p.plot(x_array, fit_values)
88
89         # calculate parameters
90         pi = n_pi
91         r1, r2 = x_array[:-1], x_array[1:]
92
93         deltaH = n_abs( y_array[:-1] - y_array[1:] )
94         surfaceArea      = (pi/2) * n_abs(r1+r2) * \
95                 n_sqrt( n_power(r1-r2,2) + n_power(deltaH,2) )
96         volume = (pi/6) * deltaH * ( n_power(r1,2) \
97                 + n_power(r2,2) + r1*r2 )
98         radius = (n_max( x_array ) - n_min( x_array )) / 2
99         height = max_y - min_y
100        sum_rh_squared = n_power(radius,2) + \
101                n_power(height,2)
102        areaSphericalCap = pi * sum_rh_squared
103        calculatedArea = n_sum( surfaceArea )
104        percentDifferenceArea = n_abs(areaSphericalCap-\
105                calculatedArea)/calculatedArea*100
106        volumeSphericalCap = (pi/6) * height * 3 * \
107                sum_rh_squared
```

```
108             calculatedVolume = n_sum(volume)
109             percentDifferenceVolume = n_abs( \
110                     volumeSphericalCap-calculatedVolume)/ \
111                     calculatedVolume*100
112
113             errv1, errv2 = n_sum( volume[:max_y_index] ), \
114                     n_sum( volume[max_y_index:] )
115             errv = (errv1 - errv2) / 2
116
117             erra1, erra2 = n_sum(surfaceArea[:max_y_index] ), \
118                     n_sum( surfaceArea[max_y_index:] )
119             erra = (erra1 - erra2)/2
120
121             data = dict()
122             data['deltaH'] = deltaH
123             data['surfaceArea'] = surfaceArea
124             data['volume'] = volume
125             data['radius'] = radius
126             data['height'] = height
127             data['sum_rh_squared'] = sum_rh_squared
128             data['areaSphericalCap'] = areaSphericalCap
129             data['calculatedArea'] = calculatedArea
130             data['percentDifferenceArea'] = percentDifferenceArea
131             data['volumeSphericalCap'] = volumeSphericalCap
132             data['calculatedVolume'] = calculatedVolume
133             data['percentDifferenceVolume'] = percentDifferenceVolume
134             data['errv1'] = wonkyv1
135             data['errv2'] = wonkyv2
136             data['errv'] = wonkyv
137             data['erra1'] = wonkya1
138             data['erra2'] = wonkya2
139             data['erra'] = wonkya
140             #data['flatArea'] = flatArea
141             #data['flatVolume'] = flatVolume
142
143             profile = Profile(i)
144             profile.set_data( data )
145             list_of_profiles.append( profile )
146             del profile
147
148
149 p.subplot(222)
150 p.title('Norm. Volume')
151 v0 = list_of_profiles[0]['calculatedVolume']
152 norm_vol = [x['calculatedVolume']/v0 for x in list_of_profiles]
153 p.plot(norm_vol)
154
155 p.subplot(223)
156 p.title('Norm. Height')
157 h0 = list_of_profiles[0]['height']
158 norm_height = [x['height']/h0 for x in list_of_profiles]
159 p.plot(norm_height)
160
161 p.subplot(224)
162 p.title('Norm. Area')
163 a0 = list_of_profiles[0]['calculatedArea']
164 norm_area = [x['calculatedArea']/a0 for x in list_of_profiles]
165 p.plot(norm_area)
166
167 p.show()
```

F

Solution of $\zeta_{\min}$ Depressed Cubic

We start with the unknown $\zeta_{\min}$ in terms of known parameters

$$\zeta_{\min}^3 + 3\zeta_{\min} = \frac{c_0}{c_{\text{sat}}}\left(\zeta_0^3 + 3\zeta_0\right) = 2D, \tag{F.1}$$

in which D is a constant. We can then use del Ferro's method [243, 244] to solve for $\zeta_{\min}$ by finding s and t where

$$3st = 3 \tag{F.2}$$
$$s^3 - t^3 = 2D. \tag{F.3}$$

Solving for s in F.2 and substituting into F.3 gives

$$\frac{1}{t^3} - t^3 = 2D, \tag{F.4}$$

which multiplied by t^3 gives

$$\begin{aligned} -t^6 - 2Dt^3 + 1 &= 0 \\ \therefore t^6 + 2Dt^3 - 1 &= 0. \end{aligned} \tag{F.5}$$

Treating this as a quadratic in t^3 we then obtain

$$\begin{aligned} t^3 &= -\frac{2D}{2} \pm \sqrt{\frac{(2D)^2}{4} - (-1)} \\ \therefore t &= \sqrt[3]{-D \pm \sqrt{D^2+1}}. \end{aligned} \tag{F.6}$$

Bibliography

[1] H. Rasa, M. Mohsen-Nia, and H. Modarress. Measurement and modeling of density, kinematic viscosity, and refractive index for poly(ethylene glycol) aqueous solution at different temperatures. *J. Chem. Eng. Data*, 50:1662 – 1666, 2005.

[2] Y. Aray, M. Marquez, J. Rodriguez, D. Vega, Y. Simon-Manso, S. Coll, C. Gonzalez, and D.A. Weitz. Electrostatics for exploring the nature of the hydrogen bonding in polyethylene oxide hydration. *J. Phys. Chem. B*, 108:2418 – 2424, 2004.

[3] T.A. Waigh. Microrheology of complex fluids. *Rep. Prog. Phys.*, 72:685 – 742, 2005.

[4] T. Pezeril, C. Klieber, S. Andrieu, D. Chateigner, and K.A. Nelson. Picosecond shear waves in nano-sized solids and liquids. *Proceedings of SPIE*, 7214, 2009.

[5] P.P Borwankar. Food texture and rheology: a tutorial review. *J. Food. Eng.*, 16 (1-2):1 – 16, 1992.

[6] J.F Steffe. *Rheological Methods in Food Processing.* Freeman Press, 1996.

[7] H.-H. Lee, K.-S. Chou, and K.-C. Huang. Inkjet printing of nanosized silver colloids. *Nanotechnology*, 16:2436 – 2441, 2005.

[8] B.-J. de Gans, P.C. Duineveld, and U.S. Schubert. Inkjet printing of polymers: State of the art and future developments. *Advanced Materials*, 16(3):203 – 213, 2004.

[9] N.A. Krylov, A.A. Bokserman, and E.R. Stavrovskii. *The oil industry of the former Soviet Union: reserves and prospects, extraction, transportation.* Gordon and Breach, 1998.

[10] M. Berthiaume and J. Jachowicz. The effect of emulsifiers and oil viscosity on deposition of nonionic silicone oils from oil-in-water emulsions onto keratin fibers. *Journal of Colloid and Interface Science*, 141(2):299 – 315, 1991.

[11] R. Zana and E.W Kaler. *Giant Micelles: Properties and Applications.* CRC Press, 2007.

[12] R. Zana. *Dynamics of surfactant self-assemblies: Micelles, Microemulsions, Vesicles and Lyotropic Phases*. CRC Press, 2005.

[13] Z. Zhou, C. Chaibundit, A. D'Emanuele, K. Lennon, D. Attwood, and C. Booth. Solubilisation of drugs in worm-like micelles of block copolymers of ethylene oxide and 1,2-butylene oxide in aqueous solution. *International Journal of Pharmaceutics*, 354(1-2):82 – 87, 2007.

[14] S. Bontha, A.V. Kabanov, and T.K Bronich. Polymer micelles with cross-linked ionic cores for delivery of anticancer drugs. *Journal of Controlled Release*, 114(2): 163 – 174, 2006.

[15] M. Grmela and H.C. Öttinger. Dynamics and thermodynamics of complex fluids. i. development of a general formalism. *Phys. Rev. E*, 56:6620 – 6632, 1997.

[16] M. Grmela and H.C. Öttinger. Dynamics and thermodynamics of complex fluids. ii. illustrations of a general formalism. *Phys. Rev. E*, 56:6633 – 6655, 1997.

[17] J. Casademunt. Nonequilibrium physics: From complex fluids to biological systems. i. instabilities and pattern formation. *Physics Reports*, 447(3–6):67 – 68, 2007.

[18] T. Gisler and D.A. Weitz. Tracer microrheology in complex fluids: Dynamic aspects of colloids and interfaces. *Current Opinion in Colloid and Interface Science*, 3:586 – 592, 1998.

[19] I.G. Donhowe and O. Fennema. The effects of plasticizers on crystallinity, permeability, and mechanical properties of methylcellulose films. *Journal of Food Processing and Preservation*, 17(4):247 – 257, 1993.

[20] J.G. Chaussee. Skin conditioning composition, 1982.

[21] E.B. Chen, A.J. Morales, C.-C. Chen, A.A. Donatelli, W.W. Bannister, and B.T. Cummings. Fluorescein and poly(ethylene oxide) hose stream additives for improved firefighting effectiveness. *Fire Technology*, 34(4):291 – 306, 1998.

[22] P. Germain. *Cours de Mécanique des Milieux Continus*. Masson, Paris, 1973.

[23] A.G. Kulikovskii and E. Sveshnikova. *Nonlinear Waves in Elastic Media*. CRC Press, 1995.

[24] K. Walters. *Rheometry*. Chapman Hall, 1975.

[25] B.G Lipták. *Instrument Engineers Handbook: Process Measurement and Analysis*. CRC Press, fourth edition, 2003.

[26] H. Yamaguchi. *Engineering Fluid Mechanics*. Springer, 2008.

[27] C.D. Han. *Rheology and Processing of Polymeric Materials Volume 1: Polymer Rheology*. Oxford University Press, 2007.

[28] W. Boyes. *Instrumentation Reference Book*. Butterworth-Heinemann, 2008.

[29] R.G. Larson. *The Structure and Rheology of Complex Fluids*. Oxford University Press, 1999.

[30] W.P. Cox and E.H. Merz. Correlation of dynamic and steady flow viscosities. *Journal of Polymer Science*, 28:619 – 622, 1958.

[31] K.S. Cole and R.H. Cole. Dispersion and absorption in dielectrics. *J. Chem. Phys.*, 9:341 – 351, 1941.

[32] B.H. Brown, R.H. Smallwood, D.C. Barber, P.V. Lawford, and D.R. Hose. *Medical Physics and Biomedical Engineering*. Taylor and Francis, 1998.

[33] S. Havriliak and S. Negami. A complex plane representation of dielectric and mechanical relaxation processes in some polymers. *Polymer*, 8(4):161, 1967.

[34] L.H Sperling. *Introduction to physical polymer science*. John Wiley and Sons, 2005.

[35] C.A. Garcia-Franco and D.W Mead. Rheological and molecular characterisation of linear backbone flexible polymers with the cole-cole model relaxation spectrum. *Rheologica Acta*, 38:34 – 47, 1999.

[36] J.A. Shashkina, O.E. Philippova, Y.D. Zaroslov, A.R. Khokhlov, T.A. Pryakhina, and I.V. Blagodatskikh. Rheology of viscoelastic solutions of cationic surfactant. effect of added associating polymer. *Langmuir*, 21:1524 – 1530, 2005.

[37] M. Buchanan, M. Atakhorrami, J.F. Palierne, F.C. MacKintosh, and C.F. Schmidt. High-frequency microrheology of wormlike micelles. *Physical Review E*, 72(011504), 2005.

[38] P.G. de Gennes. *Scaling Concepts in Polymer Physics*. Cornell University Press, 1979.

[39] J.D. Ferry. *Viscoelastic Properties of Polymers*. John Wiley and Sons, 1970.

[40] P. Flory. *Principles of Polymer Chemistry*. Cornell University Press, 1971.

[41] P.G. de Gennes. Scaling theory of polymer adsorption. *Le Journal de Physique*, 37:1445 – 1452, 1976.

[42] U.W. Gedde. *Polymer Physics*. Springer, 2001.

[43] M. Doi and S.F. Edwards. *The theory of polymer dynamics*. Oxford University Press, 1988.

[44] R.A.L. Jones. *Soft Condensed Matter*. Oxford University Press, 2002.

[45] P.E. Rouse. A theory of linear viscoelastic properties of dilute solutions of coiling polymers. *J. Chem. Phys.*, 21:1272 – 1280, 1953.

[46] R.B. Bird, R.C. Armstrong, and O. Hassager. *Dynamics of Polymeric Liquids*. John Wiley and Sons, 1977.

[47] G.R. Strobl. *The Physics of Polymers*. Springey, New York, 1997.

[48] B.H. Zimm. Dynamics of polymer molecules in dilute solution: viscoelasticity, flow birefringence and dielectric loss. *J. Chem. Phys.*, 24:269 – 278, 1956.

[49] P.G. de Gennes. Reptation of a polymer chain in the presence of fixed obstacles. *J. Chem. Phys.*, 55:572 – 579, 1971.

[50] S.F. Edwards. *Molecular Fluids*. Gordon and Breach Science Publishers, 1976.

[51] W.W. Graessley, T. Masuda, J. Roovers, and N. Hajichristidis. Unknown. *Macromolecules*, 9:127 – 141, 1976.

[52] W.W. Graessley. Viscoelasticity and flow in polymer melts and concentrated solutions, in *Physical Properties of Polymers*. American Chemical Society, Washington DC, 1984.

[53] M.E Cates. Reptation of living polymers: dynamics of entangled polymers in the presence of reversible chain-scission reactions. *Macromolecules*, 20:2289 – 2296, 1987.

[54] M.E. Cates and S.J. Candau. Statics and dynamics of worm-like surfactant micelles. *J. Phys. Cond. Mat.*, 2:6869 – 6892, 1990.

[55] P. Mukerjee. Size distribution of small and large micelles: Multiple equilibrium analysis. *J. Phys. Chem.*, 76:565 – 570, 1972.

[56] C.A. Dreiss. Wormlike micelles: where do we stand? recent developments, linear rheology and scattering techniques. *Soft Matter*, 3:956 – 970, 2007.

[57] P.A. Hassan, J. Narayanan, and C. Manohar. Vesicles and worm-like micelles: structure, dynamics and transformations. *Current Science*, 80(8):980 – 989, 2001.

[58] F. Kern, F. Lequeux, R. Zana, and S.J. Candau. Dynamical properties of salt-free viscoelastic micellar solutions. *Langmuir*, 10:1714, 1994.

[59] L.J. Magid, Z. Li, and P.D. Butler. Unknown. *Langmuir*, 16:10028 – 10036, 2000.

[60] W.-R. Chen, P.D Butler, and L.J. Magid. Unknown. *Langmuir*, 22:6539 – 6548, 2006.

[61] B.A. Schubert, E.W. Kaler, and N.J. Wagner. Unknown. *Langmuir*, 19:4079 – 4089, 2003.

[62] D. Willmer, D.J. Fairhurst, A. Ferrante, S. Puntambekar, and S. Amin. In preparation, 2010.

[63] D. Danino, Y. Talmon, H. Levy, G. Beinert, and R. Zana. Unknown. *Science*, 269: 1420, 1995.

[64] F.E. Bailey and J.V. Koleske. *Poly(ethylene oxide)*. Academic Press, 1976.

[65] P.J. Flory. Kinetics of condensation polymerisation; the reaction of ethylene glycol with succinic acid. *J. Am. Chem. Soc.*, 59(3), 1937.

[66] D.J. Worsfold and A.M. Eastham. Cationic polymerization of ethylene oxide. i. stannic chloride. *J. Am. Chem. Soc.*, 79(4):897 – 899, 1957.

[67] D.J. Worsfold and A.M. Eastham. Cationic polymerisation of ethylene oxide. ii. boron triflouride. *J. Am. Chem. Soc.*, 79(4):900 – 902, 1957.

[68] K.S. Kazanskii, A.A. Solovyanov, and S.G. Entelis. Polymerization of ethylene oxide by alkali metal-naphthalene complexes in tetrahydrofuran. *European Polymer Journal*, 7(10):1421 – 1433, 1971.

[69] R.C. Stavisky, J.M. Britt, A. Zuzek, E. Truong, and G.D. Bittner. Melatonin enhances the in vitro and in vivo repair of severed rat sciatic axons. *Neuroscience Letters*, 376:98 – 101, 2005.

[70] R.B. Borgens and D. Bohnert. Rapid recovery from spinal cord injury after subcutaneously administered polyethylene glycol. *Journal of Neuroscience Research*, 66(6):1179 – 1186, 2001.

[71] R.M. Seborg and R.B. Inverarity. Preservation of old, waterlogged wood by treatment with polyethylene glycol. *Science*, 136(3516):649 – 650, 1962.

[72] C.C. Ruiz. *Sugar-Based Surfactants: Fundamentals and Applications*. CRC Press, 2008.

[73] K. Devanand and J.C. Selser. Asymptotic behavior and long-range interactions in aqueous solutions of poly(ethylene oxide). *Macromolecules*, 24:5943 – 5947, 1991.

[74] F. Kienberger, V.P. Pastushenko, G. Kada, H.J. Gruber, C. Riener, H. Schindler, and P. Hinterdorfer. Static and dynamical properties of single poly(ethylene glycol) molecules investigated by force spectroscopy. *Single Mol.*, 1(2):123 – 128, 2000.

[75] H. Lee, R.M. Venable, A.D. MacKerell Jr., and R.W. Pastor. Molecular dynamics studies of polyethylene oxide and polyethylene glycol: hydrodynamic radius and shape anisotropy. *Biophysical Journal*, 95:1590 – 1599, 2008.

[76] H.J.M. Bowen and L.E. Sutton. *Tables of Interatomic Distances and Configurations in Molecules and Ions*. The Chemical Society, London, 1958.

[77] H. Tadokoro, Y. Chatani, T. Yoshihara, S. Tahara, and S. Murahashi. Unknown. *Makromol. Chem.*, 73:109, 1964.

[78] W.B. Russel, D.A. Saville, and W.R. Schowalter. *Colloidal Dispersions*. Cambridge University Press, 1992.

[79] K.W. Ebagninin, A. Benchabane, and K. Bekkour. Rheological characterisation of poly(ethylene oxide) solutions of difference molecular weights. *Journal of Colloid and Interface Science*, 336(1):360 – 367, 2009.

[80] D.L. Ho, B. Hammouda, and S.R. Kline. Clustering of poly(ethylene oxide) in water revisited. *Journal of Polymer Science: Part B: Polymer Physics*, 41:135 – 138, 2003.

[81] B. Hammouda, D.L. Ho, and S. Kline. Insight into clustering in poly(ethylene oxide) solutions. *Macromolecules*, 37:6932 – 6937, 2004.

[82] B. Hammouda. Solvation characteristics of a model water-soluble polymer. *Journal of Polymer Science: Part B: Polymer Physics*, 44:3195 – 3199, 2006.

[83] K.-J. Liu and J.L. Parsons. Solvent effects on the preferred conformation of poly(ethylene glycols). *Macromolecules*, 2(5):529 – 533, 1969.

[84] T. Takei, K Kurosaki, Y. Nishimoto, and Y. Sugitani. Behavior of bound water in polyethylene oxide studied by dsc and high-frequency spectroscopy. *Analytical Sciences*, 18:681 – 684, 2002.

[85] C. Branca, S. Magazu, G. Masiano, F. Migliardo, and G. Romeo. Hydration parameters of aqueous solutions of poly(ethylene glycol)s by viscosity data. *Physica Scripta*, 66:175 – 179, 2002.

[86] T. Shikata, R. Takahashi, and A. Sakamoto. Hydration of poly(ethylene oxide)s in aqueous solution as studied by dielectric relaxation measurements. *J. Phys. Chem. B*, 110:8941 – 8945, 2006.

[87] J.L. Koenig and A.C. Angood. Unknown. *Journal of Polymer Science*, 23:1787, 1970.

[88] R. Kjellander and E. Florin. Water structure and changes in thermal stability of the system poly(ethylene oxide)-water. *J. Chem. Soc. Faraday Trans 1*, 77:2053 – 2077, 1981.

[89] K. Devanand and J.C. Selser. Polyethylene oxide does not necessarily aggregate in water. *Nature*, 343:739 – 741, 1990.

[90] S. Kinugasa, H. Nakahara, N. Fudagawa, and Y. Koga. Aggregation behaviour of poly(ethylene oxide) in water and methanol. *Macromolecules*, 27:6889 – 6892, 1994.

[91] M. Duval. Monitoring of cluster formation and elimination in poly(ethylene oxide) solutions. *Macromolecules*, 33:7862 – 7867, 2000.

[92] L.R. Cox, E.H. Dunlop, and A.M. North. Role of molecular aggregates in liquid drag reduction by polymers. *Nature*, 249:243 – 245, 1974.

[93] Johannes Kepler. *Mysterium Cosmographicum.* Unknown, 1596.

[94] Girolamo Fracastoro. *Homocentrica.* Unknown, 1538.

[95] A. Einstein. Zur elektrodynamik bewegter körper. *Annalen der Physik*, 17:891, 1905.

[96] A.P. French. *Special Relativity.* CRC Press, 1968.

[97] Poynting J.H. On the transfer of energy in the electromagnetic field. *Phil. Trans.*, 175:277, 1884.

[98] A.L. Schawlow and C.H. Townes. Infrared and optical masers. *Phys. Rev.*, 112: 1940, 1958.

[99] A. Ashkin. Acceleration and trapping of particles by radiation pressure. *Phys. Rev. Lett.*, 24(4):156 – 159, 1970.

[100] A. Ashkin. Atomic-beam deflection by resonance-radiation pressure. *Phys. Rev. Lett.*, 25:1321 – 1324, 1970.

[101] A. Ashkin and J.M. Dziedzic. Optical levitation by radiation pressure. *Appl. Phys. Lett.*, 24:283 – 285, 1971.

[102] A. Ashkin and J.M. Dziedzic. Optical levitation of liquid drops by radiation pressure. *Science*, 40:1073 – 1075, 1975.

[103] A. Ashkin. Trapping of atoms by resonance radiation pressure. *Phys. Rev. Lett.*, 40:729 – 732, 1978.

[104] A. Ashkin, J.M. Dziedzic, J.E. Bjorkholm, and S. Chu. Observation of a single-beam gradient force optical trap for dielectric particles. *Optics Letters*, 11(5):288 – 290, 1986.

[105] S. Chu. Laser trapping of neutral particles. *Scientific American*, page 71, 1992.

[106] J.S. Plewa, T. Del Sol, R.W. Lancelot, W.A. Lopes, D.M. Mueth, K.F. Bradley, and L.S. Gruber. Prospects for holographic optical tweezers. Technical report, Arryx, Inc., 316 N. Michigan Ave. Suite CL-20, Chicago, IL 60601, 2002.

[107] M.D. Wang, H. Yin, R. Landick, J. Gelles, and S.M. Block. Stretching dna with optical tweezers. *Biophysical Journal*, 72:1335 – 1346, 1997.

[108] H. Miyata, R. Yasuda, and K. Kinosita. Strength and lifetime of the bond between actin and skeletal muscle alpha-actinin studied with an optical trapping technique. *J. Biochim. Biophys. Acta*, 1290(1):83 – 88, 1996.

[109] D.E. Dupuis, W.H. Guilford, J. Wu, and D.M. Warshaw. Actin filament mechanics in the laser trap. *J. Muscle Res. Cell Motil.*, 18(1):17 – 30, 1997.

[110] A. Ashkin, K. Schütze, J.M. Diedzic, U. Euteneuer, and M. Schliwa. Force generation of organelle transport measured in vivo by an infrared laser trap. *Nature*, 348:346 – 348, 1990.

[111] G. Mie. Beiträge zur optik trüber medien, speziell kolloidaler metallösungen. *Ann. Phys.*, 25:377 – 452, 1908.

[112] H.C. van de Hulst. *Light Scattering by Small Particles*. John Wiley and Sons, 1957.

[113] S. Chu, R.M. Simmons, J.T. Finer, and J.A. Spudich. Quantitative measurements of force and displacement in an optical trap. *Biophys. J.*, 70:1813 – 1822, 1996.

[114] K. Svoboda and S.M. Block. Biological application of optical forces. *Annual Reviews of Biophysics and Biomolecular Structure*, 23:247 – 285, 1994.

[115] N.B. Simpson, L. Allen, and M.J. Padgett. Optical tweezers and optical spanners with laguerre-gaussian modes. *Journal of Modern Optics*, 43(12):2485 – 2491, 1996.

[116] V. Garces-Chavez, D. McGloin, H. Melville, W. Sibbett, and K. Dholakia. Simultaneous micromanipulation in multiple planes using a self-reconstructing light beam. *Nature*, 419:125, 2002.

[117] L.D. Landau and E.M. Lifschitz. *Statistical Physics*. Butterworth-Heinemann, third edition, 1980.

[118] D.J. Fairhurst. Private Communication, 2009.

[119] R. Brown. A brief account of microscopical observations made in the months of june, july and august, 1827, on the particles contained in the pollen of plants; and on the general existence of active molecules in organic and inorganic bodies. *Philosophical Magazine*, 4:161 – 173, 1827.

[120] R. Brown. Additional remarks on active molecules. *Philosophical Magazine*, 6:161 – 166, 1829.

[121] M. Haw. *Middle world: the restless heart of matter and life*. Palgrave Macmillan, 2007.

[122] M.L. Bachelier. *Théorie de la Spéculation*. PhD thesis, École Normale Supérieure, 1900.

[123] A. Einstein. On the motion of small particles suspended in liquids at rest required by the molecular-kinetic theory of heat. *Annalen der Physik*, 17:549 – 560, 1905.

[124] A. Einstein. *A New Determination of Molecular Dimensions*. PhD thesis, Universität Zurich, 1905.

[125] J. Perrin. *Atomes*. Constable (London), 1916.

[126] J. Perrin and F. Soddy. *Brownian Movement and Molecular Reality*. Taylor and Francis Ltd., 1966.

[127] R. Clausius. Ueber die art der bewegung, welche wir wärme nennen. *Annalen der Physik*, 100:353 – 379, 1857.

[128] A. Einstein and L. Infeld. *The evolution of physics: the growth of ideas from early concepts to relativity and quanta*. Simon and Schuster, 1938.

[129] A.I. Burshtein. *Introduction to thermodynamics and kinetic theory of matter*. J.Wiley and Sons, 1996.

[130] T. Preston and J.R. Cotter. *The theory of heat*. Macmillan, 1904.

[131] R. Kubo. The fluctuation-disspation theorem. *Rep. Prog. Phys.*, 29:255 – 284, 1966.

[132] H. Wang, L. Xiaohui, L. Yinmei, B. Han, L. Lou, and K. Wang. Isolation of a single rice chromosome by optical micromanipulation. *J. Opt. A: Pure Appl. Opt.*, 6:89 – 93, 2004.

[133] J. Scrimgeour, E. Eriksson, and M. Goksör. Laser surgery and optical trapping in a laser scanning microscope. *Methods in Cell Biology*, 82:629 – 646, 2004.

[134] A.D. Ward, A.W Parker, S.W. Botchway, and M Towrie. Development of raman tweezers. Technical Report 95, Central Laser Facility, CLRC Rutherford Appleton Laboratory, Chilton, Didcot, Oxon, 2001.

[135] K. Ajito and K. Torimitsu. Single nanoparticle trapping using a raman tweezers microscope. *Applied Spectroscopy*, 56:541 – 544, 2002.

[136] C.T. Lim, M. Dao, S. Suresh, C.H. Sow, and K.T. Chew. Large deformation of living cells using laser traps. *Acta Materialia*, 52(7):1837 – 1845, 2004.

[137] M.M. Brandao, A. Fontes, M.L. Barjas-Castro, L.C. Barbosa, F.F Costa, C.L. Cesar, and S.T.O Saad. Optical tweezers for measuring red blood cell elasticity: application to the study of drug response in sickle cell disease. *Eur. J. Haematology*, 70(4):207 – 211, 2003.

[138] J. Wu, Y. Li, Z. Liu, Z. Cheng, and L. He. Measurement of the membrane elasticity of red blood cell with osmotic pressure by optical tweezers. *Cryoletters*, 7(2):89 – 95, 2009.

[139] J. Gelles, B.J. Schnapp, and M.P. Sheetz. Tracking kinesin-driven movements with nanometre-scale precision. *Nature*, 331(6155):450 – 453, 1988.

[140] K. Svoboda, C.F. Schmidt, B.J. Schnapp, and S.M Block. Direct observation of kinesin stepping by optical trapping interferometry. *Nature*, 365(6448):721 – 727, 1993.

[141] F. Gittes and C.F. Schmidt. Interference model for back-focal-plane displacement detection in optical tweezers. *Optics Letters*, 23(1):7 – 9, 1998.

[142] S.F. Tolić-Nørrelykke, E. Schäffer, J. Howard, F.S. Pavone, F. Jülicher, and H. Flyvbjerg. Calibration of optical tweeers with positional detection in the back focal plane. *Review of Scientific Instruments*, 77:103101, 2006.

[143] R. Hooke. *Micrographia*. Unknown, 1664.

[144] A.D. Ward. Private Communication, 2009.

[145] D.A. Weitz, D.J. Pine, P.M. Chaikin, and E. Herbolzheimer. Diffusing-wave spectroscopy. *Phys. Rev. Lett*, 60:1134 – 1137, 1988.

[146] J.C. Crocker and D.G. Grier. Methods of digital video microscopy for colloidal studies. *J. Coll. Interf. Sci.*, 179:298 – 310, 1996.

[147] L. Starrs and P. Bartlett. One- and two-point micro-rheology of viscoelastic media. *J. Phys. Cond. Mat.*, 15:251 – 256, 2003.

[148] M. Buchanan, M. Atakhorrami, J.F. Palierne, and C.F. Schmidt. Comparing macrorheology and one- and two-point microrheology in wormlike micelle solutions. *Macromolecules*, 38(21):8840 – 8844, 2005.

[149] H. Faxen. Der widerstand gegen die bewegung einer starren kugel in einer zähen flüssigeit, die zwischen zwei parallelen ebenen wänden eingeschlossen ist. *Annalen der Physik*, 373(10):89 – 119, 1922.

[150] R.M.L. Evans, M. Tassieri, D. Auhl, and T.A. Waigh. Direct conversion of rheological compliance measurements into storage and loss moduli. *Phys. Rev. E*, 80: 012501, 2009.

[151] A.V. Oppenheim and A.S. Willsky. *Signals and Systems*. Prentice-Hall, 1983.

[152] D.A. Weitz and T.G. Mason. Optical measurements of frequency-dependent linear viscoelastic moduli of complex fluids. *Phys. Rev. Lett.*, 74(7):1250 – 1253, 1995.

[153] H. Grabert, P. Hänggi, and P. Talkner. Non-markovian equilibrium dynamics and fluctuation-dissipation theorem. *Physics Letters*, 66(4):255 – 257, 1978.

[154] D. Bonn and W.K. Kegel. Stokes-einstein relations and the fluctuation-dissipation theorem in a supercooled colloidal fluid. *J. Chem. Phys.*, 118(4):2005 – 2009, 2003.

[155] T.G. Mason, H. Gang, and D.A. Weitz. Diffusing-wave-spectroscopy measurements of viscoelasticity of complex fluids. *J. Opt. Soc. Am. A*, 14(1):139 – 149, 1997.

[156] H.A. Kramers. La diffusion de la lumiere par les atomes. *Atti Congresso Internatzionale dei Fisici Como*, 2:545 – 557, 1927.

[157] R.d.L. Kronig. On the theory of dispersion of x-rays. *J. Opt. Soc. Am.*, 12:547 – 556, 1926.

[158] M. Schmiedeberg and H. Stark. One-bead microrheology with rotating particles. *Europhys. Lett.*, 69:629 – 635, 2005.

[159] R.M.L. Evans and C. Kalelkar. Bsr bulletin review: Transforming from time to frequency with minimal artefacts. in press, 2009.

[160] G.W.C. Kaye and T.H Laby. *Tables of physical and chemical constants*. Longman, sixteenth edition, 1995.

[161] S.J. Parkin, G. Knöner, T.A. Nieminen, N.R. Heckenberg, and H. Rubinsztein-Dunlop. Picolitre viscometry using optically rotated particles. *Phys. Rev. E*, 76 (4):014507, 2007.

[162] C. Gosse and V. Croquette. Magnetic tweezers: Micromanipulation and force measurement at the molecular level. *Biophysical Journal*, 82(6):3314 – 3329, 2002.

[163] A.H.B. de Vries, B.E. Krenn, R. van Driel, and J.S. Kanger. Micro magnetic tweezers for nanomanipulation inside live cells. *Biophysical Journal*, 88(3):2137 – 2144, 2005.

[164] J. Shi, D. Ahmed, X. Mao, S.L. Sz-Chin, A. Lawit, and T. Huang. Acoustic tweezers: patterning cells and microparticles using surface acoustic waves (saw). *Lab Chip*, 9:2890, 2009.

[165] D. Mizuno, D.A. Head, F.C. MacKintosh, and C.F. Schmidt. Active and passive microrheology in equilibrium and nonequilibrium systems. *Macromolecules*, 41(19): 7194 – 7202, 2008.

[166] Y. Kimura. Microrheology of soft matter. *J. Phys. Soc. Jpn.*, 78:041005, 2009.

[167] J. Liu, M.J. Casavant, M. Cox, D.A. Walters, P. Boul, W. Lu, A.J. Rimberg, K.A. Smith, Colbert D.T., and R.E. Smalley. Controlled deposition of individual single-walled carbon nanotubes on chemically functionalized templates. *Chemical Physics Letters*, 303:125 – 129, 1999.

[168] E.A. Whitsitt and A.R. Barron. Effect of surfactant on particle morphology for liquid phase deposition of submicron silica. *Journal of Colloid and Interface Science*, 287(1):318 – 325, 2005.

[169] L.E. Pena and J.L. Peters. Self-preserving conditioning shampoo formulation, 1990.

[170] L.A. Duvel. Stable conditioning shampoo containing compatible anionic surfactant/cationic conditioning agent-non-volatile silicone emulsion, 1990.

[171] U. Zoller. Nonionic surfactants in household detergents and their distribution in the environment. *Tenside, surfactants, detergents*, 26:394 – 399, 1989.

[172] M.J. Rosen. *Surfactants and interfacial phenomena*. John Wiley and Sons, 2004.

[173] D.A. Weitz, D.J. Pine, P.N. Pusey, and R.J.A. Tough. Nondiffusive brownian motion studied by diffusing-wave spectroscopy. *Phys. Rev. Lett.*, 63:1747, 1989.

[174] P. Mukerjee and K.J. Mysels. Critical micelle concentration of aqueous surfactant solutions. NSRDS-NBS 36, US Government Printing Office, Washington, 1971.

[175] G.J. Lee and F. Jones. Hair-styling mousse. United States Patent 5,681,546, 1997.

[176] S.T. Adamy and F.R. Cala. Toothpaste compositions containing cetylpyridinium chloride. United States Patent 6,471,948, 2002.

[177] A. Hekmat, A.A. Saboury, A.A. Moosavi-Movahedi, H. Ghourchian, and F. Ahmad. Effects of ph on the activity and structure of choline oxidase from alcaligenes species. *Acta Biochimica Polonica*, 55(3):549 – 557, 2008.

[178] K.K. Shaffer, J.P. Jaimes, M.K. Hordinsky, G.R. Zielke, and E.M. Warshaw. Allergenicity and cross-reactivity of coconut oil derivatives: A double-blind randomized controlled pilot study. *Dermatitis*, 17(2):71 – 76, 2006.

[179] M.S. Dahanayake, S. Kesavan, and A. Colaco. Composition and method for thickening heavy aqueous brines with cationic guar. United States Patent 7,629,296, 2005.

[180] J.C.T. Kwak. *Polymer-Surfactant Systems.* CRC Press, 1998.

[181] E.S. Reid and A.M. Murray. Conditioning shampoo comprising a surfactant, a non-volatile silicone oil and guar hydroxypropyltrimonium chloride as a cationic conditioning polymer. United States Patent 5,085,857, 1992.

[182] J. Anthony and M. Mossman. Hair conditioning composition containing a non-guar galactomannan polymer derivative. United States Patent 20070292380, 2007.

[183] A. Ferrante. Private Communication, 2009.

[184] N.C Christov, N.D. Denkov, P.A. Kralchevsky, K.P. Ananthapadmanabhan, and A. Lips. Synergistic sphere-to-rod micelle transition in mixed solutions of sodium dodecyl sulfate and cocoamidopropyl betaine. *Langmuir*, 20(3):565 – 571, 2004.

[185] L. Ramos and C. Ligoure. Structure of a new type of transient network: Entangled wormlike micelles bridged by telechelic polymers. *Macromolecules*, 40(4):1248 – 1251, 2007.

[186] E.D. Goddard and J.V. Gruber. *Principles of polymer science and technology in cosmetics and personal care.* CRC Press, 1999.

[187] J.-F. Argiller, R. Ramachandran, W.C. Harris, and M. Tirrell. Polymer-surfactant interactions studied with the surface force apparatus. *Journal of Colloid and Interface Science*, 146(1):242 – 250, 1991.

[188] F. Tokiwa and J. Imamura. *J. Am. Chem. Soc.*, 49:166, 1972.

[189] J.J. Parran. United States Patent 3,761,418, 1973.

[190] S.S. Sandhu, C.R. Robbins, and W.-M. Cheng. Hair conditioning shampoo. WO94/06409 A1, 1994.

[191] F.J. Prescott, E. Hahnel, and D. Day. *Drug. Cosmet. Ind.*, 93:443, 1963.

[192] D. Voisin and B. Vincent. Flocculation in mixtures of cationic polyelectrolytes and anionic surfactants. *Advances in Colloid and Interface Science*, 106:1 – 22, 2003.

[193] K. Nakaya-Yaegashi, L. Ramos, H. Tabuteau, and C. Ligoure. Linear viscoelasticity of entangled wormlike micelles bridged by telechelic polymers: An experimental model for a double transient network. *Journal of Rheology*, 52(2):359 – 378, 2008.

[194] F. Fox, P. McSweeney, T. Cogan, and T. Guinee. *Cheese: Chemistry, Physics and Microbiology.* Academic Press, 2004.

[195] C. Flood. Wormlike micelles mediated by polyelectrolyte. *Langmuir*, 21(17):7646 – 7652, 2005.

[196] A.R. Khokhlov, E.Y. Kramarenko, E.E. Makhaeva, and S.G. Starodubtzev. Collapse of polyelectrolyte networks induced by their interaction with an oppositely charged surfactant. theory. *Macromolecular Theory and Simulations*, 1:105 – 118, 2003.

[197] Z. Lin, L.E. Scriven, and H.T. Davis. Cryogenic electron microscopy of rodlike or wormlike micelles in aqueous solutions of nonionic surfactant hexaethylene glycol monohexadecyl ether. *Langmuir*, 8(9):2200 – 2205, 1992.

[198] Y.I. Gonzalez and E.W. Kaler. Cryo-tem studies of worm-like micellar solutions. *Current Opinion in Colloid and Interface Science*, 10(5 – 6):256 – 260, 2005.

[199] A. Ferrante. Private Communication, 2007.

[200] W. Jia and H.-H. Qiu. Experimental investigation of droplet dynamics and heat transfer in spray cooling. *Experimental Thermal and Fluid Science*, 27(7):829 – 838, 2003.

[201] R.L. Matlosz, S. Leipziger, and T.P. Torda. Investigation of liquid drop evaporation in a high temperature and high pressure environment. *International Journal of Heat and Mass Transfer*, 15(4):831 – 846, 1972.

[202] K. Harstad and J. Bellan. Isolated liquid oxygen drop behaviour in fluid hydrogen at rocket chamber pressures. *International Journal of Heat and Mass Transfer*, 41: 3537 – 3550, 1998.

[203] L. Pauchard and C. Allain. Buckling instability induced by polymer solution drying. *Europhys. Lett.*, 62:897–903, 2003.

[204] R.D. Deegan, O. Bakajin, T.F. Dupont, G. Huber, S.R. Nagel, and T.A. Witten. Capillary flow as the cause of ring stains from dried liquid drops. *Nature*, 389:827 – 829, 1997.

[205] H. Hu and R.G. Larson. Analysis of the effects of marangoni stresses on the microflow in an evaporating sessile droplet. *Langmuir*, 21:3972 – 3980, 2005.

[206] H. Hu and R.G. Larson. Marangoni effect reverses coffee-ring depositions. *J. Phys. Chem. B*, 110:7090 – 7094, 2006.

[207] F. Parisse and C. Allain. Unknown. *Langmuir*, 13:3598 – 3602, 1997.

[208] D.A. Head. Modelling the elastic deformation of polymer crusts formed by sessile droplet evaporation. *Phys. Rev. E: Stat., Nonlinear, Soft Matter Phys.*, 74:021601, 2006.

[209] S.M. Rowan, M.I. Newton, F.W. Driewer, and G. McHale. Evaporation of microdroplets of azeotropic liquids. *J. Phys. Chem. B*, 104(34):8217 – 8220, 2000.

[210] H.-J. Butt, K. Graf, and M. Kappl. *Physics and Chemistry of Interfaces*. Wiley-VCH, 2003.

[211] A. Mistlberger, J.M. Liebmann, D.S. Greenfield, M.E. Pons, S.T. Hoh, H. Ishikawa, and R. Ritch. Heidelberg retina tomography and optical coherence tomography in normal, ocular-hypertensive and glaucomatous eyes. *Opthalmology*, 106(10):2027 – 2032, 1999.

[212] S.T. Hoh, D.S. Greenfield, A. Mistlberger, J.M. Liebmann, H. Ishikawa, and R. Ritch. Optical coherence tomography and scanning laser polarimetry in normal, ocular hypertensive and glaucomatous eyes. *American Journal of Opthalmology*, 129(2):129 – 135, 2000.

[213] M.E. Brezinski, G.J. Tearney, B.E. Bouma, S.A. Boppart, M.R. Hee, E.A. Swanson, J.F. Southern, and J.G. Fujimoto. Imaging of coronary artery microstructure (in vitro) with optical coherence tomography. *American Journal of Cardiology*, 77(1): 92 – 93, 1996.

[214] M.E. Brezinski. *Optical Coherence Tomography: Principles and Applications*. Academic Press, 2006.

[215] W. Drexler. *Optical Coherence Tomography: Technology and Applications*. Springer, 2008.

[216] J.W. McBridge and C. Maul. The 3d measurement and analysis of high-precision surfaces using con-focal optical methods. *IEICE Transactions on Electronics*, E87-C(8):1261 – 1267, 2004.

[217] V. Fadeyev, C. Haber, C. Maul, J.W. McBride, and M. Golden. Reconstruction of recorded sound from an edison cylinder using three-dimensional noncontact optical surface metrology. *Journal of the Audio Engineering Society*, 53(6):485 – 508, 2005.

[218] F. Sbalzarini and P. Koumoutsakos. Feature point tracking and trajectory analysis for video imaging in cell biology. *Journal of Structural Biology*, 151(2):182 – 195, 2005.

[219] R.B. Buxton. *Introduction to functional magnetic resonance imaging: principles and techniques*. Cambridge University Press, 2002.

[220] M.T. Vlaardingerbroek and J.A. den Boer. *Magnetic resonance imaging: theory and practice*. Springer, 2003.

[221] C.E. Lyman. *Scanning Electron Microscopy, X-Ray Microanalysis, and Analytical Electron Microscopy: A Laboratory Workbook*. Springer, 1990.

[222] J. Goldstein, D.E. Newbury, D.C. Joy, P. Echlin, C.E. Lyman, and E. Lifshin. *Scanning Electron Microscopy and X-Ray Microanalysis*. Springer, 2003.

[223] P. Beltrame, P. Hänggi, and U. Thiele. Depinning of three-dimensional drops from wettability defects. *Europhysics Letters*, 86(2):24006, 2009.

[224] M. Haw. Private Communication, 2010.

[225] W.D. Ristenpart, P.G. Kim, C. Domingues, J. Wan, and H.A. Stone. Influence of substrate conductivity on circulation reversal in evaporating drops. *Physics Review Letters*, 99(23):234502, 2007.

[226] D.I.R. Willmer, K.A. Baldwin, C. Kwartnik, and D.J. Fairhurst. Growth of solid conical structures during multistage drying of sessile poly(ethylene oxide) droplets. *Phys. Chem. Chem. Phys.*, 12:3998 – 4004, 2010.

[227] A.J. Lovinger and C.C. Gryte. The morphology of directionally solidified poly(ethylene oxide) spherulites. *Macromolecules*, 9(2):247 – 253, 1976.

[228] F.P. Price and R.W. Kilb. The morphology and internal structure of poly(ethylene oxide) spherulites. *Journal of Polymer Science*, 57(165):395 – 403, 2003.

[229] Y.O. Popov. Evaporative deposition patterns: Spatial dimensions of the deposit. *Physics Review E*, 71:036313, 2005.

[230] M.W. Kim and B.H. Cao. Additional reduction of surface tension of aqueous polyethylene oxide (peo) solution at high polymer concentration. *Europhysics Letters*, 24:229, 1993.

[231] L.F. Francis, A.V. McCormick, D.M. Vaessen, and J.A. Payne. Unknown. *J. Mater. Sci.*, 37:4717 – 4731, 2002.

[232] W.J. Barnes, W.G. Luetzel, and F.P. Price. Crystallization of poly(ethylene oxide) in bulk. *J. Phys. Chem.*, 65(10):1742 – 1748, 1961.

[233] L.E. Cohen and A.M. Rocco. Study of the crystallisation kinetics. poly(ethylene oxide) and a blend of poly(ethylene oxide) and poly(bisphenol a-co-epichlorohydrin). *Journal of Thermal Analysis and Calorimetry*, 59(3):625 –632, 2000.

[234] H. Wang, J.K. Keum, A. Hiltner, E. Baer, B. Freeman, A. Rozanski, and A. Galeski. Confined crystallisation of polyethylene oxide in nanolayer assemblies. *Science*, 323(5915):757 – 760, 2009.

[235] J. Kepler. Strena seu de nive sexangula. Monograph, 1611.

[236] J. Nittmann and H.E. Stanley. Non-deterministic approach to anisotropic growth patterns with continuously tunable morphology: the fractal properties of some real snowflakes. *Journal of Physics A: Mathematical and General*, 20(17), 1987.

[237] J. Zebrowski, V. Prasad, W. Zhang, L.M. Walker, and D.A. Weitz. Shake-gels: shear-induced gelation of laponite-peo mixtures. *Colloids and Surfaces A: Physicochem. Eng. Aspects*, 213:189 – 197, 2003.

[238] K.A. Baldwin. Undergraduate dissertation, 2009.

[239] E. Widjaja and M.T. Harris. Particle deposition study during sessile drop evaporation. *American Institute of Chemical Engineers Journal*, 54(9):2250 – 2260, 2008.

[240] S. Lawman. Private Communication, 2010.

[241] R.D. Deegan. *Deposition at pinned and depinned contact lines: Pattern formation and applications*. PhD thesis, University of Chicago, 1998.

[242] R.D. Deegan, O. Bakajin, G. Huber, S.R. Nagel, and T.A. Witten. Contact line deposits in an evaporating drop. *Phys. Rev. E*, 62(1):756 – 765, 2000.

[243] S. del Ferro. Unpublished, c.1500.

[244] G. Cardano. *Ars Magna*. 1545.